TECHNISCHE UNIVERSITÄT MÜNCHEN
Fakultät für Chemie

Ab Initio On-the-Fly Trajectory Surface-Hopping Dynamics: Photocatalytic Water-Splitting Reaction and Femtosecond Pump-Probe Spectroscopy

DISSERTATION

Zur Erlangung des akademischen Grades
Doktor der Naturwissenschaften

vorgelegt von
Xiang Huang

Garching bei München, 2022

TECHNISCHE UNIVERSITÄT MÜNCHEN
Fakultät für Chemie

Ab Initio On-the-Fly Trajectory Surface-Hopping Dynamics: Photocatalytic Water-Splitting Reaction and Femtosecond Pump-Probe Spectroscopy

Xiang Huang

Vollständiger Abdruck der von der
Fakultät für Chemie der Technischen Universität München
zur Erlangung des akademischen Grades eines
Doktors der Naturwissenschaften
genehmigten Dissertation

Vorsitzende:
Prof. Dr. Sebastian Günter
Prüfer der Dissertation:
1. Prof. Dr. Wolfgang Domcke
2. Prof. Dr. Jürgen Hauer

Die Dissertation wurde am 15.07.2022 bei der Technischen Universität München eingereicht und durch die Fakultät für Chemie am 04.08.2022 angenommen.

Abstract

The trajectory surface-hopping (TSH) method has emerged in recent decades as a computationally efficient tool for the simulation of photoinduced chemical dynamics. In the TSH method, the motion of the nuclei is described with classical mechanics, while the electrons are described with quantum mechanics. At near-degeneracies of Born-Oppenheimer electronic potential-energy surfaces, nonadiabatic transitions occur, which are taken into account by surface-hopping events of classical trajectories. Combined with modern ab initio electronic-structure methods for the calculation of energy gradients and surface-hopping probabilities, the TSH method is a powerful tool for first-principles simulations of nonadiabatic photochemical dynamics. In the present work, a novel variant of TSH has been further developed which is based on the time-honored Landau-Zener formula, termed Landau-Zener surface hopping (LZSH). Two up-to-date scientific problems in photochemistry and spectroscopy were addressed with this computational technique: (i) the photooxidation of water molecules with organic photooxidants and (ii) the computation of femtosecond time-resolved nonlinear signals from first principles. Concerning (i), the photochemical mechanisms of water oxidation and hydrogen evolution in hydrogen-bonded complexes of N-heterocycles with water molecules were explored by ab initio nonadiabatic dynamics simulations for the example of the heptazine (tri-s-triazine) chromophore. A structurally and temporally resolved picture of the proton-coupled electron transfer (PCET) reaction leading to water oxidation in the heptazine-H_2O complex has been developed. Stimulated by recent experimental data, the PCET reaction in complexes of trianisoleheptazine (TAHz) with phenol and methoxyphenol was explored with TSH calculations. Concerning (ii), an ab initio theoretical framework for the simulation of femtosecond time-resolved spectroscopic signals with quasi-classical trajectories was developed. The feasibility and computational efficiency of this novel approach is demonstrated by the calculation of transient-absorption pump-probe spectra and two-dimensional electronic spectra for the pyrazine molecule.

Zusammenfassung

Die “Trajektorien-Surface-Hoppping” (TSH) Methode hat sich in den vergangenen Dekaden als ein rechentechnisch effizientes Werkzeug für die Simulation photoinduzierter chemischer Prozesse erwiesen. In der TSH-Methode wird die Bewegung der Atomkerne mit klassischer Dynamik beschrieben, während die Elektronen quantenmechanisch beschrieben werden. Nichtadiabatische Übergänge finden an Entartungen von Born-Oppenheimer-Potentialenergieflächen statt und werden als elektronische Hüpfprozesse (hoppings) berücksichtigt. Zusammen mit modernen ab initio Methoden für die Berechnung von elektronischen Energiegradienten und von nichtadiabatischen Hüpf-Wahrscheinlichkeiten stellt die TSH-Methode ein mächtiges Werkzeug für die Simulation von nichtadiabatischer photochemischer Dynamik dar. In der vorliegenden Arbeit wurde eine neuartige Variante von TSH weiterentwickelt, welche auf der berühmten Landau-Zener-Formel beruht und als Landau-Zener-Surface-Hopping (LZSH) Methode bezeichnet wird. Zwei aktuelle Probleme in Photochemie und Spektroskopie wurden mit dieser Methode untersucht: (i) die Photooxidation von Wasser mit organischen Photooxidantien und (ii) die ab initio Berechnung von Femtosekunden-zeitaufgelösten nichtlinearen Spektren. Bezüglich (i) wurden die photochemischen Mechanismen der Oxidation von Wasser und der Erzeugung von Wasserstoff in Wasserstoff-Brücken-gebundenen Komplexen von N-Heterozyklen mit Wasser-Molekülen mit der ab initio TSH-Methode für das Beispiel von Heptazin (Tri-s-Triazin) erforscht. Es wurde ein strukturell und zeitlich aufgelöstes Bild der Protonen-gekoppelten Elektron-Transfer (PCET) Reaktion, welche zur Oxidation von Wasser in Heptazin-Wasser-Komplexen führt, entwickelt. Stimuliert durch neuere experimentelle Daten wurde die PCET-Reaktion in Komplexen von Trianisoleheptazin (TAHz) mit Phenol und Methoxyphenol mit TSH-Rechnungen untersucht. Hinsichtlich (ii) wurde eine ab initio Rechenmethode für die Simulation von Femtosekunden-zeitaufgelösten spektroskopischen Signalen mit quasi-klassischen Trajektorien entwickelt. Die Durchführbarkeit und die rechentechnische Effizienz dieser neuartigen Methode wird durch die Berechnung von Pump-Prob-Spektren und von zweidimensionalen elektronischen Spektren für das Molekül Pyrazin demonstriert.

Coming from China to study in Germany is not an easy task for me. To make it a worthwhile journey is yet a more challenging duty. First, I would like to address my thanks to Prof. Domcke, for his patient, instructive and foresighted guide throughout my PhD study as well as the underlying influence on me in the way of interpreting things in life. He supported me during the struggle with problems and helped me not to be lost in front of choices. Without it, I would not be as confident as I am now to defend my limited understanding on academic topics and to move forward in other fields.

I would also like to thank other group members and visitors for providing all the fruitful discussions and a pleasant working atmosphere. Special thanks to Prof. Maxim F. Gelin for his open-minded and insightful discussions on spectroscopy.

Finally, I would like to thank my family for all their support during my study, especially Lilian, who continues encouraging me despite failure or success.

Thank you all!

This doctoral thesis is a publication-based thesis and the work presented herein has been published in international peer-reviewed scientific journals. This thesis provides a compact literature review on nonadiabatic trajectory surface-hopping (TSH) dynamics, especially its application in photocatalytic water-splitting reactions and nonlinear time-resolved spectroscopy. An overview of the employed TSH method, especially the Landau-Zener surface-hopping algorithm, is given. For each of the five published papers, a short summary as well as a description of my contribution to each piece of work is provided. The last section provides a short summary of the content of the thesis and possible future extensions and research directions are discussed.

The presented work was performed from Nov 2018 to May 2022 in the Department of Chemistry of the Technical University of Munich under the supervision of Prof. Dr. Wolfgang Domcke.

Xiang Huang

Garching, June 2022

"Two states do not intersect with each other; their energies do"
Wolfgang Domcke

Contents

1 Introduction

The time-resolved characterization of ultrafast nonadiabatic electronic transitions is an essential topic in the current research on photoinduced chemical reactions. Information on the excited-state dynamics of molecules at ultrafast (femtosecond) time scales is crucial for the understanding of the photochemistry which typically occurs on longer (nanosecond to microsecond) time scales.

While exact numerical solutions of the time-dependent Schrödinger equation (TDSE) for molecular problems remain unaffordable with current computational facilities, the Born-Oppenheimer approximation[1] (BOA) opens the way for practically feasible calculations by the separation of the nuclear and electronic motions due to their vastly different intrinsic speeds. While the BOA generally is perfectly suitable for the chemical dynamics in the electronic ground state, the BOA often fails for the dynamics in excited electronic states due to the occurrence of degeneracies or near degeneracies of electronic potential-energy surfaces (PESs). For excited-state dynamics, strong nonadiabatic effects and the complete breakdown of the BOA are the rule rather than the exception.[2-6]

Pursing a fully quantum mechanical approach, one can make use of the Born-Huang expansion[7] of the total wave function, which includes off-diagonal coupling terms between electronic states in addition to the diagonal potential-energy terms of electronic Hamiltonian. However, nuclear quantum dynamics calculations on nonadiabatically coupled PES are a challenging task for polyatomic molecules. Early applications were restricted to only a few relevant nuclear modes and the harmonic oscillator approximation was invoked for the nuclear motion. Domcke, Köppel and Cederbaum[8] introduced the linear vibronic coupling approach based on ab initio-based few-state few-vibrational-mode models. These models are defined in a diabatic electronic representation[8]

in which the electronic wave functions do not depend on the nuclear coordinates, in contrast to the adiabatic electronic wave functions of the Born-Huang expansion.

While the computational cost of nuclear quantum dynamics calculations scales exponentially with the number of degrees of freedom, classical dynamics scales only linearly with the number of degrees of freedom. This fact is the motivation for various semi-classical (with phase information) and quasi-classical (without phase information) approximation schemes.[9-13] The most widely used methods are derived from the classical path approximation.[14] In the classical path approximation, the nuclei propagate on electronic PES according to Newton's equation. Newton's equation is solved numerically with a sufficiently short time step. The forces on the nuclei are computed at each time step "on-the-fly" with a suitable electronic-structure method. The nonadiabatic transitions during the propagation of the nuclear motion are taken into account by different algorithms.

There exist three main approximation schemes in ab initio on-the-fly nonadiabatic dynamics: the mean-field Ehrenfest (MFE) approach,[15] the trajectory surface-hopping (TSH)[16] approach and the multiple spawning (MS) method.[17] In the MFE method, the dynamics of the slow degrees of freedom (the nuclei) is described by Newton's equation and the forces driving the nuclear motion are determined by the mean energy of the fast degrees of freedom (the electrons). In TSH algorithms, the nuclei propagate on individual electronic PES and nonadiabatic transitions are taken into account by stochastic transitions between PESs, so-called surface-hopping events. The different algorithms differ by the computation of the transition probability at near-degeneracies of electronic PESs. The TSH propagation algorithm is straightforward to implement and numerically robust. Therefore, this simulation method is most widely employed in the field of nonadiabatic dynamics.[18] The MS method[17] utilizes Gaussian basis functions to represent the nuclear wave functions. The positions and

momenta of the Gaussian basis functions follow classical equations of motion on individual PES. The bifurcation of nuclear wave packets in regions of strong nonadiabaticity is taken into account by "spawning" events.

After the introduction of the TSH concept in 1971,[19] Tully proposed the so-called fewest-switches surface hopping (FSSH) algorithm in which the transition probability is evaluated from the coefficients of the time-dependent electronic wave function.[16] This algorithm became the most widely used algorithm in TSH calculations.[18, 20-22] Grannucci and Persico proposed the correction taking account of the decoherence problem.[23] Truhlar and coworkers compared the performances of many variants of the TSH method[24-26] and developed corrections for classically forbidden electronic transitions.[27-29] Mitrić and coworkers introduced the field-induced surface hopping (FISH) algorithm.[30] Lan developed the on-the-fly surface-hopping program JADE for polyatomic systems.[31] The González group developed the SHARC (surface hopping with arbitrary couplings) program[32] and performed many studies of photoinduced dynamics including also triplet states and intersystem crossing from singlet states to triplet states [33, 34] [35, 36]

For the nonadiabatic TSH studies of the present work, the code developed by Došlić and coworkers, named Zaghop,[37] was used and further developed. The Zaghop code was employed by the Došlić group for studies of the photodeactivation pathways of adenine,[37] hydroylamine,[38] phenylalanine,[39] Furan,[40] and kynurenines,[41] among others.

In the present work, the ab initio TSH method has been used as a computational tool to investigate the photoinduced oxidation of water in hydrogen-bonded complexes of organic photooxidants with water molecules. The key process in this photoreaction is the so-called proton-coupled electron transfer (PCET) process. In previous work of the Domcke group, the photoinduced PCET reaction in pyridine-water complexes was investigated with electronic-structure

calculations and TSH simulations.[42] Pyridine serves in this context as the simplest representative of N-heterocyclic molecules. The PCET reaction in pyridine-water complexes was characterized by static calculations of PE profiles along the intermolecular proton transfer coordinate from water to pyridine. [43, 44] Nonadiabatic TSH dynamics simulations were performed for pyridine-water clusters of different sizes.[42] The theoretical results agree well with the experimental results reported by Jouvet and coworkers.[45] In this molecular-beam experiment, the photoinduced PCET reaction in pyridine-water clusters was observed by the detection of the pyridinyl radical. The photoreaction was observed only in pyridine-$(H_2O)_n$ clusters with more than three water molecules. The ab initio dynamics simulations revealed that at least three water molecules are necessary to accommodate the excess energy of the photoreaction without dissociation, which explains the experimental observation.

The first project of my PhD research has been the investigation of the analogous photoinduced PCET reaction in pyrimidine-water complexes with ab initio on-the-fly simulations. The ADC(2) method (algebraic-diagrammatic construction of second order)[46-48] was employed in these calculations. This work was undertaken in close collaboration with the group of Christophe Jouvet in Aix-Marseille.

While pyridine-water and pyrimidine-water clusters are interesting model systems for the investigation of the basic mechanisms of water photooxidation by a PCET reaction, they are not of practical interest, because the absorption of these N-heterocycles is in the far UV and their excited-state lifetimes are in the femtosecond regime, which is detrimental for productive photochemical reactions. On the other hand, polymeric carbon nitride materials consisting of heptazine (tri-s-triazine) building blocks received enormous attention in the field of water-splitting photocatalysis since 2009, when Antonietti, Domen, Maeda and coworkers reported the observation of hydrogen evolution with these materials.[49] Historically, polymeric carbon nitride was first synthesized by

Berzelius and Justus von Liebig in 1834 and termed "melon" by Justus von Liebig due to its yellowish color.[50] About 100 years later, Pauling and Sturdivant clarified the molecular structure of melon, identifying heptazine (Hz) as its building molecular block.[51]

To obtain insight into the mechanism of water photooxidation with polymeric carbon nitrides, Ehrmaier and coworkers explored the excited states of the Hz chromophore and the photochemistry of the hydrogen-bonded Hz-H_2O complex with ab initio electronic-structure calculations.[52] It was shown that Hz possesses, in addition to a bright excited state of $^1\pi\pi^*$ character and several dark $^1n\pi^*$ states, a low-lying (excitation energy 2.6 eV) dark $^1\pi\pi^*$ state. It was discovered that this lowest singlet excited state is energetically below the lowest triplet excited state of Hz,[53] in violation of Hund's multiplicity rule. This implies that excited-state quenching by intersystem crossing (ISC) does not exist in the lowest singlet excited state of Hz. The absence of ISC together with the symmetry-forbidden fluorescence results in an exceptionally long lifetime of the S_1 state of Hz (of the order of 300 ns), which therefore can serve as a reservoir for the storage of electronic excitation energy. In the Hz-H_2O complex, a low-lying dark charge-transfer (CT) state was identified which provides the driving force for the PCET reaction in the Hz-H_2O complex.[52]

A derivative of Hz, trianisoleheptazine (TAHz), was synthesized and structurally characterized by the Schlenker group at the University of Washington.[54] In contrast to Hz, which spontaneously hydrolyzes in the presence of water and light,[55-57] TAHz was found to be chemically and photochemically exceptionally stable in organic solvents such as toluene. Irradiation of dispersions of TAHz in water, on the other hand, resulted in the generation of OH radicals and the evolution of H_2, which confirms the photocatalytic activity of TAHz for the water-splitting reaction.[54]

The experimental results of the Schlenker group on the photochemistry of TAHz in water provided the motivation for the investigation of the dynamics of

the excited-state PCET reaction of complexes of Hz and TAHz with protic substrate molecules with ab initio simulation methods. These simulations have been the main objective of my PhD research project. To make these simulations feasible, the TAHz molecule had to be replaced by the simpler Hz molecule and the aqueous environment was approximated by a single water molecule. The ab initio nonadiabatic dynamics simulations were performed with the ADC(2) electronic-structure method.[46] With the exception of an earlier simulation of the PCET reaction in the Hz-H_2O complex at the TDDFT level,[58] these represent the first ab initio computational studies of photocatalytic water oxidation with the Hz chromophore.

The poor solubility of TAHz in water precludes comprehensive experimental studies of the concentration dependence of the photoreaction. To overcome this limitation, Schlenker and coworkers turned to studies of the photochemistry of TAHz with phenol and derivatives of phenol in toluene solution.[59] The oxidation potential of phenol can be tuned over a wide range by substituents, a fact that has been exploited in previous studies of photoinduced PCET reactions with organic chromophores.[60, 61] It was shown by Schlenker and coworkers that the quenching rate of the S_1 state of TAHz in TAHz-phenol complexes is strongly enhanced by electron-donating substituents on phenol, such as methoxy. With support from ab initio electronic structure calculations, a qualitative picture of the excited-state PCET reactivity of complexes of TAHz with phenolic substrates was developed.[62]

A more quantitative analysis of the photochemistry of TAHz-phenol complexes requires theoretical support beyond static electronic-structure calculations. In the frame of the present PhD project, ab initio nonadiabatic dynamics simulations were performed for two selected complexes, TAHz-phenol and TAHz-methoxyphenol. Due to the size of these systems, on-the-fly simulations with wave-function-based ab initio electronic structure methods such as ADC(2)

were not possible. Therefore, the simulations were performed with the computationally less expensive time-dependent density functional theory (TDDFT). Using ADC(2) as reference, the accuracy of TDDFT with various exchange-correlation functionals was carefully benchmarked along the reaction path of the excited-state PCET reaction. The ωB97X-D functional[63] was selected for the dynamics simulations for the TAHz-phenol and TAHz-methoxyphenol complexes.

The second topic of my PhD research has been the computation of femtosecond time-resolved nonlinear spectra from first principles with full-dimensional quasi-classical trajectory methods. While nonadiabatic dynamics simulations are nowadays widely employed for the study of ultrafast photophysical processes in polyatomic molecules, the results typically are the time-dependent population probabilities of electronic states.[18] These electronic population probabilities are, however, not directly experimentally observable. The experimental observables rather are time-and frequency resolved signals which are generated with femtosecond laser pulses in the visible, UV or X-ray spectral ranges.

Enormous progress has been made in the past decades with the generation of ultrashort laser pulses.[64-67] In the UV and visible spectral range, pulses with durations of a few femtoseconds or less are available.[66-69] With these pulses, the fastest light-driven processes in matter, like vibrational dynamics, radiationless decay or photodissociation can be resolved in time. In addition, numerous sophisticated spectroscopic techniques, such as N-wave-mixing spectroscopies and multidimensional spectroscopies have been developed.[70-72]

The simplest, most established and most widely used time-resolved spectroscopic technique is pump-probe (PP) spectroscopy. Following the excitation of the sample by a short pump pulse, the transmission of a short probe pulse is measured as a function of the time delay between the pulses. In 1999, Ahmed Zewail won the Nobel Prize in Chemistry for his pioneering studies of chemical

reactions with femtosecond time resolved PP spectroscopy.[65, 73, 74] More recently, PP spectroscopy has been used, among many other applications, for the characterization of semiconductors.[75] Time- and frequency-resolved transient absorption (TA) PP spectra can be recorded as integral transmission signals, whereby the carrier frequency of the probe pulse is tuned, or as dispersed signals, whereby the spectrum of the transmitted probe pulse is dispersed with a spectrometer.[70]

A more sophisticated spectroscopic technique is two-dimensional (2D) electronic spectroscopy.[76] It is a four-wave-mixing (4WM) technique and a variant of three-pulse photon-echo spectroscopy.[77] The signal is resolved both in the pump frequency as well as in the probe frequency, hence the designation 2D spectroscopy. In addition, the signal carries time-resolved information via its dependence on the so-called waiting time (the time interval between the second pulse and the third pulse). While electronic 2D spectroscopy was mainly applied to multi-chromophoric systems, in particular biological antenna complexes,[78, 79] it also has been applied to single molecular chromophores and has been shown to provide unprecedentedly detailed information on the excited-state relaxation dynamics.[80-82]

The standard theoretical framework for the calculation of nonlinear time-resolved signals is the nonlinear response function formalism developed by Mukamel and coworkers[70] which is based on third-order perturbation theory in the laser-matter interaction. All 4WM signals can be expressed in terms of third-order dipole response functions which have to the convoluted with the electric fields of the laser pulses to obtain the experimental signal.

For complex material systems, the evaluation of the nonlinear response functions on a grid of three time variables can become very cumbersome and computationally expensive. For TA PP signals, Mukamel and coworkers developed the doorway-window (DW) formalism which applies for non-overlapping short laser pulses.[70, 83, 84] The DW formalism was extended to 2D spectra by Gelin and

Kosov.[85] It has been shown by Mukamel and coworkers that the DW expression for TA PP spectra is well suited for a classical description of the nuclear motion. The classical approximation greatly simplifies the calculation for spectroscopic signals for systems with many nuclear degrees of freedom.

In the present work, the classical version of the DW formalism has been implemented for the first time with on-the-fly ab initio electronic-structure calculations. I have performed calculations of TA PP as well as 2D spectra for the pyrazine molecule which is a very well established benchmark system for ultrafast photoinduced dynamics through conical intersections.[86-91] The ADC(2) electronic structure method has been combined with a computationally efficient TSH algorithm based on the Landau-Zener formula to perform these calculations.

2 Electronic-Structure Methods

2.1 MP2/ADC(2)

In principle, any ab initio method for which analytic gradients are available can be employed for quasi-classical on-the-fly nuclear dynamics simulations. Considering that the time step for the solution of Newton's equation typically is 0.5 fs or less and that ensembles of at least hundreds of trajectories have to be calculated, it is clear that many thousands of single-point electronic-structure calculations are required for a typical application. The computational cost of a single-point electronic-structure calculation therefore is an essential parameter.

The most widely used and computationally efficient post-Hartree-Fock (HF) wave-function method is the MP2 method (Møller–Plesset perturbation theory of second order).[92] MP perturbation theory exhibits oscillatory convergence behavior, that is, MP2 typically overestimates the correlation energy, while MP3 underestimates and MP4 overestimates again. In practice, only the MP2 method is useful for on-the-fly calculations of energy gradients in trajectory simulations. The cost of the MP2 energy calculation can be substantially reduced by the resolution-of-the-identity (RI) approximation which speeds up the evaluation of two-electron integrals.[93]

Electronic excitation energies can be obtained from the polarization propagator, that is, the particle-hole Green's function.[46] In the ADC(2) method, the electronic excitation energies are evaluated as the poles of the polarization propagator. The ADC(2) method yields excitation energies which generally are at the same level of accuracy as MP2. Like for MP2, the computational cost of ADC(2)

scales as $\sim N^5$, which renders the method more efficient than the coupled-cluster method with singles and doubles which scales as $\sim N^6$. Analytic gradients and the RI approximation are available for ADC(2).[94]

In the ADC(2) method, excitation energies are calculated as eigenvalues of a Hermitian matrix. Therefore, conical intersections (CIs) of excited-state potential-energy surfaces are well described by the ADC(2) method. Benchmark studies on DNA nucleobases,[95] for example, in comparison with higher-level methods such as the equation-of-motion coupled-cluster singles and doubles (EOM-CCSD) and noniterative triples (EOM-CCSD(T)) methods have confirmed the accuracy of the ADC(2) method. Despite the speed-up by the RI approximation, wave-function-based methods like ADC(2) are generally too expensive for on-the-fly dynamics simulations for large molecules. With a truncation of occupied and virtual MOs,[96] excited-state calculations at the ADC(2) level have become possible for organic semiconductors[96] and polymers.[97] Recently, the conductor-like screening model (COSMO) was implemented with ADC(2) to simulate solvation effects.[98]

Since the ADC(2) and MP2 methods are single-reference methods, CIs of the energy of the S_1 state with the energy of the S_0 state, where the wave functions necessarily are of multiconfigurational character, cannot be rigorously described with these methods. In the PCET reactions which are considered in the present work, CIs are encountered between the closed-shell electronic ground state and an open-shell CT state. In the energy scans which have been calculated for complexes of pyridine,[43] pyrimidine,[99] triazine,[100] and heptazine[52] with water molecules, the CIs involved in the PCET reaction appear to be reasonably accurately predicted by ADC(2) method, as verified by benchmark calculations with the complete-active-space self-consistent-field (CASSCF) method and the multireference perturbation (CASPT2) method.[43, 101, 102]

2.2 DFT/TDDFT

Density Functional Theory (DFT) is extensively applied in condensed matter physics, quantum chemistry and in biological sciences. In DFT, the electronic structure of atoms and molecules is not encoded in the form of wave functions, but in the electronic density. The electronic density is a much more compact object than correlated wave functions.

In 1927, Thomas proposed the homogeneous free-electron-gas approximation.[103] One year later, Fermi independently made a similar proposal.[104] Hohenberg and Kohn proposed to include other contributions which only depend on the density and applied the variational principle to determine the ground-state density.[105] In 1965, Kohn and Sham established the Kohn-Sham equations which allowed a simple calculation of the kinetic energy of the electrons. In the local density approximation (LDA), the density functional of the homogeneous Fermi gas is employed to calculate the exchange-correlation (XC) term. More sophisticated approximations were subsequently developed to improve the chemical accuracy of the DFT method. The generalized gradient approximation (GGA)[106-108] accounts for corrections to density of the homogeneous electron gas. Meta-GGAs take the second derivative of density into account. In hybrid-GGAs, part of the HF exchange functional is included. Hybrid-meta-GGAs have been introduced to improve the performance of the functionals for specific physical properties.

The DFT method has been extended to excited electronic states via the so-called time-dependent DFT (TDDFT) method.[109] By Fourier transformation of the solution of the TDSE, the excitation energies of the system can be extracted. The most common approach is to use the lowest-order approximation, i.e. linear response TDDFT (LR-TDDFT).[110]

To improve the accuracy of DFT/TDDFT, the GW method can be used, which is based on the Green's function *G* and the screened Coulomb interaction *W*.[111] Improved excitation energies and transition moments can be obtained with the Bethe-Salpeter equation (BSE)[112]. However, the GW method scales as $\sim N^4$ and the BSE method scales as $\sim N^6$, where N is the number of electrons.

Recent improvements of the XC functional have improved the performance of the TDDFT method for the calculation of excitation energies and properties. Standard XC functionals have been shown to behave incorrectly at long range.[113-115] There emerged two solutions to tackle this problem. The first is double-hybrid theory,[116] in which a second-order perturbation correction is added to the XC functional. It can be further improved by a spin-dependent scaling of the correlation energy, such as spin-component-scaled[116] or scaled-opposite-spin[117] functionals. The second solution is to split the Coulomb interaction into the long-range and short-range contributions.[118, 119] The most widely used examples of the range-separated scheme are the long-range-corrected (LC) functionals CAM-B3LYP[120] and ωB97X[121], which are range-separated hybrid GGA functionals. ωB97X-D[63] is a range-separated hybrid meta-GGA functional which includes atom-atom dispersion corrections. Although LC functionals should provide an improved description of CT states, the performance of TDDFT with LC functionals is found to be more erratic[122] for intermolecular CT states than for intramolecular CT states.[123 124 125] Therefore, the accuracy of LC functionals for problems involving CT states should be carefully checked.

Despite these limitations, there is general consensus that TDDFT calculations with carefully selected functionals are trustworthy. Considering their lower computational costs, DFT and TDDFT methods are the best choice for medium-size to large-size molecules, especially for trajectory simulations which require large numbers of evaluations of electronic energies.

3 Quasi-Classical Nonadiabatic Dynamics

3.1 Wigner Sampling and Ensemble Method

The first task in quasi-classical dynamics simulations of photoinduced processes is the definition of the initial condition for the nuclear motion in the electronic ground state, that is, prior to photoexcitation. For this purpose, one can adopt the phase-space formulation of quantum mechanics developed by Wigner. Wigner has discussed the corrections to the Boltzmann formula induced by the quantum behavior of vibrations at low temperatures.[126] The well-known Wigner phase-space distribution function has been used in many applications,[127] [128] and has been shown to be a reliable tool for the approximation of quantum observables by classical variables.

In the harmonic oscillator approximation, the eigenstates of each vibrational mode can be represented by one-dimensional harmonic oscillator wave functions. The Wigner distribution of a set of uncoupled harmonic oscillators is given by the product of Wigner functions of the individual harmonic oscillators. For a certain eigenstate n of a single oscillator, the Wigner quasi-probability distribution is:[127]

$$W_n(Q,P) = \frac{(-1)^n}{\pi\hbar} L_n\big(2(Q^2+P^2)\big)e^{-(Q^2+P^2)} \tag{1}$$

where the L_n are the Laguerre polynomials, Q and P are the dimensionless coordinate and momentum of a harmonic oscillator, $Q = \sqrt{\frac{\omega}{\hbar}}q$, $P = \frac{1}{\sqrt{\omega\hbar}}p$, and ω is the vibrational frequency, μ being the reduced mass. For the vibrational ground state (n = 0), the Wigner distribution $W_0(Q,P)$ takes the form of a product of two Gaussian functions:

$$W_0(Q,P) = \frac{1}{\pi\hbar} e^{-Q^2} e^{-P^2} \tag{2}$$

The Wigner distribution of a molecular system with N atoms in the harmonic approximation at zero temperature is given by:

$$W^{3N-6}(Q_i,P_i) = \frac{1}{(\pi\hbar)^{3N-6}} \prod_{i=1}^{3N-6} e^{-Q_i{}^2} e^{-P_i{}^2} \tag{3}$$

For a harmonic system at finite temperature T, the Wigner distribution reads:[127]

$$W(Q,P,T) = \frac{1}{\pi\hbar} tanh\left(\frac{\hbar\omega\beta}{2}\right) \exp\left[-\tanh\left(\frac{\hbar\omega\beta}{2}\right)(Q^2+P^2)\right] \tag{4}$$

where $\beta = 1 / k_B T$ and k_B is the Boltzmann constant.

Alternatively to the Wigner distribution, one can take the Husimi Q function[129] for the sampling of eigenstates,[130, 131] or one may sample the coordinates and momenta in an unconjugated way.[132, 133]

The electronic absorption spectrum can be simulated with the so-called nuclear ensemble method by computing the vertical electronic excitation energies and oscillator strengths at the nuclear geometries generated by Wigner sampling.[134] The integral absorption cross section is given by

$$\sigma(E) = \frac{\pi e^2 \hbar}{2mc\varepsilon_0 E} \sum_n^{N_S} \frac{1}{N_W} \sum_i^{N_W} \Delta E_{0,n}(\boldsymbol{R}_i)\, f_{0,n}(\boldsymbol{R}_i) \times g\big(E - \Delta E_{0,n}(\boldsymbol{R}_i), \delta\big) \tag{5}$$

where N_S is the number of excited states, N_W is the number of Wigner phase-space points, $\Delta E_{0,n}$ and $f_{0,n}$ are the excitation energies and oscillator strengths at the nuclear configuration $\boldsymbol{R}_i$, c is the speed of light, ε_0 is the vacuum permittivity, e and m are the electron charge and mass, and g is a normalized broadening function, which can be a Lorentzian (for lifetime broadening) or a Gaussian (for inhomogeneous broadening):

$$g_{Lorentzian}\left(E - \Delta E_{0,n}(\boldsymbol{R}_i), \delta\right) = \frac{1}{\pi} \frac{\frac{\delta}{2}}{\left(E - \Delta E_{0,n}(\boldsymbol{R}_i)\right)^2 + \left(\frac{\delta}{2}\right)^2} \tag{6}$$

$$g_{Gaussian}\left(E - \Delta E_{0,n}(\boldsymbol{R}_i), \delta\right) = \frac{1}{\sqrt{2\pi \left(\frac{\delta}{2}\right)^2}} \exp\left[-\frac{\left(E - \Delta E_{0,n}(\boldsymbol{R}_i)\right)^2}{2\left(\frac{\delta}{2}\right)^2}\right] \tag{7}$$

The parameter δ accounts for the phenomenological broadening of the electronic stick spectrum. The absorption spectrum simulated with the nuclear ensemble method accounts for so-called Herzberg-Teller intensity borrowing through the dependence of the electronic oscillator strengths on the nuclear geometry. The often observed slight red-shift of the maximum of the absorption profile from the vertical excitation energy results from the fact that some of the vibrational frequencies in excited electronic states typically are lower than the vibrational frequencies in the electronic ground state.[135] A benchmark study covering 28 small organic molecules predicted a mean red-shift of 0.11±0.08 eV for 60 electronic transitions.[135] The effect of finite temperature on absorption spectra has been investigated for several small molecules, e.g. for NF_3 and $CFCl_3$,[136, 137] and was found to be minor at room temperature.

3.2 Trajectory Surface Hopping

One important feature of TSH is that the nuclear motion evolves classically, while the electronic population follow quantum mechanics. The neglect of nuclear quantum effects saves computational cost comparing to quantum mechanical methods. Nonadiabatic transitions between electronic states are responsible for nonradiative electronic transitions such as internal conversion or intersystem crossing and are essential elements of photochemical reactions. The TSH method stands out among other semi-classical or quasi-classical methods as an efficient tool in simulating ultrafast photochemical reactions.

In the TSH method, trajectories of nuclear motion are propagated in time on a given electronic potential-energy surface by solving Newton's equation of motion. In ab initio implementations of TSH, the nuclear forces are calculated on-the-fly. Nonadiabatic transitions between electronic states are taken into account by a surface-hopping algorithm. The most widely used surface-hopping algorithms is Tully's Fewest-Switches Surface-Hopping[16] (FSSH) algorithm. The transition probability from one adiabatic state j to another state k, $P_{\mathrm{FSSH}}^{j\to k}$, is governed by the nonadiabatic coupling (NAC) element d_{jk} between two states j and k, whose electronic time-dependent coefficient are C_j and C_k,and can be written in adiabatic basis as the following form:[16]

$$P_{\mathrm{FSSH}}^{j\to k} = \max\left\{0, -\frac{2\dot{\boldsymbol{R}}(t)d_{jk}Re\left[C_k^* C_j\right]dt}{\left|C_j\right|^2}\right\} \tag{8}$$

A hop takes place from state j to k when

$$\sum_{i=1}^{k-1} P_{\mathrm{FSSH}}^{j\to i} \leq \xi \leq \sum_{i=1}^{k} P_{\mathrm{FSSH}}^{j\to i} \tag{9}$$

where ξ is a normalized random number from 0 to 1. The FSSH algorithm can to some extent be derived from the quantum-classical Liouville equation (QCLE) as has been discussed by Subotnik et. al.[138]

Simulations with the FSSH algorithm require the calculation of the NAC elements which usually is done by finite differencing which requires the calculation of overlaps of adiabatic electronic wave functions.[16] Granucci et al.[11] proposed the calculation of the NACs via a local diabatization algorithm.

In 1974, Tully and Preston[19] proposed to use the Landau-Zener (LZ) expression, which originally was derived for collision problems,[139-141] to calculate the transition probability between electronic states in SH simulations

$$P_{\mathrm{LZSH}}^{j\to k} = \exp\left(-\frac{2\pi}{\hbar}\frac{A^2}{Bv_\perp}\right) \tag{10}$$

where j and k represent the states before and after the hopping, A is coupling element of the diabatic states at the energy crossing, B is the difference of slopes of the two diabatic potential-energy functions and $v_\perp$ is the velocity component perpendicular to the crossing seam. Interestingly, the minimum energy gap of the adiabatic states at the point of degeneracy of the diabatic states is 2A, which suggests that the LZ expression might be used without the knowledge of the diabatic coupling element. However, the diabatic slope difference B also has to be extracted from the adiabatic potentials in order to use Eq. (10).

In 2011, Belyaev and Lebedev[142] showed that the LZ transition probability can be expressed in terms of only the adiabatic energy gap at an avoided crossing of the adiabatic potential-energy functions and the second time derivative of the gap at its minimum as follows:

$$P_{\mathrm{BLSH}}^{j\to k} = \exp\left(-\frac{\pi}{2\hbar}\sqrt{\frac{Z_{jk}^3}{\ddot{Z}_{jk}}}\right) \tag{11}$$

where Z_{jk} is the adiabatic energy gap between two neighboring electronic states. The Belyaev-Lebedev formula can be employed in an SH algorithm, the Belyaev-Lebedev surface-hopping (BLSH) algorithm. The essential advantage of the BLSH method is that it obviates the need of propagating the electronic wave function in time which eliminates the so-called decoherence problem of the electronic wave function.[143] Moreover, the numerically cumbersome and expensive evaluation of NAC elements is avoided.[144] The BLSH method exploits the fact that for CIs or avoided crossings, the NAC elements are implicitly encoded in the topography of the adiabatic potential-energy functions. The ab initio computation of adiabatic electronic energies is intrinsically more stable and accurate than the calculation of electronic wave functions.

Because the NAC elements are not calculated in the BLSH algorithm, rescaling of the nuclear velocities along the NAC vector after electronic hops, which is common practice in the FSSH algorithm,[16] is not applicable in BLSH. Instead, energy conservation is achieved by rescaling the current nuclear velocities by a factor which ensures energy conservation. So-called frustrated hops, for which the available kinetic energy is smaller than the necessary change of the potential energy after hopping, are excluded in BLSH. As for all quasi-classical methods, barrier tunneling on adiabatic potential-energy surfaces is not taken into account.

Wittig has developed an alternative derivation of LZ formula using contour integration[145] and Chibotaru et al.[146] improved the derivation by correcting the asymptotic behavior of the eigenfunctions. Zhu and Nakamura have developed extended and more complicated versions of the LZ formula.[147-149] Surface-hopping algorithms based on the Zhu-Nakamura (ZN) formula have been developed by Zhu and coworkers and Zhou and coworkers.[147-150]

The BLSH algorithm was tested by Xie et al. in comparison with the FSSH algorithm and exact quantum dynamics results for a model of the photodissociation

of phenol.[151] It was also tested for a four-state nine-mode model of the ultrafast photoinduced dynamics of the pyrazine molecule in comparison with numerically exact quantum dynamics results obtained with the multi-configuration time-dependent Hartree[152] (MCTDH) method.[91] These benchmark studies demonstrated that the BLSH method is a reliable method for the simulation of the ultrafast photoinduced dynamics of polyatomic molecules.

The ab initio on-the-fly implementation of the BLSH algorithm was developed by Xie et al.[153] and tested for the photoinduced dynamics of pyrazine in comparison with the FSSH method. It was shown that the BLSH and FSSH algorithms yield essentially identical results for this well-established benchmark system of excited-state nonadiabatic dynamics. The adiabatic LZSH method was also employed for electron dynamics in nanocrystals with several hundreds of atoms to investigate electron cooling dynamics.[154] Slavíček and coworkers independently benchmarked the BLSH method against the FSSH method for several molecular systems and extended the method to include spin-orbit coupling for the simulation of ISC[155].

3.3 Technical Details of Belyaev-Lebedev Surface-Hopping Dynamics

The propagation of trajectories with ab initio on-the-fly calculation of energy gradients was performed with the Zaghop code developed in the group of Nađa Došlić.[37]

The selection of the initial conditions for the propagation of trajectories in excited electronic states depends on the optical excitation process. When the electronic excitation occurs with an ultrafast laser pulse (instantaneous excitation), the adiabatic excited electronic states are stochastically populated according to their oscillator strengths and the initial nuclear positions and momenta are determined by Wigner sampling. When the excitation occurs by a laser pulse of finite spectral width, which typically is resonant with the maximum of the absorption spectrum, the initial conditions are randomly sampled from a corresponding spectral window centred at the maximum of the absorption spectrum.

Newton's equation of motion is integrated with the velocity Verlet algorithm. The default value of the time step is 0.5 fs. The energy gradients are computed with an ab initio electronic structure method, typically ADC(2) or TDDFT. At each time step, the energy gaps between neighbouring electronic states are recorded. If a minimum of the energy gap between two electronic states is detected, the transition probability between the two states is evaluated with the BL formula. The computed probability is compared with a normalized random number. If the transition probability is larger than the random number, the hop occurs, provided the available kinetic energy is larger than the gap (for hops upward in energy). If the kinetic energy is insufficient (so-called frustrated hop), the hop is rejected. When a hop occurs, the velocities are rescaled along the current momentum direction to ensure energy conservation.

The numerical accuracy of the BLSH algorithm depends on the precision of the location of the minimum of the gap and the precision of the evaluation of the second derivative of the gap. When a minimum of the gap between the current state and one of the neighbouring states is detected, the trajectory is propagated with a smaller time step which is chosen as 0.1 fs by default. The second derivative of the gap is evaluated by second-order finite differencing with the smaller time step.

The computational cost of the BLSH algorithm can be further reduced by a dynamical adjustment of the number of electronic excitation energies to be computed. At the beginning of the photoinduced dynamics, typically higher-lying bright electronic states are populated. As the system relaxes from these higher states to lower states, the computational cost can be reduced by computing only the energies of those electronic states which are required in the nonadiabatic dynamics. To ensure that no artificial bias towards relaxation to lower states is built into the algorithm, the next higher electronic state above the currently populated state is always included in the dynamics. In the simulations of water oxidation with Hz and photodissociation of the HzH radical, more than 50% of the computational cost could be saved by this optimization of the algorithm.[102]

4 Femtosecond Time-Resolved Nonlinear Spectroscopy

Femtosecond nonlinear electronic spectroscopy with ultraviolet/visible (UV/vis) light is an important diagnostic tool for the characterization of the structure and dynamics of molecular species. The goal of femtosecond spectroscopy is the monitoring of electronic and vibrational dynamics "in real time", that is, with ultimate time resolution of photophysical or photochemical processes. Two popular spectroscopic techniques relevant for the present thesis, transient-absorption (TA) pump-probe (PP) spectroscopy and electronic two-dimensional (2D) spectroscopy, are briefly described below.

4.1 Transient-Absorption Pump-Probe Spectroscopy

Femtosecond time-resolved TA PP experiments are designed to detect the ground-state and excited-state wave packet dynamics which is induced by a short pump pulse. In the TA PP experiment, the sample is excited by the pump pulse which is in resonance with a certain optically-bright excited electronic state. After a time delay T, the probe pulse interacts with the sample and the transmission of the probe pulse is measured as a function of time delay and the carrier frequency of the probe pulse (integral TA PP signal). Alternatively, the spectrum of the probe pulse at fixed carrier frequency can be dispersed with a spectrometer (dispersed TA PP signal). The TA signal without the pump pulse serves as a reference, so that the detected TA PP signal is defined as a difference between the pump-on and pump-off signals.[70]

Usually, only a small fraction of molecules is excited by the pump pulse. These molecules are not available for absorbing probe-pulse photons from the ground state, which decreases the TA signal. This negative contribution is known as

ground-state bleach (GSB) signal. In addition, the field of the probe pulse can stimulate the emission of photons from the transient excited state(s). This process is called stimulated emission (SE). The stimulated emission process also gives a negative contribution to the transmission signal. The measured probe absorbance contains another contribution which is called excited-state absorption (ESA). This contribution corresponds to the situation when the system prepared by the pump pulse is excited to higher electronic states by the absorption of a probe photon. ESA gives a positive contribution to the TA signal. While the frequency range of GSB and SE is determined by the carrier frequency of the pump pulse, the ESA can be recorded with radiation of any wavelength, for example with X-ray pulses.

The time delay T between the pump and probe pulses reveals the wave packet dynamics in the electronic ground state (GSB) and lower-lying excited electronic states (SE, ESA).

TA PP signals have extensively been studied for many molecular systems of interest in photochemistry, for instance, photoisomerization of rhodopsin[156] and transazobenzene,[157] internal conversion and intersystem crossing in thiouracil[158] and deep-UV photophysics of pyrene.[159]

4.2 Two-Dimensional Electronic Spectroscopy

2D spectroscopy is a variant of the three-pulse photon echo spectroscopy, see Fig. 1. Three laser pulses with wave vectors k_i (i = 1, 2, 3) interact with the sample and generate a third-order polarization $\mathcal{P}_j(\tau, T, t)$.[160] The signal can be detected in the rephasing (j=R) phase-matching direction (k_s = - k_1 + k_2 + k_3) and nonrephasing (j=NR) phase-matching direction[76] (k_s = k_1 - k_2 + k_3). The so-called "coherence time" τ is the time delay between the first and second pulse while the so-called "population time" T is the time delay between the second and third pulse. The 2D signal, $S_j(\omega_\tau, T, \omega_t)$, is then defined through the Fourier transform of the polarization $\mathcal{P}_j(\tau, T, t)$ with respect to τ and t. Usually, 2D spectra exhibit several diagonal and off-diagonal peaks, whose T-evolutions provide valuable information on the photophysical and photochemical processes in molecular systems.[161]

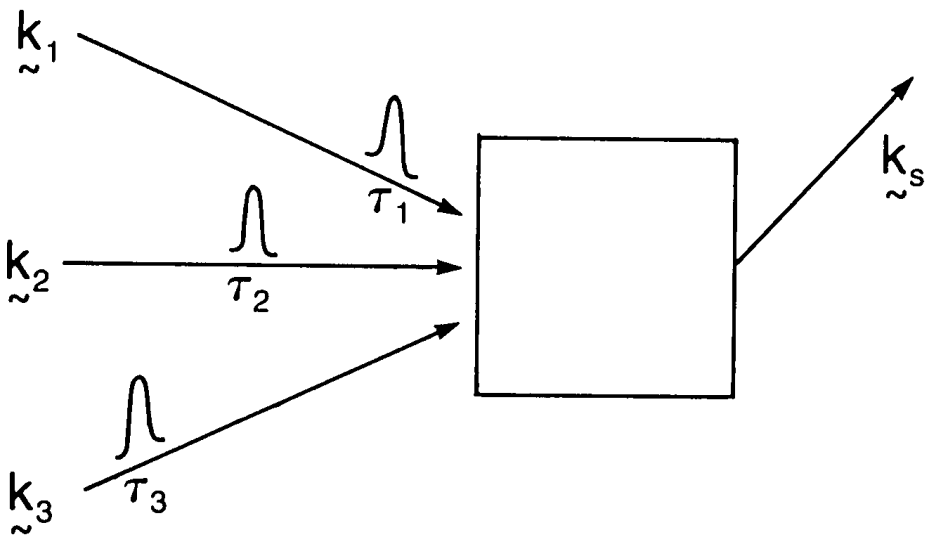

Figure 1. Sketch of the formation of the third-order polarization $\mathcal{P}_j(\tau, T, t)$.

In the present thesis, we use a common convention for plotting the signals, in which the SE and GSB contributions are positive while the ESA contribution is negative.

In the experimental 2D signals, the GSB, SE and ESA contributions overlap with each other and often are difficult to separate. In the nonlinear response function formalism, which is briefly considered below, these contributions can be calculated independently, which can be of great help for the interpretation of the experimental signals.

4.3 Nonlinear Response Functions and Doorway-Window Approximation

The nonlinear response functions formalism is a well-established tool for the simulation of nonlinear spectroscopic signals.[162, 163] For isotropic systems, the lowest nonlinear polarization is the third-order polarization. It is convenient to introduce the nonlinear response function formalism by considering the TA PP signal is an example. The TA PP polarization induced by the pump and probe pulses with temporal envelopes $\mathcal{E}_{\mathrm{pu}}(t)$ and $\mathcal{E}_{\mathrm{pr}}(t)$ can be expressed as follows:[70, 164, 165]

$$\mathcal{P}(T,t) \sim -i \int_0^\infty dt_3 \int_0^\infty dt_2 \int_0^\infty dt_1\, \mathcal{E}_1(t+T-t_3-t_2-t_1)\mathcal{E}_2(t+T-t_3-t_2)\mathcal{E}_{\mathrm{pr}}(t-t_3)\left\{e^{-i\omega_{pu}t_1}e^{i\omega_{pr}(t_3-t)}R_{\mathrm{R}}(t_3,t_2,t_1) + e^{i\omega_{pu}t_1}e^{i\omega_{pr}(t_3-t)}R_3(t_3,t_2,t_1)\right\}. \tag{12}$$

Here $R_{\mathrm{R}}(t_3,t_2,t_1)$ and $R_{\mathrm{NR}}(t_3,t_2,t_1)$ are the rephasing and nonrephasing response functions. The interrelation between the integration variables t_3, t_2, t_1 and the pulse arrival times τ_k ($\tau = \tau_2 - \tau_1, T = \tau_3 - \tau_2$) is clarified by Fig. 2 (for TA PP, $\tau = 0$).

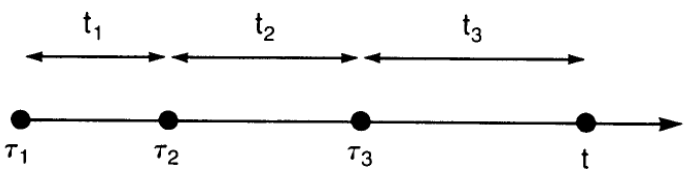

Figure 2. Interrelation between the integration variables t_k and pulse arrival times τ_k.

The response functions $R_{\mathrm{R}}(t_3,t_2,t_1)$ and $R_{\mathrm{NR}}(t_3,t_2,t_1)$ can be expressed through two fundamental four-time correlation functions[70, 163, 166]

$$\phi^{s}(\tau_4,\tau_3,\tau_2,\tau_1) = \langle X(\tau_4)X^{\dagger}(\tau_3)X(\tau_2)X^{\dagger}(\tau_1)\rangle \tag{13}$$

$$\phi^{d}(\tau_4,\tau_3,\tau_2,\tau_1) = \langle X(\tau_4)X(\tau_3)X^{\dagger}(\tau_2)X^{\dagger}(\tau_1)\rangle \tag{14}$$

Here the angular brackets indicate trace over electronic and nuclear degrees of freedom. The X and $X^{\dagger}$ are the downward and upward components of transition dipole moment operator in the Heisenberg representation:

$$X(\tau) = e^{iH_M\tau}Xe^{-iH_M\tau} \tag{15}$$

ϕ^{s} describes nonlinear response in the electronic ground state and lower-lying excited electronic states. It is responsible for the SE and GSB contributions. ϕ^{d} involves higher-lying electronic states and is responsible for ESA.

The four-time nonlinear response functions can be used for the evaluation of the eight three-time response functions:[70, 163, 165-168]

$$R_1^j(t_3,t_2,t_1) = \phi^{j}(t_1, t_1+t_2, t_1+t_2+t_3, 0) \tag{16}$$

$$R_2^j(t_3,t_2,t_1) = \phi^{j}(0, t_1+t_2, t_1+t_2+t_3, t_1) \tag{17}$$

$$R_3^j(t_3,t_2,t_1) = \phi^{j}(0, t_1, t_1+t_2+t_3, t_1+t_2) \tag{18}$$

$$R_4^j(t_3,t_2,t_1) = \phi^{j}(t_1+t_2+t_3, t_1+t_2, t_1, 0) \tag{19}$$

($j = s, d$). In terms of the three-time response functions, rephasing and non-rephasing response functions read:

$$R_{\mathrm{R}}(t_3,t_2,t_1) = R_2^s(t_3,t_2,t_1) + R_3^s(t_3,t_2,t_1) - R_1^d(t_3,t_2,t_1)^* \tag{20}$$

$$R_{\mathrm{NR}}(t_3,t_2,t_1) = R_1^s(t_3,t_2,t_1) + R_4^s(t_3,t_2,t_1) - R_2^d(t_3,t_2,t_1)^* \tag{21}$$

The nonlinear response functions represent the spectroscopic responses in the idealized limit of infinitely short laser pulses. The expressions for the nonlinear response functions contain time-ordered propagators of the field-free material system. For simplified material systems, such as few-level systems or damped harmonic oscillators, the propagators can be calculated analytically. As the material systems become more complex, however, the numerical evaluation of the nonlinear response functions becomes progressively tedious.

To simplify calculation of nonlinear response functions, Yan, Fried, and Mukamel[83] introduced the doorway-window (DW) representation of TA PP signals. The DW representation is valid for non-overlapping pulses and can be qualitatively interpreted as follows: The pump pulse generates the doorway operators in the electronic ground state and lower-lying excited states. During the time delay T, the doorway operators evolve with the field-free molecular Hamiltonian H_M. The probe pulse generates the window operator and the contraction of the time-evolved doorway operator with the window operator generates the TA PP signal.

The DW representation can be introduced as follows. The general heterodyne-detected PP signal is defined as:

$$S(\omega_{pu}, T, \omega_{pr}, \tau_t) \sim \mathrm{Im} \int_{-\infty}^{\infty} dt \mathcal{P}(T,t) \mathcal{E}_{pr}(t-\tau_t) e^{i\omega_{pr}(t-\tau_t)} \tag{22}$$

Inserting Eq. 12 into the above expression and taking $t = t' + t_3$, $t_2 = t' + T - t_2'$, we obtain:

$$\begin{aligned} S(\omega_{pu}, T, \omega_{pr}, \tau_t) \sim \mathrm{Re} \int_{-\infty}^{\infty} dt' \int_0^{\infty} dt_3 \int_{-\infty}^{t'+T} dt_2' \int_0^{\infty} dt_1\, \mathcal{E}_{\mathrm{pr}}(t' + t_3 - \tau_t) \\ \mathcal{E}_{\mathrm{pr}}(t') \mathcal{E}_{\mathrm{pu}}(t_2') \mathcal{E}_{\mathrm{pu}}(t_2' - t_1) \\ \{ e^{-i\omega_{pu} t_1} e^{i\omega_{pr}(t_3 - \tau_t)} R_{\mathrm{R}}(t_3, t' + T - t_2', t_1) \\ + e^{i\omega_{pu} t_1} e^{i\omega_{pr}(t_3 - \tau_t)} R_{\mathrm{NR}}(t_3, t' + T - t_2', t_1) \} \end{aligned} \tag{23}$$

If pulses 2 and 3 are well separated in time, namely the delay time T is much larger than the pulse duration τ_p, we can extend the upper integration limit for t_2' to ∞. Then we can write the response functions R_α (α = R or NR) in the DW representation as:[169]

$$R_\alpha(t_3, t_2, t_1) \sim \mathrm{Tr}[\mathcal{W}(t_3)\mathcal{L}(t_2)\mathcal{D}_\alpha(t_1)] \tag{24}$$

where $\mathcal{W}$ and $\mathcal{D}_\alpha$ are the doorway and window operators, $\mathcal{L}$ being the operator governing electronic population evolution. The heterodyne-detected signal can be written as:

$$S(\tau, T, \omega_{pr}, \tau_t) \sim Re\mathrm{Tr}[W(\tau_t)\mathcal{L}(T)D_\alpha(\tau)] \tag{25}$$

Assuming the wave packet evolution during the pulse duration τ_p can be neglected, the doorway and window operators can be expressed as:

$$D_\alpha(\tau) = \int_{-\infty}^{\infty} dt_2' \int_0^{\infty} dt_1 E_2(t_2')E_1(t_2' + \tau - t_1)\, e^{i\omega(t_1-\tau)}\mathcal{D}_\alpha(t_1) \tag{26}$$

$$W(\tau_t) = \int_{-\infty}^{\infty} dt' \int_0^{\infty} dt_3 E_4(t' + t_3 - \tau_t)\, E_3(t')e^{i\omega(t_3-\tau_t)}\mathcal{W}(t_3) \tag{27}$$

For obtaining explicit expressions for the DW operators, it is convenient to introduce the electronic ground state {0} as well as the manifold of lower-lying electronic states {I} and upper-lying electronic states {II}. In this notation,

the molecular Hamiltonian can be written as:

$$H_M = \begin{pmatrix} H_0 & 0 & 0 \\ 0 & H_I & 0 \\ 0 & 0 & H_{II} \end{pmatrix} \tag{28}$$

and the transition dipole moment operators in Eq. 13 and 14 assume the form:

$$X = \begin{pmatrix} 0 & \mu_{0,I} & 0 \\ 0 & 0 & \mu_{I,II} \\ 0 & 0 & 0 \end{pmatrix}, \; X^{\dagger} = \begin{pmatrix} 0 & 0 & 0 \\ \mu_{0,I} & 0 & 0 \\ 0 & \mu_{I,II} & 0 \end{pmatrix}. \tag{29}$$

Then, by using several approximations, of which the most important is the classical Condon approximation, one can employ the DW representation for the evaluation of any nonlinear spectroscopic signal on-the-fly. For example, the integral TA PP signal in can be obtained through averaging over the swarm of quasiclassical trajectories specified by the nuclear position $\boldsymbol{R}$ and momenta $\boldsymbol{P}$ and sampled from the Wigner distribution $\rho_g^{Wig}(\boldsymbol{R}_g, \boldsymbol{P}_g)$ as follows[170]:

$$\begin{aligned} S(\omega_{pu}, T, \omega_{pr}) \sim & \langle D_0(\omega_{pu}, \boldsymbol{R}_g, \boldsymbol{P}_g) W_0(\omega_{pr}, \tau_t, \boldsymbol{R}_g(T), \boldsymbol{P}_g(T)) \rangle \\ & + \langle D_I(\omega_{pu}, \boldsymbol{R}_g, \boldsymbol{P}_g) W_I\left(\omega_{pr}, \tau_t, \boldsymbol{R}_e(T), \boldsymbol{P}_e(T)\right) \rangle \\ & - \langle D_I(\omega_{pu}, \boldsymbol{R}_g, \boldsymbol{P}_g) W_{II}\left(\omega_{pr}, \tau_t, \boldsymbol{R}_e(T), \boldsymbol{P}_e(T)\right) \rangle . \end{aligned} \tag{30}$$

Here

$$D_0(\omega_{pu}, \boldsymbol{R}_g, \boldsymbol{P}_g) = \sum_e E_{pu}^2\left(\omega_{pu} - U_{eg}(\boldsymbol{R}_g)\right) \left|\mu_{ge}(\boldsymbol{R}_g)\right|^2 \rho_g^{Wig}(\boldsymbol{R}_g, \boldsymbol{P}_g) \tag{31}$$

$$D_I(\omega_{pu}, \boldsymbol{R}_g, \boldsymbol{P}_g) = E_{pu}^2\left(\omega_{pu} - U_{eg}(\boldsymbol{R}_g)\right) \left|\mu_{ge}(\boldsymbol{R}_g)\right|^2 \rho_g^{Wig}(\boldsymbol{R}_g, \boldsymbol{P}_g) \tag{32}$$

are the doorway functions and

$$W_0(\omega_{pr}, \boldsymbol{R}_g(T), \boldsymbol{P}_g(T)) = \sum_e E_{pr}^2\left(\omega_{pr} - U_{eg}(\boldsymbol{R}_g(T))\right) \left|\mu_{ge}(\boldsymbol{R}_g)\right|^2 \tag{33}$$

$$W_I(\omega_{pr}, \boldsymbol{R}_e(T), \boldsymbol{P}_e(T)) = E_{pr}^2\left(\omega_{pr} - U_{e(T)g}(\boldsymbol{R}_e(T))\right) \left|\mu_{ge(T)}(\boldsymbol{R}_e(T))\right|^2 \tag{34}$$

$$W_{II}(\omega_{pr}, \boldsymbol{R}_e(T), \boldsymbol{P}_e(T)) = \sum_f E_{pr}^2\left(\omega_{pr} - U_{fe(T)}(\boldsymbol{R}_e(T))\right) \left|\mu_{e(T)f}(\boldsymbol{R}_e(T))\right|^2 \tag{35}$$

are the window functions. In the above formulas, *g, e, f* denote electronic states in the manifolds {0}, {I}, {II}; U_{eg}, U_{fe} are the electronic energy differences between the corresponding states; μ_{ge}, μ_{ef} are the transition dipole moments; the Fourier transforms of the pulse envelopes $E_{pu}(t), E_{pr}(t)$ are denoted by $E_{pu}(\omega), E_{pr}(\omega)$. The explicit DW expressions for dispersed TA PP signals and 2D signals can be found in the attached publications[170, 171]

5 Summary of Publications

This section consists of five articles. Each of them is presented by a short summary and the contributions of the candidate are specified. The five papers are attached at the end of the thesis.

The first three papers are concerned with ab initio quasi-classical simulations of excited-state PCET reactions in hydrogen-bonded complexes of selected photobases with selected protic substrate molecules. In the first paper, the photochemistry of pyrimidine in clusters with up to four water molecules has been investigated in a joint experimental and computational study. In the second paper, the photocatalytic cycle of water oxidation and hydrogen evolution with the heptazine chromophore was explored with quasi-classical trajectory simulations. In the third paper, the excited-state PCET reaction in complexes of trianisoleheptazine with phenol and methoxyphenol was investigated with ab initio trajectory simulations to reveal the mechanisms and the time scales of the photoinduced reactions.

The fourth and the fifth paper are concerned with first-principles simulations of femtosecond time-resolved nonlinear spectra for the example of the pyrazine molecule. This work is based on the evaluation of spectroscopic signals in terms of third-order nonlinear response functions and quasi-classical approximations of the doorway-window representation. In the fourth paper, the formalism for the computational evaluation of transient absorption pump-probe spectra has been developed and implemented. In the fifth paper, the methodology has been extended to compute electronic two-dimensional spectra of the pyrazine molecule from first principles.

5.1 Photoinduced Water Oxidation in Pyrimidine-Water Clusters: A Combined Experimental and Theoretical Study

Summary of *"Photoinduced Water Oxidation in Pyrimidine-Water Clusters: A Combined Experimental and Theoretical Study"* by *Xiang Huang, Juan-Pablo Aranguren, Johannes Ehrmaier, Jennifer A. Noble, Weiwei Xie, Andrzej L. Sobolewski, Claude Dedonder-Lardeux, Christophe Jouvet and Wolfgang Domcke; Phys. Chem. Chem. Phys.*, **2020**, *22*, 12502-12514.

In collaboration with the group of Christophe Jouvet at the University of Aix-Marseille, a combined experimental and theoretical study of the photoinduced PCET reaction in clusters of pyrimidine (Pm) with water molecules in a molecular beam was undertaken. In the experiments it was found that a PCET reaction from water molecules to photoexcited pyrimidine results in the formation of the PmH radical which was detected via its exceptionally low ionization potential.

The excited-state potential-energy surfaces of clusters of pyrimidine with one and four water molecules were characterized with wave-function based ab initio electronic-structure calculations. The photochemical dynamics was explored with ab initio on-the-fly trajectory surface-hopping simulations with the ADC(2) electronic-structure method. It was found that the abstraction of an H-atom from a water molecule by photoexcited pyrimidine, resulting in the PmH and OH radicals, is a low-barrier reaction. Analysis of the relevant electronic states and the frontier molecular orbitals of Pm-$(H_2O)_n$ clusters revealed that the H-atom transfer reaction is driven by hole transfer from photoexcited pyrimidine to a hydrogen-bonded water molecule. Upon absorption of a second photon, the excess H-atom can be detached from the PmH radical via a $\pi\sigma^*$ state

which is repulsive with respect to the N-H bond. This photodetachment reaction regenerates pyrimidine, which thus becomes a photocatalyst. The water oxidation reaction in pyrimidine-water clusters occurs in competition with ultrafast intramolecular excited-state deactivation of pyrimidine via ring-puckering S_1-S_0 conical intersections. The branching ratio of OH radical formation was found to be low, but increases with the size of the cluster.

Individual contributions of the candidate:

Together with my supervisor Wolfgang Domcke, I devised the computational studies. I determined the ground-state equilibrium geometries of pyrimidine-water clusters of different sizes. I performed static electronic-structure calculations to explore the reaction path of the excited-state PCET reaction. I performed the excited-state nonadiabatic dynamics simulations with classical trajectories. I also communicated with the collaborating experimentalists to steer the progress of the cooperation. I evaluated the computational data and performed the interpretations of the experimental and computational results.

5.2 Ab Initio Nonadiabatic Surface-Hopping Trajectory Simulations of Photocatalytic Water Oxidation and Hydrogen Evolution with the Heptazine Chromophore

Summary of *"Ab Initio Nonadiabatic Surface-Hopping Trajectory Simulations of Photocatalytic Water Oxidation and Hydrogen Evolution with the Heptazine Chromophore"* by *Xiang Huang and Wolfgang Domcke; J. Phys. Chem A,* **2021**, *125*, 9917–9931

Recently, heptazine-based polymeric carbon nitride materials have received extensive attention as metal-free photocatalysts for hydrogen evolution from water. In this work, nonadiabatic trajectory surface-hopping dynamics calculations have been performed for hydrogen-bonded Hz-water complexes with the ADC(2) ab initio method. The excited-state PCET reaction from water to Hz, resulting in the heptazinyl (HzH) and hydroxyl radicals, has been studied. The follow-up thermal disproportionation reaction of two HzH radicals to yield HzH_2 and Hz was studied with static reaction-path calculations. It was shown that the disproportionation reaction is a low-barrier process. The photodetachment of an H-atom from HzH_2 was studied with excited-state quasi-classical dynamics simulations. The sequential two-photon reaction studied in this work illustrates a low-barrier photocatalytic cycle for water splitting into free H atoms and OH radicals.

Individual contributions of the author:

I performed the static electronic-structure calculations and the dynamics simulations for the PCET reaction in the Hz-water complex and the H-atom photodetachment reaction in HzH_2. I proposed the investigation of the disproportionation scenario of HzH radicals and the investigation of the photodissociation of

HzH_2. I performed the statistical analysis of the trajectory data. I also performed are comprehensive computational characterization of all tautomers of HzH_2.

5.3 Ab Initio Trajectory Surface-Hopping Dynamics Studies of Excited-State Proton-Coupled Electron Transfer Reactions in Trianisoleheptazine-Phenol Complexes

Summary of *"Ab Initio Trajectory Surface-Hopping Dynamics Studies of Excited-State Proton-Coupled Electron Transfer Reactions in Trianisoleheptazine-Phenol Complexes"* by *Xiang Huang, Wolfgang Domcke; Phys. Chem. Chem. Phys.* **2022**, *24*, 15925 - 15936

The PCET reaction in hydrogen-bonded complexes of trianisoleheptazine (TAHz), a chromophore related to polymeric carbon nitrides widely used in hydrogen-evolution photocatalysis, with several phenol derivatives were recently studied by Schlenker and coworkers with time-resolved photoluminescence quenching and pump-probe experiments. A pronounced dependence of the PCET reactivity on the electron-donating/electron-withdrawing character of the substituents on phenol was found, with indications of a barrierless or nearly barrierless PCET reaction for the most strongly electron-donating substituent, methoxy. In this work, the excited-state PCET dynamics was explored with first-principles nonadiabatic dynamics simulations using the TDDFT/ωB97X-D electronic-structure model for two selected complexes, TAHz-phenol and TAHz-methoxyphenol. The qualitative reliability of the TDDFT/ωB97X-D electronic-structure model was assessed by extensive benchmarking of excitation energies and potential-energy profiles against a wave-function-based ab initio method, ADC(2). The nonadiabatic dynamics simulations provide temporally and structurally resolved insights into paradigmatic PCET reactions in TAHz-phenol complexes. The radiationless relaxation of the photoexcited bright $^1\pi\pi^*$ state to the long-lived dark S_1 state of TAHz occurs in less than 100 fs. The ensuing PCET reaction on the adiabatic S_1 surface is faster in TAHz-methoxyphenol complexes than in TAHz-phenol complexes due to a lower H-atom-transfer

barrier, as observed in the experiments. The relaxation of the complexes to the electronic ground state is found to occur exclusively via PCET within the 250 fs time window covered by the present simulations, confirming the essential role of the hydrogen bond for the fluorescence quenching process. The absolute values of the computed PCET time constants are significantly shorter than those extracted from time-resolved photoluminescence measurements for mixtures of TAHz with phenolic substrates in toluene. The possible origins of this discrepancy are discussed.

Individual contributions of the candidate:

After extensive test calculations for various hydrogen-bonded heptazine-substrate complexes, I realized that ab initio excited-state surface-hopping dynamics simulations might be possible with the TDDFT method for complexes of TAHz with phenol molecules. I performed extensive calculations to benchmark the TDDFT method with different exchange-correlation functionals in comparison with the ADC(2) wave-function-based method. I designed the trajectory simulations for complexes of TAHz and with phenol as well as methoxyphenol and I performed the analysis of the data. I developed the novel concept of a dynamic map for PCET reactions.

5.4 Ab Initio Surface-Hopping Simulation of Femtosecond Transient-Absorption Pump–Probe Signals of Nonadiabatic Excited-State Dynamics Using the Doorway–Window Representation

Summary of *"Ab Initio Surface-Hopping Simulation of Femtosecond Transient-Absorption Pump–Probe Signals of Nonadiabatic Excited-State Dynamics Using the Doorway–Window Representation"* by *Maxim F. Gelin, Xiang Huang, Weiwei Xie, Lipeng Chen, Nađa Došlić, and Wolfgang Domcke; J. Chem. Theory Comput.* **2021**, *17*, 2394–2408

An ab initio theoretical framework for the simulation of femtosecond time-resolved TA PP spectra with quasi-classical trajectories is presented. The simulations are based on the classical approximation to the DW representation of third-order four-wave-mixing signals. The DW formula accounts for the finite duration and spectral shape of the pump and probe pulses. In the classical DW formalism, classical trajectories are stochastically sampled from a positive definite doorway distribution, and the signals are evaluated by averaging over a positive definite window distribution. Nonadiabatic excited-state dynamics is described by a stochastic surface-hopping algorithm. The method has been implemented for the pyrazine molecule with the ADC(2) ab initio electronic-structure method. The methodology is illustrated by ab initio simulations of the ground-state bleach, stimulated emission, and excited-state absorption contributions to the TA PP spectrum of gas-phase pyrazine.

Individual contributions of the candidate:

In discussions with Maxim Gelin, I developed the protocol for the simulation of transient-absorption pump-probe spectra with ab initio on-the-fly quasiclassical trajectory calculations. I wrote the code for the simulations of the spectra

from the scratch. I performed additional trajectory simulations for the evaluation of the ground state bleach signal and I performed the electronic-structure calculations required for the excited-state absorption signal. I performed the convergence tests for the different contributions to the PP signal with the number of trajectories, both for the integral signal and the dispersed signal.

5.5 Ab Initio Quasiclassical Simulation of Femtosecond Time-Resolved Two-Dimensional Electronic Spectra of Pyrazine

Summary of *"Ab Initio Quasiclassical Simulation of Femtosecond Time-Resolved Two-Dimensional Electronic Spectra of Pyrazine"* by *Xiang Huang, Weiwei Xie, Nađa Došlić, Maxim F. Gelin, and Wolfgang Domcke; J. Phys. Chem. Lett.* **2021**, *12, 11736–11744*

2D electronic spectroscopy is a powerful nonlinear technique which provides spectroscopic information on two frequency axes as well as dynamical information as a function of the so-called waiting time. In this work, an ab initio theoretical framework for the simulation of electronic 2D spectra has been developed for the first time. The method is based on the classical approximation to the DW representation of three-pulse photon-echo signals and the description of nuclear motion by classical trajectories. Nonadiabatic effects are taken into account by a trajectory surface-hopping algorithm. 2D electronic spectra were simulated with ab initio on-the-fly trajectory calculations using the ADC(2) electronic-structure method for the pyrazine molecule, which is a benchmark system for ultrafast radiationless decay through conical intersections. It is demonstrated that 2D spectroscopy with subfemtosecond UV pulses can provide unprecedented detailed information on the ultrafast photodynamics of polyatomic molecules.

Individual contributions of the candidate:

Together with Maxim Gelin, I developed the protocol for the simulation of electronic 2D spectra with quasi-classical trajectories in the framework of the classical doorway-window approximation. I adapted the code developed for the simulation of transient-absorption pump-probe spectra to the simulation of 2D

spectra. I performed the trajectory calculations and evaluated the data. Extensive efforts were undertaken to assign the main features of the time- and frequency resolved spectra to specific electronic transitions in pyrazine. In addition, a movie was produced which illustrates the dynamic evolution of the ESA component of the 2D spectrum of pyrazine.

6 Summary

The photochemistry of pyridine-H_2O,[43, 44] pyrimidine-H_2O[99] and heptazine-H_2O[52] complexes has been explored by Domcke and coworkers with static ab initio electronic-structure calculations. Based on these calculations, a general mechanism for the photooxidation of water with N-heterocycles has been proposed.[172] In the present work, this proposed scenario was more deeply explored with ab initio nonadiabatic dynamics simulations which provide more detailed and more quantitative insights into the reaction dynamics.

In the study of pyrimidine-water clusters it has been found that CT states of both $^1\pi\pi^*$ character and $^1n\pi^*$ character are involved in the PCET reaction. Frequent and fast transient proton-transfer events in several excited states are observed in the dynamics simulations. Although the fundamental PCET mechanism is clearly revealed by the complex of pyrimidine with a single water molecule, the quantitative reaction dynamics depends sensitively on the number of water molecules in the complex. In the pyrimidine-$(H_2O)_4$ cluster, the concerted effects of the hydrogen-bonds among all four water molecules assist in the lowering of the PCET barrier. Moreover, the hydrogen bonds between the water molecules accept the excess energy of the photoreaction and thus stabilize the biradicalic reaction product.

The heptazine (Hz) chromophore is of particular interest in the context of photocatalytic water splitting. It is the building block of the polymeric carbon nitride material “melon”, which is currently considered as one of the most promising photocatalysts for water splitting. The simulations of the photoinduced dynamics of the Hz-H_2O complex performed in the present work provide insight into the role of the unique low-lying $^1\pi\pi^*$ state of Hz for the water oxidation reaction. The simulations provide insight into the time scales of the electron and proton processes and the branching ratios of competing processes.

After excitation of the bright $^1\pi\pi^*$ state, most of the Hz-H_2O complexes relax via intermediate $^1n\pi^*$ states to the exceptionally long-lived $S_1(\pi\pi^*)$ state of Hz. A fraction of 38% of the trajectories populate transiently the reactive CT state. At the CI of the CT state with the S_1 state, most of the trajectories are captured on the S_1 PES, while 9% of trajectories remain in the CT state at hit the CI between the CT state and the S_0 state, potentially forming the HzH and OH radicals in their electronic ground states. This relatively low yield of radicals represents only the ultrafast component of the reaction. A significant part of the predicted population of the S_1 state (91%) at the end of the present simulation (100 fs) may yield radical pairs by H-atom tunneling on the S_1 PES on longer time scales (picoseconds to nanoseconds).

The photoinduced hydrogen evolution mechanism was studied in the present work for the doubly reduced Hz molecule, HzH_2, which can be formed by the exothermic disproportionation of two HzH radicals. HzH_2 possesses two $^1\pi\sigma^*$ excited states which are antibonding with respect to the respective NH bonds and drive the photodissociation of HzH_2 when they become populated by non-radiative transitions from the dense manifold of absorbing $^1\pi\pi^*$ states. The nonadiabatic dynamics simulations reveal that the reactive $^1\pi\sigma^*$ state becomes populated with a probability of 56% and that 20% of the population passes through CIs with low-lying bound $^1\pi\pi^*$ states to hit CIs with the electronic ground state. Photodetachment of H atoms from photogenerated HzH_2 seems to be a promising strategy for the production of green hydrogen. The overall catalytic mechanism of water oxidation and hydrogen evolution with the Hz molecule is illustrated in Fig. 3.

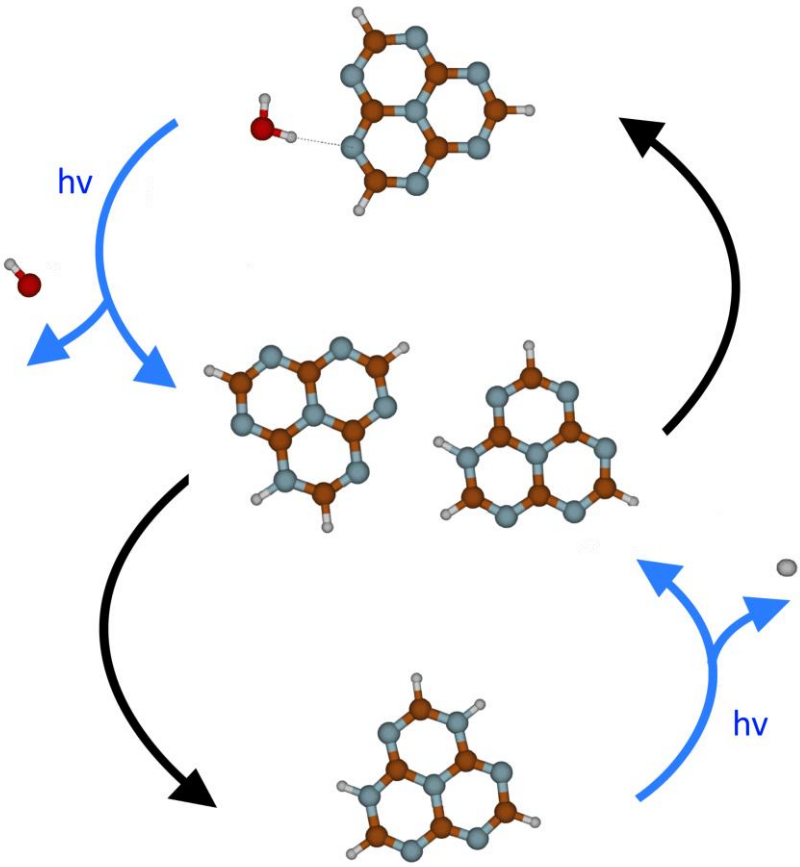

Figure 3. Photocatalytic cycle of water splitting with the Hz molecule. The blue arrows indicate light-driven reactions, while the black arrow indicates a dark disproportionation reaction. Two HzH radicals are formed by the photooxidation of water (upper part). The radicals undergo disproportionation (black arrow) to generate HzH_2 and recover Hz. By the photodetachment of a hydrogen atom from HzH_2, an HzH radical is regenerated, which closes the cycle (lower part).

The nonadiabatic dynamics simulations for the complexes of trianisoleheptazine (TAHz) with phenol and methoxyphenol were stimulated by the experimental studies of the photoreactivity of TAHz with substituted phenols in toluene solution by the Schlenker group.[59] Due to the size of these systems, the computationally less expensive TDDFT electronic-structure method had to be used

instead of the more accurate wave-function based ADC(2) method. A considerable effort was undertaken to verify the accuracy of the TDDFT method for the photoreaction under consideration. The nonadiabatic trajectory simulations provide temporally and spatially resolved insight into the PCET reactions in these complexes. The populations of the optically excited S_3, S_4 and S_5 states of mixed $^1\pi\pi^*$ and $^1n\pi^*$ character relax within about 20 fs to the S_2 state and within 50-70 fs to the S_1 state. I constructed dynamical maps which illustrate the strong correlation of the H-atom transfer reaction with the distance of the donor and acceptor atoms of the H-atom transfer reaction. Most H-atom transfer events occur after radiationless relaxation of the populations of the S_n states to the S_1 state. It can be inferred from the dynamical maps that the PCET reaction on the S_1 PES is barrier controlled. According to the simulations, the excited-state PCET reaction is four times faster in the TAHz-methoxyphenol complex than in the TAHz-phenol complex, in good agreement with the experimental findings.[59]

In collaboration with Maxim F. Gelin, an ab initio theoretical framework for the simulation of femtosecond time-resolved transient absorption (TA) pump-probe (PP) spectra with quasi-classical trajectories has been developed. The simulations are based on the classical approximation to the doorway-window (DW) approximation for third-order four-wave-mixing signals. The DW approximation for TA PP signals was implemented for the first time with ab initio on-the-fly classical trajectory simulations. The essential conditions for the validity of this approximation scheme are laser pulses which are non-overlapping in time and sufficiently short on the time scale of the system dynamics. The classical doorway and window distributions account for the durations and spectral shapes of the laser pulses. These distributions are positive definite and therefore well suited for Monte Carlo sampling by classical trajectories.

The ab initio classical DW formalism was implemented for the pyrazine molecule using the ADC(2) electronic-structure method. Pyrazine is a paradigmatic

case for ultrafast radiationless decay dynamics driven by conical intersections among the $^1B_{2u}(\pi\pi^*)$, $^1B_{3u}(n\pi^*)$ and $^1A_u(n\pi^*)$ excited states. The three components of the TA PP signal, ground-state bleach (GSB), stimulated emission (SE) and excited-state absorption (ESA), were separately evaluated and the dependence of the signals on the durations of the laser pulses was investigated. The GSB and SE signals obtained with the full-dimensional classical simulation are in good agreement with the GSB and SE signals which were obtained with quantum mechanical calculations for a four-state nine-mode model of pyrazine[173] (the ESA signal was not computed in the model study).

The ab initio quasi-classical framework has been extended to the simulation of two-dimensional (2D) electronic spectra. The method is based on the classical approximation to the DW approximation for three-pulse photon-echo signals and the description of the nuclear motion by ab initio on-the-fly surface-hopping trajectories. The computational protocol has been implemented for the pyrazine molecule with the ADC(2) electronic-structure method. The SE signal clearly reveals the rapid radiationless decay of the bright $^1B_{2u}(\pi\pi^*)$ state to the $^1B_{3u}(n\pi^*)$ and $^1A_u(n\pi^*)$ states within about 30 fs. The 2D spectra are dominated by the ESA signal. The ESA signal exhibits peaks at more or less fixed positions in frequency space. The intensities of these peaks oscillate with the waiting time, see Fig. 4. The peaks can be assigned to transitions from the $^1B_{3u}(n\pi^*)$ and $^1A_u(n\pi^*)$ states to higher excited states which are in resonance with the probe frequency. It has been shown for this example that the nonstationary populations of the $^1B_{3u}(n\pi^*)$ and $^1A_u(n\pi^*)$ states after their population by radiationless decay from the $^1B_{2u}(\pi\pi^*)$ state can be monitored with 2D spectroscopy with femtosecond time resolution.

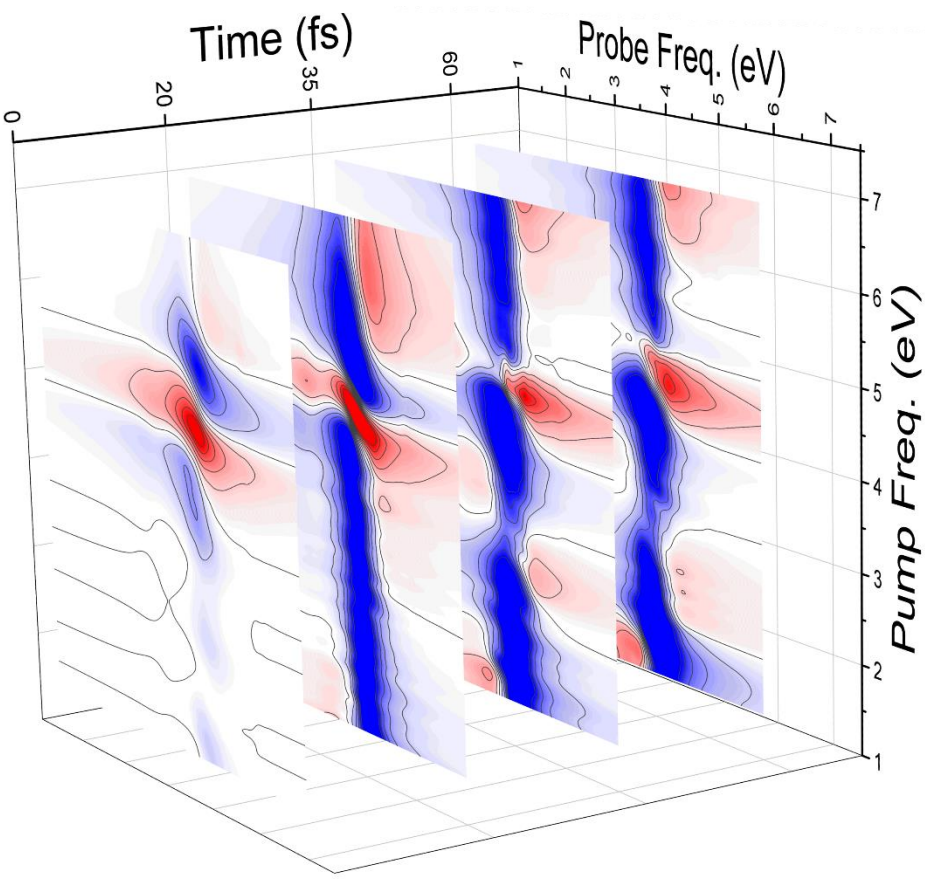

Figure 4. Snapshots of 2D spectra of pyrazine at different waiting times T = 0, 20, 35, and 60 fs. The intensity is colored in the from blue (low) to red (high).

We have presented in this work the first ab initio on-the-fly simulations of TA PP and 2D spectra for a polyatomic molecule within the classical DW approximation. The classical DW approximation is not limited to TA PP and 2D spectra and the methodology developed in this work can be applied to other four-wave-mixing or N-wave-mixing signals. Furthermore, the simulation technology can be extended to treat chromophores in solution or in other condensed-phase environments within the QM/MM approximation. By this extension of the method, solvation effects such as electronic dephasing or vibrational cooling can be included in future simulations of electronic four-wave-mixing spectra.

Bibliography

[1] M. Born, and R. Oppenheimer, Ann. Phys. **389** (1927) 457.

[2] W. Domcke, D. Yarkony, and H. Köppel, *Conical intersections: electronic structure, dynamics & spectroscopy* (World Scientific, 2004).

[3] W. Domcke, D. R. Yarkony, and H. Köppel, *Conical intersections: theory, computation and experiment* (World Scientific, 2011).

[4] H. Nakamura, *Nonadiabatic transition: concepts, basic theories and applications* (World Scientific, 2012).

[5] D. R. Yarkony, Chem. Rev. **112** (2012) 481.

[6] W. Domcke, and D. R. Yarkony, Annu. Rev. Phys. Chem. **63** (2012) 325.

[7] M. Born, and K. Huang, *Dynamical theory of crystal lattices* (Clarendon Press, 1954).

[8] W. Domcke, H. Köppel, and L. S. Cederbaum, Mol. Phys. **43** (1981) 851.

[9] E. J. Heller, J. Chem. Phys. **62** (1975) 1544.

[10] E. J. Heller, J. Chem. Phys. **75** (1981) 2923.

[11] G. Granucci, M. Persico, and A. Toniolo, J. Chem. Phys. **114** (2001) 10608.

[12] G. Stock, and M. Thoss, Phys. Rev. Lett. **78** (1997) 578.

[13] W. Bao, S. Jin, and P. A. Markowich, J. Chem. Phys. **175** (2002) 487.

[14] N. Mott, in *Math. Proc. Cambridge Philos. Soc.* (Cambridge University Press, 1931), pp. 553.

[15] X. Li, J. C. Tully, H. B. Schlegel, and M. J. Frisch, J. Chem. Phys. **123** (2005) 084106.

[16] J. C. Tully, J. Chem. Phys. **93** (1990) 1061.

[17] M. Ben-Nun, J. Quenneville, and T. J. Martínez, J. Phys. Chem. A **104** (2000) 5161.

[18] R. Crespo-Otero, and M. Barbatti, Chem. Rev. **118** (2018) 7025.

[19] J. C. Tully, and R. K. Preston, J. Chem. Phys. **55** (1971) 562.

[20] B. F. Curchod, U. Rothlisberger, and I. Tavernelli, ChemPhysChem **14** (2013) 1314.

[21] M. Persico, and G. Granucci, Theor. Chem. Acc. **133** (2014) 1.

[22] T. R. Nelson, A. J. White, J. A. Bjorgaard, A. E. Sifain, Y. Zhang, B. Nebgen, S. Fernandez-Alberti, D. Mozyrsky, A. E. Roitberg, and S. Tretiak, Chem. Rev. **120** (2020) 2215.

[23] G. Granucci, and M. Persico, J. Chem. Phys. **126** (2007) 134114.

[24] M. D. Hack, A. M. Wensmann, D. G. Truhlar, M. Ben-Nun, and T. J. Martínez, J. Chem. Phys. **115** (2001) 1172.

[25] M. S. Topaler, M. D. Hack, T. C. Allison, Y.-P. Liu, S. L. Mielke, D. W. Schwenke, and D. G. Truhlar, J. Chem. Phys. **106** (1997) 8699.

[26] M. D. Hack, A. W. Jasper, Y. L. Volobuev, D. W. Schwenke, and D. G. Truhlar, J. Phys. Chem. A **103** (1999) 6309.

[27] A. W. Jasper, and D. G. Truhlar, Chem. Phys. Lett. **369** (2003) 60.

[28] A. W. Jasper, S. N. Stechmann, and D. G. Truhlar, J. Chem. Phys. **116** (2002) 5424.

[29] A. W. Jasper, M. D. Hack, and D. G. Truhlar, J. Chem. Phys. **115** (2001) 1804.

[30] R. Mitrić, J. Petersen, and V. Bonačić-Koutecký, Phys. Rev. A **79** (2009) 053416.

[31] L. Du, and Z. Lan, J. Chem. Theory Comput. **11** (2015) 1360.

[32] M. Richter, P. Marquetand, J. González-Vázquez, I. Sola, and L. González, J. Chem. Theory Comput. **7** (2011) 1253.

[33] L. Martínez-Fernández, L. González, and I. Corral, Chem. Commun. **48** (2012) 2134.

[34] M. Marazzi, S. Mai, D. Roca-Sanjuán, M. l. G. Delcey, R. Lindh, L. González, and A. Monari, J. Phys. Chem. Lett. **7** (2016) 622.

[35] S. Mai, P. Marquetand, and L. González, J. Phys. Chem. Lett. **7** (2016) 1978.

[36] A. J. Atkins, and L. González, J. Phys. Chem. Lett. **8** (2017) 3840.

[37] S. Chaiwongwattana, M. Sapunar, A. Ponzi, P. Decleva, and N. Došlić, J. Phys. Chem. A **119** (2015) 10637.

[38] J. Thisuwan, S. Chaiwongwattana, M. Sapunar, K. Sagarik, and N. Došlić, J. Photochem. Photobiol., A **328** (2016) 10.

[39] M. Mališ, and N. Došlić, Molecules **22** (2017) 493.

[40] A. Ponzi, M. Sapunar, C. Angeli, R. Cimiraglia, N. Došlić, and P. Decleva, J. Chem. Phys. **144** (2016) 084307.

[41] D. Tuna, N. Došlić, M. Mališ, A. L. Sobolewski, and W. Domcke, J. Phys. Chem. B **119** (2015) 2112.

[42] X. Pang, C. Jiang, W. Xie, and W. Domcke, Phys. Chem. Chem. Phys. **21** (2019) 14073.

[43] X. Liu, A. L. Sobolewski, R. Borelli, and W. Domcke, Phys. Chem. Chem. Phys. **15** (2013) 5957.

[44] X. Liu, A. L. Sobolewski, and W. Domcke, J. Phys. Chem. A **118** (2014) 7788.

[45] N. Esteves-Lopez, S. Coussan, C. Dedonder-Lardeux, and C. Jouvet, Phys. Chem. Chem. Phys. **18** (2016) 25637.

[46] J. Schirmer, Phys. Rev. A **26** (1982) 2395.

[47] A. B. Trofimov, and J. Schirmer, J. Phys. B: At., Mol. Opt. Phys. **28** (1995) 2299.

[48] A. Dreuw, and M. Wormit, Wiley Interdiscip. Rev.: Comput. Mol. Sci. **5** (2015) 82.

[49] X. Wang, K. Maeda, A. Thomas, K. Takanabe, G. Xin, J. M. Carlsson, K. Domen, and M. Antonietti, Nat. Mater. **8** (2009) 76.

[50] J. Liebig, J. Ann. Pharm. **10** (1834) 1.

[51] L. Pauling, and J. H. Sturdivant, Proc. Natl. Acad. Sci. **23** (1937) 615.

[52] J. Ehrmaier, T. N. Karsili, A. L. Sobolewski, and W. Domcke, J. Phys. Chem. A **121** (2017) 4754.

[53] J. Ehrmaier, E. J. Rabe, S. R. Pristash, K. L. Corp, C. W. Schlenker, A. L. Sobolewski, and W. Domcke, J. Phys. Chem. A **123** (2019) 8099.

[54] E. J. Rabe, K. L. Corp, A. L. Sobolewski, W. Domcke, and C. W. Schlenker, J. Phys. Chem. Lett. **9** (2018) 6257.

[55] R. S. Hosmane, M. A. Rossman, and N. J. Leonard, J. Am. Chem. Soc. **104** (1982) 5497.

[56] M. Shabaz, S. Urano, P. R. LeBreton, M. A. Rossman, R. S. Hosmane, and N. J. Leonard, J. Am. Chem. Soc. **106** (1984) 2805.

[57] A. M. Halpern, M. A. Rossman, R. S. Hosmane, and N. J. Leonard, J. Phys. Chem. **88** (1984) 4324.

[58] N. Ullah, S. Chen, Y. Zhao, and R. Zhang, J. Phys. Chem. Lett. **10** (2019) 4310.

[59] E. J. Rabe, K. L. Corp, X. Huang, J. Ehrmaier, R. G. Flores, S. L. Estes, A. L. Sobolewski, W. Domcke, and C. W. Schlenker, J. Phys. Chem. C **123** (2019) 29580.

[60] C. Bronner, and O. S. Wenger, Inorg. Chem. **51** (2012) 8275.

[61] T. Hossen, and K. Sahu, J. Phys. Chem. A **122** (2018) 2394.

[62] K. L. Corp, E. J. Rabe, X. Huang, J. Ehrmaier, M. E. Kaiser, A. L. Sobolewski, W. Domcke, and C. W. Schlenker, J. Phys. Chem. C **124** (2020) 9151.

[63] J.-D. Chai, and M. Head-Gordon, Phys. Chem. Chem. Phys. **10** (2008) 6615.

[64] L. E. Hargrove, R. L. Fork, and M. A. Pollack, Appl. Phys. Lett. **5** (1964) 4.

[65] M. Dantus, M. J. Rosker, and A. H. Zewail, J. Chem. Phys. **87** (1987) 2395.

[66] P. French, Rep. Prog. Phys. **58** (1995) 169.

[67] W. Kaiser, and D. H. Auston, *Ultrashort laser pulses: generation and applications* (Springer, 1993).

[68] R. L. Fork, C. H. Brito Cruz, P. C. Becker, and C. V. Shank, Opt. Lett. **12** (1987) 483.

[69] J. Vaughan, J. Bahder, B. Unzicker, D. Arthur, M. Tatum, T. Hart, G. Harrison, S. Burrows, P. Stringer, and G. M. Laurent, Opt. Express **27** (2019) 30989.

[70] S. Mukamel, *Principles of nonlinear optical spectroscopy* (Oxford University Press, 1995).

[71] T. Buckup, and M. Motzkus, Annu. Rev. Phys. Chem. **65** (2014) 39.

[72] M. Maiuri, M. Garavelli, and G. Cerullo, J. Am. Chem. Soc. **142** (2020) 3.

[73] M. J. Rosker, M. Dantus, and A. H. Zewail, J. Chem. Phys. **89** (1988) 6113.

[74] M. Dantus, M. J. Rosker, and A. H. Zewail, J. Chem. Phys. **89** (1988) 6128.

[75] H. Yoon, D. Wake, J. Wolfe, and H. Morkoç, Phys. Rev. B **46** (1992) 13461.

[76] M. Cowan, J. Ogilvie, and R. Miller, Chem. Phys. Lett. **386** (2004) 184.

[77] P. Tian, D. Keusters, Y. Suzaki, and W. S. Warren, Science **300** (2003) 1553.

[78] T. Brixner, J. Stenger, H. M. Vaswani, M. Cho, R. E. Blankenship, and G. R. Fleming, Nature **434** (2005) 625.

[79] G. S. Engel, T. R. Calhoun, E. L. Read, T.-K. Ahn, T. Mančal, Y.-C. Cheng, R. E. Blankenship, and G. R. Fleming, Nature **446** (2007) 782.

[80] B. A. West, J. M. Womick, and A. M. Moran, J. Phys. Chem. A **115** (2011) 8630.

[81] C.-h. Tseng, P. Sándor, M. Kotur, T. C. Weinacht, and S. Matsika, J. Phys. Chem. A **116** (2012) 2654.

[82] V. I. Prokhorenko, A. Picchiotti, M. Pola, A. G. Dijkstra, and R. J. D. Miller, J. Phys. Chem. Lett. **7** (2016) 4445.

[83] Y. J. Yan, L. E. Fried, and S. Mukamel, J. Phys. Chem. **93** (1989) 8149.

[84] Y. J. Yan, and S. Mukamel, Phys. Rev. A **41** (1990) 6485.

[85] M. F. Gelin, and D. Kosov, Chem. Phys. **347** (2008) 177.

[86] A. Sobolewski, C. Woywod, and W. Domcke, J. Chem. Phys. **98** (1993) 5627.

[87] C. Woywod, W. Domcke, A. L. Sobolewski, and H. J. Werner, J. Chem. Phys. **100** (1994) 1400.

[88] R. Schneider, and W. Domcke, Chem. Phys. Lett. **150** (1988) 235.

[89] L. Seidner, G. Stock, A. Sobolewski, and W. Domcke, J. Chem. Phys. **96** (1992) 5298.

[90] T. Piteša, M. Sapunar, A. Ponzi, M. F. Gelin, N. Došlić, W. Domcke, and P. Decleva, J. Chem. Theory Comput. **17** (2021) 5098.

[91] W. Xie, M. Sapunar, N. Došlić, M. Sala, and W. Domcke, J. Chem. Phys. **150** (2019) No. 154119.

[92] C. Møller, and M. S. Plesset, Phys. Rev. **46** (1934) 618.

[93] C. Hättig, and F. Weigend, J. Chem. Phys. **113** (2000) 5154.

[94] C. Hättig, Adv. Quantum Chem. **50** (2005) 37.

[95] P. G. Szalay, T. Watson, A. Perera, V. F. Lotrich, and R. J. Bartlett, J. Phys. Chem. A **116** (2012) 6702.

[96] I. Borges, A. J. A. Aquino, A. Köhn, R. Nieman, W. L. Hase, L. X. Chen, and H. Lischka, J. Am. Chem. Soc. **135** (2013) 18252.

[97] I. Borges, E. Uhl, L. Modesto-Costa, A. J. A. Aquino, and H. Lischka, J. Phys. Chem. C **120** (2016) 21818.

[98] S. K. Khani, A. M. Khah, and C. Hättig, Phys. Chem. Chem. Phys. **20** (2018) 16354.

[99] X. Huang, J.-P. Aranguren, J. Ehrmaier, J. A. Noble, W. Xie, A. L. Sobolewski, C. Dedonder-Lardeux, C. Jouvet, and W. Domcke, Phys. Chem. Chem. Phys. **22** (2020) 12502.

[100] J. Ehrmaier, M. J. Janicki, A. L. Sobolewski, and W. Domcke, Phys. Chem. Chem. Phys. **20** (2018) 14420.

[101] T. N. V. Karsili, D. Tuna, J. Ehrmaier, and W. Domcke, Phys. Chem. Chem. Phys. **17** (2015) 32183.

[102] X. Huang, and W. Domcke, J. Phys. Chem. A **125** (2021) 9917.

[103] L. H. Thomas, Math. Proc. Cambridge Philos. Soc. **23** (1927) 542.

[104] E. Fermi, Z. Physik **48** (1928) 73.

[105] P. Hohenberg, and W. Kohn, Phys. Rev. **136** (1964) B864.

[106] J. P. Perdew, J. A. Chevary, S. H. Vosko, K. A. Jackson, M. R. Pederson, D. J. Singh, and C. Fiolhais, Phys. Rev. B **46** (1992) 6671.

[107] A. D. Becke, Phys. Rev. A **38** (1988) 3098.

[108] D. C. Langreth, and M. J. Mehl, Phys. Rev. B **28** (1983) 1809.

[109] M. E. Casida, B. Natarajan, and T. Deutsch, in *Fundamentals of time-dependent density functional theory*, edited by M. A. L. Marques, N. T. Maitra, F. M. S. Nogueira, E. K. U. Gross, and A. Rubio (Springer Berlin Heidelberg, Berlin, Heidelberg, 2012), pp. 279.

[110] R. E. Stratmann, G. E. Scuseria, and M. J. Frisch, J. Chem. Phys. **109** (1998) 8218.

[111] L. Hedin, Phys. Rev. **139** (1965) A796.

[112] G. Onida, L. Reining, and A. Rubio, Rev. Mod. Phys. **74** (2002) 601.

[113] D. J. Tozer, J. Chem. Phys. **119** (2003) 12697.

[114] A. Dreuw, and M. Head-Gordon, Chem. Rev. **105** (2005) 4009.

[115] A. Dreuw, and M. Head-Gordon, J. Am. Chem. Soc. **126** (2004) 4007.

[116] S. Grimme, J. Chem. Phys. **124** (2006) 034108.

[117] Y. Jung, R. C. Lochan, A. D. Dutoi, and M. Head-Gordon, J. Chem. Phys. **121** (2004) 9793.

[118] A. Savin, and H. J. Flad, Int. J. Quantum Chem. **56** (1995) 327.

[119] T. Leininger, H. Stoll, H.-J. Werner, and A. Savin, Chem. Phys. Lett. **275** (1997) 151.

[120] T. Yanai, D. P. Tew, and N. C. Handy, Chem. Phys. Lett. **393** (2004) 51.

[121] J.-D. Chai, and M. Head-Gordon, J. Chem. Phys. **128** (2008) No. 084106.

[122] D. Mester, and M. Kállay, J. Chem. Theory Comput. **18** (2022) 1646.

[123] B. Kozma, A. Tajti, B. Demoulin, R. Izsák, M. Nooijen, and P. G. Szalay, J. Chem. Theory Comput. **16** (2020) 4213.

[124] T. Stein, L. Kronik, and R. Baer, J. Am. Chem. Soc. **131** (2009) 2818.

[125] P.-F. Loos, M. Comin, X. Blase, and D. Jacquemin, J. Chem. Theory Comput. **17** (2021) 3666.

[126] E. Wigner, Phys. Rev. **40** (1932) 749.

[127] M. Hillery, R. F. O'Connell, M. O. Scully, and E. P. Wigner, Phys. Rep. **106** (1984) 121.

[128] L. Sun, and W. L. Hase, J. Chem. Phys. **133** (2010) 044313.

[129] K. Husimi, Proc. Phys.-Math. Soc. Jpn. 3rd Series **22** (1940) 264.

[130] K. M. Christoffel, and J. M. Bowman, J. Chem. Phys. **104** (1996) 8348.

[131] S. Kube, C. Lasser, and M. Weber, J. Chem. Phys. **228** (2009) 1947.

[132] A. García-Vela, J. Chem. Phys. **112** (2000) 8302.

[133] A. García-Vela, Chem. Phys. **285** (2002) 245.

[134] R. Crespo-Otero, and M. Barbatti, Theor. Chem. Acc. **131** (2012) 1237.

[135] S. Bai, R. Mansour, L. Stojanović, J. M. Toldo, and M. Barbatti, J. Mol. Model. **26** (2020) 107.

[136] V. C. Papadimitriou, M. R. McGillen, E. L. Fleming, C. H. Jackman, and J. B. Burkholder, Geophys. Res. Lett. **40** (2013) 440.

[137] M. R. McGillen, E. L. Fleming, C. H. Jackman, and J. B. Burkholder, Geophys. Res. Lett. **40** (2013) 4772.

[138] J. E. Subotnik, W. Ouyang, and B. R. Landry, J. Chem. Phys. **139** (2013) 211101.

[139] L. Landau, Phys. Z. Sowjetunion **2** (1932) 118.

[140] C. Zener, Proc. Roy. Soc. (London) **137** (1932) 696.

[141] E. C. G. Stückelberg, Helv. Phys. Acta **5** (1932) 369.

[142] A. K. Belyaev, and O. V. Lebedev, Phys. Rev. A **84** (2011) 014701.

[143] B. J. Schwartz, E. R. Bittner, O. V. Prezhdo, and P. J. Rossky, J. Chem. Phys. **104** (1996) 5942.

[144] L. Wang, A. Akimov, and O. V. Prezhdo, J. Phys. Chem. Lett. **7** (2016) 2100.

[145] C. Wittig, J. Phys. Chem. B **109** (2005) 8428.

[146] L. F. Chibotaru, Phys. Chem. Chem. Phys. **16** (2014) 6942.

[147] C. Zhu, and H. Nakamura, J. Chem. Phys. **97** (1992) 8497.

[148] C. Zhu, and H. Nakamura, J. Chem. Phys. **102** (1995) 7448.

[149] C. Zhu, K. Nobusada, and H. Nakamura, J. Chem. Phys. **115** (2001) 3031.

[150] L. Zhao, J. Liu, and P. Zhou, J. Chem. Phys. **149** (2018) 034309.

[151] W. Xie, and W. Domcke, J. Chem. Phys. **147** (2017) No. 184114.

[152] M. H. Beck, A. Jäckle, G. A. Worth, and H.-D. Meyer, Phys. Rep. **324** (2000) 1.

[153] W. Xie, and W. Domcke, J. Chem. Phys. **147** (2017) 184114.

[154] B. Smith, and A. V. Akimov, J. Phys. Chem. Lett. **11** (2020) 1456.

[155] J. Suchan, J. Janoš, and P. Slavíček, J. Chem. Theory Comput. **16** (2020) 5809.

[156] D. Polli, P. Altoè, O. Weingart, K. M. Spillane, C. Manzoni, D. Brida, G. Tomasello, G. Orlandi, P. Kukura, R. A. Mathies, M. Garavelli, and G. Cerullo, Nature **467** (2010) 440.

[157] A. Nenov, I. Rivalta, S. Mukamel, and M. Garavelli, Comput. Theor. Chem. **1040** (2014) 295.

[158] R. Borrego-Varillas, D. C. Teles-Ferreira, A. Nenov, I. Conti, L. Ganzer, C. Manzoni, M. Garavelli, A. Maria de Paula, and G. Cerullo, J. Am. Chem. Soc. **140** (2018) 16087.

[159] A. Picchiotti, A. Nenov, A. Giussani, V. I. Prokhorenko, R. J. D. Miller, S. Mukamel, and M. Garavelli, J. Phys. Chem. Lett. **10** (2019) 3481.

[160] P. Hamm, and M. Zanni, *Concepts and methods of 2D infrared spectroscopy* (Cambridge University Press, Cambridge, 2011).

[161] S. Biswas, J. Kim, X. Zhang, and G. D. Scholes, Chem. Rev. **122** (2022) 4257.

[162] S. Mukamel, and R. F. Loring, J. Opt. Soc. Am. B **3** (1986) 595.

[163] S. Mukamel, and D. Abramavicius, Chem. Rev. **104** (2004) 2073.

[164] M. Cho, *Two-dimensional optical spectroscopy* (CRC press, 2009).

[165] L. Valkunas, D. Abramavicius, and T. Mancal, *Molecular excitation dynamics and relaxation: quantum theory and spectroscopy* (John Wiley & Sons, 2013).

[166] D. Abramavicius, B. Palmieri, D. V. Voronine, F. Sanda, and S. Mukamel, Chem. Rev. **109** (2009) 2350.

[167] W. M. Zhang, T. Meier, V. Chernyak, and S. Mukamel, Philos. Trans. R. Soc., A **356** (1998) 405.

[168] K. Sun, M. F. Gelin, V. Y. Chernyak, and Y. Zhao, J. Chem. Phys. **142** (2015) 212448.

[169] M. F. Gelin, and W. Domcke, J. Chem. Phys. **144** (2016) 194104.

[170] M. F. Gelin, X. Huang, W. Xie, L. Chen, N. Došlić, and W. Domcke, J. Chem. Theory Comput. **17** (2021) 2394.

[171] X. Huang, W. Xie, N. Došlić, M. F. Gelin, and W. Domcke, J. Phys. Chem. Lett. **12** (2021) 11736.

[172] W. Domcke, J. Ehrmaier, and A. L. Sobolewski, ChemPhotoChem **3** (2019) 10.

[173] K. Sun, W. Xie, L. Chen, W. Domcke, and M. F. Gelin, J. Chem. Phys. **153** (2020) 174111.

Appendix: Publications

(1) Huang, X.; Aranguren, J.-P.; Ehrmaier, J.; Noble, J. A.; Xie, W.; Sobolewski, A. L.; Dedonder-Lardeux, C.; Jouvet, C.; Domcke, W. Photoinduced Water Oxidation in Pyrimidine-Water Clusters: A Combined Experimental and Theoretical Study. *Phys. Chem. Chem. Phys.* **2020,** *22*, 12502-12514.

(2) Huang, X.; Domcke, W. Ab Initio Nonadiabatic Surface-Hopping Trajectory Simulations of Photocatalytic Water Oxidation and Hydrogen Evolution with the Heptazine Chromophore. *J. Phys. Chem. A* **2021,** *125* (45), 9917-9931.

(3) Huang, X.; Domcke, W. Ab Initio Trajectory Surface-Hopping Dynamics Studies of Excited-State Proton-Coupled Electron Transfer Reactions in Heptazine-Phenol Complexes. *Phys. Chem. Chem. Phys.* **2022**, *24,* 15925 - 15936

(4) Gelin, M. F.; Huang, X.; Xie, W.; Chen, L.; Došlić, N. a.; Domcke, W. Ab Initio Surface-Hopping Simulation of Femtosecond Transient-Absorption Pump–Probe Signals of Nonadiabatic Excited-State Dynamics Using the Doorway–Window Representation. *J. Chem. Theory Comput.* **2021,** *17* (4), 2394-2408.

(5) Huang, X.; Xie, W.; Došlić, N.; Gelin, M. F.; Domcke, W. Ab Initio Quasiclassical Simulation of Femtosecond Time-Resolved Two-Dimensional Electronic Spectra of Pyrazine. *J. Phys. Chem. Lett.* **2021,** *12* (48), 11736-11744.

Coypright Agreement

PCCP

ROYAL SOCIETY OF CHEMISTRY

PAPER

View Article Online
View Journal | View Issue

Cite this: *Phys. Chem. Chem. Phys.*, 2020, **22**, 12502

Photoinduced water oxidation in pyrimidine–water clusters: a combined experimental and theoretical study†

Xiang Huang,[a] Juan-Pablo Aranguren,[bcd] Johannes Ehrmaier,[a] Jennifer A. Noble,[b] Weiwei Xie,[e] Andrzej L. Sobolewski,[f] Claude Dedonder-Lardeux,[b] Christophe Jouvet*[b] and Wolfgang Domcke*[a]

Received 22nd March 2020,
Accepted 5th May 2020

DOI: 10.1039/d0cp01562h

rsc.li/pccp

The photocatalytic oxidation of water with molecular or polymeric N-heterocyclic chromophores is a topic of high current interest in the context of artificial photosynthesis, that is, the conversion of solar energy to clean fuels. Hydrogen-bonded clusters of N-heterocycles with water molecules in a molecular beam are simple model systems for which the basic mechanisms of photochemical water oxidation can be studied under well-defined conditions. In this work, we explored the photoinduced H-atom transfer reaction in pyrimidine–water clusters yielding pyrimidinyl and hydroxyl radicals with laser spectroscopy, mass spectrometry and trajectory-based *ab initio* molecular dynamics simulations. The oxidation of water by photoexcited pyrimidine is unequivocally confirmed by the detection of the pyrimidinyl radical. The dynamics simulations provide information on the time scales and branching ratios of the reaction. While relaxation to local minima of the S_1 potential-energy surface is the dominant reaction channel, the H-atom transfer reaction occurs on ultrafast time scales (faster than about 100 fs) with a branching ratio of a few percent.

1. Introduction

Nitrogen-rich aromatic heterocycles, such as *s*-triazine or heptazine (tri-*s*-triazine, Hz), recently became of great interest as building blocks of polymeric materials or covalent organic frameworks which exhibit promising catalytic activity for the evolution of molecular hydrogen from protic solvents (amines, alcohols or water) under irradiation with near UV light.[1–5] While the synthesis of so-called graphitic carbon nitrides[6] by pyrolysis of simple precursor molecules is straightforward, neither the chemical composition nor the molecular structure of these materials are precisely defined. Despite extensive research efforts in the past ten years, the photophysical and photochemical processes underlying the photocatalytic hydrogen evolution reaction with graphitic carbon nitride materials remain a mystery.[7,8]

To gain insight into the fundamental photophysics of heptazine-based materials, a heptazine-derived molecular photocatalyst, tri-anisole-heptazine (TAHz), was recently synthesized by Schlenker and coworkers.[9] It was shown that photoexcited TAHz can oxidize water *via* an H-atom transfer reaction, resulting in the quenching of the excited state of TAHz and the liberation of OH radicals that were detected using terephthalic acid.[9] These findings provide evidence that photooxidation of water with heptazine does not inherently require transport of charge carriers in polymeric or crystalline materials, but rather may occur as a molecular photochemical reaction in homogeneous solution. Since TAHz is still of formidable size for accurate *ab initio* simulations of the photochemical dynamics, it is of interest to search for even simpler chromophores which can reveal at least some of the mechanisms which are fundamental for the light-driven water oxidation reaction.

The photoinduced oxidation of water by a molecular chromophore was first demonstrated for pyridine–water clusters in a molecular beam experiment by Jouvet and coworkers,[10] confirming the predictions of earlier computational studies.[11–13]

[a] Department of Chemistry, Technical University of Munich, Garching, Germany. E-mail: domcke@ch.tum.de
[b] CNRS, Aix Marseille Université, Physique des Interactions Ioniques et Moléculaires, Marseille, France. E-mail: christophe.jouvet@univ-amu.fr
[c] Departamento de Fisicoquímica, Facultad de Ciencias Químicas, Universidad Nacional de Córdoba, Haya de la Torre y Medina Allende, Ciudad Universitaria, X5000HUA Córdoba, Argentina
[d] Centro Láser de Ciencias Moleculares, Universidad Nacional de Córdoba, Haya de la Torre s/n, Pabellón Argentina, Ciudad Universitaria, X5000HUA Córdoba, Argentina
[e] Institute of Physical Chemistry, Karlsruhe Institute of Technology, Karlsruhe, Germany
[f] Institute of Physics, Polish Academy of Sciences, Warsaw, Poland

† Electronic supplementary information (ESI) available: Additional computational data (Fig. SI.1 and SI.2). Additional experimental data (Fig. SI.3–SI.5). See DOI: 10.1039/d0cp01562h

The pyridine (Py) chromophore in pyridine–water (Py–$(H_2O)_n$) clusters was excited to the lowest bright state ($^1\pi\pi^*$, $\approx$4.8 eV (260 nm)). The light-induced abstraction of a hydrogen atom from the water cluster was observed by the detection of the pyridinyl (PyH$^\bullet$) radical in a mass spectrometer after ionization by a probe laser.[10] The excitation energy of Py is 1.8 eV lower than the energy necessary for the direct photodissociation of the OH bond of water molecules (6.66 eV, 186 nm). While the excitation energy of Py is well outside the range of the solar spectrum on the surface of Earth, this experiment demonstrated the fundamental principle that molecular chromophores can drive the dissociation of water molecules well below the intrinsic photodissociation threshold of water. It also was shown in this work that the excess hydrogen atom of the PyH$^\bullet$ radical can be photodetached by 255 nm light. This photodetachment reaction recovers the Py molecule and thus closes the photocatalytic cycle.[10]

Photochemical reactions in the well-defined environment of cold molecular clusters were investigated in the past for a variety of chromophores and solvent molecules. These studies provided important insights into the detailed mechanisms of photochemical reactions, such as proton transfer through molecular wires,[14–17] hydrogen transfer to solvents in chromophore–solvent clusters,[18–24] solvent isomerization,[25–27] characterization of transition states of reactions[28–30] or chiral discrimination.[31] One of the advantages of investigations of the photochemistry of small chromophores in small, size-selected clusters is the possibility of comparison of experimental data with the results of theory which can be performed at a significantly higher level than is possible in the investigation of condensed-phase reactions.

In the present work, we extended this approach to the photochemistry of pyrimidine–water (Pm–$(H_2O)_n$) clusters as a first step towards studies of the photochemistry of nitrogen-rich chromophores in water clusters. The controlled extension of the complexity of photochemical systems from single chromophores in small solvent clusters *via* single chromophores in room-temperature liquid solution towards multi-chromophoric systems in solution is envisioned as a long-term strategy towards the development of a complete understanding of the mechanisms involved in the conversion of solar light to clean fuels in artificial photosynthetic devices.

2. Experimental methods

The setup that we used in this work is composed of a pulsed supersonic expansion combined with a time of flight (TOF) mass spectrometer. In the first experiment, a discharge source, the same as that used in previous experiments to produce either cold neutral van der Waals species[32] or protonated molecular ions,[33] is used to produce hydrogenated radicals. It consists of a pulsed high-voltage discharge located a few mm after the pulsed nozzle which produces pyrimidinyl radicals (hereafter PmH$^\bullet$) from a gas mixture of He/H_2/pyrimidine. The radicals are cooled down in the expansion and ionized between the extraction plates of the reflectron TOF mass spectrometer (Jordan TOF Products, Inc).

In the second experiment, the discharge is removed and Pm–$(H_2O)_n$ clusters are produced by expanding a mixture of water and Pm at their respective vapor pressures at 60 °C with He (between 2 and 6 bar). Two laser beams are temporally and spatially synchronized between the extraction plates of the mass spectrometer. The pump laser excites the clusters while the probe laser ionizes the PmH$^\bullet$ radicals.

The lasers used are YAG-pumped nanosecond OPO lasers (EXSPLA model-NT342B), which have a 10 Hz repetition rate, a resolution (FWHM) of 8 cm^{-1} and a minimum scanning step of 0.02 nm. The lasers are focused in the middle of the extraction zone of the TOF mass spectrometer. These lasers can be scanned from the visible to the UV in three regions: from 410 to 709 nm (OPO signal), from 296 to 409.9 nm (frequency mixing) and from 225 to 295.9 nm (frequency doubling).

3. Computational methods

The equilibrium geometries of Pm and Pm–H_2O complexes were determined by minimizing the energy of the electronic ground state using second-order Møller–Plesset (MP2) perturbation theory.[34] The geometries were optimized without symmetry constraints.

The second-order algebraic-diagrammatic-construction (ADC(2)) method[35–37] was used to calculate vertical excitation energies, oscillator strengths and dipole moments of excited states. The accuracy of the ADC(2) method for the calculation of excitation energies and excited-state potential-energy (PE) surfaces of clusters of heteroaromatic systems with water molecules was critically evaluated in earlier studies in comparison with CASSCF/CASPT2 and equation-of-motion coupled-cluster (EOM-CC) calculations.[12,38] ADC(2) has thereby been established as a reliable tool to describe excited-state H-atom transfer reactions in complexes of N-heterocycles with water molecules.

The driving coordinate for the construction of the minimum-energy reaction path (relaxed scan) for the H-atom transfer reaction from water to Pm is chosen as the OH bond length R_{OH} of the water molecule which is hydrogen-bonded to the N-atom of Pm. For one-dimensional relaxed scans, R_{OH} was fixed, while the energy of a given electronic state was minimized with respect to all other nuclear degrees of freedom. For technical reasons, C_s symmetry (coplanar Pm and H_2O moieties) had to be enforced to allow the minimization of the energies of the lowest excited states of A′ or A″ symmetry. The energies of the other electronic states were determined by single-point energy calculations at these optimized geometries.

Relaxed two-dimensional PE surfaces were computed in analogous manner by fixing R_{OH} as well as the distance R_{ON} between the donor O-atom of water and the acceptor N-atom of Pm. All other nuclear degrees of freedom were relaxed to minimize the energy of the lowest excited states of either A′ or A″ symmetry.

Dunning's correlation-consistent double-ζ basis set (cc-pVDZ)[39] was employed for the electronic-structure calculations.

The electronic-structure calculations were performed with the TURBOMOLE program package[40] using the resolution-of-the-identity (RI) approximation.[41]

The absorption spectra of the Pm–H_2O and Pm–$(H_2O)_4$ clusters were simulated using a protocol which was proposed, among others, by Heller and coworkers and Barbatti and coworkers.[42,43] A set of 2000 geometries was sampled from the harmonic-oscillator thermal Wigner distribution at room temperature. The lowest five vertical excitation energies and the corresponding oscillator strengths were computed for this ensemble. The line spectra generated by this ensemble were convoluted with a Lorentzian of 0.05 eV full width at half maximum to generate a smooth absorption profile.

The dynamics of the photoinduced H-atom transfer reaction from water to Pm in the Pm–H_2O and Pm–$(H_2O)_4$ complexes was studied by *ab initio* on-the-fly trajectory surface-hopping (SH) simulations with the ADC(2) method. We employed a recently developed Landau–Zener (LZ) surface-hopping algorithm.[44–47] This algorithm is a computationally efficient and accurate alternative to the widely used fewest-switches surface-hopping (FSSH) method of Tully.[48] In the LZ-based surface-hopping (LZSH) algorithm, the transition probability between electronic states is determined directly from the topography of the adiabatic potentials in energy-crossing regions, avoiding the computation of rapidly varying derivative couplings near avoided crossings and conical intersections (CIs). The results of simulations with the LZSH method have been compared with those of simulations with the FSSH method and with the results of exact quantum dynamics calculations in several studies of few-state few-mode model systems.[45–47]

In the present work, we used an implementation of the LZSH method based on MP2 and ADC(2) energies and gradients computed with the TURBOMOLE program package.[47] Similar *ab initio* on-the-fly LZ-based trajectory SH simulations of the photochemical dynamics of molecular systems were recently performed by Zhu and coworkers[49] and Kono and coworkers.[50] The initial conditions for the dynamics simulations were selected from the thermal Wigner sample which was generated for the calculation of the absorption spectra. From this ensemble, positions and moments were selected which have excited-state energies within a band of 0.1 eV around the maximum of the absorption spectrum. This sampling, which mimics excitation with a narrow-band laser near the maximum of the absorption spectrum, as is done in the present experiment, results in 207 and 224 excited-state trajectories, respectively, for the Pm–H_2O and Pm–$(H_2O)_4$ complexes. The trajectories were initiated in the adiabatic S_3 state (the bright $^1\pi\pi^*$ state of Pm) and propagated up to 500 fs with a time step of 0.5 fs. When the energy gap between the current adiabatic state and the S_0 state decreased below 0.2 eV, the trajectory was terminated. This event was counted as nonradiative transition to the S_0 state. An instantaneous H-atom transfer from water to Pm is counted when the distance of the active H-atom to the acceptor N-atom of Pm decreases below 1.3 Å. A trajectory is counted as reactive at the end of the time window (500 fs) when the cluster contains PmH• and OH• radicals, either as hydrogen-bonded biradicals or as separated radicals in the water cluster.

4. Results

4.1. Structures and absorption spectra

We selected the Pm–H_2O and Pm–$(H_2O)_4$ complexes as representative examples of Pm–$(H_2O)_n$ complexes. For the Pm–H_2O cluster, a detailed computational investigation of excited-state reaction paths and PE profiles is possible, see below. The Pm–$(H_2O)_4$ cluster, on the other hand, is expected to have a sufficient number of internal degrees of freedom to allow dissipation of the excess energy generated by the H-atom transfer reaction in the cluster. *Ab initio* simulations for significantly larger clusters are beyond the limit of our computational resources.

The calculated equilibrium geometries of the Pm–H_2O and Pm–$(H_2O)_4$ complexes are shown in Fig. 1(a) and (b), respectively. For the Pm–H_2O complex, the conformer with the in-plane orientation of the water molecule is less stable by 0.07 eV than the conformer with perpendicular orientation of the water molecule. This tiny energy difference is irrelevant for the purposes of the present investigation and we therefore restricted the exploration of the excited-state PE surfaces to the in-plane conformer of Pm–H_2O. For the Pm–$(H_2O)_4$ complex, numerous equilibrium structures with similar energies exist. We selected a structure in which the $(H_2O)_4$ cluster is bonded as H-atom donor to one of the N-atoms of Pm. A weak CH···O hydrogen bond gives this cluster additional stability, see Fig. 1(b). The hydrogen bond length between the accepting N-atom of Pm and the H-atom of the water molecule decreases from 2.023 Å for Pm–H_2O to 1.811 Å for Pm–$(H_2O)_4$, indicating a considerable strengthening of the hydrogen bond with Pm in the larger cluster. The $(H_2O)_4$ cluster of Fig. 1(b) is of the so-called double-donor double-acceptor type. Compared with cyclic $(H_2O)_4$ clusters, this cluster exhibits a stronger hydrogen bond with Pm. Moreover, the double-acceptor property of the H_2O molecule which is hydrogen-bonded to Pm softens the OH bond involved in hydrogen bonding with the N-atom of Pm. Both features are favourable for the H-atom transfer reaction.

The vertical excitation energies of the lowest singlet excited states of isolated Pm, the Pm–H_2O complex and the Pm–$(H_2O)_4$ complex are listed in Table 1, including their dominant orbital

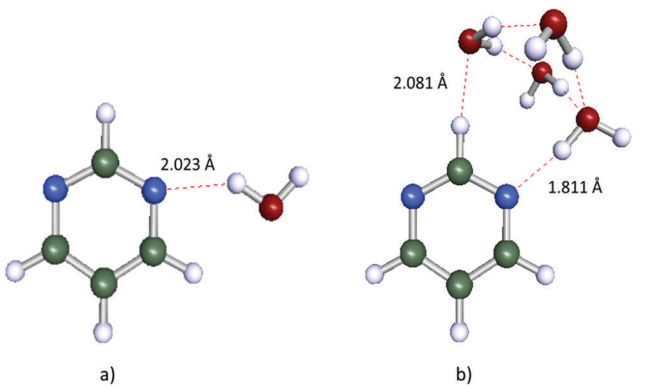

Fig. 1 Ground-state equilibrium geometries of the Pm–H_2O (a) and Pm–$(H_2O)_4$ (b) complexes.

Table 1 Vertical excitation energies (in eV) of the lowest five singlet excited states and the lowest CT state of Pm, the Pm–H_2O complex and the Pm–$(H_2O)_4$ complex, calculated at the ADC(2) level. Oscillator strengths are given in parentheses, dipole moments (in Debye) in brackets

State	Transition orbitals	Pm	Pm–H_2O	Pm–$(H_2O)_4$
$S_1(n\pi^*)$	HOMO−1 → LUMO	4.49(0.005)[0.7]	4.59(0.005)[2.7]	4.47(0.003)[5.8]
$S_2(n\pi^*)$	HOMO−1 → LUMO+1	4.80(0.000)[0.8]	4.91(0.000)[1.5]	4.88(0.001)[7.2]
$S_3(\pi\pi^*)$	HOMO → LUMO	5.53(0.023)[2.3]	5.53(0.025)[0.7]	5.50(0.032)[9.1]
$S_4(n\pi^*)$	HOMO−3 → LUMO	6.08(0.000)[0.8]	6.17(0.000)[2.6]	6.10(0.000)[5.8]
$S_5(n\pi^*)$	HOMO−3 → LUMO+1	6.32(0.006)[0.5]	6.42(0.006)[1.1]	6.41(0.004)[6.6]
CT	p(H_2O) → LUMO	—	8.16(0.028)[16.2]	8.89(0.000)[14.9]

configurations, oscillator strengths (in parentheses) and dipole moments (in brackets). The HF molecular orbitals (MOs) of Pm and Pm–$(H_2O)_4$, which are primarily involved in the electronic configurations of the lowest five excited states, are displayed in Fig. 2. The highest occupied molecular orbital (HOMO) of Pm is a π orbital and the lowest unoccupied molecular orbital (LUMO) of Pm is a π* orbital. It should be noted that the n orbitals (HOMO−1 and HOMO−3 in Pm) are partly delocalized over p orbitals of the water molecules in the Pm–$(H_2O)_4$ complex (see Fig. 2), which indicates a partially covalent character of the water–Pm hydrogen bond in this cluster. The S_1 and S_2 excited states of Pm are of nπ* character and are dark in absorption. The lowest bright excited state is the S_3 state of ππ* character with an excitation energy of 5.53 eV in isolated Pm. Unexpectedly, the excitation energies of the nπ* excited states of Pm–H_2O and Pm–$(H_2O)_4$ are negligibly affected by the hydrogen bonding with water molecules. Usually, for example for pyridine (Py) in aqueous environments,[51] it is found that hydrogen-bonding with water molecules stabilizes the n orbitals more effectively than π and π* orbitals, which results in an increase of the excitation energies of nπ* states. This effect is not observed in Pm–water clusters. To explain this observation, the variation of the orbital energies of Pm with increasing complexation with water is displayed in Fig. S1 of the ESI.† This figure shows that the n, π and π* orbitals are stabilized by approximately the same amount with increasing number of water molecules. While solvation effects on the orbital energies are substantial, they cancel approximately for the excitation energies (orbital energy differences) of Pm–water complexes.

The S_9 state in the Pm–H_2O complex and the S_{19} state in the Pm–$(H_2O)_4$ complex are water-to-Pm charge-transfer (CT) states. They correspond to the excitation of an electron from a p orbital of the hydrogen-bonded water molecule to the LUMO of Pm, as indicated by the blue arrow in Fig. 2 for the Pm–$(H_2O)_4$ cluster. The CT character of these states is confirmed by the exceptionally large dipole moment of about 15 Debye, see Table 1. The excitation energies of these CT state are higher than 8.0 eV at the ground-state equilibrium geometry. Since the p orbital of water is more strongly stabilized in the larger water cluster, the excitation energy of the CT state is about 0.7 eV higher in Pm–$(H_2O)_4$ than in Pm–H_2O. For Pm–$(H_2O)_4$, two additional transitions of CT character, S_7 and S_8, were found (not listed in Table 1). These CT states correspond to transitions of an electron from the p orbital of the water molecule which is weakly hydrogen-bonded with the CH group of the chromophore (see Fig. 1(b)) to π* orbitals of Pm. In these CT states, the water molecule adjacent to Pm is oxidized by hole transfer from Pm to H_2O. In contrast to the CT state involving the water molecule

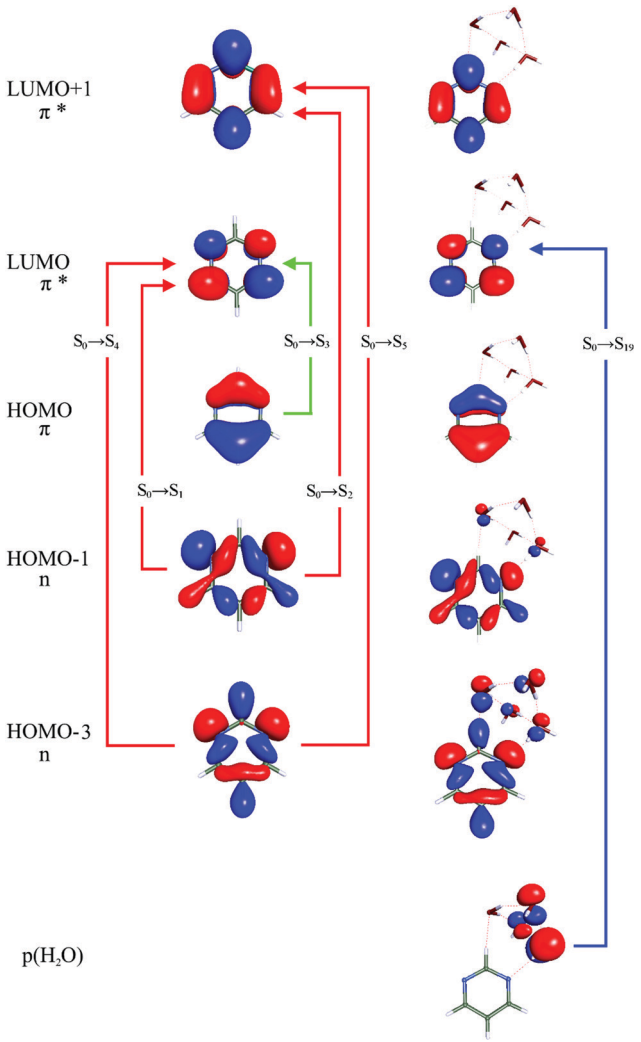

Fig. 2 Hartree–Fock molecular orbitals of Pm (left) and of the Pm–$(H_2O)_4$ complex (right) involved in the configurations of the lowest five singlet excited states and the charge-transfer state. nπ* transitions are marked in red, ππ* transitions are marked in green. p(H_2O) denotes an orbital which is mostly localized on the oxygen atom of the water molecule adjacent to Pm. Excitation from this orbital to the LUMO of Pm results in the charge-transfer state (transition marked in blue). Note that the n orbitals (HOMO−3, HOMO−1) of the Pm–$(H_2O)_4$ complex are partially delocalized over the water molecules, showing that the hydrogen bond has partially covalent character. The π and π* orbitals, on the other hand, are exclusively localized on Pm.

H-bonded to the N-atom of Pm, the driving force for proton transfer is weak in the CT states involving the CH group, since the protons are firmly H-bonded in the water cluster and the H-atom transfer requires an energetically unfavorable rehybridization of the aromatic ring. It is likely that these additional CT states are rapidly deactivated by internal conversion to lower electronic states prior to proton transfer. In the dynamics simulations (see below) we did not find evidence for any H-atom transfer event from the $(H_2O)_4$ cluster to the CH group of Pm.

The simulated absorption spectra of the Pm–H_2O and Pm–$(H_2O)_4$ complexes are shown in Fig. 3 in comparison with the experimental excitation/ionization spectrum recorded in this work for a distribution of Pm–$(H_2O)_n$ clusters. The band maximum of the Pm–H_2O complex is predicted by the ADC(2) calculations at 5.42 eV, which is 0.11 eV red-shifted from the vertical S_3 excitation energy. For the Pm–$(H_2O)_4$ complex, the band maximum is predicted at 5.38 eV, which is 0.12 eV red-shifted from the vertical excitation energy of the $S_3(\pi\pi^*)$ state. From the calculations, it seems that the maximum of the absorption profile does not depend significantly on the cluster size.

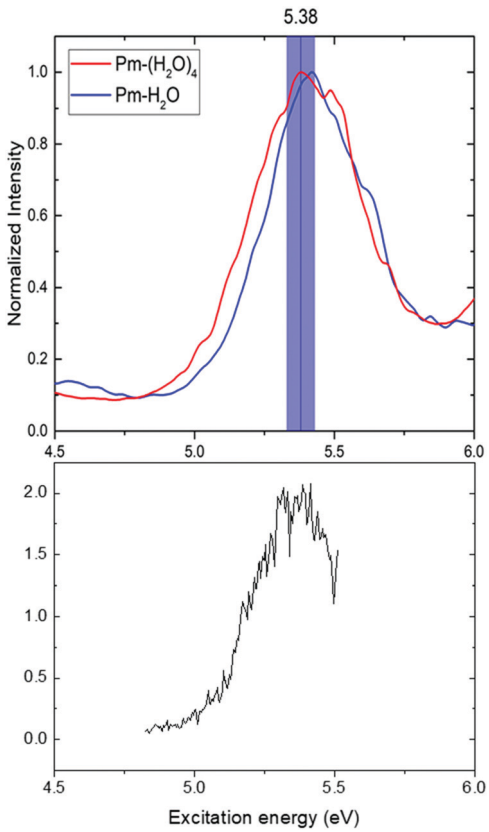

Fig. 3 Upper panel: Absorption spectra of the Pm–H_2O and Pm–$(H_2O)_4$ clusters computed with the nuclear ensemble model and the ADC(2) electronic-structure method. The initial conditions for the dynamics simulations were sampled from the energy window shaded in blue (5.38 ± 0.05 eV). Lower panel: Experimental excitation/ionization spectrum of Pm–$(H_2O)_n$ clusters obtained by two-photon ionization and recorded at the Pm–$(H_2O)_{n=1}^+$ mass. The signal presumably contains contributions from larger clusters which have evaporated water molecules after ionization.

The maximum of the experimental spectrum is at 5.35 ± 0.05 eV. The excellent agreement between simulations and experiments confirms the high accuracy of the ADC(2) method for calculating excitation energies in the Franck–Condon region.

4.2. Detection and spectroscopic characterization of the PmH• radical

Fig. 4 shows mass spectra obtained in experiments with the probe (ionization) laser set to 353.8 nm and with the discharge on (black trace) or off (red trace). In the absence of the discharge, no ion signal is observed, since pyrimidine (m/z = 80) does not absorb at this wavelength (Fig. SI.3 in the ESI† shows the REMPI spectrum of pyrimidine). When the discharge is on, an intense peak at m/z = 81 with its isotopic companion at m/z = 82 is obtained, indicating that protonated pyrimidine PmH^+ is observed *via* ionization of the PmH• radical.

The electronic spectrum of the PmH• radical is recorded by monitoring the intensity of the m/z = 81 mass peak (PmH^+) while scanning the probe (ionization) laser from the visible to the UV, as displayed in Fig. 5. Different groups of absorption bands can be clearly observed: a group at low energy (355–379 nm or 3.5–3.27 eV) which consists of well-resolved narrow bands and a group at higher energies (330–354 nm or 3.75–3.5 eV), which consists of broad vibronic bands with narrow spacings (see the inset in Fig. 5). The lines between 296 and 330 nm correspond to the spectrum of the pyrimidine isotopomer containing a ^{13}C carbon atom (see Fig. SI.3, ESI†). No signal is detected further to the blue, between 4.2 and 5.5 eV (*i.e.* off the scale in Fig. 5).

The two main band systems (the narrow band and broad band) can be due to either different states of the same species or different tautomers. The latter possibility was suggested previously for tautomers of several aromatic molecules where the protonation takes place on the aromatic ring.[52] Analogously, the hydrogenation of Pm could take place at a C-atom of the aromatic ring rather than at the N-atom. As is discussed in the ESI† (see Fig. SI.4), UV–UV hole-burning (HB) experiments reveal

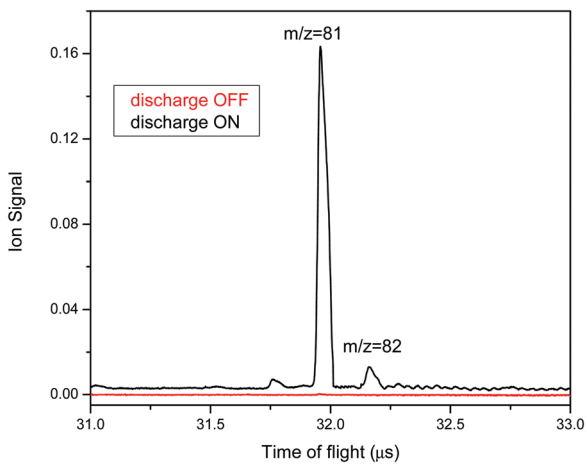

Fig. 4 Mass spectra obtained for a mixture of He/H_2/pyrimidine with the discharge source on (black) or off (red). The probe (ionization) laser is set to 353.8 nm.

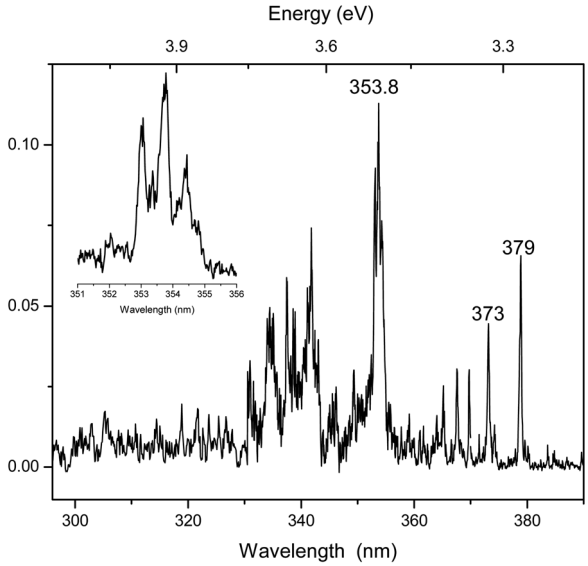

Fig. 5 Electronic spectrum of the PmH• radical produced in the discharge source and cooled down in the supersonic expansion. The spectrum is obtained by resonance enhanced one-color two-photon ionization (R2PI). The inset shows the most intense line at 353.8 nm on an enlarged scale.

that the transitions starting at 379 nm and 353.8 nm in Fig. 5 are due to same species. The transitions at 353.8 and 342 nm could be due to different electronic states or to different vibrational levels of the electronic states detailed above. The profiles of these transitions are similar, which tends to favor their attribution to vibrational levels.

To aid the assignment of the experimental electronic spectrum of the PmH• radical, vertical excitation energies were calculated with the unrestricted ADC(2) method. The equilibrium geometry of the PmH• radical is planar with an NH distance R_{NH} = 1.014 Å. The vertical excitation energies and oscillator strengths of the five lowest doublet excited states are listed in Table 2. The singly occupied molecular orbital (SOMO) of the PmH• radical is a π orbital, while the LUMO is a diffuse σ* orbital. The lowest excited state (D_1), with a calculated excitation energy of 1.98 eV (627 nm), corresponds to the excitation from the SOMO to the lowest π* orbital. The D_2 state, with an excitation energy of 2.67 eV (465 nm), is the lowest πσ* state: its main configuration corresponds to an orbital transition from the SOMO to the LUMO (see Fig. SI.2, ESI†). The computed oscillator strengths of the lowest five excited states of PmH• are very small, see Table 2. The calculation did not take into account vibronic intensity borrowing effects from higher lying bright excited states and therefore likely underestimates the actual oscillator strengths.

Table 2 Vertical excitation energies (in eV) and oscillator strengths (in parentheses) of the five lowest excited states of the PmH• radical, calculated at the ADC(2) level

State	Energy
D_1 (ππ*)	1.98 (0.001)
D_2 (πσ*)	2.67 (0.000)
D_3 (πσ*)	3.48 (0.001)
D_4 (πσ*)	3.74 (0.001)
D_5 (ππ*)	3.99 (0.005)

We assign the first experimentally observed transition starting at 3.27 eV (379 nm) to the D_5(ππ*) state with a calculated vertical excitation energy of 3.99 eV on account of the sharpness of the vibronic lines which is characteristic of a bound ^{2}ππ* state. This implies that the excitation energy of the D_5(ππ*) state is significantly overestimated by the unrestricted ADC(2) method. The transitions at around 3.50 eV (353.8 nm) and 3.65 eV (340 nm) are assigned to the ^{2}πσ* states D_3 and D_4, calculated at 3.48 eV and 3.74 eV. For these states, the agreement between theory and experiment is very good. The diffuseness of these bands is consistent with the assignment to πσ* states. The observed intensities do not correlate well with the calculated oscillator strengths, which may indicate the importance of vibronic intensity borrowing effects.

The calculated ionization potential of the PmH• radical is 5.59 eV (45 090 cm^{-1} or 222 nm), taking into account the difference in the zero-point energies. This prediction agrees with the fact that the ionization threshold has not been observed within the spectral range covered by the present experiment. This finding also implies that two-photon absorption is necessary to detect the PmH• radical. For this reason, the first two exited states D_1 and D_2 of the PmH• radical cannot be observed in the present experiment.

4.3. Experimental investigation of excited-state H-atom transfer in Pm–$(H_2O)_n$ clusters

The distribution of cluster size(s) of Pm–$(H_2O)_n$ clusters is not known explicitly. Clusters with size $n > 2$ are not detected in the expansion even when optimizing the expansion conditions for larger clusters (in general, cluster size increases with increasing backing pressure). It is likely that clusters with $n > 2$ have lifetimes that are too short to allow ionization with our ns lasers. However, since the variation of the PmH• signal as a function of the backing pressure is similar to that reported for the PyH• radical, it is anticipated that large clusters should be involved in the reaction, as was the case for Py–$(H_2O)_n$ clusters.[10]

Both Pm and Pm–$(H_2O)_n$ clusters exhibit a broad absorption band around 240 nm (see Fig. 3 and Fig. SI.5, ESI†). At this wavelength, PmH• radicals do not absorb, as discussed above. On the other hand, PmH• radicals have an absorption band at 353.8 nm, where Pm and its complexes with water do not absorb. This observation suggests that the photoinduced reaction in Pm–water clusters yielding PmH• radicals can be selectively explored by exciting the clusters at 240 nm and probing the formation of the radical at 353.8 nm. The Pm–$(H_2O)_n$ clusters produced in the supersonic jet were therefore excited at 240 nm and the PmH• radical was probed by ionization at 353.8 nm, see Scheme 1.

The delay between pump and probe lasers is chosen to be 550 ns in order to discriminate the PmH• radical from the ^{13}C isotope of pyrimidine, and to discriminate the reaction in the excited state of neutral clusters from a possible reaction

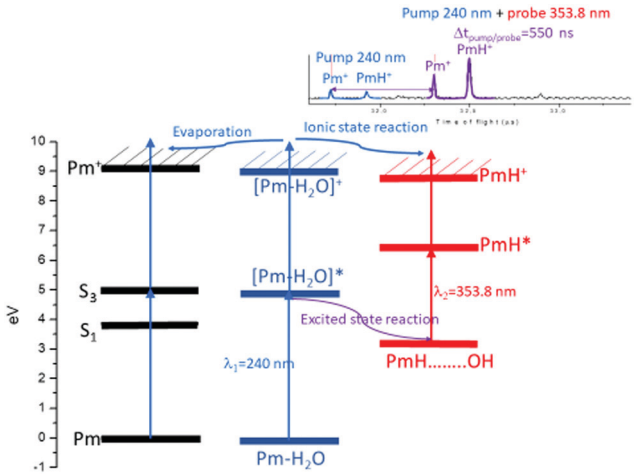

Scheme 1 Reaction scheme for Pm–$(H_2O)_n$ clusters. Pm and Pm–$(H_2O)_n$ are excited with a single 240 nm photon to the bright $^1\pi\pi^*$ state (S_3). Excited Pm–$(H_2O)_n$* clusters may absorb a second 240 nm photon leading to ionic clusters Pm–$(H_2O)_n^+$ that can either evaporate water molecules or react to give PmH^+ ionic fragments (blue arrows). Excited Pm–$(H_2O)_n$* clusters may also react to yield PmH• and OH• radicals (violet arrow), where PmH• is probed *via* two photon ionization at 353.8 nm (red arrows). These experiments were performed within the extraction region of the TOF mass spectrometer held at a constant voltage.

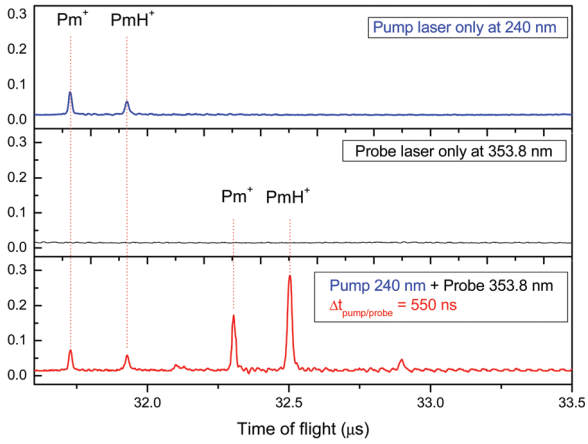

Fig. 6 Mass spectra recorded after excitation of Pm–$(H_2O)_n$ clusters. Upper trace: Pump laser only, at 240 nm; Pm–$(H_2O)_n$ clusters are excited and the PmH^+ ion is produced (by reaction in cationic clusters) through one-color two-photon absorption. Middle trace: Probe laser only, at 353.8 nm; no ion signal is observed, since neither Pm nor Pm–$(H_2O)_n$ absorb at this wavelength. Lower trace: Pump (240 nm) and probe (353.8 nm) lasers, with the probe laser delayed by 550 ns; the most intense peak is the PmH^+ ion produced by a PCET reaction in the neutral clusters (excited by one photon at 240 nm) followed by ionization of the product PmH• radical (*via* a two-photon process at 353.8 nm).

in cationic clusters due to two-photon absorption at 240 nm (the latter process is reflected by the PmH^+ peak in the upper panel of Fig. 6). Besides, this delay precludes absorption of the probe laser by excited states of the clusters which have much shorter lifetimes. The PmH^+ ions generated by ionization of PmH• with the probe laser are observed 550 ns after the PmH^+ ions produced solely by the pump laser (240 nm), since the $t = 0$ setting for the time of flight is synchronized with the pump laser.

Evidence for the formation of the PmH• radical is presented in Fig. 6. The PmH^+ signal is absent if the pump laser is off and the probe laser is on (middle trace). When both lasers are present (lower trace), the PmH• radical, which is detected *via* its ionization product PmH^+, gives rise to the most intense peak (see Scheme 1). The H-atom transfer reaction in excited states of Pm–water clusters is thus clearly confirmed.

In the upper trace of Fig. 6, a small amount of the PmH^+ ion is observed through a one-color two-photon ionization scheme with only the pump laser at 240 nm. This signal does not correspond to excitation/ionization of the PmH• radical, which does not absorb in this spectral region, and thus is not related to the H-atom transfer reaction in the excited states of neutral Pm–water clusters. The signal, rather, comes from an H-atom transfer reaction in ionic Pm–water clusters (see Scheme 1, blue arrows). The spectral signatures of the H-atom transfer reaction in the (neutral) excited state or in the ionic state of Pm–$(H_2O)_n$ clusters are totally different. The PmH^+ signal arising from the ionic reaction appears at wavelengths corresponding to the two-photon absorption of Pm–$(H_2O)_n$ clusters, between 230 nm and 245 nm (see Fig. SI.5, ESI†), while the excited-state reaction in neutral pyrimidine–water clusters yields PmH• radicals, which cannot be ionized in the 230–245 nm spectral region, but will be ionized in the 320–380 nm spectral region, as observed when PmH• radicals produced in the discharge source are ionized (Fig. 5).

Aside from the signatures in mass spectra at fixed wavelengths (Fig. 6), the PmH• radical produced *via* excited-state reactivity in Pm–$(H_2O)_n$ clusters can be detected through a two-photon ionization scheme in the spectral region where it absorbs. In Fig. 7, we present the pump/probe PmH• action spectrum (with PmH• the product of an excited-state reaction in Pm–$(H_2O)_n$ clusters) compared to the spectrum obtained for the cold species generated in the discharge source. This comparison unambiguously confirms that the PmH^+ signal detected with the probe laser is due to the ionization of the PmH• radical. It can be observed that the peaks in the action spectrum resulting from the reaction in clusters are broadened in comparison with the spectrum of the cold species produced in the discharge source, which indicates that the PmH• reaction products in clusters are generated with significant internal energy.

4.4. Computational investigation of excited-state PCET in Pm–H_2O and Pm–$(H_2O)_4$ clusters

We have performed quasi-classical trajectory surface-hopping simulations of the photoinduced reaction dynamics in the Pm–H_2O and Pm–$(H_2O)_4$ complexes. For the simple Pm–H_2O complex, it is possible to compute one-dimensional and two-dimensional relaxed energy profiles which are helpful for the interpretation of the reaction mechanism. The Pm–$(H_2O)_4$ complex is a more realistic model of the photochemical water oxidation reaction occurring in Pm–water clusters. Briefly, the simulations for the Pm–$(H_2O)_4$ complex provide evidence of

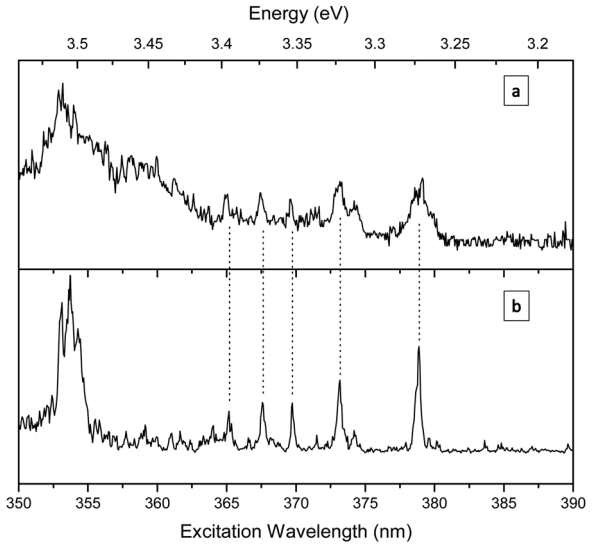

Fig. 7 Comparison between PmH• spectra obtained *via* two-photon ionization for (a) PmH• produced in the H-atom transfer reaction in Pm–$(H_2O)_n$ clusters, excited at 240 nm; and (b) cold PmH• produced in the discharge source (from Fig. 5).

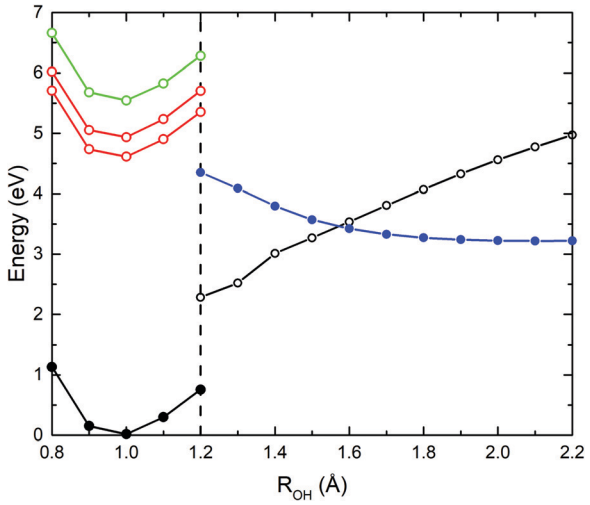

Fig. 8 Energy profiles of the electronic ground state and the lowest excited states of the Pm–H_2O complex. Solid dots indicate that the geometry was optimized for this electronic state. Hollow dots represent energies calculated at geometries which were optimized for another electronic state. Black: electronic ground state; green: excited states of A′ symmetry; red: excited states of A″ symmetry; blue: CT state.

three reaction mechanisms following excitation of the bright $^1\pi\pi^*$ state of Pm: (i) radiationless relaxation of the $S_3(\pi\pi^*)$ state *via* the $S_2(n\pi^*)$ state to the $S_1(n\pi^*)$ state on a time scale of about 100 fs, (ii) H-atom transfer from water to Pm occurring on about the same timescale, yielding ground-state PmH•···OH•$(H_2O)_3$ biradicals, and (iii) radiationless decay of the $S_1(n\pi^*)$ state to the S_0 state of Pm on longer timescales (picoseconds and beyond). The H-atom transfer reaction is found to occur only within the first 150 fs in competition with the electronic relaxation from the $S_3(\pi\pi^*)$ to the $S_1(n\pi^*)$ state.

4.4.1. PE profiles and PE surface for the Pm–H_2O cluster. To assist the interpretation of the dynamics simulations, we computed one-dimensional and two-dimensional relaxed energy profiles for the excited-state H-atom transfer reaction in the Pm–H_2O complex. These data are also useful at a qualitative level for the interpretation of the H-atom transfer reaction in the Pm–$(H_2O)_4$ cluster.

Electronic energy profiles along the relaxed scan for the H-atom transfer reaction from H_2O to Pm in the Pm–H_2O complex are shown in Fig. 8. The driving coordinate R_{OH} is defined as the bond length of the OH group of the water molecule involved in hydrogen bonding with the N-atom of Pm. For small values of R_{OH} (<1.2 Å), the complex consists of a water molecule which is hydrogen-bonded to the Pm molecule (see Fig. 1(a)). For large R_{OH} (>1.2 Å), on the other hand, the complex consists of a hydrogen-bonded PmH•···OH• radical pair. For small R_{OH}, the relaxed scan has been computed in the electronic ground state and the excited-state energy profiles are found to be parallel to the energy profile of the electronic ground state, representing locally excited $n\pi^*$ (red) and $\pi\pi^*$ (green) states of Pm. For $R_{OH} > 1.2$ Å, the relaxed scan has been computed for the lowest state of A″ symmetry and the energy of this state is shown in the right part of the graph (blue curve with solid dots). It represents a CT state involving the transition of an electron from a $p_{x/y}$ orbital of the hydrogen-bonded water molecule to the π^* orbital of Pm. The energy of the closed-shell S_0 state at these CT-state-optimized geometries is given by the open black circles. While the energy of the CT state decreases with increasing R_{OH}, the energy of the closed-shell S_0 state increases steeply with R_{OH}. As a result, the energy profile of the CT state crosses the ground-state energy profile with increasing R_{OH} and becomes the electronic state of lowest energy for $R_{OH} > 1.58$ Å, see Fig. 8. In this region of R_{OH}, the electronic charge transfer is neutralized by the transferred proton. The dramatic stabilization of the energy of the CT state by proton transfer from the water molecule to Pm illustrates the pronounced driving force for proton transfer once the CT state is populated by hole transfer from Pm to the H_2O molecule. This interplay of electron transfer and proton transfer is usually termed proton-coupled electron transfer (PCET) in the literature.[53] The net effect is the transfer of an H-atom. Herein, we use the terms "H-atom transfer" and "PCET" synonymously. Due to the strong driving force and the low mass of the proton, the PCET reaction can compete with ultrafast radiationless deactivation pathways of the $n\pi^*$ and $\pi\pi^*$ excited states of Pm (see below). The crossing of the energy of the CT state of A″ symmetry with the energy of the S_0 state of A′ symmetry in Fig. 8 is a symmetry-allowed energy crossing which becomes a CI when out-of-plane vibrational modes are taken into account.

A relaxed two-dimensional PE surface of the lowest state of A″ symmetry (which is the $n\pi^*$ state in the Franck–Condon region) of the Pm–H_2O complex spanned by the reaction coordinates R_{OH} and R_{ON} (the distance between the O-atom of water and the N-atom of Pm) is displayed as contour plot in Fig. 9. This surface provides a more complete picture of the PCET reaction in the Pm–H_2O complex. The energy minimum

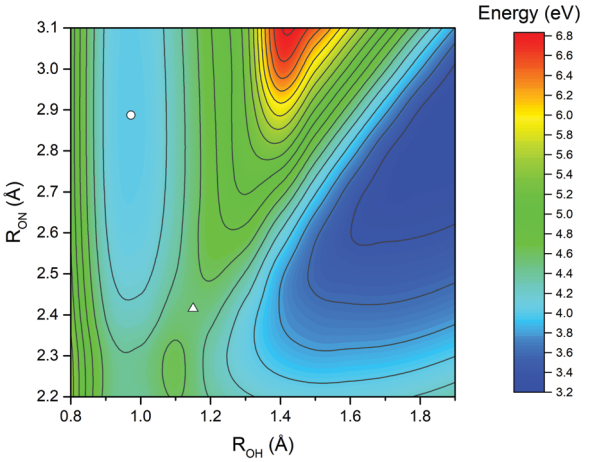

Fig. 9 Relaxed 2D PE surface of the lowest state of A″ symmetry of the Pm–H_2O complex, computed with the ADC(2) method. The contour lines are spaced by 0.2 eV. The circle marks the equilibrium geometry of the lowest $^1n\pi^*$ state. The triangle marks the saddle point of the PCET reaction.

located at small OH bond length (upper-left part) corresponds to the minimum of the lowest locally excited nπ* state of the chromophore (it corresponds to the left part of Fig. 8). The deep valley for large OH distance (right part) corresponds to the $PmH^{\bullet}\cdots OH^{\bullet}$ biradical. The region of high energy (colored in red) represents the lower cone of a CI with the next higher excited state. The saddle point (marked by the triangle in Fig. 9) separating the local S_1 minimum from the valley leading to the biradical is located at R_{OH} = 1.15 Å, R_{ON} = 2.42 Å, at an estimated energy of 4.54 eV. The height of the barrier relative to the local S_1 energy minimum (4.07 eV) is 0.50 eV, which is about 0.30 eV above the zero-point energy of the OH stretching vibration in the S_1 state.

4.2.2. Trajectory surface-hopping dynamics simulations. The trajectories were started in the bright $S_3(\pi\pi^*)$ adiabatic state of Pm with initial positions and momenta sampled from the thermal Wigner distribution as described in the computational methods section. The time-dependent population probabilities of the four lowest adiabatic excited electronic singlet states and the ground state are plotted in Fig. 10 up to 500 fs for the Pm–H_2O and Pm–$(H_2O)_4$ complexes. Overall, the two complexes exhibit similar electronic population dynamics. The initial population in the $S_3(\pi\pi^*)$ state generated by the pump laser is initially transferred to the $S_2(n\pi^*)$ state and subsequently to the $S_1(n\pi^*)$ state within about 100 fs. Weak recurrences of the S_2 population in the Pm–H_2O complex (green curve in Fig. 10(a)) are reduced in the Pm–$(H_2O)_4$ complex (green curve in Fig. 10(b)). The main difference between the two complexes is in the population of the S_0 state (black line). In the Pm–H_2O complex, no population is transferred to the S_0 state within the first 200 fs. In the Pm–$(H_2O)_4$ complex, on the other hand, the S_0 population increases around 50 fs, during the decay of the S_3 and S_2 populations. As will be discussed below, this short-time increase of the S_0 population in the Pm–$(H_2O)_4$ complex arises from H-atom transfer processes which generate biradicals in the electronic ground state. These H-atom transfer reactions die out when the electron population has settled in the S_1 state after about 100 fs. The S_1 population decays slowly (on a timescale of picoseconds) by internal conversion to the S_0 state. Interestingly, this slow decay is more pronounced for the Pm–$(H_2O)_4$ complex than for the Pm–H_2O complex. The S_0 population reaches about 13% at 500 fs in the Pm–$(H_2O)_4$ complex, while it reaches only 8% in the Pm–H_2O complex. At t = 500 fs, about 86% (82%) of the electronic population is in the S_1 state for the Pm–H_2O (Pm–$(H_2O)_4$) complex. The distribution of the adiabatic electronic state populations at the end of the simulation interval is shown on the right hand side of Fig. 10.

The H-atom transfer dynamics is monitored by the time evolution of the bond length between the acceptor N-atom of

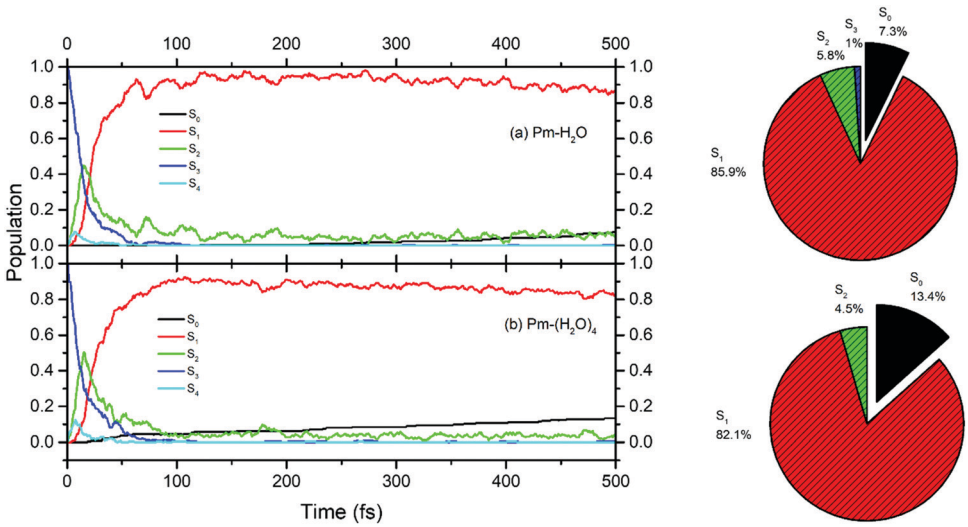

Fig. 10 Population probabilities of the four lowest energy excited states (S_1 to S_4) and the S_0 state for (a) the Pm–H_2O complex and (b) the Pm–$(H_2O)_4$ complex. The population distribution at t = 500 fs is shown on the right hand side.

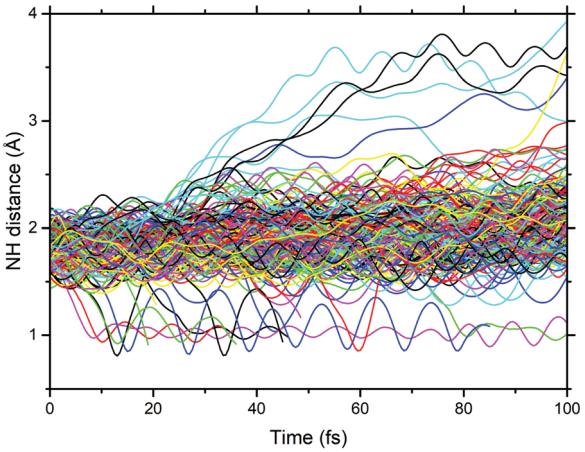

Fig. 11 NH bond lengths of the ensemble of trajectories for the Pm–$(H_2O)_4$ complex. An oscillating NH distance around 1.0 Å indicates a successful H-atom transfer from water to Pm.

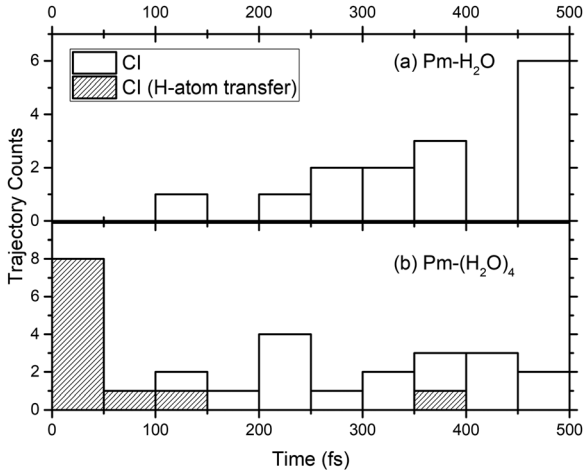

Fig. 12 Histogram recording hits of S_1–S_0 CIs for (a) the Pm–H_2O complex and (b) the Pm–$(H_2O)_4$ complex. CIs located in the non-hydrogen-transferred region are represented by white boxes, those located in the hydrogen-transferred region are marked by hatched boxes.

Pm and the H-atom of the hydrogen-bonded water molecule. In the Pm–H_2O complex, no persistent H-atom transfer processes could be identified. In the Pm–$(H_2O)_4$ complex, 11 out of 224 trajectories (6%) lead to sustained proton transfer from the water cluster to Pm. The time evolution of the distances between the transferred H-atom and the accepting N-atom of Pm for the ensemble of trajectories of the Pm–$(H_2O)_4$ complex within the first 100 fs is presented in Fig. 11. A persistent small value of the NH distance ($\approx$1.0 Å) indicates that a successful H-atom transfer reaction from the hydrogen-bonded water molecule to the Pm chromophore, whereas intermediate ($\approx$1.5–2.0 Å) or overall increasing NH distances indicate non-reactive trajectories. Large oscillations of the NH bond length indicate large excess energy in the NH vibration after relaxation to the electronic ground state.

Histograms recording all hits of S_1–S_0 CIs by trajectories (see Section 3 for details) in the Pm–H_2O and Pm–$(H_2O)_4$ complexes are shown in Fig. 12. The events represented by white boxes represent relaxation to the electronic ground state at CIs which do not involve proton transfer (internal conversion within Pm). The events shown by hatched boxes represent H-atom transfer reactions producing ground-state biradicals. They are responsible for the increase of the S_0 population near 50 fs in Fig. 10(b). Interestingly, most of the successful H-atom transfer events occur within the first 50 fs during and in competition with the radiationless deactivation of the S_3 and S_2 states of Pm.

After about 200 fs, most of the electronic population resides in the S_1 electronic state (see Fig. 10) and the trajectories gradually relax towards the local minimum of the S_1 electronic PE surface. PCET from this relaxed distribution requires tunneling through the barrier of about 0.5 eV on the S_1 surface (see Fig. 9) and is expected to take place on picosecond to nanosecond time scales. There exists a single trajectory in the Pm–$(H_2O)_4$ complex with a late proton transfer event at t = 361.5 fs. The mechanism of this delayed proton transfer reaction is a reorganization within the $(H_2O)_4$ cluster which precedes the proton transfer.

We analyzed in detail all 11 trajectories undergoing proton transfer in the Pm–$(H_2O)_4$ complex. A fluctuation of the N···H–O hydrogen bond length prior to electron transfer from water to Pm is a characteristic feature of these trajectories. After the electron transfer, the proton of the hydrogen-bonded water molecule is driven from water to Pm, which neutralizes the electronic charge separation, resulting in a neutral biradical. To illustrate a typical H-atom transfer process in the Pm–$(H_2O)_4$ complex, a detailed analysis of a representative trajectory is presented in Fig. 13. The time evolution of the NH distance in Fig. 13(c) reveals a proton transfer event at about 6 fs (NH distance $<$1.3 Å, marked by the vertical dashed line in Fig. 13). The hole jumps from the π orbital of Pm to a p orbital of water for the first time at about 5 fs and continues to oscillate between Pm and water before it finally settles on water at about 20 fs. The S_1–S_0 energy gap decreases rapidly around 6 fs and then more slowly until a S_1–S_0 degeneracy is reached at 34 fs, where the trajectory is stopped. The images at the bottom of Fig. 13 are three snapshots of the hole orbital, illustrating the hole transfer from Pm to the water cluster.

5. Discussion and conclusions

It has been shown in this work that excitation of the Pm molecule in water clusters to the $\pi\pi^*$ excited singlet state with 240 nm light can result in an H-atom transfer reaction from a hydrogen-bonded water molecule to the Pm molecule. The reaction is demonstrated experimentally by the detection of the $PmH^\bullet$ radical *via* its ionization product, the PmH^+ ion, in a TOF mass spectrometer. The simultaneously generated $OH^\bullet$ radical could not be detected in the present experimental setup. These results confirm that photoexcited Pm, like photoexcited Py,[10] can oxidize water by a H-atom transfer reaction in a cold aqueous environment. In addition, the electronic spectrum of the $PmH^\bullet$ radical has been characterized for the first time in

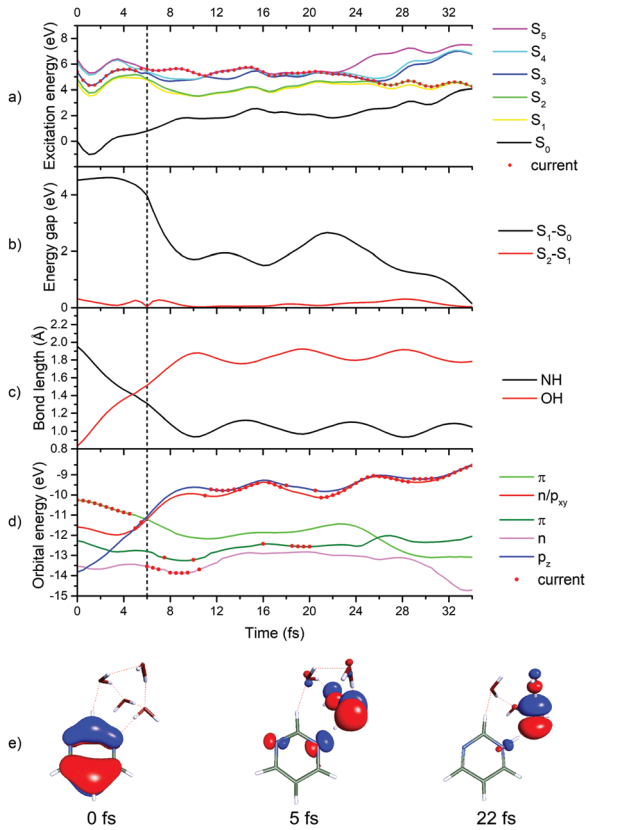

Fig. 13 Time evolution of characteristic features of a representative trajectory (from the ensemble of Fig. 11) undergoing proton transfer before deactivation to the electronic ground state. From top to bottom: (a) energies of excited states and ground state; the dots mark the currently populated electronic state. (b) S_1–S_0 and S_2–S_1 energy gaps. (c) distances of the active H-atom from the donor (O–H) and acceptor (N–H) atoms. (d) time evolution of orbital energies; the dots mark the current electronic hole. (e) hole orbital at selected times. The vertical dashed line in (a)–(d) marks the moment (t = 6 fs) when R_{NH} drops below 1.3 Å.

the range 380–330 nm. This data should be useful for future studies of photoinduced radical generation in Pm–solvent clusters.

The experiments, performed with ns pulsed lasers, did not deliver information on the time scale of the H-atom transfer reaction in the clusters, nor did they provide information on the quantum yield of the water oxidation reaction. To obtain deeper insight into the reaction dynamics, we performed first-principles numerical reaction dynamics simulations, using a quasi-classical trajectory SH algorithm in combination with *ab initio* ADC(2) electronic-structure calculations. The simulations were performed for two selected clusters, Pm–H_2O and Pm–$(H_2O)_4$, to gather some information on the cluster-size dependence of the reactions. We were able to cover 500 fs of *ab initio* simulation time. The trajectory-based simulations reveal the characteristic features of the competition between ultrafast non-reactive radiationless deactivation within the Pm chromophore and the excited-state PCET reaction with water.

The majority of the initially prepared population of the $S_3(\pi\pi^*)$ state of Pm was found to decay *via* the intermediate $S_2(n\pi^*)$ state to the $S_1(n\pi^*)$ state within about 100 fs. In the Pm–$(H_2O)_4$ complex, H-atom transfer from the hydrogen-bonded water molecule to Pm is found to take place within 100 fs in competition with the radiationless relaxation to the S_1 state, generating ground-state biradicals with a probability of a few percent. This ultrafast PCET reaction is absent in the Pm–H_2O complex. On longer (picosecond) timescales, the population of the $S_1(n\pi^*)$ state decays by internal conversion to the S_0 state. This radiationless decay in Pm is moderately enhanced by the water environment. For the Pm–$(H_2O)_4$ cluster, 13% of the electronic population is found in the S_0 state at 500 fs. On longer time scales (not covered by the present simulations), PCET yielding pyrimidinyl and hydroxyl radicals can occur from the relaxed population in the S_1 state by H-atom tunneling through the H-atom transfer barrier on the S_1 PE surface, see Fig. 9.

The analysis of individual trajectories reveals that the PCET reactivity is driven by an interplay of hydrogen-bond dynamics in the initially prepared S_3 state and electron-transfer dynamics. Upon shortening of the NH bond distance (or extension of the OH bond distance) in the Pm–H_2O hydrogen bond, the hole in the highest π orbital (for the ππ* excited state) or n orbital (for nπ* excited states) of Pm jumps to the O-atom of the water molecule. This hole transfer is followed by the transfer of the proton from the positively charged water molecule to the negatively charged Pm molecule, resulting in the irreversible formation of the $PmH^{\bullet}(H_2O)_{n-1}OH^{\bullet}$ radical pair.

It is interesting to consider the Pm–water system in the context of other hydrogen-bonded clusters of N-heterocycles. The photophysical and photochemical dynamics of Py–H_2O and Py–$(H_2O)_4$ clusters has been theoretically explored earlier with the same methodology and comparable statistics,[54] which allows a qualitative comparison of the reaction mechanisms in Py–$(H_2O)_n$ and Pm–$(H_2O)_n$ clusters. Overall, the reaction dynamics of these clusters is very similar. The yield of the PCET reaction is strongly reduced in the cluster with a single water molecule compared to larger clusters. This is likely due to the lack of sufficient dynamical degrees of freedom which can accept the excess energy liberated by the H-atom transfer reaction. In the Py–$(H_2O)_4$ and Pm–$(H_2O)_4$ clusters, the yield of radical pairs is around a few percent and the H-atom transfer reaction occurs during the fast initial radiationless decay of the bright $^1\pi\pi^*$ state. The vast majority of trajectories (about 90%) relax to a local minimum of the $S_1(n\pi^*)$ PE surface. The ensuing non-reactive internal conversion in the chromophores occurs on picosecond timescales and is moderately enhanced by the water environment.

The rather fast excited-state deactivation of the Py and Pm chromophores is an undesirable competing process for the photoinduced water oxidation with these chromophores and is responsible for the low overall yield of biradicals. In this respect, the heptazine chromophore stands out by exhibiting a truly long-lived (≈300 ns) first excited singlet state in which the energy of the absorbed photon can be stored. While Py and Pm are non-fluorescent, a fluorescence quantum yield of ≈70% was measured for the S_1 state of TAHz in toluene.[9]

Investigations of the water oxidation reaction in clusters of Hz or Hz derivatives with water in a molecular beam would therefore be of great interest.

Conflicts of interest

The authors declare no competing financial interests.

Acknowledgements

This work has been conducted within the International Associated Laboratory LEMIR (CNRS/CONICET) and with the support of the ANR Research Grant ANR17CE05000502-Wsplit. The work at the Technical University of Munich was supported by the Deutsche Forschungsgemeinschaft (DFG) by a research grant and through the Munich Centre for Advanced Photonics (MAP).

References

1 X. Wang, K. Maeda, A. Thomas, K. Takanabe, G. Xin, J. M. Carlsson, K. Domen and M. Antonietti, *Nat. Mater.*, 2009, **8**, 76–80.
2 W.-J. Ong, L.-L. Tan, Y. H. Ng, S.-T. Yong and S.-P. Chai, *Chem. Rev.*, 2016, **116**, 7159–7329.
3 J. Wen, J. Xie, X. Chen and X. Li, *Appl. Surf. Sci.*, 2017, **391**, 72–123.
4 G. Liao, Y. Gong, L. Zhang, H. Gao, G.-J. Yang and B. Fang, *Energy Environ. Sci.*, 2019, **12**, 2080–2147.
5 T. Banerjee, K. Gottschling, G. Savaski, C. Ochsenfeld and B. V. Lotsch, *ACS Energy Lett.*, 2018, **3**, 400–409.
6 Y. Wang, X. Wang and M. Antonietti, *Angew. Chem., Int. Ed.*, 2012, **51**, 68–89.
7 Y. Wang, A. Vogel, M. Sachs, R. S. Sprick, L. Wilbraham, S. J. A. Moniz, R. Godin, M. A. Zwijnenburg, J. R. Durrant, A. I. Cooper and J. Tang, *Nat. Energy*, 2019, **4**, 746–760.
8 W. Domcke, J. Ehrmaier and A. L. Sobolewski, *ChemPhotoChem*, 2019, **3**, 10–23.
9 E. J. Rabe, K. L. Corp, A. L. Sobolewski, W. Domcke and C. W. Schlenker, *J. Phys. Chem. Lett.*, 2018, **9**, 6257–6261.
10 N. Esteves-López, S. Coussan, C. Dedonder-Lardeux and C. Jouvet, *Phys. Chem. Chem. Phys.*, 2016, **18**, 25637–25644.
11 J. R. Reimers and Z.-L. Cai, *Phys. Chem. Chem. Phys.*, 2012, **14**, 8791–8802.
12 X. Liu, A. L. Sobolewski, R. Borrelli and W. Domcke, *Phys. Chem. Chem. Phys.*, 2013, **15**, 5957–5966.
13 X. Liu, A. L. Sobolewski and W. Domcke, *J. Phys. Chem. A*, 2014, **118**, 7788–7795.
14 T. Droz, R. Knochenmuss and S. Leutwyler, *J. Chem. Phys.*, 1990, **93**, 4520–4532.
15 A. Müller, F. Talbot and S. Leutwyler, *J. Am. Chem. Soc.*, 2002, **124**, 14486–14494.
16 K. Sakota, C. Okabe, N. Nishi and H. Sekiya, *J. Phys. Chem. A*, 2005, **109**, 5245–5247.
17 G. A. Pino, I. Alata, C. Dedonder, C. Jouvet, K. Sakota and H. Sekiya, *Phys. Chem. Chem. Phys.*, 2011, **13**, 6325–6331.
18 G. Pino, C. Dedonder-Lardeux, G. Grégoire, C. Jouvet, S. Martrenchard and D. Solgadi, *J. Chem. Phys.*, 1999, **111**, 10747–10749.
19 S.-I. Ishiuchi, M. Sakai, K. Daigoku, T. Ueda, T. Yamanaka, K. Hashimoto and M. Fujii, *Chem. Phys. Lett.*, 2001, **347**, 87–92.
20 C. Dedonder-Lardeux, D. Grosswasser, C. Jouvet and S. Martrenchard, *PhysChemComm*, 2001, **4**, 21–23.
21 V. Stert, L. Hesse, H. Lippert, C. Schulz and W. Radloff, *J. Phys. Chem. A*, 2002, **106**, 5051–5053.
22 O. David, C. Dedonder-Lardeux and C. Jouvet, *Int. Rev. Phys. Chem.*, 2002, **21**, 499–523.
23 A. Carrera, I. Nielsen, P. Carcabal, C. Dedonder, M. Broquier, C. Jouvet, W. Domcke and A. L. Sobolewski, *J. Chem. Phys.*, 2009, **130**, 024302.
24 G. Pino, A. Oldani, E. Marceca, M. Fujii, S.-I. Ishiuchi, M. Miyazaki, M. Broquier, C. Dedonder and C. Jouvet, *J. Chem. Phys.*, 2010, **133**, 124313.
25 A. Courty, M. Mons, I. Dimicoli, F. Piuzzi, M.-P. Gaigeot, V. Brenner, P. de Pujo and P. Millié, *J. Phys. Chem. A*, 1998, **102**, 6590–6600.
26 H. M. Kim, K. Y. Han, J. Park, G.-S. Kim and S. K. Kim, *J. Chem. Phys.*, 2008, **128**, 041104.
27 K. Tanabe, M. Miyazaki, M. Schmies, A. Patzer, M. Schütz, H. Sekiya, M. Sakai, O. Dopfer and M. Fujii, *Angew. Chem., Int. Ed.*, 2012, **51**, 6604–6607.
28 C. Jouvet and B. Soep, *Chem. Phys. Lett.*, 1983, **96**, 426–428.
29 W. Breckenridge, C. Jouvet and B. Soep, *J. Chem. Phys.*, 1986, **84**, 1443–1450.
30 M. Dantus, M. J. Rosker and A. H. Zewail, *J. Chem. Phys.*, 1987, **87**, 2395–2397.
31 A. Zehnacker and M. A. Suhm, *Angew. Chem., Int. Ed.*, 2008, **47**, 6970–6992.
32 C. Dedonder-Lardeux, C. Jouvet, M. Richard-Viard and D. Solgadi, *J. Chem. Phys.*, 1990, **92**, 2828–2836.
33 I. Alata, R. Omidyan, M. Broquier, C. Dedonder and C. Jouvet, *Chem. Phys.*, 2012, **399**, 224–231.
34 C. Møller and M. S. Plesset, *Phys. Rev.*, 1934, **46**, 618–622.
35 J. Schirmer, *Phys. Rev. A: At., Mol., Opt. Phys.*, 1982, **26**, 2395–2416.
36 A. B. Trofimov and J. Schirmer, *J. Phys. B: At., Mol. Opt. Phys.*, 1995, **28**, 2299–2324.
37 C. Hättig, in *Adv. Quantum Chem.*, ed. H. J. Å. Jensen, Academic Press, 2005, vol. 50, pp. 37–60.
38 J. Ehrmaier, M. J. Janicki, A. L. Sobolewski and W. Domcke, *Phys. Chem. Chem. Phys.*, 2018, **20**, 14420–14430.
39 T. H. Dunning Jr., *J. Chem. Phys.*, 1989, **90**, 1007–1023.
40 TURBOMOLE (V7.2), a development of University of Karlsruhe and Forschungszentrum Karlsruhe GmbH, 1989–2007, TURBOMOLE GmbH, since 2007.
41 C. Hättig and F. Weigend, *J. Chem. Phys.*, 2000, **113**, 5154–5161.
42 J. P. Bergsma, P. H. Berens, K. R. Wilson, D. R. Fredkin and E. J. Heller, *J. Phys. Chem.*, 1984, **88**, 612–619.

43 M. Barbatti, *Wiley Interdiscip. Rev.: Comput. Mol. Sci.*, 2011, **1**, 620–633.
44 A. K. Belyaev and O. V. Lebedev, *Phys. Rev. A: At., Mol., Opt. Phys.*, 2011, **84**, 014701.
45 A. K. Belyaev, W. Domcke, C. Lasser and G. Trigila, *J. Chem. Phys.*, 2015, **142**, 104307.
46 W. Xie and W. Domcke, *J. Chem. Phys.*, 2017, **147**, 184114.
47 W. Xie, M. Sapunar, N. Doslic, M. Sala and W. Domcke, *J. Chem. Phys.*, 2019, **150**, 154119.
48 J. C. Tully, *J. Chem. Phys.*, 1990, **93**, 1061–1071.
49 L. Yu, C. Xu, Y. Lei, C. Zhu and Z. Wen, *Phys. Chem. Chem. Phys.*, 2014, **16**, 25883–25895.
50 K. Hanasaki, M. Kanno, T. A. Niehaus and H. Kono, *J. Chem. Phys.*, 2018, **149**, 244117.
51 X. Pang, J. Ehrmaier, X. Wu, C. Jiang, W. Xie, A. L. Sobolewski and W. Domcke, *Chem. Phys.*, 2018, **515**, 550–556.
52 I. Alata, J. Bert, M. Broquier, C. Dedonder, G. Feraud, G. Gregoire, S. Soorkia, E. Marcea and C. Jouvet, *J. Phys. Chem. A*, 2013, **117**, 4420–4427.
53 M. H. V. Huynh and J. J. Meyer, *Chem. Rev.*, 2007, **107**, 5004–5064.
54 X. Pang, C. Jiang, W. Xie and W. Domcke, *Phys. Chem. Chem. Phys.*, 2019, **21**, 14073–14079.

THE JOURNAL OF PHYSICAL CHEMISTRY A
A JOURNAL OF THE AMERICAN CHEMICAL SOCIETY

pubs.acs.org/JPCA Article

Ab Initio Nonadiabatic Surface-Hopping Trajectory Simulations of Photocatalytic Water Oxidation and Hydrogen Evolution with the Heptazine Chromophore

Xiang Huang and Wolfgang Domcke*

Cite This: J. Phys. Chem. A 2021, 125, 9917−9931 Read Online

ABSTRACT: In the past decade, polymeric carbon nitrides consisting of heptazine (Hz) building blocks emerged as highly promising materials for photocatalytic hydrogen evolution from water or sacrificial electron donors with near-ultraviolet light. However, the complexity of these materials and their poor characterization at the atomic level are detrimental to the unraveling of the detailed mechanisms of the reactions leading to hydrogen evolution. Recently, it has been shown that a derivative of the Hz molecule, trianisole-heptazine (TAHz), is a potent photobase, which readily oxidizes various derivatives of phenol and even water by an excited-state proton-coupled electron-transfer (PCET) reaction. Energy profiles along minimum-energy reaction paths and relaxed PCET potential-energy surfaces, which previously were computed with ab initio electronic-structure methods for complexes of Hz and TAHz with protic substrates, led to qualitative insights. To obtain more quantitative insight, reaction dynamics simulations are required. In the present work, the time scales of the electron and proton transfer processes and the branching ratios of competing channels were explored with ab initio on-the-fly quasiclassical surface-hopping trajectory simulations for the hydrogen-bonded Hz-H_2O complex. By the analysis of representative trajectories, detailed insight into the interplay of various nonadiabatic electronic transitions, electron transfer, proton transfer, and vibrational energy relaxation is obtained. The HzH radicals which are formed by the photoreduction of Hz can disproportionate to Hz and HzH_2 in an exothermic reaction with a low reaction barrier. The time scales and branching ratios of competing channels in H-atom photodetachment from the HzH_2 molecule also were explored with ab initio surface-hopping simulations. These results delineate for the first time a quantitatively supported scenario of water oxidation and hydrogen evolution with a molecular carbon nitride photocatalyst.

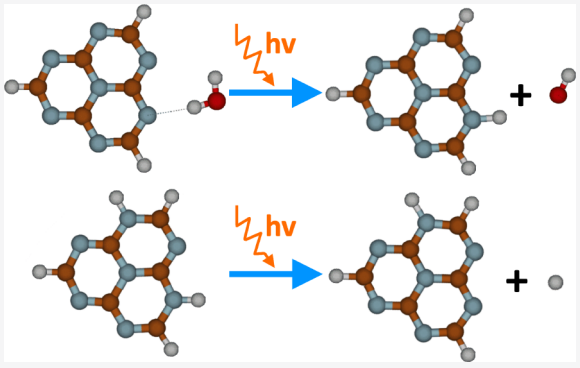

1. INTRODUCTION

Polymeric carbon nitrides recently emerged as a very promising new class of materials for hydrogen evolution from water in the presence of sacrificial reagents. Consisting of Earth-abundant elements and being photochemically surprisingly stable, carbon nitrides have found great attention in the materials science and renewable energy communities.[1−3] Oxygen evolution and hydrogen evolution reactions usually are considered as separate half-reactions. Most of the research activity is currently focused on the hydrogen evolution reaction.[1−3] While a few reports of stoichiometric evolution of H_2 and O_2 with carbon nitrides exist,[4−6] the overwhelming majority of investigations is concerned with the hydrogen evolution half-reaction using sacrificial hole scavengers.

The interpretation of the data of hydrogen evolution experiments with carbon nitrides is based on a mechanistic scenario which has been adapted from photoelectrochemical water splitting with transition-metal oxides, in particular TiO_2.[7,8] In this scenario, it is assumed that photoabsorption by carbon nitrides results in the generation of excitons which spontaneously separate into free charge carriers (electrons and holes).[2,3] The latter migrate toward interfaces of the solid photocatalyst with liquid water, where eventually protons are neutralized by the electrons and OH^- anions or water molecules are oxidized by the holes. However, the details of the reactions of the charge carriers with water remain unclear. In view of the fact that the ionization potential of heptazine (Hz), the building block of so-called graphitic carbon nitrides (g-C_3N_4),[9] is 9.6 eV,[10] while the ionization potential of the water molecule is 12.6 eV,[11] it seems unlikely that relaxed holes on the surface of carbon nitrides have the potential to oxidize water.

Received: September 20, 2021
Revised: October 21, 2021
Published: November 8, 2021

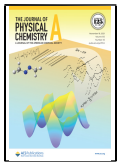

https://doi.org/10.1021/acs.jpca.1c08291
J. Phys. Chem. A 2021, 125, 9917−9931

Recently, a fundamentally different mechanistic scenario of photocatalytic water oxidation and hydrogen evolution with carbon nitrides has been proposed.[12−14] It is based on the observation that certain N-heterocycles are strong photobases which, upon photoexcitation, can abstract hydrogen atoms directly from water molecules in hydrogen-bonded chromophore−water complexes, thereby oxidizing water molecules to OH radicals, for example,

$$\mathrm{Hz}\cdots\mathrm{H_2O} + h\nu \rightarrow \mathrm{HzH} + \mathrm{OH} \tag{1}$$

(the dots denote a hydrogen bond). The theoretical prediction of low-barrier excited-state proton-coupled electron transfer (PCET)[15] reactions in pyridine$\cdots(\mathrm{H_2O})_n$ and pyrimidine$\cdots(\mathrm{H_2O})_n$ complexes[16,17] was confirmed by the detection of pyridinyl (pyridine+H) and pyrimidinyl (pyrimidine+H) radicals, respectively, via their electronic spectra.[17,18] The dynamics of the excited-state PCET reaction in pyridine$\cdots(\mathrm{H_2O})_n$ and pyrimidine$\cdots(\mathrm{H_2O})_n$ complexes was explored in microscopic detail with ab initio nonadiabatic dynamics simulations.[17,19] It was found by these simulations that the photoinduced PCET reaction is possible in complexes with $n > 3$, which is consistent with the experimental data.

No experimental data are available on the photochemistry of the Hz molecule because of the rapid hydrolysis of Hz in the presence of water.[20] However, a derivative of Hz, 2,5,8-tris(4-methoxyphenyl)-1,3,4,6,7,9,9b-heptaazaphenalene or trianisole-heptazine (TAHz), has been recently synthesized and was shown to be chemically and photochemically highly stable in organic solvents (toluene) as well as in water.[21] The ability of TAHz to oxidize water upon excitation with near-UV light was demonstrated by the detection of free OH radicals with terephthalic acid.[21] The initial steps of the photoreaction of TAHz with water could be kinetically resolved by the measurement of dynamic fluorescence quenching. The observed $\mathrm{H_2O/D_2O}$ kinetic isotope effect of 2.9 confirms the PCET character of the reaction.[21]

These remarkable experimental results call for the exploration of the detailed photochemistry of TAHz in aqueous environments with ab initio dynamics simulations. For TAHz$\cdots(\mathrm{H_2O})_n$ complexes or TAHz in liquid water, such simulations are currently not possible with sufficiently accurate ab initio electronic-structure methods. We therefore adopted in the present work Hz as a computationally tractable model for TAHz, and we reduce the water cluster to a single water molecule. There exists experience on the role of the size of the water cluster from the simulations for pyridine−water and pyrimidine−water complexes. For example, the proton transfer (PT) rate increases by 3% when the water cluster size increases from one water molecule to four water molecules in pyridine−water complexes. For pyrimidine−water complexes, the corresponding increase is 6%. While the size of the cluster matters for the quantitative prediction of reaction rates and branching ratios, all essential phenomena can qualitatively be understood with simulations of the hydrogen-bonded complex of the photobase with a single water molecule.[17,19] We thus take the Hz$\cdots\mathrm{H_2O}$ complex as the model system for the computational exploration of the photochemistry of TAHz in liquid water.

Simulations of the photochemical dynamics of the Hz$\cdots\mathrm{H_2O}$ complex were performed earlier by Ullah et al.[22] using time-dependent density functional theory (TDDFT) with the ωB97XD functional.[23] Ullah et al. reported that the PCET reaction occurs within tens of femtoseconds and is the dominant excited-state deactivation process in the Hz$\cdots\mathrm{H_2O}$ complex.[22] However, although the TDDFT method is usually reasonably accurate for vertical excitation energies of organic molecules, little is known about the accuracy of the TDDFT method for nuclear geometries which are far from the ground-state equilibrium geometry. An independent confirmation of the conclusions of Ullah et al. therefore is desirable. In the present simulations, we employ the wave-function-based ADC(2) (algebraic diagrammatic construction of second order) method,[24−26] which is computationally more expensive than TDDFT, but is definitely of higher accuracy. In particular, the accuracy of the ADC(2) method has extensively been benchmarked for PCET reactions in several chromophore−water complexes in comparison with complete-active-space self-consistent-field (CASSCF) and multireference perturbation (CASPT2) calculations.[16,27]

The photoinduced abstraction of a hydrogen atom from a water molecule is the initial step of photocatalytic water oxidation in the scenario considered in this work. To close the catalytic cycle, the chromophore has to be regenerated, which can be achieved with either dark radical−radical recombination reactions or by light-driven photochemical reactions. The most obvious light-driven reaction is the photodetachment of the excess hydrogen atom from the HzH radical, generating free hydrogen atoms

$$\mathrm{HzH} + h\nu \rightarrow \mathrm{Hz} + \mathrm{H} \tag{2}$$

The mechanism of the photodetachment reaction in the HzH radical has been explored by the calculation of one-dimensional scans of the potential-energy (PE) functions of the ground state and the excited states along the NH bond distance of the Hz radical.[12] As is characteristic for heterocycles with acidic groups, such as pyrrole, indole, or phenol,[28−30] there exists a $\pi\sigma^*$ state in the HzH radical with a PE function which is repulsive along the NH bond. The PE function of the $\pi\sigma^*$ state crosses the PE functions of two low-lying bound $\pi\pi^*$ states as well as the PE function of the electronic ground state.[12] If the conical intersections (CIs) associated with these one-dimensional curve crossings are passed diabatically in the photodissociation reaction, a free H atom is photodetached. Otherwise, the photoexcited HzH radical will relax back to the minimum of the electronic ground state and the energy of the photon is lost. The branching ratio of photodissociation versus internal conversion (IC) to the ground state can only be estimated by ab initio nonadiabatic dynamics simulations.

Alternatively to the photodetachment reaction, two HzH radicals can recombine in a diffusion-controlled dark reaction and disproportionate to Hz and $\mathrm{HzH_2}$

$$\mathrm{HzH} + \mathrm{HzH} \rightarrow \mathrm{Hz} + \mathrm{HzH_2} \tag{3}$$

As will be shown below, the disproportionation of HzH radicals is exothermic. The resulting $\mathrm{HzH_2}$ is a closed-shell molecule and as such long-lived. The energy of two photons is thus stored as chemical energy in $\mathrm{HzH_2}$.

Free hydrogen atoms can be harvested by photodetachment from $\mathrm{HzH_2}$

$$\mathrm{HzH_2} + h\nu \rightarrow \mathrm{HzH} + \mathrm{H} \tag{4}$$

The HzH radical can undergo another disproportionation reaction, regenerating Hz and $\mathrm{HzH_2}$. By this cycle, a continuous production of free H atoms can be sustained. The undesired recombination of H and OH radicals has to be

https://doi.org/10.1021/acs.jpca.1c08291
J. Phys. Chem. A 2021, 125, 9917−9931

avoided by efficient scavenging of the OH radicals either by sacrificial hole scavengers or by cocatalysts which recombine OH radicals to H_2O_2 (two-electron water splitting)[4,31] or to H_2O and O_2 (four-electron water splitting).[2,3]

In the present work, we combined the ab initio study of the dynamics of the water oxidation reaction (1) with the ab initio study of the hydrogen evolution reaction (4). The simulated absorption spectrum of the Hz···H_2O complex predicts a broad peak centered at 4.02 eV, which arises from the electronic transition to the lowest bright $^1\pi\pi^*$ state (S_4) of Hz. The lowest excited state of Hz (S_1) is a dark $\pi\pi^*$ state with an excitation energy of 2.57 eV. In between S_1 and S_4 are two $n\pi^*$ states (one of them degenerate) which nominally are dark but can borrow some intensity from the bright S_4 state by vibronic coupling. In addition to these four locally excited (LE) states of the Hz chromophore, a charge-transfer (CT) state of $\pi\pi^*$ character, corresponding to electron transfer (ET) from the H_2O molecule to Hz, plays a decisive role in the photochemical dynamics of the Hz···H_2O complex. This CT state provides the driving force for the PCET reaction. The reaction dynamics at short time scales (≈100 fs) is dominated by the competition between radiationless transitions within Hz with fast nonadiabatic PT processes driven by the CT state. On longer time scales, the PCET reaction can occur by adiabatic H-atom tunneling from the H_2O molecule to Hz through the barrier which separates the potential well of the S_1 state from the energy minimum of the HzH···OH biradical.

The simulation of the absorption spectrum of the HzH_2 molecule predicts two bands, a moderately intense band near 2.0 eV and a strong band near 4.5 eV, which arise from low-lying and high-lying $^1\pi\pi^*$ states, respectively. In between these groups of $^1\pi\pi^*$ states, there exist two $^1\pi\sigma^*$ states which are associated with the two NH groups of HzH_2. These states exhibit repulsive PE functions along the respective NH bond length, as discussed for the HzH radical above. When the upper $^1\pi\pi^*$ band is excited, the reactive $^1\pi\sigma^*$ states can be populated by fast radiationless transitions which provide ample excess energy for the photodissociation reaction. When the lower $^1\pi\pi^*$ states are populated, a substantial barrier exists along the NH dissociation coordinate and the photodissociation reaction is in the deep tunneling regime. The corresponding time scale of picoseconds or nanoseconds is currently not accessible with ab initio on-the-fly dynamics simulations.

Overall, we present in this work the first ab initio quasiclassical reaction dynamics study of photocatalytic water oxidation and hydrogen evolution with the Hz chromophore.

2. COMPUTATIONAL METHODS

2.1. Electronic-Structure Calculations. *2.1.1. Hz···H_2O Complex.* The ground-state geometry and the Hessian of the hydrogen-bonded Hz···H_2O complex were calculated with the second-order Møller−Plesset (MP2) method.[32] Vertical excitation energies, dipole moments, and oscillator strengths of Hz···H_2O were calculated with the ADC(2) method.[24−26] The correlation-consistent double-ζ basis set, cc-pVDZ,[33] was augmented by the diffuse functions of the aug-cc-pVDZ basis set on the water molecule and on the neighboring two N atoms of Hz in the Hz···H_2O complex. It has been checked that the excitation energies obtained with this partially augmented basis set agree within a few tenths of an electron volt with those obtained with the fully augmented basis, while the saving of computing time is significant. The TURBOMOLE program package[34] was used for the MP2 and ADC(2) calculations, and the resolution-of-the-identity approximation[35] was employed.

The absorption spectrum of the Hz···H_2O complex was simulated with the nuclear ensemble method.[36] Two thousand phase-space points were sampled from the harmonic-oscillator Wigner distribution[37] at room temperature (300 K). Excitation energies and oscillator strengths of the six lowest excited electronic states were computed for the 2000 sampling points. The resulting line spectrum is convoluted with a Gaussian function of 0.05 eV full width at half maximum (FWHM). The calculations of nuclear ensemble spectra were performed with the NEWTON-X package.[38]

2.1.2. Disproportionation of HzH. For the sake of consistency, the equilibrium geometries of the HzH···HzH biradical and the HzH_2···Hz closed-shell system were both optimized with the unrestricted second-order Møller−Plesset (UMP2) method without symmetry constraints. The construction of a minimum-energy reaction path for the electron/proton transfer reaction from HzH···HzH to HzH_2···Hz was not possible because of the complex rearrangement of the electronic structure in the vicinity of the transition state. Therefore, a linearly interpolated path in internal coordinates was constructed which connects the two optimized structures. Two energy profiles were computed along this path: the energy profile for the PT process, HzH···HzH → Hz^-···HzH_2^+, and the energy profile for the H-atom transfer (or PCET) process, HzH···HzH → Hz···HzH_2. The cc-pVDZ basis set was used for these calculations to reduce the basis-set superposition error.[39]

2.1.3. Photodetachment from HzH_2. The equilibrium geometry of HzH_2 was determined with the MP2 method. A partially augmented cc-pVDZ basis set was employed which includes diffuse functions on the two NH groups as described above. The local augmentation at the NH groups is needed for a proper description of the diffuse σ^* orbitals.[29] The PE functions for the detachment of an H atom from one of the NH groups were computed along a rigid scan. The NH distance of one of the NH groups was varied from 0.8 to 2.0 Å, while all other nuclear degrees of freedom were kept frozen.

The absorption spectrum of HzH_2 was simulated with the nuclear ensemble method at the ADC(2) level as described for Hz···H_2O above.

Because HzH_2 is a so far unexplored species, we also performed CASSCF and MS-CASPT2 calculations of the PE functions along the rigid scan for H-atom detachment for comparison with the ADC(2) results. The active space consisted of eight electrons in 11 molecular orbitals: four π orbitals, four π^* orbitals, and three σ^* orbitals. A standard imaginary level shift of 0.25 Hartree was used. The CASSCF and CASPT2 calculations were performed with the OpenMolcas program.[40]

2.2. Nonadiabatic Dynamics Simulations. *2.2.1. PCET in Hz-H_2O.* The initial conditions for the excited-state dynamics simulations were selected from the 2000 Wigner sampling points generated for the absorption spectrum simulation by restricting the initial excitation energy to an energy window of ±0.05 eV centered at an absorption band maximum of 4.02 eV. The resulting 188 trajectories were propagated up to 100 fs with a time step of 0.5 fs. The Landau−Zener surface-hopping (LZSH) algorithm[41−43] using the Belyaev−Lebedev formula[44] was used together with the ADC(2) electronic-structure method. In the LZSH algorithm, the hopping probability is determined directly from the adiabatic electronic energies at local minima of the energy

https://doi.org/10.1021/acs.jpca.1c08291
J. Phys. Chem. A 2021, 125, 9917−9931

gap of neighboring PE surfaces.[43] While the default time step is 0.5 fs, the step size is automatically reduced to 0.1 fs in the vicinity of adiabatic energy gap minima to ensure an accurate evaluation of the transition probability. Velocity adjustment along the current velocity is employed after hopping to a new state to ensure energy conservation.[43]

In the LZSH algorithm, the calculation of potentially divergent nonadiabatic coupling elements is avoided. Moreover, the electronic wave function is not propagated in time, which eliminates the lack-of-decoherence problem[45] of the fewest-switching surface-hopping (FSSH) algorithm of Tully.[46] The LZSH algorithm in combination with the ADC(2) method is an exceptionally robust and stable simulation tool in the vicinity of excited-state CIs. The algorithm has recently been tested for the pyrazine molecule in comparison with the FSSH method and with exact quantum dynamics calculations.[43]

The efficiency of the algorithm has been further enhanced in the present study by reducing the number of excitation energies to be calculated at each time step to $n + 1$, where n is the currently populated adiabatic electronic state. Because of the ultrafast relaxation of higher excited states to lower excited states in the Hz molecule, this modification of the algorithm strongly reduces the cost of the simulation. It should be noted that this modified algorithm still accounts for the possibility of hopping to higher excited adiabatic electronic states. If a hopping of the current state to the next higher state happens, the next-next higher electronic state is automatically included in the following time step of the simulation. Because surface hopping in the LZ algorithm exclusively occurs between next-neighbor states, the system can move upward in the ladder of electronic states without a priori constraints. Figure S2 in the Supporting Information shows the evolution of the number of adiabatic states to be calculated for a simulation with $N = 6$ initially excited adiabatic states. The single-point computational cost is roughly proportional to the number of states to be calculated, so the area below the curve represents the computational cost. The shaded area in Figure S2 indicates a saving of 51% of the computational cost. Very few trajectories experienced a three-state crossing within 0.1 fs of $t = 0$. These could not be treated with the LZ formalism and had to be eliminated.

Because of the single-reference character of the ADC(2) method, the topography of S_1-S_0 CIs cannot be described properly with ADC(2). In the present simulations, the propagation of any trajectory was stopped when the energy gap between the currently occupied state and the ground state dropped below 0.2 eV, assuming that an S_1-S_0 CI has been encountered. The propagation of the trajectory is stopped at the time of the encounter of the CI and is counted as the ground-state population thereafter. This procedure has been widely adopted in many nonadiabatic trajectory surface-hopping dynamics simulations with single-reference methods.[47]

The CT (hole transfer from H_2O to Hz) state plays a decisive role in the PCET dynamics in the Hz−H_2O complex, because the hole transfer triggers the PT.[12] Using the exceptionally large dipole moment of the CT state as the identifier of this state, we can follow the population of this state along each individual trajectory. Because the PE functions of the LE states are more or less parallel along the PT reaction coordinate, they can be divided into two groups, the lowest LE state (S_1) and the higher-lying LE states. At the reference geometry, the energy of the S_1 state is much below the energy of the CT state, while the energies of the higher-lying LE states may be above or below the energy of the CT state at the reference geometry. By these criteria, the currently occupied state along each trajectory can be classified as either the CT state, S_1 state, or high-lying LE state. The averaging over trajectories generates quasidiabatic populations of groups of states. A similar grouping of adiabatic states to mimic the population dynamics of diabatic states also was employed by Gonzalez and co-workers.[48] The convergence of these quasidiabatic populations with the size of the trajectory ensemble is displayed in Figure S3 of the Supporting Information. The sampling is essentially converged with 150 trajectories, resulting in smooth time-dependent populations of the CT state, the S_1 state, and the high-lying LE states.

2.2.2. Photodissociation of HzH_2. The HzH_2 dissociation dynamics is treated with the same computational protocol as specified above for the PCET reaction in the Hz···H_2O complex. Two hundred and thirty-nine phase-space points were selected as initial conditions for the nonadiabatic dynamics from the energy window of ±0.05 eV centered at the absorption band maximum of 4.55 eV. These trajectories were propagated for 150 fs with the LZSH algorithm using the ADC(2) method. The dynamics simulation was started with $N = 8$ excited states at $t = 0$. The computational cost saved by deleting redundant electronic states is illustrated in Figure S4 of the Supporting Information. The convergence of the quasidiabatic populations with the number of trajectories is shown in Figure S5 of the Supporting Information.

The photochemically reactive states in HzH_2 are the two $\pi\sigma^*$ states associated with the two NH groups. To identify the population of these Rydberg-like states along individual trajectories, we computed the spatial extension of the occupied virtual orbital of the excited states. The extension parameter is calculated as $\int \psi^2(x, y, z)(x^2 + y^2 + z^2)\mathrm{d}x\mathrm{d}y\mathrm{d}z$, where ψ is the appropriate Hartree−Fock MO. The integration is extended to 20 a.u. along each direction from the N9b atom (see Figure S1 for the atom numbering). The eight adiabatic electronic states of HzH_2 are thus sorted into three groups of quasidiabatic states: low-lying $\pi\pi^*$ states, high-lying $\pi\pi^*/n\pi^*$ states, and $\pi\sigma^*$ states.

3. RESULTS AND DISCUSSION

3.1. Photoinduced Water Oxidation. *3.1.1. Excitation Energies of the Hz···H_2O Complex.* The vertical excitation energies of Hz molecules at the ADC(2)/cc-pVDZ level are listed in the left column of Table 1. The atom numbering of the Hz molecule is shown in Figure S1 in the Supporting Information. The S_1 state of Hz at 2.57 eV is a dark state and exhibits the rare phenomenon of singlet−triplet inversion.[49] Because of its exceptionally long lifetime, the S_1 state plays the role of a reservoir state after radiationless relaxation from the photoexcited electronic state.[21] With increasing energy, two $n\pi^*$ states follow below the strongly absorbing degenerate state S_4 in the near UV. Above the bright state, another series of $n\pi^*$ states follows.

The ground-state equilibrium geometry of the Hz···H_2O complex is shown in Figure 1. To distinguish the two OH groups of the H_2O molecule in the dynamics, we denote the hydrogen-bonded OH group as OH(α) and the free OH group as OH(β). The lowest 10 excited states of the Hz···H_2O complex are listed in the right column of Table 1. The hydrogen-bonded water molecule significantly enlarges the

https://doi.org/10.1021/acs.jpca.1c08291
J. Phys. Chem. A 2021, 125, 9917−9931

Table 1. Left Column: Vertical Excitation Energies (in eV) of the Lowest Eight Singlet States of Hz at the Ground-State Equilibrium Geometry, Calculated with the ADC(2) Method with cc-pVDZ Basis Set and Right Column: Vertical Excitation Energies (in eV) of the Singlet States below ≈5 eV and the Lowest CT State of the Hz-H_2O Complex at the Ground-State Equilibrium Geometry, Calculated with the ADC(2) Method and a Partially Augmented cc-pVDZ Basis Set[a]

excited state	Hz	excited state	Hz-H_2O
$S_1(\pi\pi^*)$	2.57 (0.000) [0.0]	$S_1(\pi\pi^*)$	2.61 (0.000) [3.2]
$S_2(n\pi^*)$	3.76 (0.000) [0.0]	$S_2(n\pi^*)$	3.76 (0.000) [7.2]
$S_3(n\pi^*)$	3.84 (0.000) [5.8]	$S_3(n\pi^*)$	3.84 (0.000) [3.7]
$S_4(\pi\pi^*)$	4.43 (0.538) [1.8]	$S_4(n\pi^*)$	3.94 (0.000) [0.7]
$S_5(n\pi^*)$	4.93 (0.004) [0.0]	$S_5(\pi\pi^*)$	4.38 (0.269) [4.0]
$S_6(n\pi^*)$	4.94 (0.000) [3.3]	$S_6(\pi\pi^*)$	4.40 (0.271) [2.8]
$S_7(n\pi^*)$	5.04 (0.000) [3.0]	$S_7(n\pi^*)$	4.86 (0.002) [8.9]
$S_8(n\pi^*)$	5.16 (0.000) [0.0]	$S_8(n\pi^*)$	4.94 (0.001) [5.0]
		$S_9(n\pi^*)$	4.96 (0.000) [1.7]
		$S_{10}(n\pi^*)$	5.02 (0.000) [8.8]
		$S_{14}(CT)$	5.81 (0.013) [16.7]

[a]Oscillator strengths are given in parentheses and dipole moments (in Debye) in brackets.

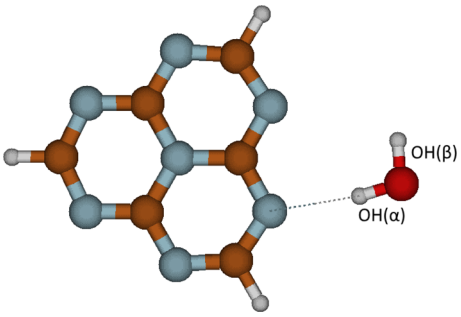

Figure 1. Ground-state equilibrium geometry of the hydrogen-bonded Hz···H_2O complex. The length of the hydrogen-bonded OH group is denoted as OH(α) and the length of the free OH group as OH(β).

dipole moments of the electronic states and moderately stabilizes the nonbonding orbitals of Hz, which results in relatively minor blue shifts of the energies of the nπ^* states. The degenerate bright state of Hz splits by 0.02 eV in the Hz···H_2O complex. The CT state (from the p_z orbital on the water molecule to the lowest unoccupied molecular orbital (LUMO) of Hz) is about 1.4 eV higher than the quasidegenerate bright states.

A one-dimensional relaxed scan of the PE functions of the Hz···H_2O complex along the H-atom transfer coordinate has been computed by Ehrmaier et al.[12] Moreover, two-dimensional relaxed PE surfaces spanned by the H-atom transfer coordinate and the donor (O)−acceptor (N) distance were computed. The energy barrier separating the minimum in the FC region of the adiabatic S_1 PE surface from the minimum of the CT state was estimated as 0.75 eV. The PCET reaction on the adiabatic S_1 PE surface is thus in the deep tunneling regime.[12]

The simulated absorption spectrum of the Hz···H_2O complex is shown in Figure 2. The stick spectrum shows the computed transition energies and oscillator strengths. The envelope has been generated by convolution with a Gaussian

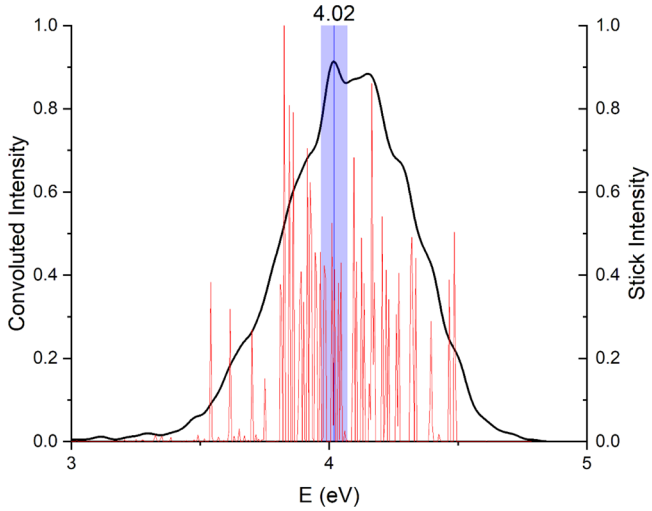

Figure 2. Absorption spectrum of the Hz···H_2O complex simulated with 2000 nuclear phase-space points selected from the room-temperature ground-state Wigner distribution. The lowest six vertical excitation energies and oscillator strengths were computed for each phase-space point. The black curve shows the convolution of the stick spectrum (red) with a Gaussian of 0.05 eV FWHM. The blue shaded area indicates the energy window at the maximum of the absorption band from which the initial conditions for the photochemical dynamics simulations were selected.

of 0.05 eV FWHM. The absorption spectrum exhibits a single intense peak with a maximum at 4.02 eV, which is redshifted by about 0.37 eV from the vertical excitation energy of the bright states (4.39 eV).

3.1.2. Nonadiabatic Excited-State Dynamics of the Hz···H_2O Complex. The time evolution of the populations of the electronic states of Hz···H_2O is shown in Figure 3a. The initial conditions are selected from the 0.1 eV-wide slice at the maximum of the absorption spectrum as described in Section 2.2.1. At $t = 0$, the two bright states S_5 and S_6 are populated with probabilities of 53.1 and 25.0%, respectively. The states S_4 and S_3 of nπ^* character are populated with probabilities of 20.3 and 1.6%, respectively, because of intensity borrowing from the bright states. The decay of the populations of the bright $^1\pi\pi^*$ states occurs within less than 10 fs, and their populations are transferred to the lower-lying ^{1}nπ^* states S_3 and S_4. After about 10 fs, the lowest ^{1}nπ^* state (S_2) is populated with the highest probability. Its population decays on a time scale of about 50 fs to the $S_1(\pi\pi^*)$ state. The population of the S_0 state arises from trajectories which encounter CIs with the electronic ground state. The earliest S_1−S_0 degeneracy event was observed at 10.8 fs and the latest event at 94.7 fs. Overall, 16 trajectories (9%) convert to the ground state. The distribution of these events in time is shown in Figure 3c. At all these events, the bond length R_{OH} for the water molecule was larger than 1.4 Å ($R_{OH(\alpha)}$ > 1.4 Å for 14 trajectories and $R_{OH(\beta)}$ > 1.4 Å of 2 trajectories). At the termination of the simulation (100 fs), 73.4% of the population is found in the S_1 state, 13.0% in the S_2 state, and 9% have reached CIs with the ground state.

When the trajectories are grouped according to the diabatic character of the currently active state as described in Section 2.2.1, the population distribution shown in Figure 3b is obtained. The identification of the diabatic character and the grouping of the higher-lying states yield a more transparent picture than the adiabatic electronic populations in Figure 3a. Nearly all trajectories (99.5%) are launched in the group of

https://doi.org/10.1021/acs.jpca.1c08291
J. Phys. Chem. A 2021, 125, 9917−9931

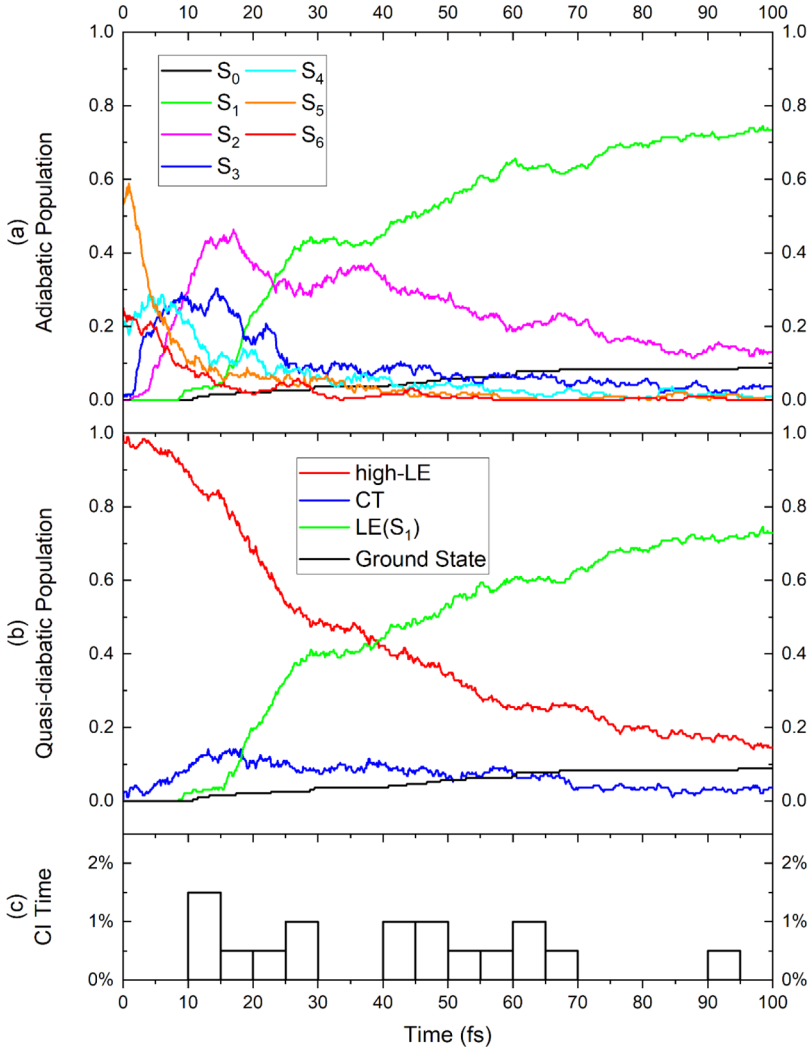

Figure 3. (a) Time evolution of the population of adiabatic electronic states. (b) Time evolution of the population of the quasidiabatic CT state and groups of LE states. The group of high-lying LE states is marked red, the CT state blue, the S_1 state green, and the ground state black. (c) Histogram of encounters of trajectories in the CT state with an S_1-S_0 conical intersection, approximated by an energy gap of less than 0.2 eV. For all trajectories, the value of R_{OH} at the time of encounter of the conical intersection was larger than 1.4 Å.

high-lying LE states. Their population decays on a time scale of about 40 fs, while the population of the $S_1(\pi\pi^*)$ state grows rapidly between 15 and 30 fs and more slowly thereafter. Despite its high energy at the reference geometry (see Table 1), the CT state gets populated within few femtoseconds, and its population attains a maximum (14%) at 16 fs. While the population of the CT state gradually decreases, the population of the S_0 state slowly increases. Figure 3b reveals that the vast majority of the trajectories starting in high-lying LE states relax to the S_1 state and are trapped there. This S_1 population may contribute to the PCET reaction via tunneling through the barrier of about 0.75 eV on picosecond to nanosecond time scales. On the other hand, fast (≈100 fs) PCET reactions can occur through trajectories which remain in the CT state until a CI with the electronic ground state is encountered.

A schematic summary of the photoinduced dynamics of the Hz−H_2O complex within 100 fs is shown in Figure 4. It is seen that a fraction of 62% of the population of the initially populated states relaxes "vertically" to the long-lived S_1 state, while a fraction of 38% of the population is transferred to the reactive CT state. The mean transition time from the high-lying LE states to the CT state is 22 fs, which is faster than the

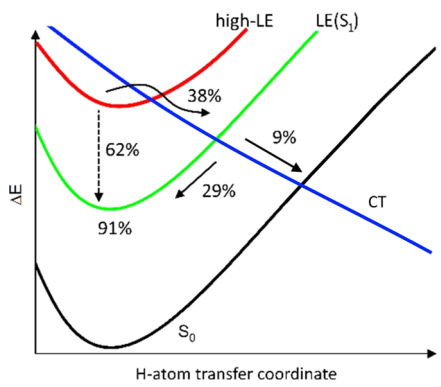

Figure 4. Schematic overview of the photochemical dynamics of the Hz−H_2O complex within 100 fs. The numbers give the branching ratios of nonadiabatic processes. In the dynamics simulation up to 100 fs, a residual population of 18% survives in the high-lying LE states. For clarity, this residual population has been added to the population of the S_1 state at 100 fs, anticipating the ultrafast relaxation of this residual population to the S_1 state.

https://doi.org/10.1021/acs.jpca.1c08291
J. Phys. Chem. A 2021, 125, 9917−9931

mean transition time from the high-lying LE states to the S_1 state (37 fs). The population dynamics bifurcates at the CI of the CT state with the S_1 state. The majority of the population (29%) follows the adiabatic path and relaxes to the minimum of the S_1 state, while 9% of the population follows the diabatic path and arrives at the CI of the CT state with the S_0 state. The present simulations with the ADC(2) method cannot predict the branching ratio at the CT-S_0 CI. The fraction of 9% of trajectories which arrives at the CT-S_0 intersection represents an upper limit for the yield of HzH and OH radicals which are formed by a direct and fast photoreaction. The population of the long-lived S_1 state (91%) can either relax to the ground state by fluorescence or slow IC or can yield HzH and OH radicals via tunneling through the barrier which separates the S_1 minimum from the biradical channel. As shown in the scheme in Figure 4, the tunneling wave packet has to pass the CI with the S_0 state to yield biradicals. The tunneling process on the adiabatic S_1 PE surface occurs on time scales which are beyond the limit which can be explored with ab initio direct dynamics simulations.

To provide more detailed insight into the dynamical processes involved in the excited-state PCET reaction in the Hz−H_2O complex, we discuss three representative trajectories. A trajectory which is representative for the ultrafast relaxation from the high-lying LE states to the S_1 state is shown in Figure 5. In panel (a), the time evolution of the energies of the

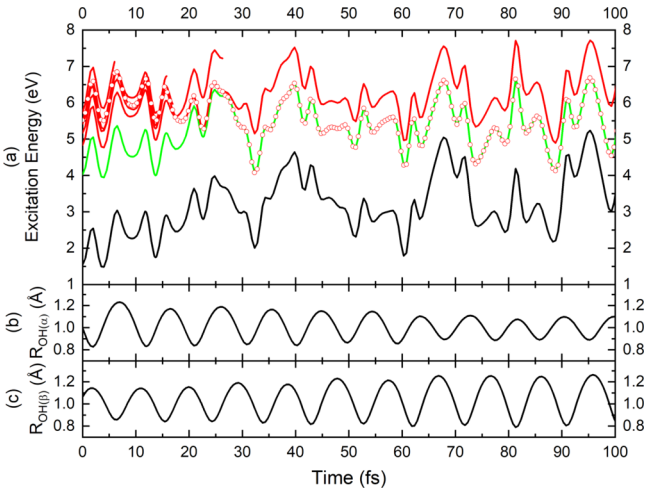

Figure 5. Representative trajectory illustrating ultrafast relaxation to the S_1 state of the Hz···H_2O complex. Panel (a) illustrates the evolution of the PEs of the adiabatic states. The color code is the same as in Figure 3b: high-lying LE states (red), S_1 state (green), and ground state (black). The CT state is not populated for this trajectory. The currently occupied adiabatic electronic state is marked by red circles. Panels (b) and (c) display the bond distances of the OH(α) and OH(β) groups.

adiabatic electronic states is shown. The high-lying LE states are colored red, the S_1 state green, and the ground state black. The CT state (blue) is not populated for this particular trajectory. The currently populated state is marked by the red circles. As explained in Section 2.2.1, only the neighboring upper state of the current state is computed. Higher-lying states are successively deleted as the trajectory evolves toward lower-lying electronic states. However, "upward" nonadiabatic transitions are always possible to the next higher adiabatic electronic state.

The trajectory shown in Figure 5 is launched in the $S_5(\pi\pi^*)$ state with an initial energy of 5.5 eV. The ground-state PE at the initial geometry of this trajectory is 1.5 eV higher than the energy minimum of the ground state, which is slightly lower than half of the harmonic zero-point energy. Within the first 18 fs, the trajectory switches to the $S_2(n\pi^*)$ state. The transition to the $S_1(\pi\pi^*)$ state occurs at 27 fs. It can be seen that the PE of the ground state gradually increases as the trajectory relaxes toward the minimum of the S_1 PE surface. To visualize the PCET dynamics, the time evolution of the bond lengths of the two OH bonds of the water molecule is shown. For this trajectory, the hydrogen bond between the H_2O molecule and Hz is preserved throughout the dynamics. The $R_{OH(\alpha)}$ and $R_{OH(\beta)}$ distances oscillate approximately out of phase, but no H-atom transfer occurs.

The second representative trajectory is shown in Figure 6. This trajectory is excited at t = 0 by a 4.03 eV photon. The

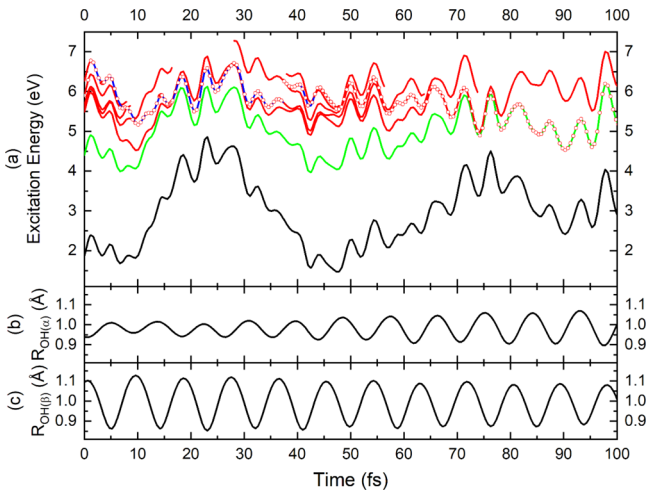

Figure 6. Representative trajectory illustrating transient dynamics in the CT state. Panel (a) illustrates the evolution of the PEs of the high-lying LE states (red), the CT state (blue), the S_1 state (green), and the ground state (black). The currently occupied state is marked by red circles. Panels (b) and (c) display the bond distances of the OH(α) and OH(β) groups.

ground-state energy at the initial geometry is 1.9 eV. This trajectory switches to the CT state very quickly, at 1.0 fs. The trajectory propagates diabatically in the CT state until it switches back to the high-lying LE states at 43 fs. After another series of hops within the LE states, the trajectory switches to the S_1 state in which it remains until 100 fs. This trajectory is an example of an ET reaction which is aborted at an early stage. This can also be observed from the oscillations of the two OH bond lengths. As the CT state is occupied, $R_{OH(\alpha)}$ oscillates weakly with an amplitude of only 0.05 Å, being attracted by the negatively charged Hz molecule. The duration of the population of the CT state was not sufficient to drive the PT reaction and the complex remains in the S_1 state with enhanced oscillation of the OH(α) bond.

The third representative trajectory, shown in Figure 7, illustrates a rapid PCET process which avoids trapping in the S_1 state. This trajectory is launched by a 4.06 eV photon. It switches to the CT state already at 1.5 fs. It remains in the CT state, crossing the S_1 state diabatically, until a degeneracy with the ground state occurs at 13.2 fs and the propagation is stopped. The OH(α) bond is strongly stretched to 1.7 Å at this

https://doi.org/10.1021/acs.jpca.1c08291
J. Phys. Chem. A 2021, 125, 9917−9931

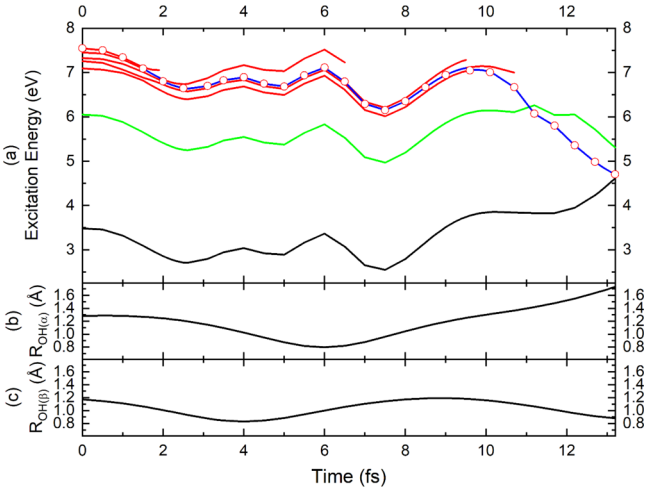

Figure 7. Representative trajectory illustrating a PCET reaction. Panel (a) illustrates the evolution of the PEs of the high-lying LE states (red), the CT state (blue), the S_1 state (green), and the ground state (black). The currently occupied state is marked by red circles. Panels (b) and (c) display the bond distances of the OH(α) and OH(β) groups. The trajectory was terminated at 13.2 fs at a CI with the electronic ground state.

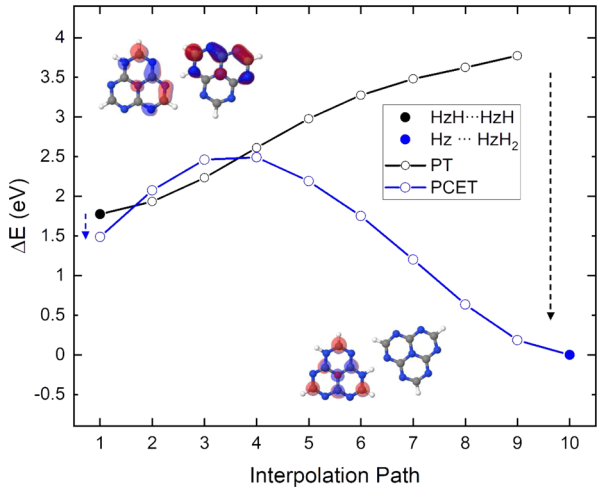

Figure 8. Linearly interpolated scan between the equilibrium geometry of the HzH···HzH biradical (black dot) and the equilibrium geometry of the Hz···HzH_2 closed-shell system (blue dot) at the UMP2/cc-pVDZ level. The black curve shows the energy profile of the biradical system, and the blue curve shows the energy profile of the closed-shell system along the interpolated PT path. The singly occupied orbitals of the HzH···HzH biradical are displayed in the upper left corner. The HOMO of HzH_2 is displayed at the bottom. At point 10, the calculation for the biradical (black curve) failed to converge.

time, which indicates that an HzH···OH biradical has been generated.

The dynamics of the PCET process in the Hz···H_2O complex also has been studied earlier by Ullah et al. with FSSH trajectory calculations at the TDDFT level.[22] They reported a population probability of the S_1 state of 77% and a PCET reaction probability of 23% after 300 fs. The present calculations predict a probability of 91% for the S_1 state and an upper limit of 9% for the PCET reaction at 100 fs. Considering that some trajectories in the hot S_1 state may undergo PCET between 100 and 300 fs, the results of the two simulations are not in contradiction, although our data tend to suggest a somewhat lower PCET reaction probability.

3.2. Disproportionation of HzH Radicals. It is expected that the Hz + HzH_2 closed-shell system is more stable than the HzH + HzH biradical, that is, the disproportionation of two HzH radicals to Hz + HzH_2 is expected to be exothermic. The disproportionation reaction can occur via three pathways: (i) ET followed by PT

$$\mathrm{HzH{\cdots}HzH} \rightarrow \mathrm{HzH^{+}{\cdots}HzH^{-}} \rightarrow \mathrm{Hz} + \mathrm{HzH_2} \tag{5}$$

(ii) PT followed by ET

$$\mathrm{HzH{\cdots}HzH} \rightarrow \mathrm{Hz^{-}{\cdots}HzH_2{}^{+}} \rightarrow \mathrm{Hz} + \mathrm{HzH_2} \tag{6}$$

or (iii) concerted ET and PT (PCET),[15] nominally H-atom transfer,

$$\mathrm{HzH{\cdots}HzH} \rightarrow \mathrm{Hz} + \mathrm{HzH_2} \tag{7}$$

To characterize the energetics of these processes, we optimized the energies of the HzH···HzH biradical and the closed-shell Hz···HzH_2 system and computed the energies along a linearly interpolated scan between these geometries, see Section 2.1.2. The resulting energy profiles are shown in Figure 8. The full black dot on the left denotes the optimized energy of the HzH···HzH biradical. The full blue dot on the right denotes the optimized energy of the closed-shell Hz···HzH_2 system. The blue circle on the left represents the energy of the closed-shell ion pair HzH^{+}···HzH^{-} at the nuclear geometry of the HzH···HzH biradical. The dashed arrow on the left indicates ET in the HzH···HzH dimer to form HzH^{-}···HzH^{+} at fixed nuclear geometry. The black circle on the right denotes the energy of the ionic biradical Hz^{-}···$HzH_2{}^{+}$ at the optimized geometry of the neutral Hz + HzH_2 system. The dashed arrow on the right indicates ET in Hz^{-}···$HzH_2{}^{+}$ to form Hz···HzH_2 at fixed nuclear geometry. The blue curve represents the energy of the closed-shell system along the interpolated PT coordinate, while the energy of the biradicalic system along the PT coordinate is represented by the black curve. The ET from HzH···HzH to HzH^{-}···HzH^{+} (left side) is slightly exothermic, while the ET from Hz^{-}···$HzH_2{}^{+}$ to Hz + HzH_2 (right side) is strongly exothermic.

Figure 8 confirms that the disproportionation reaction of two HzH radicals is significantly exothermic. The blue curve in Figure 8 exhibits an energy maximum about 0.7 eV above the energy of the HzH···HzH biradical. Because the geometry is not relaxed, this maximum represents an upper limit for the reaction barrier of the PT reaction. Solvation effects in the condensed phase may further reduce the PT barrier. Based on the computational results shown in Figure 8, it can be concluded that the disproportionation HzH radical pairs may occur spontaneously by thermal fluctuations and/or H-atom tunneling.

3.3. Photoinduced H-Atom Photodetachment from HzH_2. *3.3.1. Structures and Excitation Energies of HzH_2 Tautomers.* The equilibrium geometries of the four different tautomers of HzH_2 are displayed in Figure 9. Given one NH group, the second NH group can be either on the opposite side or the same side of the triangle. In the first case, there exist three different tautomers, 1,4-HzH_2 or 1,7-HzH_2 (tautomer I in Figure 9), 1,6-HzH_2 (tautomer II), and 1,3-HzH_2 (tautomer III). In the second case, there exists only one tautomer, namely, 1,9-HzH_2 (tautomer IV). The relative energies of the tautomers are given in the figure and are smaller than one

https://doi.org/10.1021/acs.jpca.1c08291
J. Phys. Chem. A 2021, 125, 9917−9931

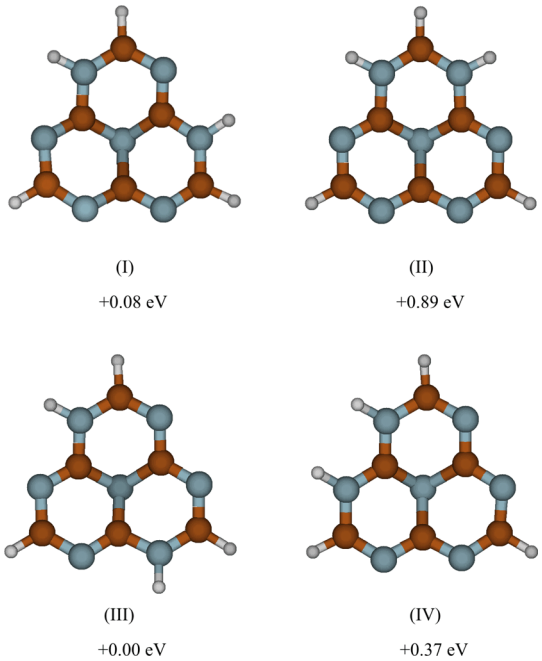

Figure 9. Equilibrium geometries of the four HzH_2 tautomers in their singlet ground-states. The ground-state energies relative to the most stable tautomer III are indicated. Tautomer I is selected as the exemplar of HzH_2 for this work.

electron volt. The two NH bond lengths are equal in all tautomers. The highest occupied molecular orbitals (HOMOs) of all four tautomers are shown in Figure S6.

We selected tautomer I as the exemplar for the study of the photodissociation dynamics. The double reduction of Hz breaks the planarity of the aromatic system. The central nitrogen atom (N9b) protrudes out of the plane, resulting in an out-of-plane angle of the three CN bonds of about 20°. The three central CN bond lengths are stretched by 0.05 to 0.1 Å compared to Hz. Referring to Figure 10a, we denote the NH group on the upper left side as NH(α) and the NH group on the lower right side as NH(β). The bond lengths from the N-atom of the NH(α) group to the adjacent C atoms are both 1.36 Å (0.2 Å longer than the corresponding CN bond length of Hz). For the NH(β) group, one of the adjacent CN bonds is elongated to 1.39 Å, which is similar to the CN bond length of the HzH radical.

The frontier MOs of HzH_2 are shown in Figure 10b. Because the distortion from planarity is minor, the orbitals and the excited electronic states of HzH_2 can be classified by C_s symmetry labels. The HOMO is a nondegenerate π orbital which correlates with the nondegenerate LUMO of Hz. The LUMO and LUMO + 1 are σ^* orbitals which are plus/minus linear combinations of σ^* orbitals located on the two NH groups. We denote the LUMO as the σ^*_+ orbital and the LUMO + 1 as the σ^*_- orbital. The LUMO + 2 and LUMO + 3 are π^* orbitals.

The vertical excitation energies of the 10 lowest singlet states of HzH_2 are listed in Table 2. The S_1 and S_2 states are of $\pi\pi^*$ character and correspond to excitations from the HOMO to LUMO + 2 and LUMO + 3, respectively, see Figure 10b. They possess moderate oscillator strengths (f = 0.071 and 0.113). The S_3 and S_4 states are dark $\pi\sigma^*$ states, arising from excitations from the HOMO to the σ^*_+ and σ^*_- orbitals, respectively, see Figure 10b. The bright $\pi\pi^*$ states S_7 (4.35 eV) and S_8 (4.66 eV) are related to the bright degenerate $^1\pi\pi^*$ state of Hz. The S_9 state is a diffuse Rydberg state, and the S_6 and S_{10} states are $^1n\pi^*$ states. The double reduction of Hz saturates the two N atoms and raises the $^1n\pi^*$ excitation energies relative to Hz.

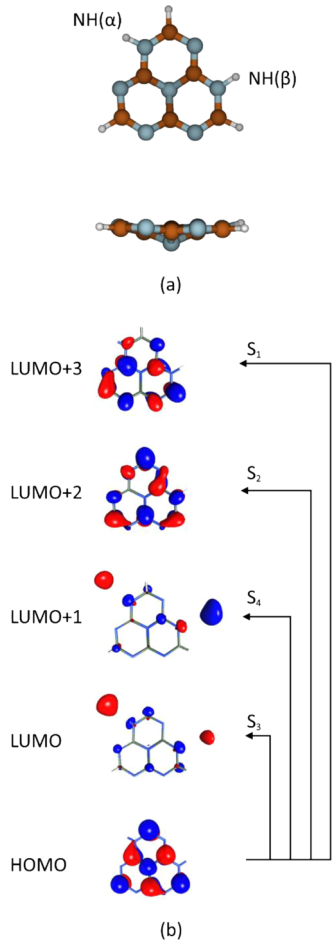

Figure 10. (a) Ground-state equilibrium structure of tautomer I of HzH_2 in top and side views. (b) Frontier MOs of HzH_2. The HOMO is a π orbital, LUMO and LUMO + 1 are σ^* orbitals, and LUMO + 3 and LUMO + 4 are π^* orbitals. The arrows indicate the dominant configurational characters of the electronic transitions.

Table 2. Vertical Excitation Energies (in eV) of the Lowest 10 Singlet States of HzH_2 at the Ground-State Equilibrium Geometry, Calculated with the ADC(2) Method and a Partially Augmented cc-pVDZ Basis Set[a]

excited state	energy
$S_1(\pi\pi^*)$	2.07 (0.071) [5.2]
$S_2(\pi\pi^*)$	2.31 (0.113) [5.3]
$S_3(\pi\sigma^*)$	3.21 (0.002) [2.8]
$S_4(\pi\sigma^*)$	3.61 (0.002) [3.4]
$S_5(\pi\pi^*)$	4.08 (0.005) [5.0]
$S_6(n\pi^*)$	4.32 (0.002) [2.3]
$S_7(\pi\pi^*)$	4.35 (0.015) [3.3]
$S_8(\pi\pi^*)$	4.66 (0.303) [2.4]
$S_9(\pi\sigma^*)$	4.70 (0.004) [3.0]
$S_{10}(n\pi^*)$	4.73 (0.047) [2.4]

[a]Oscillator strengths are given in parentheses and dipole moments (in Debye) in brackets.

https://doi.org/10.1021/acs.jpca.1c08291
J. Phys. Chem. A 2021, 125, 9917−9931

Photodissociation reactions in heteroaromatic systems driven by $^1\pi\sigma^*$ states with repulsive PE functions were extensively studied experimentally and theoretically over the past two decades.[28−30,50] It is established that a rigid scan of the PE profiles of $^1\pi\sigma^*$ states along NH or OH bonds describes the photoreactivity of these groups to a good approximation. Therefore, we computed a rigid scan along the bond length $R_{NH(\alpha)}$ of the NH(α) group for the excited states with vertical excitation energies below 6 eV. The PE profiles calculated with the ADC(2) method are displayed in Figure 11a. The calculation of this scan and its interpretation was greatly simplified by constraining HzH_2 to be planar (C_s symmetry), such that crossings of the energies of A′ and A″ states become allowed.

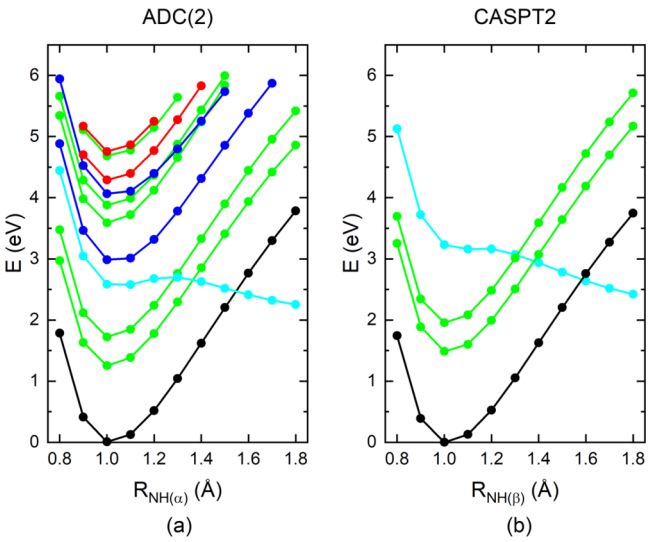

Figure 11. PE functions of planar HzH_2 for a rigid scan along the NH dissociation coordinate $R_{NH(\alpha)}$ at the ADC(2) level (a) and the CASPT2 level (b). At the ADC(2) level, electronic states with vertical excitation energies up to 6 eV are included. At the CASPT2 level, the ground state and the lowest three excited electronic states are included. Black: ground state, green: $\pi\pi^*$ states, red: nπ^* states, light blue: $\pi\sigma^*_+$ state, and dark blue: $\pi\sigma^*_-$ states.

Figure 11a shows that the energy of the $\pi\sigma^*_+$ state is strongly stabilized with increasing $R_{NH(\alpha)}$, while the energy of the $\pi\sigma^*_-$ state behaves similarly to the energies of the other excited states and the ground state. Upon stretching of $R_{NH(\alpha)}$, the density of the σ^*_+ orbital localizes in the vicinity of the NH(α) group. The σ^*_- orbital, on the other hand, localizes on the NH(β) group. The excitation energy of the $\pi\sigma^*_-$ state therefore is insensitive to the stretching of $R_{NH(\alpha)}$, and its PE curve is roughly parallel to that of the electronic ground state in Figure 11a.

The energy of the dissociative $S_3(\pi\sigma^*_+)$ state crosses the energies of two $^1\pi\pi^*$ excited states near $R_{NH(\alpha)}$ = 1.3 Å and further crosses the energy of the ground state near $R_{NH(\alpha)}$ = 1.55 Å. For larger $R_{NH(\alpha)}$, the open-shell $\pi\sigma^*_+$ state becomes the electronic ground state, and the closed-shell state becomes the lowest excited state, see Figure 11a. The rigid scan along $R_{NH(\beta)}$ is analogous to the scan along $R_{NH(\alpha)}$.

To benchmark the ADC(2) results in Figure 11a against a multiconfiguration multireference electronic-structure method, we repeated the rigid scan with the CASPT2 method. The results are shown in shown in Figure 11b. The geometries of the CASPT2 scan are identical to those of the scan performed with the ADC(2) method. Not unexpectedly, difficulties were encountered with the CASSCF and CASPT2 calculations for the higher excited states over an extended region of $R_{NH(\alpha)}$. Therefore, the energies of only the lowest three electronic states could be computed with the CASPT2 method. The profiles of the lowest three excited states, namely the two low-lying $^1\pi\pi^*$ states and the $S_3(\pi\sigma^*_+)$ state, show qualitatively good agreement with the ADC(2) results. The CASPT2 energy of the $\pi\sigma^*_+$ state is ∼0.7 eV blueshifted relative to the ADC(2) energy. For the $\pi\pi^*$ states, the blue shift is ∼0.3 eV. The CASPT2 energy profile of the $\pi\sigma^*_+$ state is barrierless, while a tiny barrier exists at the ADC(2) level near $R_{NH(\alpha)}$ = 1.3 Å.

The simulated absorption spectrum of HzH_2 is shown in Figure 12. The energies and oscillator strengths of eight adiabatic excited states were calculated for each of the 2000 Wigner sampling points. The convoluted absorption exhibits two clearly separated peaks. The absorption peak near 2.2 eV arises from the two low-lying $^1\pi\pi^*$ states. The dark $\pi\sigma^*$ states are not visible in the absorption spectrum. The strong absorption peak at 4.55 eV arises from the bright $S_8(\pi\pi^*)$ state. Comparing the absorption maxima with the vertical excitation energies in Table 2, both peaks are redshifted by about 0.1 eV.

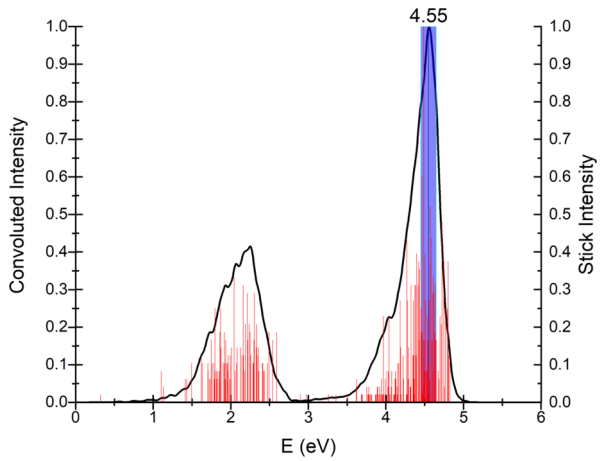

Figure 12. Simulated absorption spectrum of HzH_2. At each of the 2000 phase-space points sampled from the room-temperature Wigner distribution, the vertical excitation energies and oscillator strengths of the lowest eight electronic states were calculated, yielding the line spectrum (red). The envelope was obtained by convolution of the line spectrum with a Gaussian of 0.05 eV FWHM. The blue shaded area indicates the 0.1 eV-wide energy window around the absorption maximum at 4.55 eV from which the initial conditions for the dynamics simulations were sampled.

3.3.2. Photodissociation Dynamics of HzH_2. The time evolution of the population probabilities of the adiabatic electronic states S_0−S_8 of HzH_2 up to 150 fs is shown in Figure 13a. The initial conditions were selected from the shaded spectral window at the maximum of the absorption spectrum, see Figure 12 and Section 2.2.2. At t = 0, the population is primarily in the bright $\pi\pi^*$ states S_7 and S_8. These states are depopulated by nonadiabatic transitions on a time scale of about 10 fs. The electronic population is distributed over the lower-lying singlet states until the population flows to the electronic ground state on a time scale of less than 100 fs.

https://doi.org/10.1021/acs.jpca.1c08291
J. Phys. Chem. A 2021, 125, 9917−9931

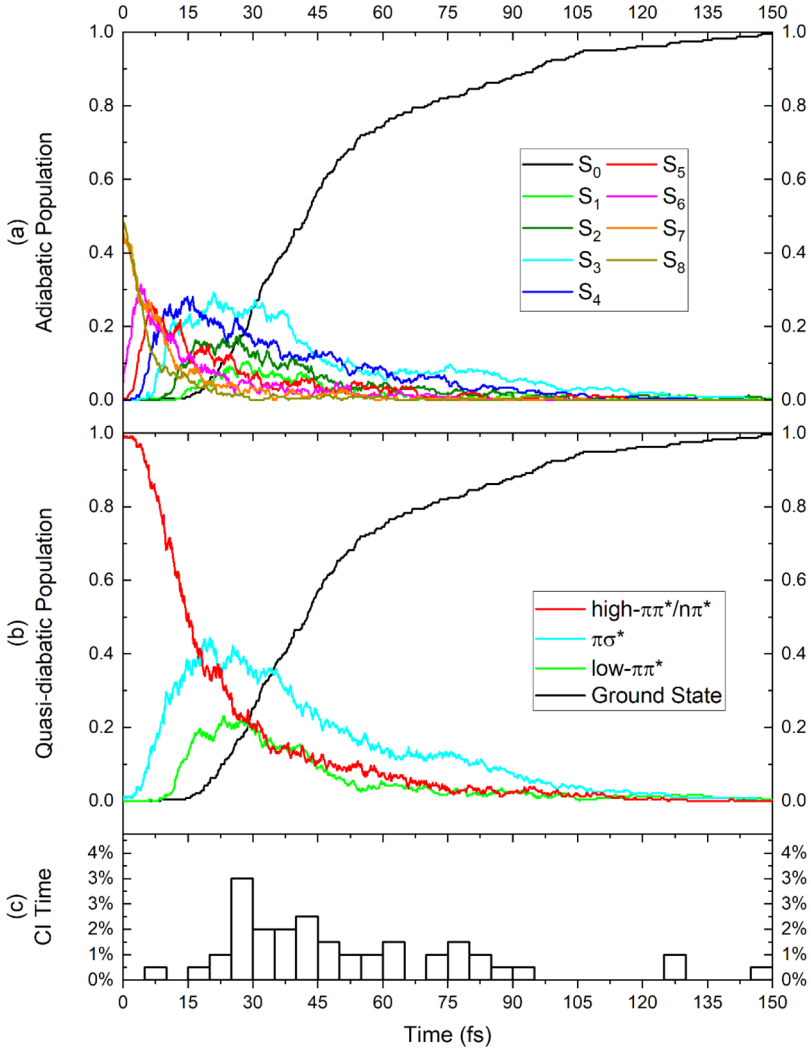

Figure 13. (a) Time evolution of the populations of the adiabatic electronic states of HzH_2. (b) Time evolution of the quasidiabatic populations of the $\pi\sigma^*$ state and groups of $\pi\pi^*/n\pi^*$ states. (c) Histogram of encounters of trajectories with S_1-S_0 CIs.

Because of the large number of populated states, the data in Figure 13a are difficult to analyze. The picture becomes more transparent when the $\pi\sigma^*$ state is identified by the diffuseness of its electronic density and the remaining states are grouped into the categories "low-lying $\pi\pi^*$ states," "high-lying $n\pi^*/\pi\pi^*$ states," and electronic ground state. The population evolution of these groups of states is displayed in Figure 13b. Almost all trajectories are launched in the group high-lying $\pi\pi^*/n\pi^*$ states. The transfer of population to the $\pi\sigma^*$ state starts at less than 5 fs. At about 18 fs, the population of the $\pi\sigma^*$ state attains a maximum (45%) and then slowly decays to zero. About 25% of the population appears transiently in the low-lying $\pi\pi^*$ states. Beginning at about 20 fs, trajectories encounter degeneracies with the electronic ground state. They are counted as ground-state population thereafter. The histogram of the encounters of S_1-S_0 CIs is shown in Figure 13c. For each of these trajectories, at least one of the two NH distances $R_{NH(\alpha)}$ and $R_{NH(\beta)}$ is larger than 1.4 Å, indicating that the excited-state trajectories hit the ground state upon dissociation into a free HzH radical and a free H atom. It can be seen (Figure 13b,c) that the distribution of the encounters with the ground state is proportional to the population of the $\pi\sigma^*$ state. Twenty-six (~11%) trajectories result in dissociation of the NH(β) group and 21 (~9%) lead to dissociation of the NH(α) group.

A schematic overview of the reaction dynamics of photoexcited HzH_2 is given in Figure 14. After photoexcitation, a

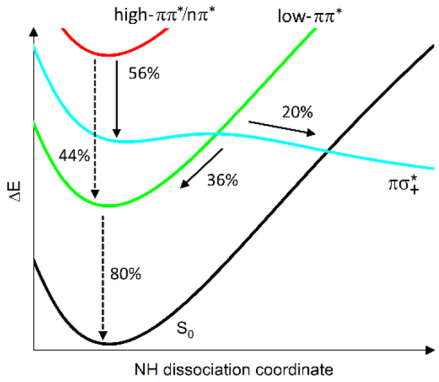

Figure 14. Schematic overview of the photochemical dynamics of HzH_2 within 150 fs. The numbers give the branching ratios of nonadiabatic processes. Twenty percent of the trajectories encounter CIs of the diabatic $\pi\sigma^*$ state with the electronic ground state at stretched NH bond lengths.

https://doi.org/10.1021/acs.jpca.1c08291
J. Phys. Chem. A 2021, 125, 9917−9931

fraction of 56% of the initial excited-state population is transferred to the dissociative $\pi\sigma^*$ state, while 44% of the initial population relaxes directly the the low-lying $\pi\pi^*$ states. At the intersection of the $\pi\sigma^*$ PE surface with the surfaces of the low-lying $\pi\pi^*$ states, 20% of trajectories pass diabatically and hit the electronic ground state, while 36% follow the adiabatic path and are captured in the low-lying $\pi\pi^*$ states. Remarkably, no long-lived excited-state populations exist in HzH_2. The system relaxes completely to the electronic ground state within 150 fs, which can be either the initial closed-shell ground state or the biradical, which is the ground state for large HzH···H distances. This behavior is in stark contrast to the dynamics of the Hz···H_2O complex in which most of the population is trapped in the long-lived S_1 state.

We selected again three representative trajectories for a more detailed analysis of the dynamics. The data for the first trajectory are shown in Figure 15. The trajectory starts in the

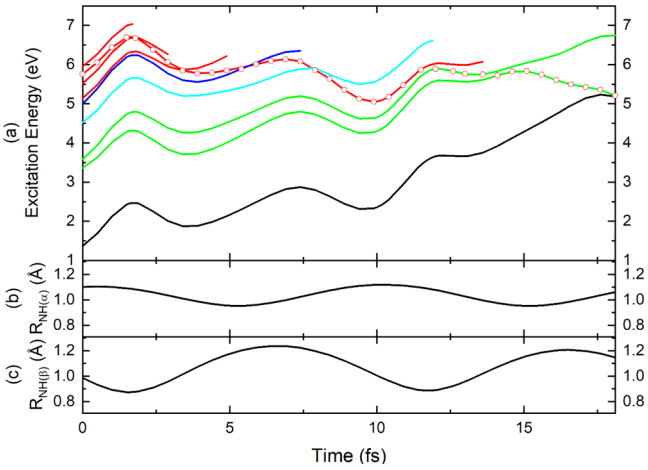

Figure 15. Representative trajectory illustrating ultrafast IC in HzH_2. Panel (a) shows the time evolution of the PEs of the high-lying $\pi\pi^*$/nπ^* states (red), the $\pi\sigma^*_-$ state (dark blue), the $\pi\sigma^*_+$ state (light blue), the low-lying $\pi\pi^*$ states (green), and the ground state (black). The currently occupied state is marked by red circles. Panels (b) and (c) show the time evolution of the NH distances $R_{NH(\alpha)}$ and $R_{NH(\beta)}$. At 15.7 fs, an S_1-S_0 CI near degeneracy is encountered and the trajectory is stopped.

state S_7 by the absorption of a photon of 4.39 eV. The trajectory switches at about 12 fs to the low-lying $\pi\pi^*$ states without occupying the $\pi\sigma^*$ state. At 15.7 fs, the trajectory hits a CI with the ground state, and the propagation is terminated. The time evolution of $R_{NH(\alpha)}$ and $R_{NH(\beta)}$ (Figure 15b,c) shows that the NH groups are spectators of the IC dynamics in this case.

The second representative trajectory illustrates dynamics driven by the $\pi\sigma^*$ states, see Figure 16. The trajectory starts in the state S_8 and switches to the $\pi\sigma^*_-$ state at 5 fs. This state does not drive predissociation (see Figure 11). At 17.6 fs, the trajectory switches to the $\pi\sigma^*_+$ state and $R_{NH(\beta)}$ starts to increase. At 22.7 fs, the trajectory switches to one of the low-lying $\pi\pi^*$ states, and the NH dissociation reaction is aborted. Although the dissociative state is occupied only for about 5 fs, 2 eV of electronic energy is converted into kinetic energy, part of which drives the relatively large oscillation of the bond length of the NH(α) group. The degeneracy with the electronic ground state is encountered at 25.7 fs.

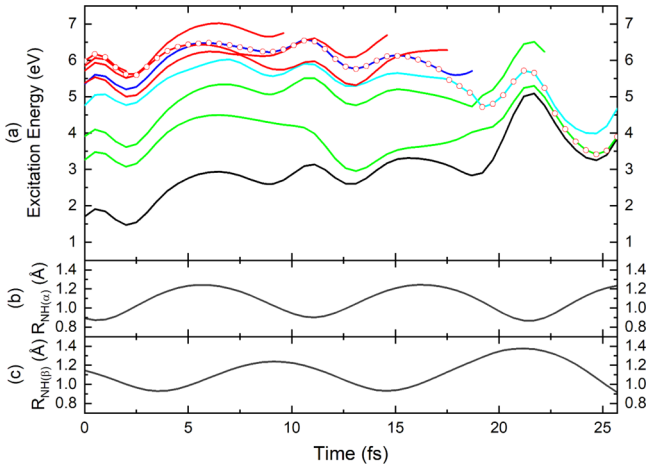

Figure 16. Representative trajectory illustrating transient evolution in $\pi\sigma^*$ states of HzH_2. Panel (a) shows the evolution of the PEs of the high-lying $\pi\pi^*$/nπ^* states (red), the $\pi\sigma^*_-$ state (dark blue), the $\pi\sigma^*_+$ state (light blue), the low-lying $\pi\pi^*$ states (green), and the ground state (black). The currently occupied state is marked by red circles. Panels (b) and (c) show the time evolution of the NH distances $R_{NH(\alpha)}$ and $R_{NH(\beta)}$. At 26 fs, a near-degeneracy of the energies of the S_1 and S_0 states is encountered, and the trajectory is stopped.

The third representative trajectory, shown in Figure 17, is an example of photodissociation. The trajectory is launched in the

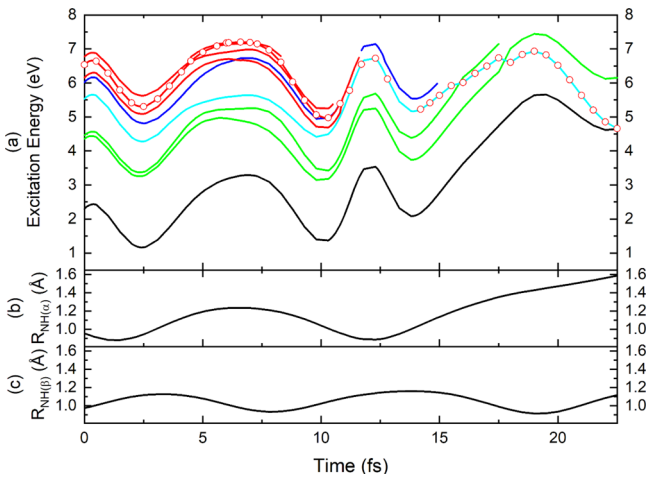

Figure 17. Representative trajectory illustrating H-atom photodetachment. Panel (a) shows the time evolution of the PEs of the high-lying $\pi\pi^*$/nπ^* states (red), the $\pi\sigma^*_-$ state (dark blue), the $\pi\sigma^*_+$ state (light blue), the low-lying $\pi\pi^*$ states (green), and the ground state (black). The currently occupied state is marked by red circles. Panels (b) and (c) display the NH distances $R_{NH(\alpha)}$ and $R_{NH(\beta)}$. At 22.5 fs, the diabatic $\pi\sigma^*$ state encounters a quasidegeneracy with the electronic ground state. $R_{NH(\alpha)}$ is stretched to 1.6 Å at the S_1-S_0 CI, which indicates detachment of the H atom of the NH(α) group.

S_6 state. The trajectory bypasses the $\pi\sigma^*_-$ state and populates the dissociative $\pi\sigma^*_+$ state at 11.2 fs. The trajectory then propagates diabatically, crossing the two low-lying $\pi\pi^*$ states at 16 and 18 fs, respectively. It hits a CI of the $\pi\sigma^*_+$ state with the ground state at 22.5 fs. During the propagation in the $\pi\sigma^*_+$ state, the NH distance $R_{NH(\alpha)}$ extends to 1.6 Å which represents dissociation of a free H atom.

https://doi.org/10.1021/acs.jpca.1c08291
J. Phys. Chem. A 2021, 125, 9917−9931

4. DISCUSSION AND CONCLUSIONS

Previous computational and experimental evidence indicates that the Hz molecule is a photobase which is able to oxidize water molecules directly in an excited-state PCET reaction, yielding HzH and OH radicals.[12,21] In the present work, we explored the nonadiabatic nuclear dynamics of the water oxidation reaction in the Hz···H_2O complex and the photodissociation dynamics in the HzH_2 molecule. Using the computationally efficient and robust ADC(2) electronic-structure method and the efficient LZSH algorithm, we were able to perform the first simulation of the water oxidation reaction in the Hz···H_2O complex with a wave-function-based ab initio method. The water oxidation reaction is initiated by the excitation of the bright $^1\pi\pi^*$ state of the Hz chromophore with a near-UV photon. While the majority of Hz···H_2O complexes relax via intermediate $^1n\pi^*$ states toward the exceptionally long-lived $S_1(\pi\pi^*)$ state of Hz, a fraction of 38% of trajectories populate the reactive CT state. After bifurcation of the population flow at the CI of the CT state with the S_1 state, a fraction of 9% of trajectories is predicted to encounter a CI with the electronic ground state, potentially forming HzH + OH radicals in the ground state. This relatively low yield of radicals represents only the direct and ultrafast (≈100 fs) component of the reaction. Part of the predicted population of the S_1 state (91%) of the Hz···H_2O complex at the end of the present simulation (100 fs) may either overcome the barrier for H-atom transfer because of residual excess energy from the initial radiationless decay process or by H-atom tunneling. The time scales of these processes are, however, too long to be simulated with ab initio on-the-fly dynamics simulations.

There exist several reaction mechanisms by which the energy stored in transient HzH radicals can be harvested. Photodissociation of HzH radicals to yield Hz and free H atoms is one possibility. Photoexcitation of HzH radicals in aqueous environments can lead to the formation of transient hydrated electrons[51] which have higher reduction potentials than free hydrogen atoms.[52] Another possibility, considered herein, is the formation of doubly reduced Hz molecules via the spontaneous disproportionation of HzH radicals. Upon excitation of mixed $^1\pi\pi^*/^1n\pi^*$ excited states in HzH_2 with near-UV photons, a dissociative $^1\pi\sigma^*$ state can be accessed by radiationless transitions and can drive the photodetachment of an H atom from HzH_2. The nonadiabatic dynamics simulations of the present work show that the reactive $^1\pi\sigma^*$ state becomes populated with a probability of 56% and that 20% of the population passes through CIs with low-lying bound $^1\pi\pi^*$ states to encounter CIs with the electronic ground state. According to these results, the photodetachment of H atoms from HzH_2 is a promising strategy for hydrogen evolution.

An essential advantage of organic molecular photocatalysts compared with crystalline inorganic photocatalysts is the wide tunability of the properties of molecular systems by chemical modification. Apart from the tuning of the excitation energy of the bright state (the optical band gap), the barrier for the PCET reaction in the Hz···H_2O complex can be lowered, for example, by at least 0.4 eV by electron-withdrawing substituents on the three carbon sites of Hz.[53] The excitation energies of the $^1\pi\pi^*$ and $^1\pi\sigma^*$ states of HzH_2 can likewise be tuned by substituents. To exploit these possibilities of photocatalyst optimization, it is essential that the basic mechanisms of the photoreactions involved in water oxidation and hydrogen evolution are fully understood, such that photocatalysts can be optimized in the future by rational design rather than by empirical trial and error procedures.

■ ASSOCIATED CONTENT

Supporting Information

The Supporting Information is available free of charge at https://pubs.acs.org/doi/10.1021/acs.jpca.1c08291.

Atom numbering of Hz, additional results of trajectory calculations, and molecular orbitals of HzH_2 (PDF)

■ AUTHOR INFORMATION

Corresponding Author

Wolfgang Domcke − *Department of Chemistry, Technical University of Munich, Garching D-85747, Germany;* orcid.org/0000-0001-6523-1246; Email: domcke@ch.tum.de

Author

Xiang Huang − *Department of Chemistry, Technical University of Munich, Garching D-85747, Germany*

Complete contact information is available at: https://pubs.acs.org/10.1021/acs.jpca.1c08291

Notes

The authors declare no competing financial interest.

■ ACKNOWLEDGMENTS

This work was supported by a grant of the Deutsche Forschungsgemeinschaft (DFG), grant No. DO256/42-2. The authors would like to thank Sebastian Pios and Marin Sapunar for helpful discussions and help with the CASSCF/CASPT2 calculations and further developments of the LZSH algorithm.

■ REFERENCES

(1) Wang, X.; Maeda, K.; Thomas, A.; Takanabe, K.; Xin, G.; Carlsson, J. M.; Domen, K.; Antonietti, M. A Metal-Free Polymeric Photocatalyst for Hydrogen Production from Water under Visible Light. *Nat. Mater.* **2009**, *8*, 76−80.

(2) Ong, W.-J.; Tan, L.-L.; Ng, Y. H.; Yong, S.-T.; Chai, S.-P. Graphitic Carbon Nitride (g-C_3N_4)-Based Photocatalysts for Artificial Photosynthesis and Environmental Remediation: Are We a Step Closer to Achieving Sustainability? *Chem. Rev.* **2016**, *116*, 7159−7329.

(3) Wen, J.; Xie, J.; Chen, X.; Li, X. A Review on g-C_3N_4-Based Photocatalysts. *Appl. Surf. Sci.* **2017**, *391*, 72−123.

(4) Liu, J.; Liu, N. Y.; Li, H.; Wang, L. P.; Wu, X. Q.; Huang, H.; Liu, Y.; Bao, F.; Lifshitz, Y.; Lee, S.-T.; Kang, Z. H. A Critical Study of the Generality of the Two Step Two Electron Pathway for Water Splitting by Application of a C_3N_4/MnO_2 Photocatalyst. *Nanoscale* **2016**, *8*, 11956−11961.

(5) Zhang, G.; Lan, Z.-A.; Lin, L.; Lin, S.; Wang, X. Overall Water Splitting by Pt/C_3N_4 Photocatalysts without Using Sacrificial Agents. *Chem. Sci.* **2016**, *7*, 3062−3066.

(6) Guo, F.; Shi, W.; Zhu, C.; Li, H.; Kang, Z. Coo and g-C_3N_4 Complement Each Other for Highly Efficient Overall Water Splitting under Visible Light. *Appl. Catal., B* **2018**, *226*, 412−420.

(7) Fujishima, A.; Honda, K. Electrochemical Photolysis of Water at a Semiconductor Electrode. *Nature* **1972**, *238*, 37−38.

(8) Walter, M. G.; Warren, E. L.; McKone, J. R.; Boettcher, S. W.; Mi, Q.; Santori, E. A.; Lewis, N. S. Solar Water Splitting Cells. *Chem. Rev.* **2010**, *110*, 6446−6473.

(9) Wang, Y.; Wang, X.; Antonietti, M. Polymeric Graphitic Carbon Nitride as a Heterogeneous Organocatalyst: From Photochemistry to

Multipurpose Catalysis to Sustainable Chemistry. *Angew. Chem., Int. Ed.* **2012**, *51*, 68−89.
(10) Shahbaz, M.; Urano, S.; LeBreton, P. R.; Rossman, M. A.; Hosmane, R. S.; Leonard, N. J. Tri-s-Triazine: Synthesis, Chemical Behavior, and Spectroscopic and Theoretical Probes of Valence Orbital Structure. *J. Am. Chem. Soc.* **1984**, *106*, 2805−2811.
(11) Turner, D. W.; Baker, C.; Baker, A. D.; Brundle, C. R. *Molecular Photoelectron Spectroscopy*; Wiley: New York, 1970.
(12) Ehrmaier, J.; Karsili, T. N. V.; Sobolewski, A. L.; Domcke, W. Mechanism of Photocatalytic Water Splitting with Graphitic Carbon Nitride: Photochemistry of the Heptazine-Water Complex. *J. Phys. Chem. A* **2017**, *121*, 4754−4764.
(13) Domcke, W.; Ehrmaier, J.; Sobolewski, A. L. Solar Energy Harvesting with Carbon Nitrides and N-Heterocyclic Frameworks: Do We Understand the Mechanism? *ChemPhotoChem* **2019**, *3*, 10−23.
(14) Domcke, W.; Sobolewski, A. L.; Schlenker, C. W. Photo-oxidation of Water with Heptazine-Based Molecular Photocatalysts: Insights from Spectroscopy and Computational Chemistry. *J. Chem. Phys.* **2020**, *153*, No. 100902.
(15) Weinberg, D. R.; Gagliardi, C. J.; Hull, J. F.; Murphy, C. F.; Kent, C. A.; Westlake, B. C.; Paul, A.; Ess, D. H.; McCafferty, D. G.; Meyer, T. J. Proton-Coupled Electron Transfer. *Chem. Rev.* **2012**, *112*, 4016−4093.
(16) Liu, X.; Sobolewski, A. L.; Borrelli, R.; Domcke, W. Computational Investigation of the Photoinduced Homolytic Dissociation of Water in the Pyridine-Water Complex. *Phys. Chem. Chem. Phys.* **2013**, *15*, 5957−5966.
(17) Huang, X.; Aranguren, J.-P.; Ehrmaier, J.; Noble, J. A.; Xie, W.; Sobolewski, A. L.; Dedonder-Lardeux, C.; Jouvet, C.; Domcke, W. Photoinduced Water Oxidation in Pyrimidine-Water Clusters: A Combined Experimental and Theoretical Study. *Phys. Chem. Chem. Phys.* **2020**, *22*, 12502−12514.
(18) Esteves-López, N.; Coussan, S.; Dedonder-Lardeux, C.; Jouvet, C. Photoinduced Water Splitting in Pyridine-Water Clusters. *Phys. Chem. Chem. Phys.* **2016**, *18*, 25637−25644.
(19) Pang, X.; Jiang, C.; Xie, W.; Domcke, W. Photoinduced Electron-Driven Proton Transfer from Water to an N-Heterocyclic Chromophore: Nonadiabatic Dynamics Studies for Pyridine−Water Clusters. *Phys. Chem. Chem. Phys.* **2019**, *21*, 14073−14079.
(20) Hosmane, R. S.; Rossman, M. A.; Leonard, N. J. Synthesis and Structure of Tri-S-Triazine. *J. Am. Chem. Soc.* **1982**, *104*, 5497−5499.
(21) Rabe, E. J.; Corp, K. L.; Sobolewski, A. L.; Domcke, W.; Schlenker, C. W. Proton-Coupled Electron Transfer from Water to a Model Heptazine-Based Molecular Photocatalyst. *J. Phys. Chem. Lett.* **2018**, *9*, 6257−6261.
(22) Ullah, N.; Chen, S.; Zhao, Y.; Zhang, R. Photoinduced Water-Heptazine Electron-Driven Proton Transfer: Perspective for Water Splitting with g-C_3N_4. *J. Phys. Chem. Lett.* **2019**, *10*, 4310−4316.
(23) Chai, J.-D.; Head-Gordon, M. Systematic Optimization of Long-Range Corrected Hybrid Density Functionals. *J. Chem. Phys.* **2008**, *128*, No. 084106.
(24) Schirmer, J. Beyond the Random-Phase Approximation: A New Approximation Scheme for the Polarization Propagator. *Phys. Rev. A* **1982**, *26*, 2395−2416.
(25) Trofimov, A. B.; Schirmer, J. An Efficient Polarization Propagator Approach to Valence Electron Excitation Spectra. *J. Phys. B: At., Mol. Opt. Phys.* **1995**, *28*, 2299−2324.
(26) Dreuw, A.; Wormit, M. The Algebraic Diagrammatic Construction Scheme for the Polarization Propagator for the Calculation of Excited States. *WIREs: Comput. Mol. Sci.* **2015**, *5*, 82−95.
(27) Karsili, T. N. V.; Tuna, D.; Ehrmaier, J.; Domcke, W. Photoinduced Water Splitting Via Benzoquinone and Semiquinone Sensitization. *Phys. Chem. Chem. Phys.* **2015**, *17*, 32183−32193.
(28) Sobolewski, A. L.; Domcke, W. Conical Intersections Induced by Repulsive $^1\pi\sigma^*$ States in Planar Organic Molecules: Malonaldehyde, Pyrrole and Chlorobenzene as Photochemical Model Systems. *Chem. Phys.* **2000**, *259*, 181−191.
(29) Sobolewski, A. L.; Domcke, W.; Dedonder-Lardeux, C.; Jouvet, C. Excited-State Hydrogen Detachment and Hydrogen Transfer Driven by Repulsive $^1\pi\sigma^*$ States: A New Paradigm for Nonradiatie Decay in Aromatic Biomolecules. *Phys. Chem. Chem. Phys.* **2002**, *4*, 1093−1100.
(30) Ashfold, M. N. R.; Cronin, B.; Devine, A. L.; Dixon, R. N.; Nix, M. G. D. The Role of $\pi\sigma^*$ Excited States in the Photodissociation of Heteroaromatic Molecules. *Science* **2006**, *312*, 1637−1640.
(31) Liu, J.; Liu, Y.; Liu, N. Y.; Han, Y.; Zhang, X.; Huang, H.; Lifshitz, Y.; Lee, S. T.; Zhong, J.; Kang, Z. Metal-Free Efficient Photocatalyst for Stable Visible Water Splitting Via a Two-Electron Pathway. *Science* **2015**, *347*, 970−974.
(32) Møller, C.; Plesset, M. S. Note on an Approximation Treatment for Many-Electron Systems. *Phys. Rev.* **1934**, *46*, 618−622.
(33) Dunning, T. H., Jr. Gaussian Basis Sets for Use in Correlated Molecular Calculations. I. The Atoms Boron through Neon and Hydrogen. *J. Chem. Phys.* **1989**, *90*, 1007−1023.
(34) Turbomole, V7.4; A Development of University Karlsruhe and Forschungszentrum Karlsruhe GmbH, 1989−2007; TURBOMOLE GmbH since 2008 (access July 14, 2021).
(35) Hättig, C.; Weigend, F. CC2 Excitation Energy Calculations on Large Molecules Using the Resolution of the Identity Approximation. *J. Chem. Phys.* **2000**, *113*, 5154−5161.
(36) Crespo-Otero, R.; Barbatti, M. Spectrum Simulation and Decomposition with Nuclear Ensemble: Formal Derivation and Application to Benzene, Furan and 2-Phenylfuran. *Theor. Chem. Acc.* **2012**, *131*, No. 1237.
(37) Hillery, M.; O'Connell, R. F.; Scully, M. O.; Wigner, E. P. Distribution Functions in Physics: Fundamentals. *Phys. Rep.* **1984**, *106*, 121−167.
(38) Barbatti, M.; Ruckenbauer, M.; Plasser, F.; Pittner, J.; Granucci, G.; Persico, M.; Lischka, H. Newton-X: A Surface-Hopping Program for Nonadiabatic Molecular Dynamics. *WIREs Comput. Mol. Sci.* **2014**, *4*, 26−33.
(39) Liedl, K. R. Dangers of Counterpoise Corrected Hypersurfaces: Advantages of Basis Set Superposition Improvement. *J. Chem. Phys.* **1998**, *108*, 3199−3204.
(40) OpenMolcas, A Quantum Chemistry Package. https://gitLab.com/Molcas/OpenMolcas (access Sept. 20, 2021).
(41) Belyaev, A. K.; Lasser, C.; Trigila, G. Landau-Zener Type Surface Hopping Algorithms. *J. Chem. Phys.* **2014**, *140*, No. 224108.
(42) Belyaev, A. K.; Domcke, W.; Lasser, C.; Trigila, G. Nonadiabatic Nuclear Dynamics of the Ammonia Cation Studied by Surface Hopping Classical Trajectory Calculations. *J. Chem. Phys.* **2015**, *142*, No. 104307.
(43) Xie, W.; Sapunar, M.; Došlić, N.; Sala, M.; Domcke, W. Assessing the Performance of Trajectory Surface Hopping Methods: Ultrafast Internal Conversion in Pyrazine. *J. Chem. Phys.* **2019**, *150*, No. 154119.
(44) Belyaev, A. K.; Lebedev, O. V. Nonadiabatic Nuclear Dynamics of Atomic Collisions Based on Branching Classical Trajectories. *Phys. Rev. A* **2011**, *84*, No. 014701.
(45) Schwartz, B. J.; Bittner, E. R.; Prezhdo, O. V.; Rossky, P. J. Quantum Decoherence and the Isotope Effect in Condensed Phase Nonadiabatic Molecular Dynamics Simulations. *J. Chem. Phys.* **1996**, *104*, 5942−5955.
(46) Tully, J. C. Molecular Dynamics with Electronic Transitions. *J. Chem. Phys.* **1990**, *93*, 1061−1071.
(47) Crespo-Otero, R.; Barbatti, M. Recent Advances and Perspectives on Nonadiabatic Mixed Quantum-Classical Dynamics. *Chem. Rev.* **2018**, *118*, 7026−7068.
(48) Zobel, J. P.; Nogueira, J. J.; González, L. Finite-Temperature Wigner Phase-Space Sampling and Temperature Effects on the Excited-State Dynamics of 2-Nitronaphtalene. *Phys. Chem. Chem. Phys.* **2019**, *21*, 13906−13915.
(49) Ehrmaier, J.; Rabe, E. J.; Pristash, S. R.; Corp, K. L.; Schlenker, C. W.; Sobolewski, A. L.; Domcke, W. Singlet−Triplet Inversion in Heptazine and in Polymeric Carbon Nitrides. *J. Phys. Chem. A* **2019**, *123*, 8099−8108.

https://doi.org/10.1021/acs.jpca.1c08291
J. Phys. Chem. A 2021, 125, 9917−9931

(50) Ashfold, M. N. R.; King, G. A.; Murdock, D.; Nix, M. G. D.; Oliver, T. A. A.; Sage, A. G. $\pi\sigma^*$ Excited States in Molecular Photochemistry. *Phys. Chem. Chem. Phys.* **2010**, *12*, 1218−1238.
(51) Pios, S.; Huang, X.; Domcke, W. Can Hydrated Electrons Be Produced from Water with Visible Light? *ChemPhotoChem* **2021**, *5*, 680−690.
(52) Buxton, G. V.; Greenstock, C. L.; Helman, W. P.; Ross, A. B. Critical Review of Rate Constants for Reactions of Hydrated Electrons, Hydrogen Atoms and Hydroxyl Radicals ($\cdot OH/\cdot O^-$) in Aqueous Solution. *J. Phys. Chem. Ref. Data* **1988**, *17*, 513−886.
(53) Ehrmaier, J.; Huang, X.; Rabe, E. J.; Corp, K. L.; Schlenker, C. W.; Sobolewski, A. L.; Domcke, W. Molecular Design of Heptazine-Based Photocatalysts: Effect of Substituents on Photocatalytic Efficiency and Photostability. *J. Phys. Chem. A* **2020**, *124*, 3698−3710.

https://doi.org/10.1021/acs.jpca.1c08291
J. Phys. Chem. A 2021, 125, 9917−9931

PCCP

PAPER

Cite this: *Phys. Chem. Chem. Phys.*, 2022, **24**, 15925

Ab initio trajectory surface-hopping dynamics studies of excited-state proton-coupled electron transfer reactions in trianisoleheptazine–phenol complexes†

Xiang Huang and Wolfgang Domcke *

The excited-state proton-coupled electron-transfer (PCET) reaction in hydrogen-bonded complexes of trianisoleheptazine (TAHz), a chromophore related to polymeric carbon nitrides widely used in hydrogen-evolution photocatalysis, with several phenol derivatives were recently studied by Schlenker and coworkers with time-resolved photoluminescence quenching and pump–probe experiments. A pronounced dependence of the PCET reactivity on the electron-donating/electron-withdrawing character of the substituents on phenol was found, with indications of a barrierless or nearly barrierless PCET reaction for the most strongly electron-donating substituent, methoxy. In the present work, the excited-state PCET dynamics was explored with first-principles nonadiabatic dynamics simulations using the TDDFT/ωB97X-D electronic-structure model for two selected complexes, TAHz–phenol and TAHz–methoxyphenol. The qualitative reliability of the TDDFT/ωB97X-D electronic-structure model was assessed by extensive benchmarking of excitation energies and potential-energy profiles against a wave-function-based *ab initio* method, the algebraic-diagrammatic construction of second order (ADC(2)). The nonadiabatic dynamics simulations provide temporally and structurally resolved insights into paradigmatic PCET reactions in TAHz–phenol complexes. The radiationless relaxation of the photo-excited bright $^1\pi\pi^*$ state to the long-lived dark S_1 state of TAHz occurs in less than 100 fs. The ensuing PCET reaction on the adiabatic S_1 surface is faster in TAHz–methoxyphenol complexes than in TAHz–phenol complexes due to a lower H-atom-transfer barrier, as observed in the experiments. The relaxation of the complexes to the electronic ground state is found to occur exclusively *via* PCET within the 250 fs time window covered by the present simulations, confirming the essential role of the hydrogen bond for the fluorescence quenching process. The absolute values of the computed PCET time constants are significantly shorter than those extracted from time-resolved photoluminescence measurements for mixtures of TAHz with phenolic substrates in toluene. The possible origins of this discrepancy are discussed.

Received 16th March 2022,
Accepted 13th June 2022

DOI: 10.1039/d2cp01262f

rsc.li/pccp

1. Introduction

Heptazine (Hz) is the building block of graphitic carbon nitride (g-C_3N_4). This polymeric material has attracted vast attention since the first report of hydrogen evolution from sacrificial electron donors under irradiation with visible light (λ > 420 nm) by Antonietti, Domen and coworkers.[1–4] A second extensively explored field of application of carbon nitrides is the photocatalytic generation of oxidizing radials for waste-water treatment.[5,6] Due to the complexity and structural as well as compositional variability of polymeric carbon nitrides (PCNs), the microscopic reaction mechanisms leading to hydrogen evolution and radical generation are, despite of thousands of publications since 2009, still poorly understood. According to the prevailing paradigm, PCNs are semiconductors in which charge carriers (electrons and holes) are produced by the absorption of light. The electrons are supposed to reduce protons at the solid–liquid interface, while the holes are supposed to oxidize water or other substrate molecules.[2,3,7] However, neither the charge-transport processes in the polymer nor the reactions with substrate molecules were hitherto precisely characterized.

In 2019, Schlenker and coworkers synthesized a molecular Hz derivative, trianisoleheptazine (TAHz), and discovered that this derivative, in contrast to the Hz molecule itself,[8] is

Department of Chemistry, Technical University of Munich, D-85747 Garching, Germany. E-mail: domcke@ch.tum.de

† Electronic supplementary information (ESI) available. See DOI: https://doi.org/10.1039/d2cp01262f

chemically and photochemically highly stable in organic solvents.[9] In aqueous suspension, on the other hand, TAHz exhibits photochemical reactivity. The excited-state lifetime of TAHz is reduced from 287 ns in toluene to 16 ns in aqueous suspension.[9] Moreover, a blue-shifted fluorescence was detected with a time constant of 190 ps and a D/H isotope effect of 2.9, indicating that the excited-state reactivity involves a proton-coupled electron transfer (PCET)[10] reaction with water. The oxidation of water was confirmed by the detection of OH radicals and the evolution of hydrogen was demonstrated with nano-Pt as co-catalyst and triethanolamine (TEOA) as sacrificial electron donor.[9]

A molecular chromophore in aqueous solution thus exhibits the photocatalytic phenomena which usually are associated with the semiconducting properties of bulk PCN materials. This is interesting, because it implies that the basic photochemical mechanisms of water oxidation with PCNs can be explored in a simpler setting, namely for dilute solutions of purified molecular chromophores in neat solvents. In particular, the chromophore and photocatalyst TAHz can thus be applied in low concentrations as appropriate for catalytic reactions, in contrast to the excessive amount of photocatalytic material applied in studies with bulk PCNs, which may obscure important competing reactions, such as irreversible photodamage of the catalyst.[11] However, the solubility of TAHz in liquid water at room temperature is very low, which precludes precise studies of the concentration dependence of the photoreactions with extrapolation to infinite dilution.[9]

To overcome this limitation, Schlenker and coworkers turned to studies of the photochemistry of TAHz with phenol (substituted water) in toluene.[12–14] Both TAHz and phenol (H–PhOH) are soluble in toluene over a wide range of concentrations, allowing the determination of association constants for hydrogen bonding and the exploration of the reaction kinetics. Moreover, the oxidation potential of phenol can be tuned over a wide range by substituents in the *para* position, a fact that has been exploited in earlier systematic studies of excited-state PCET reactions.[15–18] The photoinduced reactivity of TAHz toward phenol and a series of five *para*-substituted phenol derivatives was explored through measurements of ground-state absorption spectra and time-resolved photoluminescence spectra.[12] In addition, association constants, excited-state (S_1) quenching rate constants, kinetic isotope effects and reaction barriers were determined. It was found that the quenching rate of the lowest excited state of the TAHz chromophore in TAHz–phenol complexes is strongly enhanced by electron-donating substituents on phenol, such as MeO, but is reduced by electron-withdrawing substituents, such as CN. With support from *ab initio* electronic-structure calculations, a picture of hydrogen-bond formation and excited-state PCET reactivity of complexes of TAHz with phenolic substrates was developed.[12]

In addition, Schlenker and coworkers were able to demonstrate laser control of the photochemical dynamics in TAHz–phenol complexes by picosecond time-resolved pump-push-probe experiments.[13] Guided by predictions from *ab initio* electronic-structure calculations, the push pulse, delayed by 6 ps from the pump pulse, was chosen to excite TAHz···HOPh–R complexes (the dots denote a hydrogen bond) from the long-lived S_1 state to an S_n state of mixed $\pi\pi^*/n\pi^*$ character, from which a rapid (sub-picosecond) PCET reaction occurred. For substituents R with electron-withdrawing character, the push-induced PCET was recorded as a persistent step-like decrease of the S_1 population. For substituents R with electron-donating character, on the other hand, the step-like decrease of the S_1 population was found to be absent because the S_1 state appears to be depopulated by PCET before the arrival of the push pulse at 6 ps.[13]

The observed ground-state absorption spectra, excited-state photoluminescence spectra and transient absorption pump-probe spectra were found to be strongly dependent on the relative concentrations of the reactants TAHz and R-PhOH in the solvent toluene. The absorption profiles of the TAHz···HOPh–H mixtures in toluene exhibit a single peak which continuously shifts from 365 nm for pure TAHz to 373 nm for a 400 mM concentration of H–PhOH.[12] For photoluminescence measurements, TAHz was dissolved at a concentration of 100 μM and the phenolic substrates were added with concentrations up to 400 mM. For pump–probe measurements, the concentration of TAHz was 50 μM and the phenolic substrates were added in 1 M concentration to enhance the signal-to-noise ratio. The observed peak shift of 0.073 eV of the ground-state absorption spectrum of TAHz is smaller than the computed shift of the excitation energy of the bright $^1\pi\pi^*$ state of TAHz by hydrogen-bond formation with H–PhOH (0.169 eV), which indicates that even at the highest concentration of H–PhOH considered in ref. 12, only part of the TAHz chromophores are hydrogen-bonded to H–PhOH. The measured spectra and rate constants therefore do not represent the properties of a pure ensemble of hydrogen-bonded TAHz···HOPh–R complexes.

The interpretation of these data in terms of specific photochemical reactions therefore requires theoretical support. The information which can be obtained by static *ab initio* electronic-structure calculations, such as reaction energies or reaction barriers, is only indirectly related to the reaction dynamics and the measured data. A more substantial support of the experiments can be provided by first-principles simulations of the photoinduced reaction dynamics. This includes the simulation of the ultrafast nonadiabatic relaxation of the initially populated bright $^1\pi\pi^*$ state of TAHz to the long-lived dark $S_1(\pi\pi^*)$ state and the concurrent or ensuing electron/proton transfer reaction to form the TAHzH···OPh–R radical pair. With this in mind, we performed full-dimensional first-principles simulations of the photochemical reaction dynamics for isolated hydrogen-bonded TAHz–phenol complexes. The initial nuclear geometries and momenta were sampled from thermal Wigner distributions[19–21] which were determined from the Hessians at the ground-state equilibrium geometries of isolated hydrogen-bonded TAHz–phenol complexes. These simulations can provide predictions of the intrinsic time scales of the photoinduced PCET reaction and the branching ration of reactive *vs.* nonreactive deactivation of the TAHz chromophore in hydrogen-bonded complexes. By sampling the initial geometries of the trajectories from a Wigner distribution at the global minimum of the ground-state potential-energy (PE) surface of the TAHz–phenol complexes, the possibility that

other local minima might partially be populated in the liquid phase at room temperature is ignored. The insights obtained by this study should nevertheless be useful for future explorations of the condensed-phase reaction dynamics at various concentrations of the reaction partners.

Even with neglect of the solvent environment, the size of the complexes (at least 44 non-hydrogen atoms) is daunting. First-principles nonadiabatic quantum wave-packet dynamics simulations[22] are impossible in full dimensionality and more approximate quasi-classical surface-hopping (SH) simulation methods[23] have to be employed. The size of the system forces us, moreover, to resort to linear-response time-dependent density functional theory (TDDFT)[24] for the electronic-structure calculations. While TDDFT with various exchange-correlation functionals is very popular and has been shown to provide reasonably accurate vertical excitation energies of organic molecules,[25–27] the TDDFT method is not *a priori* reliable for nuclear geometries which are far from the Franck–Condon region. We therefore performed a careful benchmarking of the accuracy of TDDFT in comparison with a more accurate wave-function-based *ab initio* method, the algebraic-diagrammatic construction of second order, ADC(2).[28–30] The benchmarking was performed for four R–PhOH derivatives (R = H, Cl, CH_3, OCH_3) and three widely employed functionals (CAM-B3LYP,[31] ωB97X[32] and ωB97X-D[33]). CAM-B3LYP and ωB97X are range-separated hybrid GGA functionals and ωB97X-D is a range-separated hybrid meta-GGA functional which includes dispersion corrections. Calculations of the energies of the electronic ground state and excited electronic states for relaxed scans along the PCET reaction coordinate with the ADC(2) method and the ωB97X-D method for TAHz···HOPh–H and TAHz···HOPh–MeO reveal that the ωB97X-D results are quite accurate in the Franck–Condon region of the TAHz···HOPh–R complexes and are at least qualitatively (albeit not quantitatively) accurate along the reaction path to the TAHzH···OPh–R biradical. TDDFT/ωB97X-D dynamics simulations should thus provide a qualitatively reliable picture of the dynamics of the PCET reaction in TAHz···HOPh–R complexes.

The second ingredient which renders statistically converged simulations possible for TAHz···HOPh–R complexes is a pragmatic SH algorithm which is computationally efficient and highly robust when implemented with the ADC(2) or TDDFT methods. The algorithm is based on the well-known Landau–Zener (LZ) formula for nonadiabatic transitions at avoided crossings of one-dimensional potential-energy (PE) functions.[34,35] As shown by Belyaev and Lebedev, the parameters of the LZ formula, which refer to diabatic electronic PE functions, can be extracted from the local adiabatic electronic energies at avoided crossings.[36] In the LZ surface-hopping (LZSH) algorithm, nonadiabatic transitions can occur at minima of energy gaps of neighboring adiabatic electronic states.[37–40] The Belyaev–Lebedev (BL) formula exploits the fact that the nonadiabatic coupling elements near conical intersections (CIs) are completely determined by the local topography of the adiabatic electronic PE surfaces. The computation of potentially singular nonadiabatic coupling elements as wave-function derivatives is thus avoided, which saves computing time and greatly enhances the numerical stability of the algorithm. The accuracy of the LZSH algorithm was benchmarked in comparison with the widely used fewest-switches SH (FSSH) algorithm of Tully[41] and in comparison with exact quantum dynamics calculations for multi-dimensional models of CIs.[38,39,42]

The goal of this work is the elaboration of a qualitative *ab initio* based picture of the reaction dynamics which is initiated by the photoexcitation of TAHz in hydrogen-bonded complexes with phenolic substrates. Due to the high computational cost, the simulations were restricted to two representative exemplars, TAHz···HOPh–H and TAHz···HOPh–MeO. Previous static *ab initio* calculations for Hz–phenol complexes indicated that the PCET reaction barrier for MeO–PhOH is substantially lower than for H–PhOH.[12] Herein, we explore to what extent the differences in the topography of the excited-state PE surfaces of TAHz–phenol complexes are reflected in the time scales and branching rations of the photoinduced PCET reactions.

2. Computational methods

2.1. Benchmarking TDDFT

To test the accuracy of different exchange-correlation functionals, we first performed calculations of vertical excitation energies of TAHz···HOPh–R complexes with R = H, Cl, Me, MeO. The ground-state equilibrium geometries of the four complexes were optimized with C_s symmetry constraint (R–PhOH perpendicular to the molecular plane of TAHz) with the Møller–Plesset (MP2) method[43] and the cc-pVDZ basis set.[44] The C_s symmetry constraint allows us to distinguish the CT state from locally excited (LE) states of TAHz in the FC region. Without symmetry constraints, the CT state is highly mixed with the LE states in the FC region in some of the complexes. At these S_0 equilibrium geometries, the vertical excitation energies were computed with the ADC(2) method and with the TDDFT method, using the CAM-B3LYP, ωB97X and ωB97X-D functionals.

To test the performance of TDDFT for the PCET reaction in TAHz–phenol complexes, energy profiles were computed along relaxed scans for H-atom transfer for two representative complexes, TAHz···HOPh–H and TAHz···HOPh–MeO. Along the H-atom transfer coordinate, the CT state is dramatically stabilized and behaves distinctly from the LE states. Therefore, these calculations could be performed without the C_s symmetry constraint which allows the phenol molecules to adjust to minimize steric repulsion effects.

To generate the relaxed scans, the bond length of the OH group of phenol, R_{OH}, was varied between 0.8 and 2.0 Å, while the energy of a selected electronic state was minimized with respect to all other internal coordinates of the TAHz···HOPh–H and TAHz···HOPh–MeO complexes. As in previous studies,[12,45] the energy of the S_0 state was minimized for short OH distances (0.8 Å $\leq R_{OH} \leq$ 1.3 Å), while for R_{OH} in the range from 1.3 Å to 2.0 Å, the energy of the charge-transfer (CT) state (from R-PhOH to TAHz) was minimized. The former range corresponds to the Franck–Condon (FC) region of the TAHz···HOPh–R complex, while the latter range corresponds to the TAHzH···OPh–R biradical. The equilibrium geometries of the electronic ground

state of these complexes were optimized with the DFT/ωB97X-D method and the def2-SV(P) basis set.[46] The excited-state geometry optimizations were performed with the TDDFT/ωB97X-D method and the def2-SV(P) basis set. Vertical excitation energies were computed at these geometries with the ADC(2) method and the TDDFT/ωB97X-D method, respectively. The TURBOMOLE program package[46] was used for the MP2, ADC(2), DFT and TDDFT calculations.

2.2. Absorption spectra and nonadiabatic dynamics simulations

The absorption spectra of the TAHz···HOPh–H and TAHz···HOPh–MeO complexes were simulated with the nuclear ensemble method[23,47] at the DFT/TDDFT level with the ωB97X-D functional. For both complexes, 2000 phase-space points were sampled from the ground-state harmonic Wigner distribution at room temperature (300 K).[19,20] The vertical excitation energies and oscillator strengths of the lowest five excited electronic states were calculated with TDDFT. The line spectra were convoluted with a Gaussian function of 0.05 eV full width at half maximum (FWHM). The nuclear ensemble spectra were calculated with the NEWTON-X package.[48]

The initial coordinates which mainly control the photo-induced PCET reaction are the OH bond length (the H-atom transfer coordinate) and the ON bond length (the donor–acceptor distance of the H-atom transfer). The distributions of these coordinates in the ground-state thermal Wigner sample are displayed in Fig. S1 in the ESI,† for the TAHz···HOPh–H complex. The figure shows that Wigner sampling generates a well-behaved and physically reasonable distribution of these critical bond lengths.

We consider resonant photoexcitation by a pulsed laser with a spectral width of about 0.1 eV. The excitation process is modelled by stochastically selecting phase-space points from the ground-state thermal Wigner distribution. 200 phase-space points were randomly selected from a 0.1 eV wide slice at the maximum of the absorption spectrum. The initial population probability of the adiabatic excited electronic states is stochastically sampled from the oscillator strengths. The nominally dark $^1n\pi^*$ states and the CT state can gain intensity by vibronic mixing with the bright $^1\pi\pi^*$ states (Herzberg–Teller effect). The character of the excited states at the ground-state equilibrium geometry is specified in Table 3. This character is not conserved when adiabatic electronic PE surfaces cross in nuclear coordinate space.

In nonadiabatic SH simulations, the population probability of adiabatic electronic states is determined. The adiabatic populations can only approximately be associated in certain limits with the populations of diabatic electronic states which preserve the character ($^1n\pi^*$, $^1\pi\pi^*$, CT) of the electronic states. An explicit diabatization of the electronic states is challenging in the present application due to the complexity of the electronic structure of the TAHz···R–PhOH complexes. There are five aromatic entities involved (Hz, three anisoles and PhOH) within which local electronic excitations can occur and between which CT excitations can occur. This complexity prevents a pragmatic and computationally feasible diabatization of the adiabatic electronic states in terms of LE states and CT states.

The 200 selected trajectories were propagated up to 250 fs with the on-the-fly LZSH algorithm.[39] In the LZSH algorithm, SH events occur at minima of energy gaps of neighboring adiabatic electronic states and are restricted to next-neighbour electronic states. Hopping events are stochastically sampled from the hopping probabilities computed by the BL formula.[36]

The restriction of surface hoppings to neighboring states in the LZSH algorithm can be exploited to achieve further substantial savings of computing time in computationally demanding applications. The initially populated electronic states in polyatomic molecules are often higher excited states. The populations of these states typically relax to the lowest excited state (S_1) within tens of femtoseconds. Therefore, the energies of the higher electronic states need not be computed beyond the first few tens of femtoseconds, which significantly reduces the computational cost especially for large systems.[49] It is emphasized that at each time step the next higher electronic state to the currently occupied electronic state is included in the algorithm. Hopping events upwards in energy are therefore not suppressed and no artificial bias toward fast relaxation of the populations to the lowest electronic states is introduced. In the vicinity of avoided crossings involving the currently populated state, the default time step of 0.5 fs is reduced to 0.1 fs to ensure accurate numerical evaluation of the LZ transition probability. The code is a development version of the SH code developed by Doslic and coworkers[50] which is interfaced with TURBOMOLE.[46]

Owing to their single-reference character, the ADC(2) and TDDFT methods cannot reliably describe the topography of the PE surfaces in the vicinity of S_1–S_0 CIs.[51,52] The branching ratios of reaction channels at S_1–S_0 CIs therefore cannot be predicted with these single-reference electronic-structure methods. In the present simulations, an S_1–S_0 energy gap smaller than 0.2 eV is counted as a CI and the population is assigned to the S_0 state, which is common practice in nonadiabatic dynamics simulations with single-reference methods.[23] Alternatively, trajectories can hop from the S_1 state to the S_0 state at energy-gap minima which are larger than 0.2 eV. Once a trajectory has arrived in the S_0 state, it is terminated.

The observables of the SH simulations are the time-dependent populations of the adiabatic electronic states. In addition, we evaluated the statistical distributions of the H-atom transfer coordinate (R_{OH}) and the donor–acceptor distance (R_{ON}) over all trajectories and the distribution of locations of S_1–S_0 CIs in R_{OH}–R_{ON} space.

3. Results

3.1. Benchmarking TDDFT functionals for vertical excitation energies

In the context of an earlier study, the ground-state equilibrium geometries of the TAHz···HOPh–R (R = H, Cl, Me, MeO) complexes were optimized with the MP2 method and C_s symmetry constraint.[12] These structures are shown in Fig. S2 in the ESI.† The phenol molecule is perpendicular to the molecular

plane of TAHz and positioned symmetrically with respect to the Hz core.

The vertical excitation energies of the lowest eight excited states of the four complexes were computed with the ADC(2) method and with the TDDFT method, using the three functionals CAM-B3LYP, ωB97X and ωB97X-D, at MP2/cc-pVDZ optimized ground-state equilibrium geometries of C_s symmetry (see Section 2.1). Table 1 lists the ADC(2) excitation energies and oscillator strengths of the four complexes, while Table 2 lists the TDDFT/ωB97X-D excitation energies and oscillator strengths. The excitation energies and oscillator strengths computed with all three TDDFT functionals for the four complexes are listed in Table S1 (ESI†). All data are displayed graphically in Fig. 1.

The ADC(2) method (Table 1 and Fig. 1a) predicts the energy of the lowest excited state at 2.65 eV for all four complexes. The experimental estimate for the excitation energy of the S_1 state of TAHz in toluene is 2.7 eV.[9] The energy of this state is not affected by hydrogen bonding with phenols. The next higher states are the bright LE $^1\pi\pi^*$ states at 3.45 eV and 3.62 eV in the TAHz···HOPh–H complex. These states are derived from the degenerate $^1\pi\pi^*$ state of free TAHz at 3.62 eV. These states contribute to the strongly allowed band in the experimental spectrum of TAHz in toluene which peaks at 365 nm (3.4 eV). It should be noted that the lowest bright $^1\pi\pi^*$ states of TAHz are considerably lower in energy than the bright $^1\pi\pi^*$ state of Hz, which is located at 4.43 eV at the ADC(2) level. This lowering of the energies of the bright $^1\pi\pi^*$ states in TAHz compared to Hz results from the mixing of the π and π* orbitals of Hz with the orbitals of the three anisole groups. The fourth $^1\pi\pi^*$ state at 4.12 eV in TAHz···HOPh–H (4.17 eV in free TAHz) also is a bright state.

There exist three LE states of $^1n\pi^*$ character between the third and the fourth $^1\pi\pi^*$ states at the ADC(2) level in all four TAHz···HOPh–R complexes, see Table 1 and Fig. 1a. These states arise from transitions from n orbitals to the lowest unoccupied orbital (LUMO) of TAHz. The experimental absorption spectrum of the TAHz–phenol complex in toluene exhibits two weak transitions slightly below the onset of the absorption of the lowest bright $^1\pi\pi^*$ state, while ADC(2) places the three $^1n\pi^*$ state above the lowest two bright $^1\pi\pi^*$ states. Apart from this deficiency, the excitation spectrum predicted by the ADC(2) method is in very good agreement with the experimental data. As Fig. 1 shows, the energies of all locally excited states of the TAHz···HOPh–R

Table 1 Vertical excitation energies (in eV) and oscillator strengths (in parentheses) of the lowest eight singlet excited states of the TAHz···HOPh–R (R = H, Cl, Me, MeO) complexes computed with the ADC(2)/cc-pVDZ method at MP2/cc-pVDZ ground-state equilibrium geometries of C_s symmetry. The CT state is marked bold

State	TAHz···HOPh–H	State	TAHz···HOPh–Cl
S_1 (ππ*)	2.65 (0.003)	S_1 (ππ*)	2.65 (0.004)
S_2 (ππ*)	3.45 (1.117)	S_2 (ππ*)	3.45 (1.112)
S_3 (ππ*)	3.62 (0.793)	S_3 (ππ*)	3.60 (0.802)
S_4 (CT)	**3.63 (0.000)**	**S_4 (CT)**	**3.64 (0.000)**
S_5 (nπ*)	3.70 (0.000)	S_5 (nπ*)	3.70 (0.000)
S_6 (nπ*)	3.78 (0.000)	S_6 (nπ*)	3.78 (0.001)
S_7 (nπ*)	3.87 (0.002)	S_7 (nπ*)	3.89 (0.003)
S_8 (ππ*)	4.12 (0.578)	S_8 (ππ*)	4.11 (0.567)
State	**TAHz···HOPh-Me**	**State**	**TAHz···HOPh–MeO**
S_1 (ππ*)	2.64 (0.003)	S_1 (ππ*)	2.64 (0.003)
S_2 (CT)	**3.43 (0.065)**	**S_2 (CT)**	**3.09 (0.001)**
S_3 (ππ*)	3.46 (1.049)	S_3 (ππ*)	3.46 (1.112)
S_4 (ππ*)	3.62 (0.791)	S_4 (ππ*)	3.62 (0.792)
S_5 (nπ*)	3.69 (0.000)	S_5 (nπ*)	3.69 (0.000)
S_6 (nπ*)	3.77 (0.000)	S_6 (nπ*)	3.77 (0.000)
S_7 (nπ*)	3.87 (0.002)	S_7 (nπ*)	3.87 (0.001)
S_8 (ππ*)	4.12 (0.580)	S_8 (CT)	3.99 (0.042)

Table 2 Vertical excitation energies (in eV) and oscillator strengths (in parentheses) of the lowest eight singlet excited states of the TAHz···HOPh–R (R = H, Cl, Me, MeO) complexes computed at MP2/cc-pVDZ ground-state equilibrium geometries of C_s symmetry at the TDDFT/ωB97X-D/def2-SV(P) level. The CT state is marked bold

State	TAHz···HOPh–H	State	TAHz···HOPh–Cl
S_1 (ππ*)	3.23 (0.004)	S_1 (ππ*)	3.23 (0.005)
S_2 (ππ*)	3.95 (1.436)	S_2 (ππ*)	3.94 (1.432)
S_3 (CT)	**3.99 (0.001)**	**S_3 (CT)**	**4.02 (0.000)**
S_4 (ππ*)	4.09 (1.146)	S_4 (ππ*)	4.08 (1.156)
S_5 (nπ*)	4.13 (0.000)	S_5 (nπ*)	4.12 (0.000)
S_6 (nπ*)	4.23 (0.000)	S_6 (nπ*)	4.23 (0.001)
S_7 (nπ*)	4.32 (0.001)	S_7 (nπ*)	4.33 (0.002)
S_8 (ππ*)	4.56 (0.275)	S_8 (ππ*)	4.55 (0.270)
State	**TAHz···HOPh-Me**	**State**	**TAHz···HOPh–MeO**
S_1 (ππ*)	3.23 (0.004)	S_1 (ππ*)	3.22 (0.004)
S_2 (CT)	**3.81 (0.002)**	**S_2 (CT)**	**3.56 (0.001)**
S_3 (ππ*)	3.95 (1.430)	S_3 (ππ*)	3.95 (1.429)
S_4 (ππ*)	4.10 (1.145)	S_4 (ππ*)	4.10 (1.145)
S_5 (nπ*)	4.13 (0.000)	S_5 (nπ*)	4.13 (0.000)
S_6 (nπ*)	4.22 (0.000)	S_6 (nπ*)	4.22 (0.000)
S_7 (nπ*)	4.32 (0.001)	S_7 (nπ*)	4.32 (0.000)
S_8 (ππ*)	4.56 (0.291)	S_8 (CT)	4.39 (0.024)

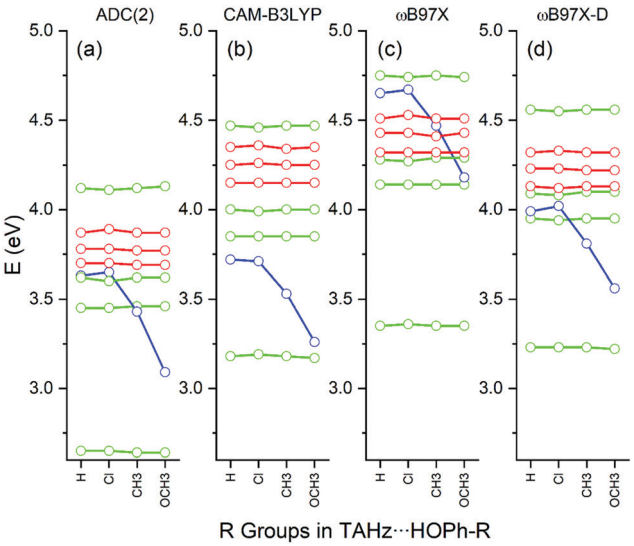

Fig. 1 Vertical excitation energies of TAHz···HOPh–R (R = H, Cl, Me, MeO) at MP2/cc-pVDZ optimized ground-state equilibrium geometries of C_s symmetry, computed with the ADC(2) (a) and TDDFT (b–d) methods. nπ* states are shown in red, ππ* states in green and the CT state in blue.

Table 3 Vertical excitation energies (in eV) and oscillator strengths (in parentheses) of the lowest eight singlet states of the TAHz···HOPh–H and TAHz···HOPh–MeO complexes at the TDDFT/ωB97X-D/def2-SV(P) level at DFT-optimized ground-state equilibrium geometries of C_1 symmetry. The assigned characters of transitions refer to planar TAHz geometry. The CT state is marked bold

States	TAHz···HOPh–H	States	TAHz···HOPh–MeO
S_1 (ππ*)	3.25 (0.01)	S_1 (ππ*)	3.25 (0.00)
S_2 (ππ*)	4.02 (1.37)	**S_2 (CT)**	**3.65 (0.00)**
S_3 (ππ*)	4.03 (1.43)	S_3 (ππ*)	4.01 (1.30)
S_4 (nπ*)	4.04 (0.02)	S_4 (ππ*)	4.03 (1.30)
S_5 (nπ*)	4.10 (0.00)	S_5 (nπ*)	4.04 (0.21)
S_6 (CT)	**4.21 (0.00)**	S_6 (nπ*)	4.10 (0.00)
S_7 (nπ*)	4.25 (0.01)	S_7 (nπ*)	4.25 (0.00)
S_8 (ππ*)	4.49 (0.02)	S_8 (nπ*)	4.49 (0.02)

complexes exhibit a negligible dependence on the substituent R on PhOH.

The situation is very different for the excitation energy of the intermolecular (from R-PhOH to TAHz) CT state. The CT state is accidentally degenerate with the third locally excited ^{1}ππ* state in the TAHz···HOPh–H complex at the ADC(2) level. The substituent Cl slightly increases the energy of the CT state, while the substituents Me and MeO strongly stabilize the energy of the CT state. The excitation energy of the CT state varies between 3.64 eV for Cl–PhOH and 3.09 eV for MeO–PhOH, see Fig. 1a and Table 1.

Panels b, c, d in Fig. 1 and Table S1 (ESI†) present the excitation energies of the four TAHz···HOPh–R complexes obtained with TDDFT and the CAM-B3LYP, ωB97X and ωB97X-D functionals, respectively. All three functionals overestimate the excitation energies of the locally excited states of TAHz. Notably, the energy of the low-lying S_1(ππ*) state is overestimated with TDDFT by up to 0.7 eV. The relative ordering of the LE states, however, is the same as obtained with ADC(2). For the TAHz···HOPh–H complex, the CT state is located too low with CAM-B3LYP relative to the locally excited states and considerably too high with ωB97X. The ωB97X-D functional predicts the best state ordering in comparison with ADC(2).

The pronounced dependence of the energy of the CT state on the substituent R is well reproduced by the TDDFT calculations (see Fig. 1 and Table 2). All three functionals correctly predict the strong stabilization of the CT state by electron-donating substituents (Me, MeO) on PhOH. Overall, the TDDFT results with the ωB97X-D functional are closest to the ADC(2) results as far as the energy of the CT state relative to the energies of the locally excited states is concerned. The ωB97X-D functional was therefore selected for the nonadiabatic dynamics explorations of the photochemistry of TAHz···HOPh–R complexes.

3.2. Benchmarking TDDFT functionals for the PCET reaction

Since the computing resources required for the calculation of relaxed scans for TAHz···HOPh–R complexes are substantial, this benchmarking was performed for only two complexes, TAHz···HOPh–H and TAHz···HOPh–MeO. The ground-state equilibrium geometries of these complexes optimized with DFT/ωB97X-D without symmetry constraints are displayed in Fig. 2. The phenyl ring is oriented approximately perpendicular to the molecular plane of TAHz and is slightly tilted towards one of the anisole substituents on the Hz core. The predicted hydrogen-bond lengths are 2.05 Å for H–PhOH and 2.02 Å for MeO–PhOH.

The vertical excitation energies of the lowest eight excited states of the two complexes calculated with TDDFT/ωB97X-D at DFT-optimized ground-state equilibrium geometries without symmetry constraints are listed in Table 3. The relaxation of the ground-state equilibrium geometry from C_s to C_1 symmetry results in minor changes of the excitation energies of the locally excited states (less than 0.1 eV). The energy of the CT state is more sensitive, with a shift of ≈0.2 eV in TAHz···HOPh–MeO.

Fig. 3 shows the energy profiles of the relaxed scan along the H-atom transfer coordinate from H–PhOH to TAHz computed with the ADC(2) and TDDFT methods (see Section 2.1 for the construction of the relaxed scan). The PE functions to the left of

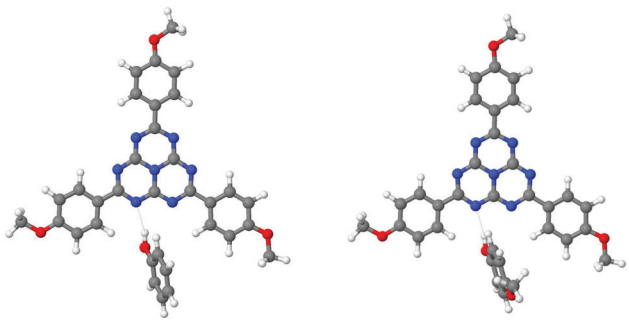

Fig. 2 Ground-state equilibrium geometries of TAHz···HOPh–H (left) and TAHz···HOPh–MeO (right) computed at the DFT/ωB97X-D/def2-SV(P) level. The hydrogen bond lengths are 2.05 Å (left) and 2.02 Å (right). The NO bond lengths are 2.98 Å (left) and 2.99 Å (right).

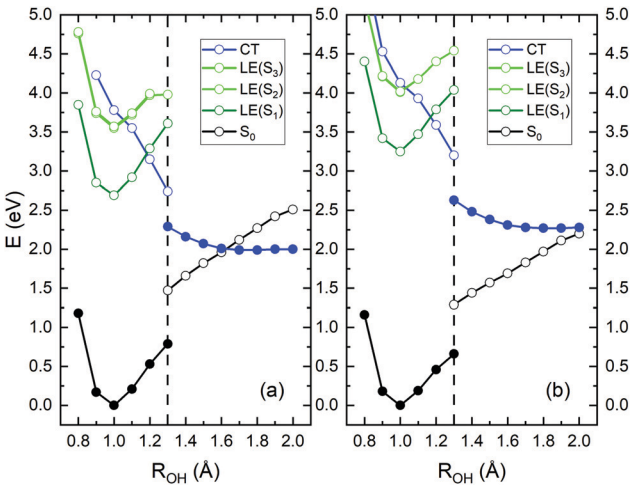

Fig. 3 Relaxed scan along the H-atom transfer coordinate R_{OH} for the TAHz···HOPh–H complex, computed with the ADC(2) method (a) and the TDDFT/ωB97X-D method (b). Solid symbols indicate the electronic state for which the nuclear geometry was optimized. Hollow symbols indicate energies which were computed at the optimized geometry of a different electronic state. The color code is given in the insets.

the broken vertical line (0.8 Å ≤ R_{OH} ≤ 1.3 Å) represent the FC region of the TAHz···HOPh–H complex. The PE functions to the right of the broken vertical line (R_{OH} ≥ 1.3 Å) represent the TAHzH···OPh–H biradical. To the left of the broken line, the nuclear geometry is optimized in the S_0 state. To the right of the broken line, the energy is optimized in the lowest CT state. Full circles in Fig. 3 indicate that the nuclear geometry was optimized in this state. Open circles denote energies of other electronic states calculated at the nuclear geometries indicated by the full circles. For clarity, the PE functions of the $^1n\pi^*$ states are omitted. In the FC region, the energies of the S_0 state (black), the lowest two locally excited $^1\pi\pi^*$ states (green) and the lowest CT state (blue) are shown. In the biradicalic region, the energy of the closed-shell state (black) and the lowest biradicalic state (blue) are shown (the CT state becomes the biradicalic state by the transfer of the proton which neutralizes the electronic charge separation).

The ADC(2) PE functions are displayed in Fig. 3a. In the FC region, the PE functions of the two locally excited $^1\pi\pi^*$ states are essentially parallel to the PE function of the ground state. The PE function of the CT state, on the other hand, is strongly stabilized by the transfer of the proton from H–PhOH to TAHz. The CT state becomes the lowest excited state at R_{OH} = 1.2 Å. For R_{OH} ≥ 1.3 Å, the optimized energy of the CT decreases further and crosses the energy of the closed-shell state (calculated at the optimized geometries of the CT state) near R_{OH} = 1.6 Å. The open-shell biradicalic state becomes the electronic ground state of the complex. The energy minimum of the biradical is about 2.0 eV above the energy minimum of the closed-shell state.

The corresponding results obtained with TDDFT/ωB97X-D are shown in Fig. 3b. The PE functions in the FC region are well described by TDDFT, apart from a blue-shift of all excitation energies. The energy profile of the CT state in the biradicalic region also exhibits a qualitatively correct behaviour, but the energy is about 0.5 eV higher than the energy predicted by ADC(2). As a consequence, the crossing of the energy of the biradicalic state with the energy of the closed-shell state occurs at a larger bond length (R_{OH} ≈ 2.0 Å) than predicted by ADC(2).

The corresponding relaxed scans obtained for TAHz···HOPh–MeO are displayed in Fig. 4. The ADC(2) results (Fig. 4a) show that the MeO substituent on PhOH lowers the energy of the CT state relative to the energies of the locally excited states in the FC region (as discussed above) as well as in the biradicalic region. At the ADC(2) level, the crossing of the energy of the CT state with the energy of the closed-shell state occurs at an OH distance of 1.4 Å, ≈0.2 Å shorter than for TAHz···HOPh–H. The TDDFT/ωB97X-D calculation reproduces this trend. The crossing of the energy of the CT state with the energy of the closed-shell state is found at R_{OH} ≈ 1.7 Å, ≈0.3 Å shorter than for TAHz···HOPh–H.

Overall, we conclude from these benchmarking studies that TDDFT with the ωB97X-D functional provides a qualitatively correct description of the excited states in the FC region of the four TAHz–phenol complexes. It also yields qualitatively correct PE profiles for the excited-state H-atom transfer reaction. The TDDFT/ωB97X-D electronic-structure model was therefore chosen for the on-the-fly nonadiabatic dynamics simulations of the PCET reaction in TAHz–phenol complexes.

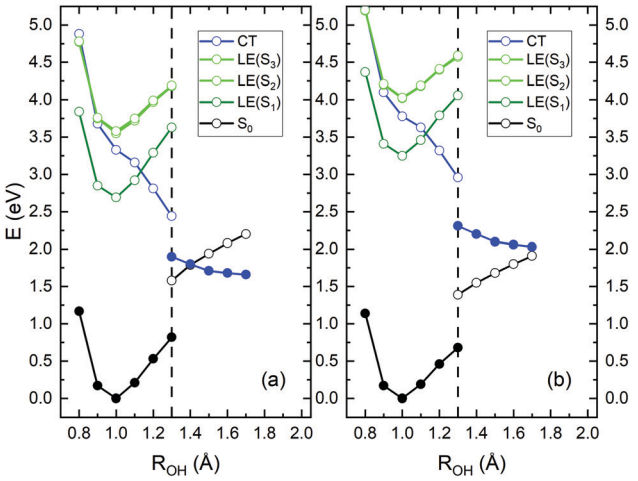

Fig. 4 Relaxed scan along the H-atom transfer coordinate R_{OH} for the TAHz···HOPh–MeO complex, computed with the ADC(2) method (a) and the TDDFT/ωB97X-D method (b). Solid symbols indicate the electronic state for which the nuclear geometry was optimized. Hollow symbols indicate energies which were computed at the optimized geometry of a different electronic state. The color code is given in the insets.

3.3. Absorption spectra of TAHz···HOPh–H and TAHz···HOPh–MeO

The absorption spectra of TAHz···HOPh–H and TAHz···HOPh–MeO simulated with the nuclear ensemble method[23] at the TDDT/ωB97X-D level at room temperature (300 K) are shown in Fig. 5. The stick spectra represent the computed transition energies and oscillator strengths. The envelope shows the convolution with a Gaussian of 0.05 eV FWMH. For both systems, the spectrum peaks at 320 nm (3.87 eV). The experimental spectrum of a solution of 100 μM TAHz and 400 mM H–PhOH in toluene peaks at 373 nm (3.33 eV). The blue-shift of the simulated spectra compared to experiment of about 0.6 eV reflects the overestimation of vertical excitation energies by TDDFT discussed above. Two bright electronic states contribute to the absorption band, see Table 3. The high-energy flank and to a lesser extent the low-energy flank of the TAHz···HOPh–MeO spectrum exhibit a slight red-shift relative to the TAHz···HOPh–H spectrum. Inspection of Table 3 reveals that this shift is not due to a red-shift of the vertical excitation energies. The mixing of the bright $^1\pi\pi^*$ states with the CT state, which is at lower energy in TAHz···HOPh–MeO, may be responsible for this effect.

3.4. Simulation of the photochemical dynamics

3.4.1. Time-evolution of electronic population probabilities. The time-dependent population probabilities of the adiabatic electronic states of TAHz···HOPh–H up to 250 fs are shown in Fig. 6a. The excitation at t = 0 populates the nominally bright states S_2 and S_3 with probabilities of 0.17 and 0.42, respectively. The $^1n\pi^*$ states are populated with probabilities of 0.30 and 0.19, respectively, by intensity borrowing from the diabatic $^1\pi\pi^*$ states. The S_1 state and the CT state (S_6) are not populated at t = 0.

Fig. 6a reveals that the populations of the S_3, S_4 and S_5 states decay on a time scale of less than 50 fs. The population of the S_2

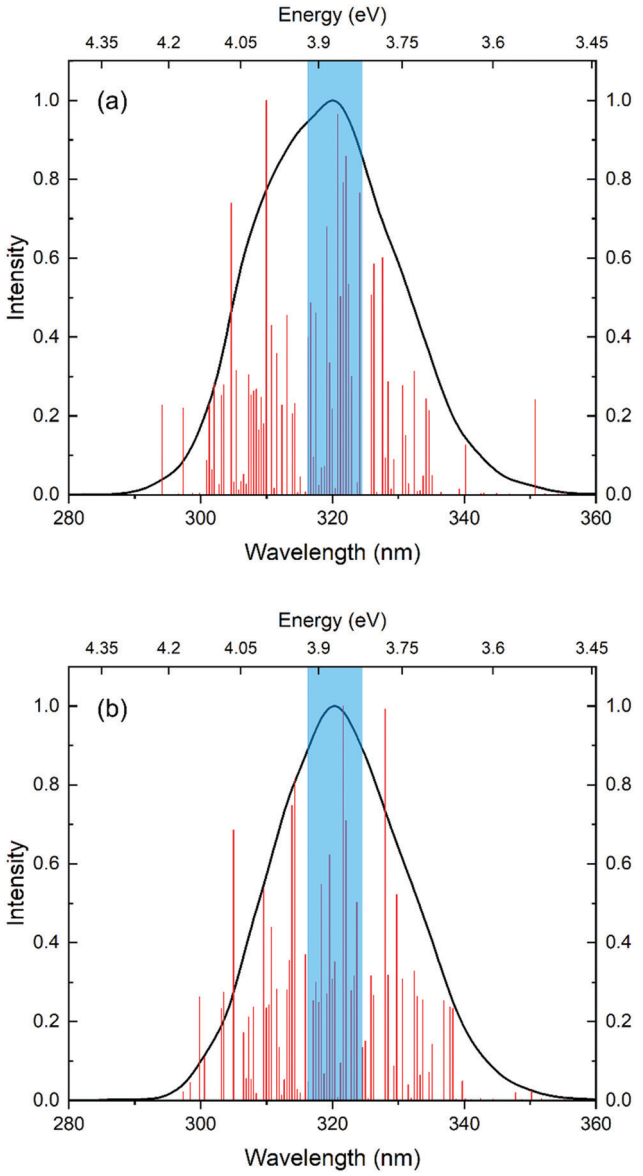

Fig. 5 Simulated absorption spectra of TAHz···HOPh–H (a) and TAHz···HOPh–MeO (b) complexes at room temperature (300 K). The red sticks represent the computed transition energies and oscillator strengths. The envelope shows the convolution with a Gaussian of 0.05 eV FWMH. The blue-shaded area indicates the 0.1 eV-wide energy window at the absorption maximum from which the initial conditions for the excited-state dynamics simulations were selected.

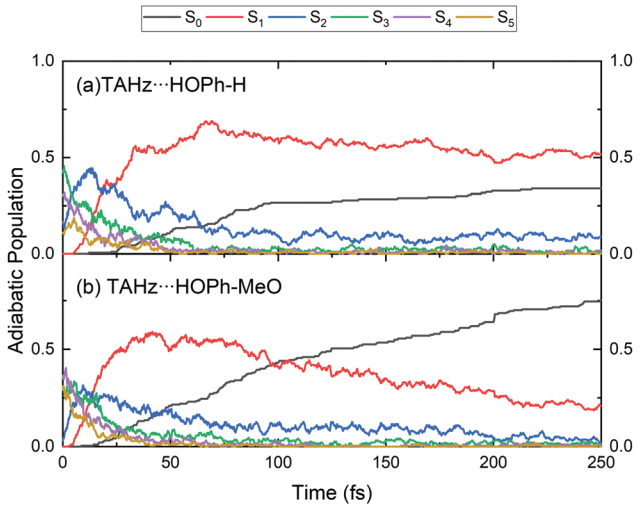

Fig. 6 Time-dependent population probabilities of adiabatic electronic states for the TAHz···HOPh–H (a) and TAHz···HOPh–MeO (b) complexes up to 250 fs, computed with the TDDFT/ωB97X-D method. The color code is given at the top.

state (blue), on the other hand, increases within the first 10 fs. After 10 fs, the S_2 population also decays and the population of the S_1 state increases on a time scale of about 50 fs. The population of the S_0 state (which is the closed-shell state for small R_{OH} and the open-shell biradicalic state for large R_{OH}) increases more slowly on a time scale of about 200 fs. At the termination of the simulation (250 fs), 50% of the population are in the S_1 state and 37% are in the S_0 state.

The lifetime of the S_1 population of the TAHz···HOPh–H complex is estimated as 751 fs (see Fig. S3 of the ESI†). The S_0 state is populated by trajectories which hop to the S_0 state or terminate at S_1–S_0 CIs (see Section 2.2). At all these CIs, the H-atom of phenol has been transferred to TAHz, that is, these CIs are accessed by PCET. No S_1–S_0 CIs with short OH distances are detected by the simulation, that is, no evidence for internal conversion processes driven by other reaction coordinates, such as out-of-plane deformations of the Hz core or torsions of the anisole groups, is found by the simulations within 250 fs.

The adiabatic electronic population dynamics of the TAHz···HOPh–MeO complex is presented in Fig. 6b. In this case, the S_3, S_4 and S_5 states are populated at $t = 0$ with probabilities of 0.27, 0.15, 0.15, respectively. The S_2 population grows rapidly and attains a maximum of about 0.25 at $t = 10$ fs. This maximum of the S_2 population is significantly lower than in the TAHz···HOPh–H complex. The population of the S_1 state increases more rapidly than in TAHz···HOPh–H and attains a maximum at $t \approx 40$ fs. Beyond 50 fs, the S_1 population decays faster than in TAHz···HOPh and the S_0 population grows faster, attaining a value of 0.75 at $t = 250$ fs. The S_1 lifetime is estimated as 194 fs (see Fig. S3 in the ESI†), significantly shorter than in TAHz···HOPh–H. The geometries of nearly all S_1–S_0 CIs encountered by the trajectories exhibit large OH distances, that is, they correspond to biradicalic species.

3.4.2. Two-dimensional dynamic map on the S_1 PE surface. To visualize the essential features of the PCET reaction dynamics on the S_1 PE surface, we monitor the H-atom transfer coordinate R_{OH} and the donor–acceptor distance R_{ON} for all trajectories propagating in the S_1 state in time steps of 0.5 fs. We also monitor the positions of the encountered S_1–S_0 CIs in the two-dimensional R_{OH}–R_{ON} space. The PE of each trajectory is color-coded on a scale varying from dark blue for high PE ($\approx$5.0 eV) to red for low PE ($\approx$1.0 eV). Since the energy of each trajectory is conserved, low PEs imply high kinetic energies.

The two-dimensional dynamic map for TAHz···HOPh–H is displayed in Fig. 7. The distribution of trajectories located at $R_{OH} \approx 1.0$ Å and 4.3 Å $> R_{ON} >$ 2.5 Å represents the dynamics

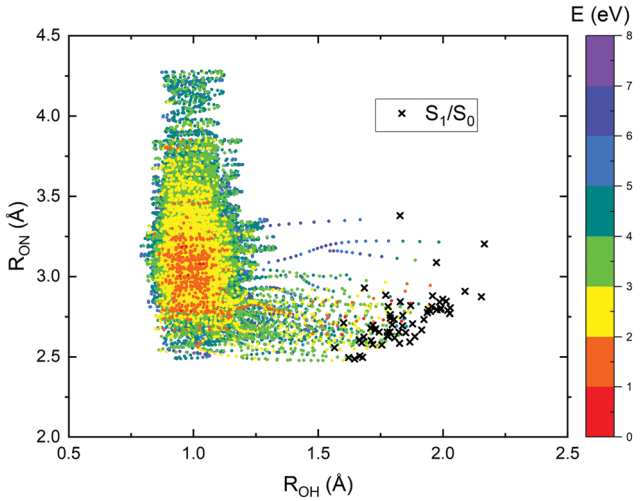

Fig. 7 Dynamic map of trajectories on the S_1 PE surface of the TAHz···HOPh–H complex. The color code gives the electronic PE. The crosses denote locations of S_1–S_0 CIs.

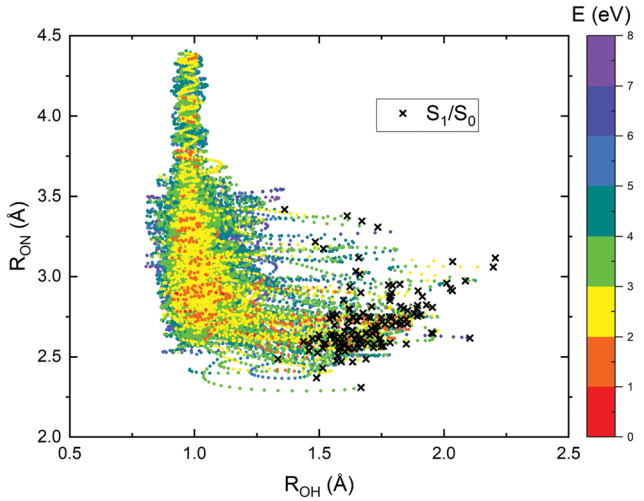

Fig. 8 Dynamic map of trajectories on the S_1 PE surface of the TAHz···HOPh–MeO complex. The color code gives the electronic PE. The crosses denote locations of S_1–S_0 CIs.

prior to the H-atom transfer from H–PhOH to TAHz. Most trajectories enter the S_1 PE surface at short R_{OH} ($\approx$1.0 Å) and long R_{ON} (4.3 Å > R_{ON} > 3.5 Å). The color change from green to yellow to red illustrates the intra-state vibrational relaxation (IVR) process on the S_1 PE surface, that is, the conversion of electronic PE to vibrational energy. Most of the trajectories are trapped in this well of the PE surface and relax toward its local minimum. The distribution of trajectories with small R_{ON} ($\approx$2.7 Å) and large R_{OH} (1.3 < R_{OH} < 2.2 Å) represents proton-transferred species in the CT region of the S_1 PE surface, that is, biradicalic species. Very few H-atom transfer processes occur quickly with high PE (blue). The vast majority of trajectories dissipates electronic PE in the well of the locally excited S_1 state before the H-atom transfer reaction takes place. The bimodal distribution qualitatively maps the two wells of the S_1 PE surface which are separated by a low barrier. It can be seen that the majority of barrier crossings occur at intermediate PE energies (3.0–4.0 eV, green color). After the H-atom transfer, many of the trajectories encounter S_1–S_0 CIs (crosses) at which the dynamics terminates in the present simulations. Barrier-tunnelling by H-atoms is not taken into account in the classical trajectory calculations, but should be a minor effect on the time scale of 250 fs. The population trapped near the minimum of the LE S_1 state may give rise to H-atom transfer *via* tunnelling on time scales which are beyond the range which can be covered with *ab initio* on-the-fly trajectory simulations. We remark that attempts to locate the saddle point of the PCET reaction by geometry optimization at the ADC(2) level were unsuccessful due to the size of the system and the cost of these calculations.

The two-dimensional dynamic map of the TAHz···HOPh–MeO complex is shown in Fig. 8. It is overall similar to the dynamic map of TAHz···HOPh–H, but exhibits also distinctive differences. The trajectories enter the S_1 surface at large R_{ON} with a much narrower distribution in R_{OH} than in TAHz···HOPh–H. This reflects the fact that the transient population of the S_2 state, which has a significant admixture of the diabatic CT state and therefore drives elongation of R_{OH}, is lower than in TAHz···HOPh–H, see Fig. 6. The trajectories of the TAHz···HOPh–MeO complex enter the S_1 surface more directly from the initially populated S_3–S_5 states, resulting in less elongation in R_{OH}. The IVR in the LE well of the S_1 surface is less pronounced than in TAHz···HOPh and more H-atom transfer reactions occur at intermediate R_{ON}. These features reflect the lower PCET barrier in the TAHz···HOPh–MeO complex.

The density of hits of CIs in the biradicalic region is much higher than in the TAHz···HOPh complex, indicating more efficient internal conversion to the S_0 state, in agreement with the electronic population dynamics shown in Fig. 6. It is noteworthy that the distribution of CI hits is located at shorter R_{OH} ($\approx$1.5 Å) in TAHz···HOPh–MeO than in TAHz···HOPh–H ($\approx$1.7 Å). This observation is explained by Fig. 3 and 4, which reveal that the location of the S_1–S_0 energy crossing in the relaxed scan occurs at shorter R_{OH} for TAHz···HOPh–MeO than for TAHz···HOPh–H. These figures also show, as discussed above, that TDDFT/ωB97X-D overestimates the bond length R_{OH} at which the S_1 and S_0 energy profiles cross. In ADC(2) dynamic maps, the distribution of S_1–S_0 CIs would peak at lower values of R_{OH}. With just two exceptions, all hits of S_1–S_0 CIs occur after H-atom transfer in the TAHz···HOPh–MeO complex.

Overall, Fig. 7 and 8 illustrate that the H-atom transfer dynamics is strongly correlated with the donor–acceptor distance R_{ON}. This feature is typical for PCET reactions: the reduction of the donor–acceptor distance lowers the barrier for the H-atom transfer reaction. In the TAHz···HOPh–MeO complex, the H-atom barrier is lower than in the TAHz···HOPh–H complex and the correlation of R_{OH} and R_{ON} therefore is less pronounced.

4. Discussion and conclusions

The present work was undertaken to obtain more detailed insight into the temporally and structurally resolved PCET dynamics in TAHz···HOPh–R complexes. In view of the high

cost of first-principles nonadiabatic dynamics simulations for such large molecular systems, the calculations had to be restricted to two exemplars of the complexes of TAHz with phenol derivatives investigated by Rabe *et al.*,[12] TAHz···HOPh–H and TAHz···HOPh–MeO. The nonadiabatic trajectory simulations paint a clear mechanistic picture of the time-resolved electronic population dynamics of the adiabatic electronic states of the two hydrogen-bonded TAHz–phenol complexes. The populations of the adiabatic states S_3, S_4, S_5 of mixed $\pi\pi^*$/$n\pi^*$ character, which are excited by photons which are resonant with the maximum of the absorption spectrum, relax within about 20 fs to the S_2 state and within 50–70 fs to the S_1 state (Fig. 6). A low tail of the S_2 population extends up to 250 fs. The population of the S_1 state is comparatively long-lived. The decay constants of the S_1 population are estimated as 751 fs for TAHz···HOPh–H and as 194 fs for TAHz···HOPh–MeO. We note that these decay constants should not be considered as precise data, because the time window of our simulations of 250 fs is too short for accurate determinations of kinetic constants in the picosecond range. The estimated S_1 lifetime of 0.19 ps for TAHz···HOPh–MeO should be more accurate than the S_1 lifetime of 0.75 ps estimated for TAHz···HOPh–H.

The dynamical maps (Fig. 7 and 8) illustrate the strong correlation of the H-atom transfer reaction with the donor–acceptor distance R_{ON}. Apart from few outliers, a shortening of R_{ON} below 3.5 Å is a requirement for the H-atom transfer reaction. While a minor fraction of H-atom-transfer processes occurs rapidly with relatively high electronic potential energy in S_n electronic states with $n > 1$, most H-atom-transfer events occur after radiationless relaxation of the populations of the S_n states to the S_1 state. The fraction of H-atom-transfer events in S_n states is significantly larger in TAHz···HOPh–MeO than in TAHz···HOPh–H, see Fig. 7, 8. No deactivation channels intrinsic to TAHz (*e.g.* out-of-plane deformations of the aromatic system) are recorded within the time window of 250 fs, in agreement with the intrinsically long lifetime of TAHz in non-protic environments.[9] It can be concluded from the dynamical maps that the PCET reaction in the S_1 state is barrier controlled. The broader distribution of trajectories with respect to R_{ON} for TAHz···HOPh–MeO is the signature of a lower barrier. According to the present simulations, the excited-state PCET reaction is about four times faster in the complex of TAHz with methoxyphenol than in the complex of TAHz with phenol.

The comparison of the present results with the data of the experimental study of Rabe *et al.*,[12] which stimulated the present work, requires a careful analysis of the experimental data. While the photoluminescence of TAHz in the absence of phenols decays exponentially, solutions with mixtures of TAHz and phenols exhibit a two-component exponential decay (see Section VI of the Supporting Material of ref. 12). By global target analysis, the decay dynamics of two species with different decay constants and different emission spectra were extracted from the data. The component with the faster decay was attributed to luminescence quenching in hydrogen-bonded complexes, while the component with the slower decay was attributed to diffusion-controlled collisional quenching without involvement of hydrogen bonds.[12]

For TAHz with H–PhOH in toluene, the emission spectrum of the species with the faster decay is blue-shifted by 0.07 eV relative to the emission spectrum of the species with slower decay. The computed vertical emission energy of the TAHz–HOPh–H complex (ADC(2) level) is blue-shifted by 0.05 eV relative to the computed emission energy of free TAHz, which supports the assignment of the blue-shifted emission spectrum to hydrogen-bonded complexes. The time constant of the fast component extracted for the mixture of TAHz with phenol in toluene was 361 ps, which is notably faster than the time constant of 3.09 ns of the slow component, but is significantly slower than the time constant of 0.75 ps estimated by the present simulations.

For mixtures of TAHz with methoxyphenol in toluene, global target analysis did not reveal a blue-shifted emission spectrum. Apparently, the decay of the hydrogen-bonded TAHz···HOPh–MeO complex was too fast to be disentangled from the measured luminescence signal.[12]

Global target analysis is an empirical decomposition of the dependence of the emission signal on wavelength and emission time. It is therefore not *a priori* clear that the extracted fast decaying component originates exclusively from hydrogen-bonded complexes. The fast decaying blue-shifted signal could include contributions from weakly bonded complexes with significantly stretched hydrogen bonds or contributions from transient TAHz–phenol collisional complexes in toluene solution, which would have emission lifetimes in between of free TAHz and optimally hydrogen-bonded TAHz–phenol complexes. The time resolution of the experiment also may have been insufficient for the detection of species with sub-ps emission decay times, as is indicated by the absence of a fast decaying signal for TAHz with MeO–PhOH.[12]

On the other hand, the possibility that the present simulations substantially underestimate the PCET time constants in TAHz–phenol complexes cannot be excluded. We consider it unlikely that the technical approximations made in the nonadiabatic SH simulations affect the results by orders of magnitude. However, the time window of our simulations (250 fs) is too short to extract accurate decay constants of the S_1 populations of TAHz–phenol complexes of the order of picoseconds. Because H-atom tunnelling effects are not included in the quasi-classical simulations, the H-atom transfer rate should be underestimated rather than overestimated by the simulations.

The main source of substantial inaccuracies of the simulations could be in the electronic-structure calculations. The relaxed scans along the H-atom transfer coordinate (Fig. 3, 4) indicate that the TDDFT method with the ωB97X-D functional rather overestimates the energy of the CT state relative to the energy of the closed-shell ground state, which is unfavourable for the H-atom-transfer reaction. There is no indication from the benchmarking calculations that TDDFT substantially underestimates the PCET barrier. It is possible, on the other hand, that ADC(2) might underestimate the energy of the biradicalic state at large OH distances (≈2.0 Å) relative to the energy of the CT state at

small (≈1.0 Å) OH distances. Benchmarking the accuracy of ADC(2) with intrinsically more accurate electronic-structure methods such as CC3 or CCSD(T), which exhibit N^7 scaling of the computational cost, is not possible at present for TAHz–phenol complexes. The determination of precise time constants for the PCET reaction in hydrogen-bonded TAHz–phenol complexes therefore remains an open research problem.

The photochemistry of TAHz–phenol complexes is of interest in so far as these systems provide model scenarios for the investigation photoinduced PECT reactions involving Hz-derived photocatalysts. The photooxidation of phenols is less challenging than the photooxidation of water due to the lower oxidation potentials of phenols. Because reaction barriers for PCET reactions in hydrogen-bonded Hz-water complexes are substantially higher than in Hz–phenol complexes, excited-state PCET reactions involved in water splitting with Hz-derived photocatalysts likely are in the deep tunnelling regime and the PCET time constants are expected to be in the regime of hundreds of picoseconds to tens of nanoseconds. Such timescales cannot be explored with brute-force *ab initio* on-the-fly quasi-classical dynamics simulations and new methods have to be developed which enable efficient first-principles non-adiabatic excited-state simulations on such timescales. In the meantime, Hz–phenol complexes may be considered as molecular laboratories for the further optimization of experimental and computational techniques needed for the exploration of unconventional approaches to photocatalytic water splitting.

Conflicts of interest

There are no conflicts of interest to declare.

Acknowledgements

We gratefully acknowledge fruitful discussions with Marin Sapunar (Ruđer Bošković Institute, Zagreb, Croatia) and his contributions to the development of the LZSH code. This work was supported by a research grant of the Deutsche Forschungsgemeinschaft (DFG), Grant No. DO 256/42-2.

References

1 X. Wang, K. Maeda, A. Thomas, K. Takanabe, G. Xin, J. M. Carlsson, K. Domen and M. Antonietti, *Nat. Mater.*, 2009, **8**, 76–80.
2 W.-J. Ong, L.-L. Tan, Y. H. Ng, S.-T. Yong and S.-P. Chai, *Chem. Rev.*, 2016, **116**, 7159–7329.
3 J. Wen, J. Xie, X. Chen and X. Li, *Appl. Surf. Sci.*, 2017, **391**, 72–123.
4 V. W.-h. Lau and B. V. Lotsch, *Adv. Energy Mater.*, 2022, **12**, 2101078.
5 S.-M. Lam, J.-C. Sin and A. R. Mohamed, *Mater. Sci. Semicond. Process.*, 2016, **47**, 62–84.
6 C. Zhang, D. Shuai, Y. Shen, W. Xiong and L. Wang, *Chemosphere*, 2019, **214**, 462–479.
7 Y. Wang, A. Vogel, M. Sachs, R. S. Sprick, L. Wilbraham, S. J. A. Moniz, R. Godin, M. A. Zwijnenburg, J. R. Durrant, A. I. Cooper and J. Tang, *Nat. Energy*, 2019, **4**, 746.
8 M. Shabaz, S. Urano, P. R. LeBreton, M. A. Rossman, R. S. Hosmane and N. J. Leonard, *J. Am. Chem. Soc.*, 1984, **106**, 2805–2811.
9 E. J. Rabe, K. L. Corp, A. L. Sobolewski, W. Domcke and C. W. Schlenker, *J. Phys. Chem. Lett.*, 2018, **9**, 6257–6261.
10 D. R. Weinberg, C. J. Gagliardi, J. F. Hull, C. F. Murphy, C. A. Kent, B. C. Westlake, A. Paul, D. H. Ess, D. G. McCafferty and T. J. Meyer, *Chem. Rev.*, 2012, **112**, 4016–4093.
11 M. Li, D. Liu, X. Chen, Z. Yin, H. Shen, A. Aiello, K. R. McKenzie, N. Jiang, X. Li, M. J. Wagner, D. P. Durkin, H. Chen and D. Shuai, *Energy Environ. Sci.*, 2021, **55**, 12414–12423.
12 E. J. Rabe, K. L. Corp, X. Huang, J. Ehrmaier, R. G. Flores, S. L. Estes, A. L. Sobolewski, W. Domcke and C. W. Schlenker, *J. Phys. Chem. C*, 2019, **123**, 29580–29588.
13 K. L. Corp, E. J. Rabe, X. Huang, J. Ehrmaier, M. E. Kaiser, A. L. Sobolewski, W. Domcke and C. W. Schlenker, *J. Phys. Chem. C*, 2020, **124**, 9151–9160.
14 E. J. Rabe, J. J. Goldwyn, D. Hwang, D. J. Masiello and C. W. Schlenker, *J. Phys. Chem. B*, 2020, **124**, 11680–11689.
15 C. Bronner and O. S. Wenger, *Inorg. Chem.*, 2012, **51**, 8275–8283.
16 C. Bronner and O. S. Wenger, *J. Phys. Chem. Lett.*, 2012, **3**, 70–74.
17 N. Barman, D. Singha and K. Sahu, *J. Phys. Chem. A*, 2013, **117**, 3945–3953.
18 T. Hossen and K. Sahu, *J. Phys. Chem. A*, 2018, **122**, 2394–2400.
19 E. Wigner, *Phys. Rev.*, 1932, **40**, 749–759.
20 F. Kossoski and M. Barbatti, *J. Chem. Theory Comput.*, 2018, **14**, 3173–3183.
21 J. P. Zobel, J. J. Nogueira and L. Gonzalez, *Phys. Chem. Chem. Phys.*, 2019, **21**, 13906–13915.
22 M. H. Beck, A. Jäckle, G. A. Worth and H.-D. Meyer, *Phys. Rep.*, 2000, **324**, 1–105.
23 R. Crespo-Otero and M. Barbatti, *Chem. Rev.*, 2018, **118**, 7025–7068.
24 M. E. Casida and M. Huix-Rotllant, *Annu. Rev. Phys. Chem.*, 2012, **63**, 287–323.
25 D. Jacquemin, B. Mennucci and C. Adamo, *Phys. Chem. Chem. Phys.*, 2011, **13**, 16987–16998.
26 S. S. Leang, F. Zahariev and M. S. Gordon, *J. Chem. Phys.*, 2012, **136**, 104101.
27 D. Jacquemin, I. Duchemin and X. Blase, *J. Chem. Theory Comput.*, 2015, **11**, 3290–3304.
28 J. Schirmer, *Phys. Rev. A: At., Mol., Opt. Phys.*, 1982, **26**, 2395–2416.
29 A. B. Trofimov and J. Schirmer, *J. Phys. B: At., Mol. Opt. Phys.*, 1995, **28**, 2299–2324.
30 A. Dreuw and M. Wormit, *Wiley Interdiscip. Rev.: Comput. Mol. Sci.*, 2015, **5**, 82–95.
31 T. Yanai, D. P. Tew and N. C. Handy, *Chem. Phys. Lett.*, 2004, **393**, 51–57.
32 J.-D. Chai and M. Head-Gordon, *J. Chem. Phys.*, 2008, **128**, 084106.

33 J.-D. Chai and M. Head-Gordon, *Phys. Chem. Chem. Phys.*, 2008, **10**, 6615–6620.
34 L. D. Landau, *Phys. Z. Sowjetunion*, 1932, **2**, 46.
35 C. Zener, *Proc. Roy. Soc. A*, 1932, **137**, 696.
36 A. K. Belyaev and O. V. Lebedev, *Phys. Rev. A: At., Mol., Opt. Phys.*, 2011, **84**, 014701.
37 A. K. Belyaev, C. Lasser and G. Triglia, *J. Chem. Phys.*, 2014, **140**, 224108.
38 A. K. Belyaev, W. Domcke, C. Lasser and G. Trigila, *J. Chem. Phys.*, 2015, **142**, 104307.
39 W. Xie, M. Sapunar, N. Došlić, M. Sala and W. Domcke, *J. Chem. Phys.*, 2019, **150**, 154119.
40 J. Suchan, J. Janos and P. Slavicek, *J. Chem. Theory Comput.*, 2020, **16**, 5809–5820.
41 J. C. Tully, *J. Chem. Phys.*, 1990, **93**, 1061–1071.
42 W. Xie and W. Domcke, *J. Chem. Phys.*, 2017, **147**, 184114.
43 C. Møller and M. S. Plesset, *Phys. Rev.*, 1934, **46**, 618–622.
44 T. H. Dunning Jr., *J. Chem. Phys.*, 1989, **90**, 1007–1023.
45 J. Ehrmaier, T. N. V. Karsili, A. L. Sobolewski and W. Domcke, *J. Phys. Chem. A*, 2017, **121**, 4754–4764.
46 TURBOMOLE V7.4 2019, a Development of University of Karlsruhe and Forschungszentrum Karlsruhe GmbH, 1989–2007, TURBOMOLE GmbH, since 2007; available from **http://www.turbomole.com**.
47 R. Crespo-Otero and M. Barbatti, *Theor. Chem. Acc.*, 2012, **131**, 1237.
48 M. Barbatti, M. Ruckenbauer, F. Plasser, J. Pittner, G. Granucci, M. Persico and H. Lischka, *Wiley Interdiscip. Rev.: Comput. Mol. Sci.*, 2014, **4**, 26–33.
49 X. Huang and W. Domcke, *J. Phys. Chem. A*, 2021, **125**, 9917–9931.
50 S. Chaiwongwattana, M. Sapunar, A. Ponzi, P. Decleva and N. Došlić, *J. Phys. Chem. A*, 2015, **119**, 10637–10644.
51 S. Gozem, F. Melaccio, A. Valentini, M. Filatov, M. Huix-Rotllant, N. Ferré, L. M. Frutos, C. Angeli, A. I. Krylov, A. A. Granovsky, R. Lindh and M. Olivucci, *J. Chem. Theory Comput.*, 2014, **10**, 3074–3084.
52 D. Tuna, D. Lefrancois, L. Wolanski, S. Gozem, I. Schapiro, T. Andruniow, A. Dreuw and M. Olivucci, *J. Chem. Theory Comput.*, 2015, **11**, 5758–5781.

JCTC Journal of Chemical Theory and Computation

pubs.acs.org/JCTC Article

Ab Initio Surface-Hopping Simulation of Femtosecond Transient-Absorption Pump−Probe Signals of Nonadiabatic Excited-State Dynamics Using the Doorway−Window Representation

Maxim F. Gelin, Xiang Huang, Weiwei Xie, Lipeng Chen, Nađa Došlić, and Wolfgang Domcke*

Cite This: J. Chem. Theory Comput. 2021, 17, 2394−2408

Read Online

ABSTRACT: An ab initio theoretical framework for the simulation of femtosecond time-resolved transient absorption (TA) pump−probe (PP) spectra with quasi-classical trajectories is presented. The simulations are based on the classical approximation to the doorway−window (DW) representation of third-order four-wave-mixing signals. The DW formula accounts for the finite duration and spectral shape of the pump and probe pulses. In the classical DW formalism, classical trajectories are stochastically sampled from a positive definite doorway distribution, and the signals are evaluated by averaging over a positive definite window distribution. Nonadiabatic excited-state dynamics is described by a stochastic surface-hopping algorithm. The method has been implemented for the pyrazine molecule with the second-order algebraic-diagrammatic construction (ADC(2)) ab initio electronic-structure method. The methodology is illustrated by ab initio simulations of the ground-state bleach, stimulated emission, and excited-state absorption contributions to the TA PP spectrum of gas-phase pyrazine.

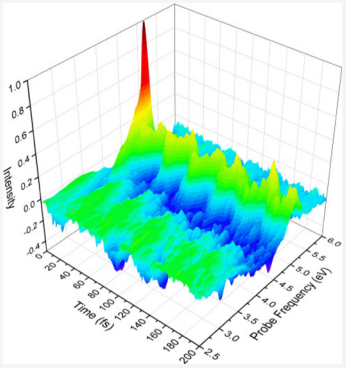

1. INTRODUCTION

First-principles studies of photoinduced nonadiabatic processes in polyatomic molecules with so-called direct dynamics simulation methods have become a flourishing field of research in recent years. Direct dynamics simulation methods allow us, in principle, to overcome two formidable bottlenecks of the traditional approach based on time-dependent nuclear quantum dynamics on precomputed ab initio potential-energy (PE) surfaces. First, nuclear quantum dynamics is nonlocal and therefore requires more or less global PE surfaces for wave-packet propagation, whereas the propagation of classical trajectories on Born−Oppenheimer adiabatic PE surfaces requires only local information which can be computed "on the fly" with ab initio electronic-structure theory.[1−8] Second, the computational cost of accurate quantum wave-packet calculations scales exponentially with the number of nuclear degrees of freedom, whereas the cost of classical trajectory dynamics scales only linearly with the number of nuclear degrees of freedom. Nonadiabatic transitions between adiabatic PE surfaces can be taken into account in quasi-classical simulations with so-called surface-hopping (SH) algorithms.[7−10] Alternatively, the nuclear dynamics can be simulated semi-classically with Gaussian wave packets or superpositions of Gaussians which follow classical trajectories.[11−17] These trajectory-based methods eliminate the need of the often time-consuming construction of global multi-sheeted multidimensional PE surfaces. In fact, it suffices for direct dynamics simulations to interface a classical molecular dynamics code with one of the available codes for excited-state electronic-structure calculations.

Classical simulations of inherently quantum mechanical observables, such as final-state rotational or vibrational intensity distributions, are computationally challenging. On the other hand, quasi-classical trajectory sampling usually converges rapidly for highly averaged quantities, such as, for example, time-dependent population probabilities of electronic states. In particular, radiationless transitions driven by conical intersections occur typically within tens or hundreds of femtoseconds and therefore are well amenable for nonadiabatic direct dynamics simulations, despite the high cost of electronic-structure calculations at each time step of the nuclear motion. Correspondingly, direct dynamics simulations of ultrafast radiationless decay processes in polyatomic molecules have become very popular in recent years, see, for example,[7,8,18−23] for reviews.

Time-dependent populations of adiabatic or diabatic electronic states are, as such, not experimentally observable. The experimental detection of ultrafast photophysical or photochemical processes is primarily based on laser spectros-

Received: January 31, 2021
Published: March 23, 2021

https://doi.org/10.1021/acs.jctc.1c00109
J. Chem. Theory Comput. 2021, 17, 2394−2408

copy with pulsed visible, UV, or X-ray light sources. The theoretical description of femtosecond time-resolved signals has been developed three decades ago within the framework of third-order perturbation theory in the light-matter interaction. In this approach, the measurable signals are expressed as convolutions of nonlinear dipole response functions with the pulsed laser fields.[24] Alternatively, methods have been developed for the calculation of nonlinear signals which are nonperturbative in the light-matter interaction[25] as well as hybrid methods, which are nonperturbative in the pump field but perturbative in the probe field.[26] In all these formulations, the dynamics of the material system is described quantum mechanically in terms of time-dependent wave packets or density operators.

In comparison with the extensive application of quasi-classical SH methods for the simulation of time-dependent population probabilities of electronic states, the calculation of experimentally observable time and frequency-resolved signals with trajectory calculations has received relatively little attention so far. Ab initio classical trajectory simulations of femtosecond time-resolved photoelectron spectra were performed by several groups.[27−31] Several authors also reported ab initio simulations of time- and frequency-resolved fluorescence spectra.[32−35] In the latter simulations, the trajectories are initiated in a selected adiabatic excited state at $t = 0$, and the radiative emission rate is calculated as the Einstein A coefficient, invoking the classical Condon approximation. This modeling of the fluorescence signal neglects the effects due to the finite duration of the pump pulse and does not account for the Fourier-limited time-frequency resolution of the fluorescence up-conversion detection scheme. Computer simulations were recently reported also for transient absorption (TA) pump−probe (PP) spectra monitoring ultrafast nonadiabatic dynamics in polyatomic molecules, for example, photoisomerization of rhodopsin[36] and transazobenzene,[37] $^1\pi\pi^*/^1n\pi^*/^3\pi\pi^*$ internal conversion and intersystem crossing in thiouracil[38] or deep-UV photophysics in pyrene[39] (see also ref 40 for a review). However, the nonadiabatic electronic population dynamics was modeled with phenomenological kinetic master equations and the finite pulse duration was taken into account in an ad hoc manner. A completely first-principles trajectory-based description of TA PP signals of nonadiabatic excited-state dynamics in polyatomic molecules measured with finite laser pulses is hitherto lacking.

In the present work, we have developed such a systematic ab initio computational scheme for the simulation of TA PP spectra. In TA PP spectroscopy, the sample is excited by a short pump pulse, and the transmission of a short probe pulse is recorded as a function of the time delay of the probe pulse with a tunable carrier frequency. Alternatively, the spectrum of the transmitted probe pulse with a fixed carrier frequency is dispersed by a spectrometer and is recorded as a function of the delay time. The detected signal is the difference of the transmitted intensity of the probe pulse with and without the pump pulse ("pump-on minus pump-off"). Due to the simplicity of implementation and interpretation, TA PP spectroscopy is the most widely applied variant of time- and frequency-resolved nonlinear spectroscopy.[41−47]

The theory of TA PP spectroscopy was developed, among others, by Mukamel and co-workers[48−51] and Pollard, Lee, and Mathies.[52,53] Yan, Fried, and Mukamel[48,50] introduced the doorway−window (DW) picture, which provides a transparent and intuitively appealing interpretation of the TA PP signal and related four-wave-mixing signals. The DW approximation is applicable when the pump and probe pulses are well separated in time (nonoverlapping pulses). The pump pulse generates the so-called doorway density operator in the electronic ground state and in the excited electronic state(s). After the preparation by the pump pulse, the doorway operator propagates with the Liouvillian of the field-free system. The probe pulse generates the so-called window operator. The signal is expressed as the contraction of the doorway operator, the field-free propagator, and the window operator. Apart from the restriction of nonoverlapping pulses, only the rotating-wave approximation (RWA) is invoked in the derivation.[48] Fried and Mukamel[54] recognized that the DW formulation of TA PP spectroscopy is well suited as the starting point for the implementation of a classical description of the TA PP signal, see also ref.[55,57] By combining Monte Carlo sampling of the doorway and window phase-space distributions with the time-dependent classical Condon approximation,[58] PP spectra were simulated for one-dimensional models of the photodissociation of I_2 or ICN.[48,56]

Herein, we describe the implementation of a first-principles direct-dynamics computational scheme for the simulation of TA PP spectra within the DW approximation for systems exhibiting multistate multimode nonadiabatic dynamics. The computational protocol is developed for a rather general scenario of PE surfaces and electronic transition dipole moments of a polyatomic chromophore. To illustrate the method, we report simulated TA PP spectra of the pyrazine molecule, which represents a widely known testbed for ultrafast excited-state dynamics driven by conical intersections.[59−63]

2. NONLINEAR POLARIZATION AND TA PP SIGNALS

In TA PP spectroscopy, the sample is excited by the pump pulse and the integral or dispersed absorption of the probe pulse is detected.[41−47] The TA signal depends on the time delay between the pump and probe pulses as well as on the durations and the carrier frequencies of the pulses. The integral TA PP signal is obtained by measuring the extinction of the probe pulse as a function of the carrier frequency and time delay. Alternatively, the transmitted probe field can be dispersed with a spectrometer, yielding the dispersed TA PP signal. Both the integral and the dispersed signal can be decomposed into three contributions which are termed ground-state bleach (GSB), stimulated emission (SE), and excited-state absorption (ESA). The individual contributions can be measured provided that they are not spectrally overlapping.

In terms of the third-order polarization radiating in the direction of the probe pulse, $\mathcal{P}(T, t)$, and its Fourier transform, $\mathcal{P}(T, \omega)$, the integral (subscript "int") and dispersed (subscript "dis") TA PP signals are defined as follows[24]

$$S_{\mathrm{int}}(T, \omega_{\mathrm{pr}}) \sim \int \mathrm{d}t \mathcal{P}(T, t) \mathcal{E}_{\mathrm{pr}}(t) \mathrm{e}^{\mathrm{i}\omega_{\mathrm{pr}} t} \tag{1}$$

$$S_{\mathrm{dis}}(T, \omega) \sim \mathcal{P}(T, \omega) \mathcal{E}_{\mathrm{pr}}(\omega - \omega_{\mathrm{pr}}) \tag{2}$$

Here, T is the time delay between the pump and probe pulses, ω_{pr} is the carrier frequency of the probe, $\mathcal{E}_{\mathrm{pr}}(t)$ is the dimensionless temporal envelope of the probe pulse, and $\mathcal{E}_{\mathrm{pr}}(\omega)$ is the Fourier transform of the probe pulse. In order to

https://doi.org/10.1021/acs.jctc.1c00109
J. Chem. Theory Comput. 2021, 17, 2394−2408

treat the integral signal (1) and the dispersed signal (2) on equal footing, it is convenient to define a general heterodyne-detected PP signal as

$$S(\omega_{\mathrm{pu}}, T, \omega_{\mathrm{pr}}, \tau_t) \sim \mathrm{Im} \int_{-\infty}^{\infty} \mathrm{d}t \mathcal{P}(T, t) \mathcal{E}_{\mathrm{pr}}(t - \tau_t) \mathrm{e}^{\mathrm{i}\omega_{\mathrm{pr}}(t-\tau_t)} \tag{3}$$

where ω_{pu} is the carrier frequency of the pump pulse and τ_t is the time delay between the probe pulse and the heterodyning pulse (the latter is assumed to have the same time envelope as the probe pulse). With the definition of eq 3, the integral and dispersed PP signals of eqs 1 and 2 are obtained as

$$S_{\mathrm{int}}(T, \omega_{\mathrm{pr}}) \sim S(\omega_{\mathrm{pu}}, T, \omega_{\mathrm{pr}}, 0) \tag{4}$$

$$S_{\mathrm{dis}}(T, \omega) \sim \int_{-\infty}^{\infty} \mathrm{d}\tau_t \, \mathrm{e}^{\mathrm{i}\omega\tau_t} S(\omega_{\mathrm{pu}}, T, \omega_{\mathrm{pr}}, \tau_t) \tag{5}$$

The evaluation of $\mathcal{P}(T, t)$ requires the calculation of the nonlinear response of the chromophore to the pump and probe pulses.

3. MOLECULAR HAMILTONIAN AND RADIATION−MATTER INTERACTION

Denoting the coordinates of electrons and nuclei by $\boldsymbol{r}$ and $\boldsymbol{R}$, respectively, the molecular Hamiltonian is given by

$$H_{\mathrm{M}} = K_{\mathrm{N}} + H_{\mathrm{E}} \tag{6}$$

$$H_{\mathrm{E}} = K_{\mathrm{E}} + V(\boldsymbol{r}, \boldsymbol{R}) \tag{7}$$

Here, K_{N} and K_{E} are the kinetic-energy operators of nuclei and electrons, respectively, and $V(\boldsymbol{r},\boldsymbol{R})$ denotes the Coulombic interactions of electrons and nuclei. The eigenfunctions $\Phi_n(\boldsymbol{r},\boldsymbol{R})$ and eigenvalues $V_n(\boldsymbol{R})$ of the fixed-nuclei Hamiltonian H_{E}

$$(H_{\mathrm{E}} - V_n(\boldsymbol{R}))\Phi_n(\boldsymbol{r}, \boldsymbol{R}) = 0 \tag{8}$$

depend parametrically on the nuclear coordinates $\boldsymbol{R}$. In the Born−Huang adiabatic representation, the eigenfunctions $\Psi(\boldsymbol{r},\boldsymbol{R})$ of the total molecular Hamiltonian

$$(H_{\mathrm{M}} - E)\Psi(\boldsymbol{r}, \boldsymbol{R}) = 0 \tag{9}$$

are expanded in the complete set of eigenstates of H_{E}

$$\Psi(\boldsymbol{r}, \boldsymbol{R}) = \sum_n \chi_n(\boldsymbol{R})\Phi_n(\boldsymbol{r}, \boldsymbol{R}) \tag{10}$$

Insertion of eq 10 into eq 9 and making use of eq 8 yields the coupled equations for the expansion coefficients $\chi_n(\boldsymbol{R})$

$$[K_{\mathrm{N}} + V_n(\boldsymbol{R}) - E]\chi_n(\boldsymbol{R}) = \sum_m \Lambda_{nm}\chi_m(\boldsymbol{R}) \tag{11}$$

where

$$\Lambda_{nm} = -\int \mathrm{d}r \Phi_n^*(\boldsymbol{r}, \boldsymbol{R})[K_{\mathrm{N}}, \Phi_m(\boldsymbol{r}, \boldsymbol{R})] \tag{12}$$

The Λ_{nm} are the nonadiabatic coupling (NAC) elements which arise from the parametric dependence of the adiabatic electronic wave functions $\Phi_n(\boldsymbol{r},\boldsymbol{R})$ on the nuclear coordinates. The Λ_{nm} exhibit singularities at conical intersections of the adiabatic PE surfaces. In the basis of the adiabatic electronic eigenstates, the molecular Hamiltonian can be written as a matrix Hamiltonian

$$\boldsymbol{H}_{\mathrm{M}} = K_{\mathrm{N}}\mathbf{1} + \boldsymbol{V}(\boldsymbol{R}) - \boldsymbol{\Lambda} \tag{13}$$

which describes the nuclear motion in the manifold of coupled adiabatic electronic states. When $\boldsymbol{\Lambda} = 0$, the adiabatic Born−Oppenheimer approximation is recovered.

In a general closed-shell molecule, the ground state Φ_0 is well separated (typically by several electron volts) from the lowest excited state. For a pump pulse of low intensity, the carrier frequency of the pump pulse has to be approximately in resonance with the energy gap between the ground state and the bright excited state of interest. This energy gap therefore defines the carrier frequency ω_{pu} of the pump pulse. The probe pulse triggers SE to the ground state but also can excite higher electronic states, giving rise to ESA. Assuming that the carrier frequency of the probe pulse ω_{pr} is similar to the carrier frequency of the pump pulse ω_{pu}, the relevant higher excited states are located at an energy of $\approx 2\hbar\omega_{\mathrm{pu}}$ above the ground state. It is therefore convenient to introduce three subsets of electronic states for the description of TA PP experiments for general closed-shell molecules, which we denote as {0}, {I}, and {II}. The set {0} includes only the closed-shell electronic ground state. The manifold {I} includes the bright and dark electronic states with vertical excitation energies $V_n(\boldsymbol{R}) \approx \hbar\omega_{\mathrm{pu}}$. The manifold {II} includes electronic states with vertical excitation energies $V_n(\boldsymbol{R}) \approx 2\hbar\omega_{\mathrm{pu}}$. Electronic states of manifold {II} which are dark in radiative transitions from manifold {I} can be ignored.

In view of the large energy gap separating the manifolds {0} and {I}, we can assume that NACs between these manifolds can be neglected on the time scale of the experiment (typically <1 ps). The manifolds {0} and {I} are then only coupled by the laser fields. Within the manifold {I}, intramolecular NACs may be important but radiative couplings are irrelevant because these radiative transitions are out of resonance with the laser fields. The states of manifold {II} may be nonadiabatically coupled with the states of manifold {I}, but due to the large energy gap of $\approx\hbar\omega_{\mathrm{pu}}$, the effect of these couplings should be negligible. The internal NACs in the manifold {II} are of limited relevance for the TA PP experiment because no electronic population is generated in these states in the third order of light-matter perturbation theory, as will be seen below.

It follows from these general considerations that the matrix Hamiltonian of eq 13 exhibits a block-diagonal structure

$$\boldsymbol{H}_{\mathrm{M}} = \begin{pmatrix} H_0 & 0 & 0 \\ 0 & H_{\mathrm{I}} & 0 \\ 0 & 0 & H_{\mathrm{II}} \end{pmatrix} \tag{14}$$

where H_0, H_{I}, and H_{II} are the matrix Hamiltonians of nuclear motion in the respective manifolds. The matrix of electronic transition moments, which are relevant for the TA PP experiment, exhibits the complementary block structure

$$\boldsymbol{\mu} = \begin{pmatrix} 0 & \mu_{0,\mathrm{I}} & 0 \\ \mu_{\mathrm{I},0} & 0 & \mu_{\mathrm{I,II}} \\ 0 & \mu_{\mathrm{II,I}} & 0 \end{pmatrix} \tag{15}$$

The matrix $\mu_{\mathrm{I},0}$ contains the transition dipole moments from the ground state to the manifold {I} of lower excited states. The matrix $\mu_{\mathrm{II,I}}$ contains the transition dipole moments from the lower excited states to the higher excited states. The intramolecular NACs are thus confined to the diagonal blocks (eq 14), while the couplings with the laser fields are confined to the off-diagonal blocks (eq 15). This structure of the

https://doi.org/10.1021/acs.jctc.1c00109
J. Chem. Theory Comput. 2021, 17, 2394−2408

molecular Hamiltonian and the light-matter coupling greatly simplifies the derivation of compact DW expressions for the TA PP signal.

Within the RWA, it is convenient to define dipole transition moments for upward and downward radiative transitions as

$$\boldsymbol{\mu}^{\uparrow} = \begin{pmatrix} 0 & \mu_{0,\mathrm{I}} & 0 \\ 0 & 0 & \mu_{\mathrm{I,II}} \\ 0 & 0 & 0 \end{pmatrix}, \qquad \boldsymbol{\mu}^{\downarrow} = \begin{pmatrix} 0 & 0 & 0 \\ \mu_{\mathrm{I},0} & 0 & 0 \\ 0 & \mu_{\mathrm{II,I}} & 0 \end{pmatrix} \tag{16}$$

The radiation-matter interaction Hamiltonian thus reads

$$\boldsymbol{H}_{\mathrm{F}}(t) = -\boldsymbol{\mu}^{\uparrow}\mathcal{E}(t) - \boldsymbol{\mu}^{\downarrow}\mathcal{E}^{*}(t) \tag{17}$$

where, for brevity, the amplitudes of the laser fields are incorporated into the transition dipole moments and

$$\mathcal{E}(t) = \mathcal{E}_{\mathrm{pu}}(t)\mathrm{e}^{\mathrm{i}\omega_{\mathrm{pu}}t} + \mathcal{E}_{\mathrm{pr}}(t-T)\mathrm{e}^{\mathrm{i}\omega_{\mathrm{pr}}t} \tag{18}$$

where $\mathcal{E}_{\mathrm{pu}}(t)$ and $\mathcal{E}_{\mathrm{pr}}(t)$ are the dimensionless envelopes of the pump and probe pulses, respectively.

4. DW FORMULA FOR AB INITIO HAMILTONIANS

The density operator of the material system is written as

$$\boldsymbol{\rho}(t) = \begin{pmatrix} \rho_{0,0}(t) & \rho_{0,\mathrm{I}}(t) & \rho_{0,\mathrm{II}}(t) \\ \rho_{\mathrm{I},0}(t) & \rho_{\mathrm{I,I}}(t) & \rho_{\mathrm{I,II}}(t) \\ \rho_{\mathrm{II},0}(t) & \rho_{\mathrm{II,I}}(t) & \rho_{\mathrm{II,II}}(t) \end{pmatrix} \tag{19}$$

It obeys the equation of motion

$$\frac{\mathrm{d}}{\mathrm{d}t}\boldsymbol{\rho}(t) = -\mathrm{i}[\boldsymbol{H}_{\mathrm{M}} + \boldsymbol{H}_{\mathrm{F}}(t), \boldsymbol{\rho}(t)] \tag{20}$$

($\hbar = 1$) with the initial condition

$$\rho(t=-\infty) = \begin{pmatrix} \rho_{0,0}^{(0)} & 0 & 0 \\ 0 & 0 & 0 \\ 0 & 0 & 0 \end{pmatrix} \tag{21}$$

where

$$\rho_{0,0}^{(0)} = Z^{-1}\exp\{-\beta H_0\} \tag{22}$$

Here, $\beta = (k_{\mathrm{B}}T)^{-1}$, Z is the partition function and T is the temperature of the molecular ensemble. The chromophores are assumed to be in the electronic ground state with vibrational temperature T before the arrival of the pump pulse.

The derivation of the DW expression for the TA PP signal follows the derivation of Yan and Mukamel[50] with the generalization that $\boldsymbol{H}_{\mathrm{M}}$ and $\boldsymbol{H}_{\mathrm{F}}(t)$ are given by the electronic block matrices defined above and $\boldsymbol{H}_{\mathrm{M}}$ includes NACs. The ESA contribution to the TA PP signal was not included in the early derivations of the DW formula.[48,50] The detailed derivation of the DW formula for block matrices including the ESA contribution is given in Appendix A. The result reads

$$S(\omega_{\mathrm{pu}}, T, \omega_{\mathrm{pr}}, \tau_t) \sim \mathrm{ReTr}[D_0(\omega_{\mathrm{pu}})W_0(\omega_{\mathrm{pr}}, \tau_t, T) + D_{\mathrm{I}}(\omega_{\mathrm{pu}})\{W_{\mathrm{I}}(\omega_{\mathrm{pr}}, \tau_t, T) - W_{\mathrm{II}}(\omega_{\mathrm{pr}}, \tau_t, T)\}] \tag{23}$$

where

$$D_0(\omega_{\mathrm{pu}}) = \int_{-\infty}^{\infty}\mathrm{d}t_2'\int_0^{\infty}\mathrm{d}t_1\mathcal{E}_{\mathrm{pu}}(t_2')\mathcal{E}_{\mathrm{pu}}(t_2'-t_1)\mathrm{e}^{\mathrm{i}\omega_{\mathrm{pu}}t_1}\,\mathrm{e}^{-\mathrm{i}H_{\mathrm{I}}t_1}\,\mu_{\mathrm{I},0}\rho_{0,0}^{(0)}\,\mathrm{e}^{\mathrm{i}H_0t_1}\,\mu_{0,\mathrm{I}} + \mathrm{H.\,c.} \tag{24}$$

$$D_{\mathrm{I}}(\omega_{\mathrm{pu}}) = \int_{-\infty}^{\infty}\mathrm{d}t_2'\int_0^{\infty}\mathrm{d}t_1\mathcal{E}_{\mathrm{pu}}(t_2')\mathcal{E}_{\mathrm{pu}}(t_2'-t_1)\mathrm{e}^{\mathrm{i}\omega_{\mathrm{pu}}t_1}\,\mu_{0,\mathrm{I}}\,\mathrm{e}^{-\mathrm{i}H_{\mathrm{I}}t_1}\,\mu_{\mathrm{I},0}\rho_{0,0}^{(0)}\,\mathrm{e}^{\mathrm{i}H_0t_1} + \mathrm{H.\,c.} \tag{25}$$

$$W_0(\omega_{\mathrm{pr}}, \tau_t) = \int_{-\infty}^{\infty}\mathrm{d}t'\int_0^{\infty}\mathrm{d}t_3\mathcal{E}_{\mathrm{pr}}(t')\mathcal{E}_{\mathrm{pr}}(t'-\tau_t+t_3)\,\mathrm{e}^{\mathrm{i}\omega_{\mathrm{pr}}(t_3-\tau_t)}\,\mathrm{e}^{\mathrm{i}H_0t_3}\,\mu_{0,\mathrm{I}}\,\mathrm{e}^{-\mathrm{i}H_{\mathrm{I}}t_3}\,\mu_{\mathrm{I},0} \tag{26}$$

$$W_{\mathrm{I}}(\omega_{\mathrm{pr}}, \tau_t) = \int_{-\infty}^{\infty}\mathrm{d}t'\int_0^{\infty}\mathrm{d}t_3\mathcal{E}_{\mathrm{pr}}(t')\mathcal{E}_{\mathrm{pr}}(t'-\tau_t+t_3)\,\mathrm{e}^{\mathrm{i}\omega_{\mathrm{pr}}(t_3-\tau_t)}\,\mu_{\mathrm{I},0}\,\mathrm{e}^{\mathrm{i}H_0t_3}\,\mu_{0,\mathrm{I}}\,\mathrm{e}^{-\mathrm{i}H_{\mathrm{I}}t_3} \tag{27}$$

$$W_{\mathrm{II}}(\omega_{\mathrm{pr}}, \tau_t) = \int_{-\infty}^{\infty}\mathrm{d}t'\int_0^{\infty}\mathrm{d}t_3\mathcal{E}_{\mathrm{pr}}(t')\mathcal{E}_{\mathrm{pr}}(t'-\tau_t+t_3)\,\mathrm{e}^{\mathrm{i}\omega_{\mathrm{pr}}(t_3-\tau_t)}\,\mu_{\mathrm{I,II}}\,\mathrm{e}^{-\mathrm{i}H_{\mathrm{II}}t_3}\,\mu_{\mathrm{II,I}}\,\mathrm{e}^{\mathrm{i}H_{\mathrm{I}}t_3} \tag{28}$$

and

$$W_0(\omega_{\mathrm{pr}}, \tau_t, T) = \mathrm{e}^{\mathrm{i}H_0T}\,W_0(\omega_{\mathrm{pr}}, \tau_t)\mathrm{e}^{-\mathrm{i}H_0T} \tag{29}$$

$$W_{\mathrm{I}}(\omega_{\mathrm{pr}}, \tau_t, T) = \mathrm{e}^{\mathrm{i}H_{\mathrm{I}}T}\,W_{\mathrm{I}}(\omega_{\mathrm{pr}}, \tau_t)\mathrm{e}^{-\mathrm{i}H_{\mathrm{I}}T} \tag{30}$$

$$W_{\mathrm{II}}(\omega_{\mathrm{pr}}, \tau_t, T) = \mathrm{e}^{\mathrm{i}H_{\mathrm{I}}T}\,W_{\mathrm{II}}(\omega_{\mathrm{pr}}, \tau_t)\mathrm{e}^{-\mathrm{i}H_{\mathrm{I}}T} \tag{31}$$

The trace operation, as shown in eq 23, includes the trace over the electronic basis states as well as the trace over the nuclear degrees of freedom. Equation 23 contains two doorway operators (D_0, D_{I}) and three window operators (W_0, W_{I}, and W_{II}). The doorway operators D_0 and D_{I} describe the preparation of the initial state by the pump pulse at $t = 0$, while the window operators describe the detection of the pump-induced wave packets by the probe pulse at the pulse delay time T. The field-free time evolution of W_0 from $t = 0$ to $t = T$ occurs in the electronic ground state with the Hamiltonian H_0, while the field-free time evolution of W_{I} and W_{II} is governed by the excited-state matrix Hamiltonian H_{I}.

Equation 23 can be interpreted as follows. The pump pulse generates the doorway operators, which represent density loss ("hole") in the electronic ground state (D_0) and light-induced density in bright excited electronic states of the manifold {I} (D_{I}). The probe pulse at delay time T generates the window operators which detect the hole (W_0, giving rise to GSB), the density in manifold {I} (W_{I}, giving rise to SE), and the density in manifold {II} (W_{II}, giving rise to ESA). The PP signal is determined by the correlation functions of the doorway operators with the window operators evaluated at pulse delay time T. In addition to the assumption of well-separated pump and probe pulses and the RWA, it has been assumed that the laser pulses are short on the time scale of the nuclear motion. Because pulse durations of less than 10 fs are nowadays widely available, the latter assumption is not a severe limitation of the theory.

5. CLASSICAL EVALUATION OF THE TA PP SIGNAL

The goal of this work is the evaluation of the quantum DW formula via stochastic sampling by classical trajectories for ab

https://doi.org/10.1021/acs.jctc.1c00109
J. Chem. Theory Comput. 2021, 17, 2394−2408

initio Hamiltonians. In the classical limit, the doorway and window operators become functions in phase space of nuclear motion, $D_i(\boldsymbol{R},\boldsymbol{P})$ and $W_i(\boldsymbol{R},\boldsymbol{P})$, where $\boldsymbol{P}$ are the momenta conjugated to $\boldsymbol{R}$. The initial nuclear density matrix $\rho_{0,0}^{(0)}$ is replaced by the Wigner distribution $\rho_g^{\mathrm{Wig}}(\mathbf{R},\mathbf{P})$.[64] The trace over nuclear degrees of freedom becomes a phase-space integral and the nuclear quantum dynamics initiated by the pump pulse is approximated by classical trajectories. According to the correspondence principle, the classical description should be a good approximation if large-amplitude vibrational/vibronic dynamics takes place in the excited state(s). Radiative transitions are described within the time-dependent classical Condon approximation.[58]

Let us denote the electronic ground state as $|\mathrm{g}\rangle$ and the ground-state PE function as $V_g(\boldsymbol{R})$. The electronic states of manifold {I} are denoted $|\mathrm{e}\rangle$, $|\mathrm{e}'\rangle$, ... with PE functions $V_e(\boldsymbol{R})$, $V_{e'}(\boldsymbol{R})$, ... The electronic states of manifold {II} are denoted $|\mathrm{f}\rangle$, $|\mathrm{f}'\rangle$, ... with PE functions $V_f(\boldsymbol{R})$, $V_{f'}(\boldsymbol{R})$, ... Ignoring, at the moment, the NACs in the Hamiltonians H_I and H_{II}, the classical (short time) Condon approximation reads[48,54,55,58]

$$\langle \mathrm{g}|\mathrm{e}^{\mathrm{i}H_0t_3}\mu_{0,\mathrm{I}}\,\mathrm{e}^{-\mathrm{i}H_\mathrm{I}t_3}|\mathrm{e}\rangle = \mathrm{e}^{\mathrm{i}U_{\mathrm{ge}}(\boldsymbol{R})t_3}\,\mu_{\mathrm{ge}}(\boldsymbol{R}) \tag{32}$$

$$\langle \mathrm{f}|\mathrm{e}^{\mathrm{i}H_{\mathrm{II}}t_3}\mu_{\mathrm{II,I}}\,\mathrm{e}^{-\mathrm{i}H_\mathrm{I}t_3}|\mathrm{e}\rangle = \mathrm{e}^{\mathrm{i}U_{\mathrm{fe}}(\boldsymbol{R})t_3}\,\mu_{\mathrm{fe}}(\boldsymbol{R}) \tag{33}$$

where

$$\mu_{\mathrm{ge}}(\boldsymbol{R}) = \langle \mathrm{g}|\mu_{0,\mathrm{I}}|\mathrm{e}\rangle \tag{34}$$

$$\mu_{\mathrm{fe}}(\boldsymbol{R}) = \langle \mathrm{f}|\mu_{\mathrm{II,I}}|\mathrm{e}\rangle \tag{35}$$

$$U_{\mathrm{ge}}(\boldsymbol{R}) = V_g(\boldsymbol{R}) - V_e(\boldsymbol{R}) \tag{36}$$

$$U_{\mathrm{fe}}(\boldsymbol{R}) = V_f(\boldsymbol{R}) - V_e(\boldsymbol{R}) \tag{37}$$

With these approximations, the double time integrals in the quantum expressions 24−28 can be evaluated. In addition, the T evolution of the operator $W_0(\omega_{\mathrm{pr}},\tau_p,T)$ of eq 29 in the Heisenberg representation is replaced by the T evolution along classical nuclear trajectories in the ground state, denoted $\boldsymbol{R}_g(T)$, $\boldsymbol{P}_g(T)$, while the T evolution of the Heisenberg operators $W_I(\omega_{\mathrm{pr}},\tau_p,T)$ and $W_{II}(\omega_{\mathrm{pr}},\tau_p,T)$ of eqs 30 and 31 is replaced by the T evolution along classical trajectories in one of the excited states of manifold {I}, denoted $\boldsymbol{R}_e(T)$, $\boldsymbol{P}_e(T)$. The detailed derivation is deferred to Appendix B. We present here the result for the integral TA PP signal. The corresponding equations for the dispersed signal are given in Appendix C.

The classical DW formula for the integral TA PP signal $S_{\mathrm{int}}(T,\omega)$ reads

$$\begin{aligned} S_{\mathrm{int}}(T,\omega_{\mathrm{pr}}) \sim{}& \langle D_0(\omega_{\mathrm{pu}},\boldsymbol{R}_g,\boldsymbol{P}_g)W_0^{\mathrm{int}}(\omega_{\mathrm{pr}},\boldsymbol{R}_g(T),\boldsymbol{P}_g(T))\rangle \\ &+ \langle D_I(\omega_{\mathrm{pu}},\boldsymbol{R}_g,\boldsymbol{P}_g)W_I^{\mathrm{int}}(\omega_{\mathrm{pr}},\boldsymbol{R}_e(T),\boldsymbol{P}_e(T))\rangle \\ &- \langle D_I(\omega_{\mathrm{pu}},\boldsymbol{R}_g,\boldsymbol{P}_g)W_{II}^{\mathrm{int}}(\omega_{\mathrm{pr}},\boldsymbol{R}_e(T),\boldsymbol{P}_e(T))\rangle \end{aligned} \tag{38}$$

The classical doorway functions are

$$\begin{aligned} D_0(\omega_{\mathrm{pu}},\boldsymbol{R}_g,\boldsymbol{P}_g) = \sum_e \mathcal{E}_{\mathrm{pu}}^2(\omega_{\mathrm{pu}} - U_{\mathrm{eg}}(\boldsymbol{R}_g)) \\ |\mu_{\mathrm{ge}}(\boldsymbol{R}_g)|^2\rho_g^{\mathrm{Wig}}(\boldsymbol{R}_g,\boldsymbol{P}_g) \end{aligned} \tag{39}$$

$$\begin{aligned} D_I(\omega_{\mathrm{pu}},\boldsymbol{R}_g,\boldsymbol{P}_g) = \mathcal{E}_{\mathrm{pu}}^2(\omega_{\mathrm{pu}} - U_{\mathrm{eg}}(\boldsymbol{R}_g))|\mu_{\mathrm{ge}}(\boldsymbol{R}_g)|^2 \\ \rho_g^{\mathrm{Wig}}(\boldsymbol{R}_g,\boldsymbol{P}_g) \end{aligned} \tag{40}$$

The classical window functions are

$$\begin{aligned} &W_0^{\mathrm{int}}(\omega_{\mathrm{pr}},\boldsymbol{R}_g(T),\boldsymbol{P}_g(T)) \\ &= \sum_e \mathcal{E}_{\mathrm{pr}}^2(\omega_{\mathrm{pr}} - U_{\mathrm{eg}}(\boldsymbol{R}_g(T)))|\mu_{\mathrm{ge}}(\boldsymbol{R}_g(T))|^2 \end{aligned} \tag{41}$$

$$\begin{aligned} &W_I^{\mathrm{int}}(\omega_{\mathrm{pr}},\boldsymbol{R}_e(T),\boldsymbol{P}_e(T)) \\ &= \mathcal{E}_{\mathrm{pr}}^2(\omega_{\mathrm{pr}} - U_{\mathrm{e}(T)\mathrm{g}}(\boldsymbol{R}_e(T)))|\mu_{\mathrm{ge}(T)}(\boldsymbol{R}_e(T))|^2 \end{aligned} \tag{42}$$

$$\begin{aligned} &W_{II}^{\mathrm{int}}(\omega_{\mathrm{pr}},\boldsymbol{R}_e(T),\boldsymbol{P}_e(T)) \\ &= \sum_f \mathcal{E}_{\mathrm{pr}}^2(\omega_{\mathrm{pr}} - U_{\mathrm{fe}(T)}(\boldsymbol{R}_e(T)))|\mu_{\mathrm{e}(T)\mathrm{f}}(\boldsymbol{R}_e(T))|^2 \end{aligned} \tag{43}$$

The three terms in eq 38 represent GSB, SE, and ESA. The angular brackets in eq 38 denote the importance sampling of the initial conditions $\boldsymbol{R}_g(0)$, $\boldsymbol{P}_g(0)$ of the classical trajectories from the positive definite distribution D_0 (for GSB) and D_I (for SE and ESA). For the GSB contribution, the classical trajectories are propagated with the classical Hamiltonian H_0 in the electronic ground state. For the SE and ESA contributions, the trajectories are propagated in the excited-state manifold {I}. The $\boldsymbol{R}_g(T)$ and $\boldsymbol{P}_g(T)$ in eq 41 are nuclear positions and momenta after propagation with the Hamiltonian H_0 up to time T. The $\boldsymbol{R}_e(T)$ and $\boldsymbol{P}_e(T)$ in eqs 42 and 43 denote positions and momenta after propagation in the excited-state manifold {I} up to time T. Note that the expression eq 39 for D_0 involves summation over the excited states of manifold {I}, which reveals that transitions to all dipole allowed excited states contribute within the spectrum of the pump pulse, $\mathcal{E}_{\mathrm{pu}}^2(\omega_{\mathrm{pu}} - U_{\mathrm{eg}}(\boldsymbol{R}))$, and according to their oscillator strengths $|\mu_{\mathrm{ge}}(\boldsymbol{R}_g)|^2$ to the formation of the hole in the ground-state density. The probability distribution D_I, on the other hand, initiates trajectories in a particular electronic state $|\mathrm{e}\rangle$ according to its oscillator strength and the resonance condition. The window functions of eqs 41−43 also are positive definite, which guarantees a well-behaved convergence of the mean values in eq 38. It should also be noted that the electronic states of manifold {II} enter only through their dipole moments $|\mu_{\mathrm{ef}}(\boldsymbol{R}_g)|^2$. No trajectories are propagated in manifold {II}. This justifies the neglect of the NACs within manifold {II}.

The NACs in manifold {I} are taken into account by an additional stochastic sampling procedure, the quasi-classical SH method.[9,10] The notation $\mathrm{e}(T)$ emphasizes that a trajectory initiated at $t = 0$ in a state e of manifold {I} can end up at time T in another state $\mathrm{e}(T)$ of manifold {I}, which, in general, does not coincide with the initial state e. In SH algorithms, nonadiabatic transitions of trajectories between adiabatic electronic states are sampled from nonadiabatic transition probabilities which usually are evaluated from the NACs defined in eq 12. The most widely used SH algorithm in molecular applications is the so-called fewest switching SH algorithm (FSSH) introduced by Tully.[10] Here, we adopt the recently developed Landau−Zener (LZ) SH algorithm (LZSH).[65−69] In this algorithm, a SH probability is computed only when the energy gap between two adiabatic electronic states attains a minimum. The hopping probability is evaluated

https://doi.org/10.1021/acs.jctc.1c00109
J. Chem. Theory Comput. 2021, 17, 2394−2408

by the Belyaev–Lebedev (BL) formula,[65] which is the reformulation of the time-honored LZ formula[70,71] in terms of the local topography of the adiabatic electronic energies. The transition probability at the minimum of the energy gap $Z_{ee'}(\boldsymbol{R})$ reads

$$P_{\mathrm{LZSH}}^{ee'} = \exp\left(-\frac{\pi}{2\hbar}\sqrt{\frac{Z_{ee'}^{\ 3}}{\ddot{Z}_{ee'}}}\right) \tag{44}$$

where $\ddot{Z}_{ee'}$ is the second-order time derivative of the adiabatic energy gap at the minimum. The hopping probability is thus completely determined by the adiabatic PE surfaces and is evaluated only at selected geometries. The second derivative of the energy gap is computed by first-order differencing of the gradients. The nonadiabatic transitions are sampled by the standard stochastic algorithm.[10,67−69] Energy is conserved by unbiased scaling of the momenta.[69] In typical applications, the LZSH algorithm is somewhat faster and more stable than the widely used FSSH algorithm because numerical derivatives of electronic wave functions (the NAC elements) need not be evaluated.[72] Moreover, the problem of the lack of decoherence of the electronic wave function[73−75] does not arise.

The BL formula exploits the fact that the values of large NAC elements are imprinted in the topography of the adiabatic PE surfaces near isolated avoided crossings or conical intersections. The LZSH algorithm was tested in comparison with the FSSH algorithm and with exact quantum wave-packet dynamics for several model systems,[67,68] among them a three-state nine-mode model of pyrazine.[69] For these examples of ultrafast nonadiabatic dynamics driven by conical intersections, the LZSH method compares well with the exact quantum dynamics results as far as the latter are available.

The angular brackets in eq 38 for the SE and ESA signals should be understood as including the sampling of SH events within the manifold {I} with the LZSH algorithm. For the GSB contribution, the trajectories are propagated in the electronic ground state which is not affected by NACs due to the clear separation of the ground state from the excited states in closed-shell molecules. Because the trajectories in the nonadiabatically coupled manifold {I} propagate in specific adiabatic states before, in between, and after the SH events; the spectroscopically relevant factors of the time-dependent classical Condon approximation in eqs 32 and 33 are correctly evaluated along each trajectory in manifold {I}.

6. SUMMARY OF THE SIMULATION PROTOCOL

The computational steps involved in the simulation of integral or dispersed TA PP signals with classical trajectories can be summarized as follows.

(A) GSB:

1 Sample an initial condition $\boldsymbol{R}_g$, $\boldsymbol{P}_g$ from the phase-space probability distribution $D_0(\omega_{pu},\boldsymbol{R}_g,\boldsymbol{P}_g)$ of eq 39.

2 Propagate and store the stochastically selected classical trajectory $\boldsymbol{R}_g(t)$, $\boldsymbol{P}_g(t)$ with the classical ground-state Hamiltonian H_0 up to the final time t_F of the simulation.

3 Evaluate $W_0^{\mathrm{int}}(\omega_{pr},\boldsymbol{R}_g(T),\boldsymbol{P}_g(T))$ via eq 41 or $W_0^{\mathrm{dis}}(\omega_{pr},\omega,\boldsymbol{R}_g(T),\boldsymbol{P}_g(T))$ via eq 62 for the desired grid of pulse delay times T.

4 Repeat these calculations until the average in eq 38 or eq 61 is converged.

(B) SE and ESA:

1 Sample an initial condition $\boldsymbol{R}_g$, $\boldsymbol{P}_g$ and an initial excited state $|e\rangle$ from the phase-space probability distribution $D_I(\omega_{pu},\boldsymbol{R}_g,\boldsymbol{P}_g)$ of eq 40.

2 Propagate and store the stochastically selected classical trajectory with the SH algorithm in the manifold {I} up to t_F.

3 Evaluate $W_I^{\mathrm{int}}(\omega_{pr},\boldsymbol{R}_e(T),\boldsymbol{P}_e(T))$ and $W_{II}^{\mathrm{int}}(\omega_{pr},\boldsymbol{R}_e(T),\boldsymbol{P}_e(T))$ via eqs 43 and 42 or, alternatively, $W_I^{\mathrm{dis}}(\omega_{pr},\omega,\boldsymbol{R}_e(T),\boldsymbol{P}_e(T))$, $W_{II}^{\mathrm{dis}}(\omega_{pr},\omega,\boldsymbol{R}_e(T),\boldsymbol{P}_e(T))$ via eqs 63 and 64 for the desired grid of pulse delay times T.

4 Repeat these calculations until the average in eq 38 or eq 61 is converged.

7. AB INITIO TA PP SIGNALS FOR PYRAZINE

We performed ab initio on-the-fly trajectory SH simulations of integral and dispersed TA PP signals of pyrazine. The photophysics of this molecule, which is characterized by conical intersections of the low-lying singlet electronic states $B_{2u}(\pi\pi^*)$, $B_{3u}(n\pi^*)$, and $A_u(n\pi^*)$ in the Franck–Condon region, has been extensively studied by quantum wave-packet calculations and classical trajectory surface hopping simulations.[59−63,69,76−83] Recent time-resolved photoelectron spectroscopy experiments confirmed the theoretically predicted ∼20 fs $B_{2u}(\pi\pi^*) \rightarrow B_{3u}(n\pi^*)$ internal conversion in pyrazine.[84] TA PP signals were calculated only for reduced-dimensional (two to three excited electronic states, three to nine vibrational modes) models of pyrazine.[76,88] On the other hand, femtosecond time-resolved photoelectron spectra of pyrazine were simulated with the on-the-fly FSSH simulations.[85−87]

The quasi-classical SH calculations of the present work for pyrazine are essentially the same as in ref 69. The Hessian matrix of the electronic ground state was computed with second-order Møller–Plesset perturbation theory (MP2)[89] using the aug-cc-pVDZ basis set.[90] The second-order algebraic-diagrammatic-construction (ADC(2)) method[91] was used to calculate the energies of excited electronic states and electronic transition dipole moments. The resolution-of-the-identity (RI) approximation implemented in TURBOMOLE[92] was employed to enhance the computational efficiency.[93,94]

Simulations of TA PP signals of pyrazine were carried out following the protocol described in Section 6. Four excited electronic states, $B_{3u}(n\pi^*)$, $A_u(n\pi^*)$, $B_{2u}(\pi\pi^*)$, and $B_{2g}(n\pi^*)$, with vertical excitation energies of 4.18, 4.83, 5.08, and 5.85 eV[63] were included in manifold {I}. The next 30 electronic states with vertical excitation energies up to ∼10 eV were included in manifold {II}. Instead of separate sampling of the D_0 and D_I phase-space distributions, we sampled from the ground-state Wigner distribution $\rho_g^{\mathrm{Wig}}(\mathbf{R}_g,\mathbf{P}_g)$ and included the $\mathcal{E}_{pu}^2(\omega_{pu} - U_{eg}[\boldsymbol{R}_g])$ and $|\mu_{ge}[\boldsymbol{R}_g]|^2$ factors in the calculation of integral and dispersed signals in eqs 38 and 61. A swarm of 1000 trajectories was initiated from $\rho_g^{\mathrm{Wig}}(\mathbf{R}_g,\mathbf{P}_g)$ and propagated for 200 fs in the four lowest excited electronic states of pyrazine (manifold {I}). A swarm of 300 trajectories was initiated from $\rho_g^{\mathrm{Wig}}(\mathbf{R}_g,\mathbf{P}_g)$ and propagated in the electronic ground state. It was observed that the integral GSB signal is well converged with 200 trajectories. The integral SE signal was found to be converged with about 500 trajectories. The GSB and SE contributions to the TA PP signal are evaluated as described in Section 5. To evaluate the ESA contribution, the vertical excitation energies from the states of manifold {I} to

https://doi.org/10.1021/acs.jctc.1c00109
J. Chem. Theory Comput. 2021, 17, 2394−2408

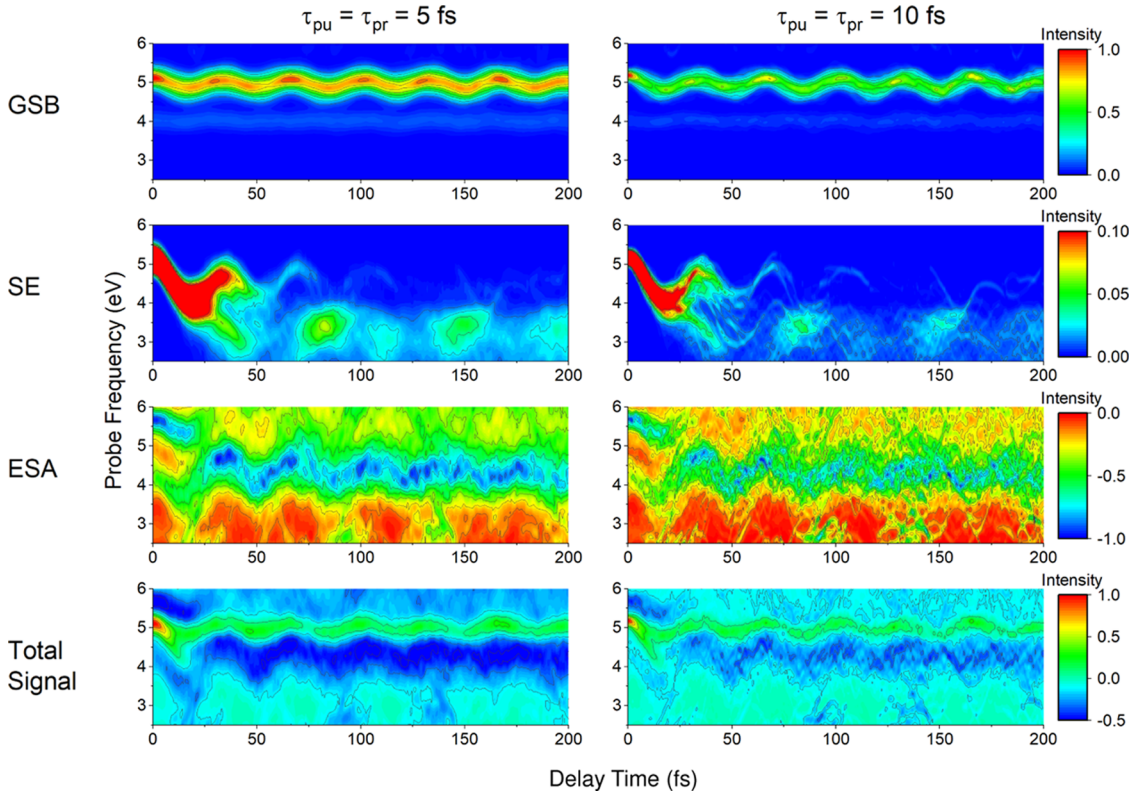

Figure 1. GSB, SE, and ESA contributions and the total integral signal $S_{int}(T,\omega_{pr})$ (from top to bottom) as a function of T and ω_{pr}. The pump pulse (ω_{pu} = 5.2 eV) is tuned into resonance with the $B_{2u}(\pi\pi^*)$ state. Left panel: τ_a = 5 fs. Right panel: τ_a = 10 fs.

the states of manifold {II} as well as the oscillator strengths for all transitions between the states of manifolds {I} and {II} were calculated for 200 trajectories randomly selected from the 1000 trajectories in manifold {I}. The integral and dispersed ESA signals were found to be reasonably converged with 200 trajectories. The nonaugmented cc-pVDZ basis set was used for the latter calculations to save computing time and to eliminate optically dark valence-Rydberg transitions (the ionization potential of pyrazine is 9.0 eV[95]). The classical equations of motion were integrated with the velocity-Verlet algorithm using a time step of 0.5 fs. Trajectories in manifold {I} were propagated with LZSH as described in Section 5. More details can be found in ref 69. TA PP signals were simulated for pump and probe pulses with Gaussian envelopes, $\mathcal{E}_a(t) = \exp\{-(t/\tau_a)^2\}$, $\mathcal{E}_a(\omega) \sim \exp\{-(\omega\tau_a)^2/4\}$, and a = pu, pr. The intensities and pulse durations τ_a are the same for both pulses. The dephasing parameter for the dispersed signal (see Appendix C) was chosen as ν = 0.01 eV, corresponding to a dephasing time constant of 66 fs.

Integral TA PP signals of pyrazine are presented in Figure 1. The GSB, SE, and ESA contributions as well as the total signals are shown separately, from top to bottom. The left panel shows the results for τ_a = 5 fs and the right panel shows the results for τ_a = 10 fs.

Let us first consider the integral signal excited and detected with short pulses (τ_a = 5 fs, Figure 1, left column).The dominant contribution to the GSB signal (first panel from top) exhibits a maximum for probe frequencies near the vertical excitation energy of the S_2 state ($\omega_{pr} \approx$ 5 eV). The location of the maximum shows a low-amplitude oscillation which corresponds to the ground-state normal mode Q_1 with a frequency of 0.126 eV and a period of 33 fs. It reflects the dynamics of the hole which is generated by the absorption of the $B_{2u}(\pi\pi^*)$ state, which has the largest transition dipole moment from the ground state. It is well known that the GSB wave packet produced by an instantaneous (Dirac delta-function) pump pulse is stationary provided the transition dipole moments $\mu_{ge}(\boldsymbol{R}_g)$ are coordinate independent. This is corroborated by eq 39, which predicts that $D_0(\omega_{pu},\boldsymbol{R}_g) \sim |\mu_{ge}[\boldsymbol{R}_g]|^2\rho_g(\boldsymbol{R}_g)$ in the case of impulsive excitation. The oscillation amplitude of the GSB signal may arise from non-Condon effects or may be an artefact of the initial sampling from the harmonic Wigner distribution. In contrast to the bending-type tuning modes Q_{6a} and Q_{8a}, the PE function of stretching-type mode Q_1 exhibits a significant anharmonicity in the electronic ground state. There is also a weak second contribution to the GSB signal at probe frequencies near 4.0 eV. This much weaker signal reflects the hole generated by the absorption of the weakly allowed $B_{3u}(n\pi^*)$ state. It does not exhibit oscillations of the peak frequency, which reflects the lower Condon activity of the totally symmetric modes in the $B_{3u}(n\pi^*)$ state.

The SE signal (second panel from top) monitors the wave-packet dynamics in manifold {I} by its projection on the ground-state PE surface. The majority of the excited-state trajectories are initiated in the $B_{2u}(\pi\pi^*)$ state because the pump pulse is tuned into resonance with this state, which also possesses the highest transition dipole moment. The SE contribution shows a rapid ~20 fs $B_{2u}(\pi\pi^*) \rightarrow B_{3u}(n\pi^*)$ population transfer, in agreement with the time-resolved photoelectron spectroscopy measurements.[84] The SE signal exhibits peaks at $T \approx$ 85 fs and $T \approx$ 150 fs, which match the electronic population revivals in the $B_{2u}(\pi\pi^*)$ state.[69] At $T \approx$ 20 fs, the SE signal reflects a bifurcation of the initial wave

https://doi.org/10.1021/acs.jctc.1c00109
J. Chem. Theory Comput. 2021, 17, 2394−2408

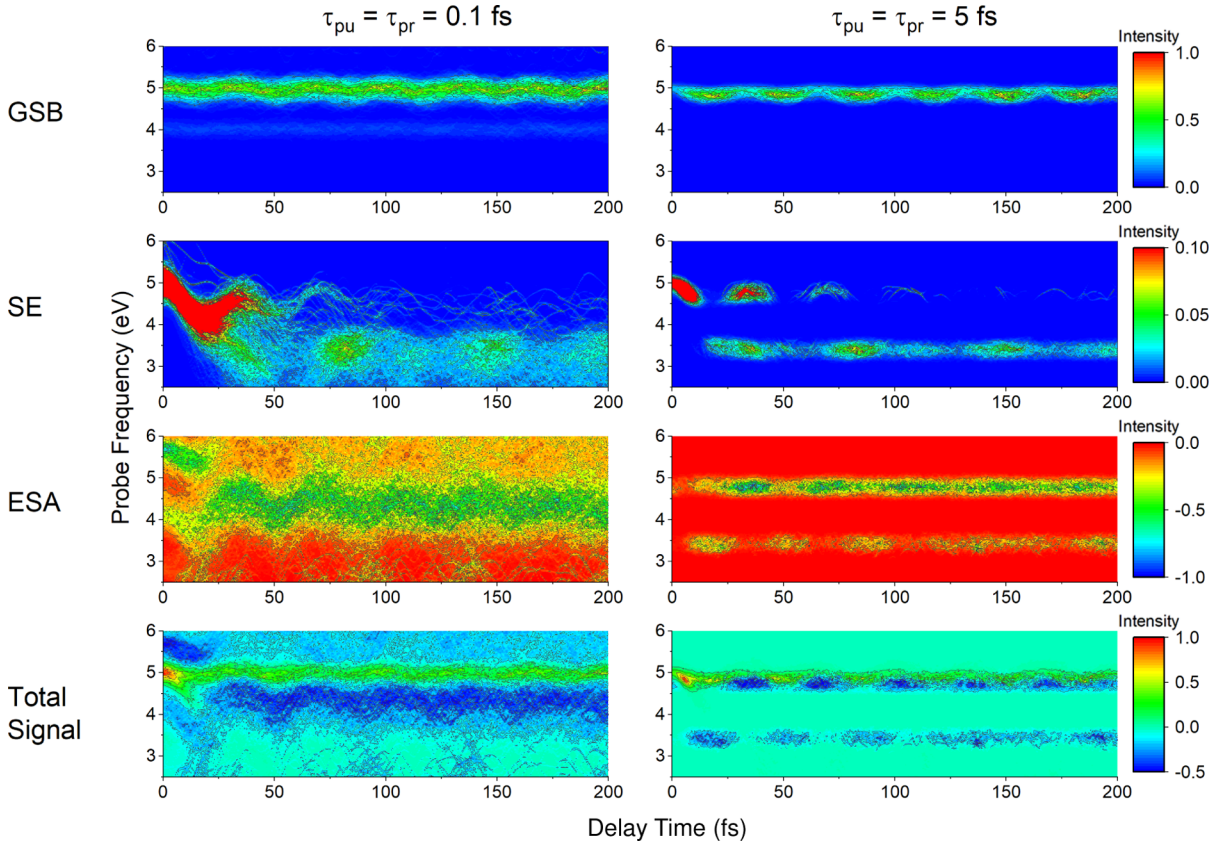

Figure 2. GSB, SE, and ESA contributions and the total dispersed signal $S_{dis}(T,\omega)$ as a function of T and ω for ν = 0.01 eV and ω_{pu} = 5.2 eV; τ_a = 100 as (left panel) and τ_a = 5 fs (right panel). In the left panel, the signals are shown for ω_{pr} = 4.8 eV. In the right panel, the signals are shown for ω_{pr} = 4.8 eV (probing around $B_{2u}(\pi\pi^*)$) and ω_{pr} = 3.4 eV (probing around $B_{3u}(n\pi^*)$).

packet in the $B_{2u}(\pi\pi^*)$ state: most of the trajectories switch to the $B_{3u}(n\pi^*)$ state through the $B_{2u}(\pi\pi^*)/B_{3u}(n\pi^*)$ conical intersection, while a smaller fraction of the trajectories remains in the $B_{2u}(\pi\pi^*)$ state. The SE signal records a large amplitude wavepacket motion with the high-frequency tuning mode Q_1. It is superimposed by a slower oscillation, which monitors wave-packet dynamics in the tuning mode Q_{6a} with a period of 56 fs. Q_1 and Q_{6a} are the dominant tuning modes of the $B_{2u}(\pi\pi^*)/B_{3u}(n\pi^*)$ conical intersection,[63] and their frequencies are approximately in a 2:1 resonance.

The ESA signal (third panel from top) records the projection of the wave packet dynamics in manifold {I} onto the PE surfaces of the resonant electronic states of manifold {II}. Due to the high density of the higher excited states, the time and frequency evolution of the ESA signal is more complex than that of the SE signal. Nevertheless, the maximum of the ESA signal exhibits a clearly visible oscillation with the frequency of normal mode Q_1.

The total signal (lowest panel) is the sum of the GSB, SE, and ESA contributions. It is dominated by the GSB signal which peaks at probe frequencies near 5.0 eV. While the SE signal revealing the dynamics at the $B_{2u}(\pi\pi^*)/B_{3u}(n\pi^*)$ conical intersection is clearly visible for delay times up to about 20 fs, the SE signal is overwhelmed by the ESA signal at longer time scales. In the case of pyrazine, the time- and frequency-resolved fluorescence up-conversion signal, which is essentially identical to the SE signal of TA PP spectroscopy, provides the best visualization of the excited-state wave-packet dynamics.[83,88] It is known that the $A_u(n\pi^*)$ state also is populated from the $B_{2u}(\pi\pi^*)$ state and that there are electronic population oscillations among the $B_{3u}(\pi\pi^*)$ and $A_u(n\pi^*)$ states.[63,69] Because the $A_u(n\pi^*)$ state is completely dark in absorption and emission from the ground state and the $B_{3u}(n\pi^*)$-associated signal is weak, the effect of the $A_u(n\pi^*)$ state on the excited-state dynamics of pyrazine cannot be clearly discerned in the TA PP spectrum.

The signals excited by longer pump and probe pulses (τ_a = 10 fs, right column of Figure 1) are similar to those excited by short pulses (τ_a = 5 fs, left column of Figure 1). As expected, longer pulses decrease the time resolution and increase the frequency resolution of TA PP signals.[96] Hence, the spectral features become narrower (better frequency resolution), while the signal in the time domain becomes more diffuse (worse time resolution). The bifurcation of the wave packet at $T \approx 20$ fs is clearly seen both in the SE and total signals.

The GSB, SE, ESA, and the total dispersed signal $S_{dis}(T,\omega)$ (from top to bottom) are depicted in Figure 2 for τ_a = 100 as (right column) and τ_a = 5 fs (left column). In contrast to the integral signal, time and frequency resolutions of the dispersed TA PP signals are not Fourier limited[24,96] and the frequency resolution of $S_{dis}(T,\omega)$ is not directly related to the duration of the probe pulse τ_a. As follows from the definition (2) of the dispersed signal, the bandwidth of the spectrum of the probe pulse determines the spectral width of $S_{dis}(T,\omega)$. The spectral width of the 100 as pulse, ≈13 eV, covers the entire spectral range of interest, from ∼2 to ∼6 eV. The spectrum of the 5 fs pulse is 50 times narrower, and its width of ≈0.25 eV covers only a fraction of the spectral domain of interest. Hence, the signals in the right panel are shown for two probe carrier frequencies, ω_{pr} = 4.8 eV (probing in resonance with the

https://doi.org/10.1021/acs.jctc.1c00109
J. Chem. Theory Comput. 2021, 17, 2394−2408

$B_{2u}(\pi\pi^*)$ state) and ω_{pr} = 3.4 eV (probing in resonance with the $B_{3u}(n\pi^*)$ state).

The GSB, SE, and ESA contributions as well as the total dispersed signal $S_{dis}(T,\omega)$ simulated with ultrashort pump and probe pulses (τ_a = 100 as, left panel of Figure 2) are qualitatively similar to their counterparts for the integral signal $S_{int}(T,\omega_{pr})$ simulated with 5 and 10 fs pulses (Figure 1). The oscillations of the GSB signal are much weaker than those shown in Figure 1. The total dispersed signal in the bottom left panel of Figure 2 resembles its counterpart simulated for the reduced-dimensional model with instantaneous pump and probe pulses.[88]

The right column of Figure 2 shows the dispersed signal excited and detected with pulses of τ_a = 5 fs. Because the spectral width of the ≈5 fs pulse is around 0.25 eV, the dispersed signal is confined to this narrow frequency window. The signals around ω_{pr} = 4.8 and 3.4 eV in the right panels look like cuts through the corresponding signals in the left panels detected with 0.1 fs pulses. The signals do not mirror an oscillatory wave-packet motion because the bandwidth of the pulses is too narrow to map even the low-amplitude oscillations of the GSB signal. Nevertheless, nonstationary wave-packet motion is manifested in the ground-state (GSB) and excited-state (SE, ESA) signals through sequences of maxima separated by the period of the tuning mode Q_1. The contribution of SE is barely seen in the total signal which is dominated by the GSB contribution featuring the spectrum of the $B_{2u}(\pi\pi^*)$ state.

8. CONCLUSIONS

The DW approximation is a well-established concept for the calculation and interpretation of femtosecond time-resolved third-order spectroscopic signals.[48,50] It was recognized early that the DW expression for TA PP signals is well suited for evaluation with classical or semi-classical approximation methods.[54−57] So far, the classical DW approximation was employed for model systems with two or three electronic states and few nuclear degrees of freedom. In the present work, the theoretical framework for the implementation of the DW approximation for TA PP signals with ab initio on-the-fly classical trajectory calculations has been developed. The essential conditions for the validity of the DW approximation are temporally well-separated pump and probe pulses and pulse durations which are short compared to the electronic/nuclear dynamics of interest. The carrier frequencies of the pump and probe pulses determine the manifolds of electronic states which are resonantly coupled by the laser fields. For TA PP spectroscopy, these are, in addition to the electronic ground state, the manifold {I} of states which are resonant with the pump pulse and the manifold {II} of states which can be resonantly excited from manifold {I} by the probe pulse. In the ab initio calculations, all the electronic states fulfilling the resonance conditions between the energetically well-separated manifolds {0}, {I}, and {II} are included. While NACs between the energetically well-separated manifolds are neglected, NACs within manifold {I} are taken into account by a SH algorithm. The classical doorway and window functions account for the durations and spectral shapes of the laser pulses and define positive definite distributions which are well suited for stochastic sampling by classical trajectories.

The on-the-fly classical DW formalism has been implemented for the pyrazine molecule in the gas phase using the ADC(2) electronic-structure method. The strongly nonadiabatic dynamics involving conical intersections of the $B_{3u}(n\pi^*)$, $A_u(n\pi^*)$, and $B_{2u}(\pi\pi^*)$ singlet states was simulated with the LZSH algorithm. The GSB and SE signals obtained with the full-dimensional classical simulation are in good agreement with the GSB and SE signals obtained by quantum mechanical calculations for a four-state nine-mode model of pyrazine[88] (the ESA signal was not computed in the model study). The dependence of the GSB, SE, and ESA signals on the duration of the laser pulses was investigated. While the integral TA PP signals are rather insensitive to the pulse lengths as long as these are comparable with the periods of the relevant vibrational modes, the dispersed signals are strongly dependent on the duration of the probe pulse because the latter determines the accessible frequency window of the dispersed PP signals. For the monitoring of the richly structured SE signal of pyrazine, which covers an energy range of nearly two electron volts, probe pulses in the sub-femtosecond range are required to map the complete spectrum for a fixed carrier frequency of the probe pulse.

The classical DW approximation is not limited to TA PP spectra. The classical simulation of the excited-state nuclear dynamics is applicable when the time evolution of the signal is dominated by coherent vibrational motion. The time- and frequency-resolved fluorescence signal (fluorescence up-conversion), for example, is closely related to the SE signal of TA PP spectroscopy and is suitable for classical modeling. However, classical trajectory dynamics cannot account for interferences of electronic phases and therefore cannot describe vibrational structures arising from wave-packet interferences. On the other hand, homogeneous and inhomogeneous line-shape broadening effects caused by thermal low-frequency modes are well described by classical dynamics.[24]

The sub-picosecond photoinduced dynamics of small molecules like pyrazine is amenable to on-the-fly nonadiabatic trajectory simulations with sufficiently accurate electronic-structure methods. For larger chromophores or multi-chromophore systems, such brute-force simulations may be prohibitively expensive. For such applications, modern artificial intelligence methods may be employed for the automated construction of reduced-dimensional global diabatic PE surfaces from ab initio trajectory data, thereby projecting the dynamics on the most relevant nuclear degrees of freedom.[97−100] Given such interpolated multisheeted multidimensional PE surfaces, the DW formula may be evaluated either with quantum wave-packet calculations or with classical trajectory simulations.

The classical simulation methodology described herein can be adapted to simulations for extended systems in the framework of all-electron DFT calculations, for example, solids[23,101−103] or liquids[104−106] as well as to chromophores in a condensed-phase environment using the so-called QM/MM approximation, where QM stands for the quantum mechanically computed PE surfaces of the chromophore (the solute) and MM stands for classical molecular dynamics simulations of the solvent with empirical force fields.[107−110] With this well-established simulation methodology, solvation effects such as electronic dephasing or vibrational cooling can be straightforwardly included in the classical simulations of electronic four-wave-mixing spectra.

Time- and frequency-resolved spectra, such as TA PP spectra, provide more detailed information on the excited-state dynamics than just electronic population probabilities. In time-

https://doi.org/10.1021/acs.jctc.1c00109
J. Chem. Theory Comput. 2021, 17, 2394−2408

and frequency-resolved fluorescence spectroscopy, for example, the excited-state wave-packet dynamics is monitored by projection on the vibrational levels of the electronic ground state.[81,111] The quantitative simulation of nonlinear spectra with classical trajectories therefore is a more stringent test of the validity of classical approximations, such as the SH algorithm, than the simulation of electronic population probabilities which are integrated over all nuclear degrees of freedom. Therefore, simulations of nonlinear signals for representative chromophores may deepen our understanding of the validity of classical approximations and thus may drive the development of improved classical approximation schemes.

■ APPENDIX A

DW Representation

The nonlinear polarization $\mathcal{P}(T, t)$ governing the TA PP signal is expressed through the third-order response functions as follows[24,112,113]

$$\mathcal{P}(T, t) \sim -\mathrm{i}\int_0^\infty \mathrm{d}t_3\int_0^\infty \mathrm{d}t_2\int_0^\infty \mathrm{d}t_1\mathcal{E}_{\mathrm{pu}}(t + T - t_3 - t_2 - t_1)\mathcal{E}_{\mathrm{pu}}(t + T - t_3 - t_2)\mathcal{E}_{\mathrm{pr}}(t - t_3)\{\mathrm{e}^{-\mathrm{i}\omega_{\mathrm{pu}}t_1}\mathrm{e}^{\mathrm{i}\omega_{\mathrm{pr}}(t_3-t)}R_{\mathrm{R}}(t_3, t_2, t_1) + \mathrm{e}^{\mathrm{i}\omega_{\mathrm{pu}}t_1}\mathrm{e}^{\mathrm{i}\omega_{\mathrm{pr}}(t_3-t)}R_{\mathrm{NR}}(t_3, t_2, t_1)\} \tag{45}$$

Here, the rephasing (R) and nonrephasing (NR) response functions are defined as[24,112,113]

$$R_{\mathrm{R}}(t_3, t_2, t_1) = R_2(t_3, t_2, t_1) + R_3(t_3, t_2, t_1) - R_6(t_3, t_2, t_1)^*$$

$$R_{\mathrm{NR}}(t_3, t_2, t_1) = R_1(t_3, t_2, t_1) + R_4(t_3, t_2, t_1) - R_5(t_3, t_2, t_1)^*$$

The R_1−R_6 are explicitly expressed in terms of blocks of the molecular Hamiltonian, eq 14, blocks of the transition dipole moment operator, eq 15, and initial vibrational distribution, eq 22, as follows[24,112,113]

$$R_1(t_3, t_2, t_1) = \mathrm{Tr}[\mathrm{e}^{\mathrm{i}H_0t_1}\mu_{0,\mathrm{I}}\,\mathrm{e}^{\mathrm{i}H_\mathrm{I}t_2}\mu_{\mathrm{I},0}\,\mathrm{e}^{\mathrm{i}H_0t_3}\mu_{0,\mathrm{I}}\,\mathrm{e}^{-\mathrm{i}H_\mathrm{I}(t_1+t_2+t_3)}\mu_{\mathrm{I},0}\rho_{0,0}^{(0)}]$$

$$R_2(t_3, t_2, t_1) = \mathrm{Tr}[\mu_{0,\mathrm{I}}\,\mathrm{e}^{\mathrm{i}H_\mathrm{I}(t_1+t_2)}\mu_{\mathrm{I},0}\,\mathrm{e}^{\mathrm{i}H_0t_3}\mu_{0,\mathrm{I}}\,\mathrm{e}^{-\mathrm{i}H_\mathrm{I}(t_2+t_3)}\mu_{\mathrm{I},0}\,\mathrm{e}^{-\mathrm{i}H_0t_1}\rho_{0,0}^{(0)}]$$

$$R_3(t_3, t_2, t_1) = \mathrm{Tr}[\mu_{0,\mathrm{I}}\,\mathrm{e}^{\mathrm{i}H_\mathrm{I}t_1}\mu_{\mathrm{I},0}\,\mathrm{e}^{\mathrm{i}H_0(t_2+t_3)}\mu_{0,\mathrm{I}}\,\mathrm{e}^{-\mathrm{i}H_\mathrm{I}t_3}\mu_{\mathrm{I},0}\,\mathrm{e}^{-\mathrm{i}H_0(t_1+t_2)}\rho_{0,0}^{(0)}]$$

$$R_4(t_3, t_2, t_1) = \mathrm{Tr}[\mathrm{e}^{\mathrm{i}H_0(t_1+t_2+t_3)}\mu_{0,\mathrm{I}}\,\mathrm{e}^{-\mathrm{i}H_\mathrm{I}t_3}\mu_{\mathrm{I},0}\,\mathrm{e}^{-\mathrm{i}H_0t_2}\mu_{0,\mathrm{I}}\,\mathrm{e}^{-\mathrm{i}H_\mathrm{I}t_1}\mu_{10}\rho_{0,0}^{(0)}]$$

$$R_5(t_3, t_2, t_1) = \mathrm{Tr}[\mathrm{e}^{\mathrm{i}H_0t_1}\mu_{0,\mathrm{I}}\,\mathrm{e}^{\mathrm{i}H_\mathrm{I}t_2}\mu_{\mathrm{I,II}}\,\mathrm{e}^{\mathrm{i}H_{\mathrm{II}}t_3}\mu_{\mathrm{II,I}}\,\mathrm{e}^{-\mathrm{i}H_\mathrm{I}(t_1+t_2+t_3)}\mu_{\mathrm{I},0}\rho_{0,0}^{(0)}]$$

$$R_6(t_3, t_2, t_1) = \mathrm{Tr}[\mu_{0,\mathrm{I}}\,\mathrm{e}^{\mathrm{i}H_\mathrm{I}(t_1+t_2)}\mu_{\mathrm{I,II}}\,\mathrm{e}^{\mathrm{i}H_{\mathrm{II}}t_3}\mu_{\mathrm{II,I}}\,\mathrm{e}^{-\mathrm{i}H_\mathrm{I}(t_2+t_3)}\mu_{\mathrm{I},0}\,\mathrm{e}^{-\mathrm{i}H_0t_1}\rho_{0,0}^{(0)}] \tag{46}$$

The trace is taken over electronic matrices and the nuclear degrees of freedom. The response functions with α = 1, 2, 3, 4 describe optical response within manifolds {0} and {I}, while the response functions with α = 5, 6 involve all three manifolds {0}, {I}, and {II}. Furthermore, R_3 and R_4 describe the GSB, R_1 and R_2 describe the SE, and R_5 and R_6 describe the ESA.

The DW approximation for TA PP signals is usually formulated in terms of the response functions R_1−R_4.[24,48,50] Below, we generalize the DW description to include R_5 and R_6, incorporating thus ESA. Inserting the PP polarization $\mathcal{P}(T, t)$ of eq 45 into eq 3, we obtain the explicit expression for $S(\omega_{\mathrm{pu}},T,\omega_{\mathrm{pr}},\tau_{\mathrm{t}})$ in terms of R_{R} and R_{NR}. Following references 24, 48, and 50 we change the integration variables

$$t = t' + t_3, \qquad t_2 = t' + T - t_2'$$

and obtain

$$S(\omega_{\mathrm{pu}}, T, \omega_{\mathrm{pr}}, \tau_t) \sim \mathrm{Re}\int_{-\infty}^{\infty}\mathrm{d}t'\int_0^\infty \mathrm{d}t_3\int_{-\infty}^{t'+T}\mathrm{d}t_2'\int_0^\infty \mathrm{d}t_1\mathcal{E}_{\mathrm{pr}}(t' + t_3 - \tau_t)\mathcal{E}_{\mathrm{pr}}(t')\mathcal{E}_{\mathrm{pu}}(t_2')\mathcal{E}_{\mathrm{pu}}(t_2' - t_1)\{\mathrm{e}^{-\mathrm{i}\omega_{\mathrm{pu}}t_1}\,\mathrm{e}^{\mathrm{i}\omega_{\mathrm{pr}}(t_3-\tau_t)}R_{\mathrm{R}}(t_3, t' + T - t_2', t_1) + \mathrm{e}^{\mathrm{i}\omega_{\mathrm{pu}}t_1}\,\mathrm{e}^{\mathrm{i}\omega_{\mathrm{pr}}(t_3-\tau_t)}R_{\mathrm{NR}}(t_3, t' + T - t_2', t_1)\} \tag{47}$$

Using eq 46, we can equivalently rewrite the response functions in terms of the doorway $D_\alpha(t_2',t_1)$ and window $W_\alpha(t_3,t')$ operators

$$R_\alpha(t_3, t' + T - t_2', t_1) = \mathrm{Tr}[\mathrm{e}^{-\mathrm{i}H_\mathrm{I}T}D_\alpha(t_2', t_1)\mathrm{e}^{\mathrm{i}H_\mathrm{I}T}W_\alpha(t_3, t')], \quad \alpha = 1,2,5,6 \tag{48}$$

$$R_\alpha(t_3, t' + T - t_2', t_1) = \mathrm{Tr}[\mathrm{e}^{-\mathrm{i}H_0T}D_\alpha(t_2', t_1)\mathrm{e}^{\mathrm{i}H_0T}D_\alpha(t_3, t')], \quad \alpha = 3,4 \tag{49}$$

The response functions 48 are propagated in time in manifold {I}, while the response functions 49 are propagated in the electronic ground state {0}. Time propagation in manifold {II} is not necessary for the evaluation of third-order spectroscopic signals. Explicitly, the doorway operators are defined as

$$D_1(t_2', t_1) = D_5(t_2', t_1) = \mathrm{e}^{-\mathrm{i}H_\mathrm{I}(t_1-t_2')}\mu_{\mathrm{I},0}\rho_{0,0}^{(0)}\,\mathrm{e}^{\mathrm{i}H_0t_1}\mu_{0,\mathrm{I}}\,\mathrm{e}^{-\mathrm{i}H_\mathrm{I}t_2'}$$

$$D_3(t_2', t_1) = \mathrm{e}^{-\mathrm{i}H_0(t_1-t_2')}\rho_{0,0}^{(0)}\mu_{0,\mathrm{I}}\,\mathrm{e}^{\mathrm{i}H_\mathrm{I}t_1}\mu_{\mathrm{I},0}\,\mathrm{e}^{-\mathrm{i}H_0t_2'}$$

$$D_2(t_2', t_1) = D_6(t_2', t_1) = (D_1(t_2', t_1))^\dagger$$

$$D_4(t_2', t_1) = (D_3(t_2', t_1))^\dagger$$

The window operators read

$$W_1(t', t_3) = \mathrm{e}^{\mathrm{i}H_\mathrm{I}t'}\mu_{\mathrm{I},0}\,\mathrm{e}^{\mathrm{i}H_0t_3}\mu_{0,\mathrm{I}}\,\mathrm{e}^{-\mathrm{i}H_\mathrm{I}(t'+t_3)}$$

$$W_3(t', t_3) = \mathrm{e}^{\mathrm{i}H_0(t'+t_3)}\mu_{0,\mathrm{I}}\,\mathrm{e}^{-\mathrm{i}H_\mathrm{I}t_3}\mu_{\mathrm{I},0}\,\mathrm{e}^{-\mathrm{i}H_0t'}$$

$$W_5(t', t_3) = \mathrm{e}^{\mathrm{i}H_\mathrm{I}t'}\mu_{\mathrm{I,II}}\,\mathrm{e}^{\mathrm{i}H_{\mathrm{II}}t_3}\mu_{\mathrm{II,I}}\,\mathrm{e}^{-\mathrm{i}H_\mathrm{I}(t'+t_3)}$$

$$W_2(t', t_3) = W_1(t', t_3)$$

$$W_4(t', t_3) = W_3(t', t_3)$$

$$W_6(t', t_3) = W_5(t', t_3)$$

https://doi.org/10.1021/acs.jctc.1c00109
J. Chem. Theory Comput. 2021, 17, 2394−2408

Let us suppose that the pump and probe pulses are well temporally separated (if necessary, this approximation can be lifted by employing the generalized DW description[114,115]). We assume that the time delay T between the pulses is longer than the pulse durations τ_a (a = pu, pr)

$$T > \tau_a \tag{50}$$

and we neglect all contributions to TA PP signals decaying on the timescale τ_a (for Gaussian pulses, we drop all terms $\sim\exp\{-(T/\tau_a)^2\}$). Because t_2' in eq 47 is controlled by the pump pulse through the term $\mathcal{E}_{pu}(t_2')$, we can replace $\int_{-\infty}^{t_t+T} dt_2'...$ by $\int_{-\infty}^{\infty} dt_2'...$ provided inequality 50 is fulfilled. We obtain

$$S(\omega_{pu}, T, \omega_{pr}, \tau_t) \sim \mathrm{ReTr}[W_0(\omega_{pr}, \tau_t)e^{-iH_0T} D_0(\omega_{pu})e^{iH_0T} + \{W_I(\omega_{pr}, \tau_t) - W_{II}(\omega_{pr}, \tau_t)\}e^{-iH_IT} D_I(\omega_{pu})e^{iH_IT}] \tag{51}$$

Here

$$D_0(\omega_{pu}) = \int_{-\infty}^{\infty} dt_2' \int_0^{\infty} dt_1 \mathcal{E}_{pu}(t_2')\mathcal{E}_{pu}(t_2' - t_1)e^{i\omega_{pu}t_1} D_4(t_2', t_1) + \text{H. c.}$$
$$D_I(\omega_{pu}) = \int_{-\infty}^{\infty} dt_2' \int_0^{\infty} dt_1 \mathcal{E}_{pu}(t_2')\mathcal{E}_{pu}(t_2' - t_1)e^{i\omega_{pu}t_1} D_1(t_2', t_1) + \text{H. c.} \tag{52}$$

and

$$W_0(\omega_{pr}, \tau_t) = \int_{-\infty}^{\infty} dt' \int_0^{\infty} dt_3 \mathcal{E}_{pr}(t')\mathcal{E}_{pr}(t' - \tau_t + t_3) e^{i\omega_{pr}(t_3-\tau_t)} W_4(t', t_3)$$
$$W_I(\omega_{pr}, \tau_t) = \int_{-\infty}^{\infty} dt' \int_0^{\infty} dt_3 \mathcal{E}_{pr}(t')\mathcal{E}_{pr}(t' - \tau_t + t_3) e^{i\omega_{pr}(t_3-\tau_t)} W_1(t', t_3)$$
$$W_{II}(\omega_{pr}, \tau_t) = \int_{-\infty}^{\infty} dt' \int_0^{\infty} dt_3 \mathcal{E}_{pr}(t')\mathcal{E}_{pr}(t' - \tau_t + t_3) e^{i\omega_{pr}(t_3-\tau_t)} W_5(t', t_3) \tag{53}$$

Equation 51 is the quantum mechanical expression for the TA PP signal in the DW approximation. It is valid for nonoverlapping pump and probe pulses, as required by eq 50. We make an additional short-pulse approximation, assuming that the laser pulses are short on the nuclear dynamics timescale.[24] With this approximation, the nuclear dynamics during the time intervals t_2' and t' can be neglected because the latter are controlled by the pump pulse through $\mathcal{E}_{pu}(t_2')$ and by the probe pulse through $\mathcal{E}_{pr}(t')$. Hence, the DW operators of eqs 52 and 53 are simplified as follows

$$D_\alpha(t_2', t_1) \to D_\alpha(0, t_1), \qquad W_\alpha(t', t_3) \to W_\alpha(0, t_3) \tag{54}$$

For vibrational periods of ≈30 fs and laser pulses of ≈10 fs, the approximation of eq 54 is well justified. Finally, swapping operators under the trace in eq 51 and moving the action of the Heisenberg propagators $e^{iH_nT}...e^{-iH_nT}$ (n = 0, I) from the doorway operators to the window operators, we obtain eqs 23−31.

APPENDIX B

DW Representation: From Quantum Description to Classical Trajectories

We make the following approximations. (i) Evolutions of electronic coherences in the DW operators are evaluated within the short-time classical Condon approximation, see Eqs. 32 and 33. This approximation is rather well justified because the time intervals t_1 and t_3 are controlled both by pulse durations and by electronic dephasing (typical electronic dephasing times for short-lived electronic states such as the B_{2u} state of pyrazine are in the range of tens of femtoseconds). (ii) T-evolutions of electronic populations, which are generated by the Heisenberg propagators $e^{iHnT}...e^{-iHnT}$ (n = 0, I), acting on the window operators as specified by eqs 29−31, are replaced by evolutions along trajectories. (iii) The quantum thermal distribution in the electronic ground state is substituted by the corresponding phase-space Wigner distribution, $\rho_{0,0}^{(0)} \to \rho_g^{Wig}(\mathbf{R}_g, \mathbf{P}_g)$, and (iv) the trace over vibrational degrees of freedom is replaced by stochastic sampling (denoted by angular brackets) of the initial conditions $\mathbf{R}_g$, $\mathbf{P}_g$ from the positive definite distributions D_0 (for GSB) and D_I (for SE and ESA). With approximations (i−iv), eq 23 reduces to

$$S(\omega_{pu}, T, \omega_{pr}, \tau_t) \sim \langle D_0(\omega_{pu}, \mathbf{R}_g, \mathbf{P}_g)W_0(\omega_{pr}, \tau_t, \mathbf{R}_g(T), \mathbf{P}_g(T))\rangle + \langle D_I(\omega_{pu}, \mathbf{R}_g, \mathbf{P}_g)W_I(\omega_{pr}, \tau_t, \mathbf{R}_e(T), \mathbf{P}_e(T))\rangle - \langle D_I(\omega_{pu}, \mathbf{R}_g, \mathbf{P}_g)W_{II}(\omega_{pr}, \tau_t, \mathbf{R}_e(T), \mathbf{P}_e(T))\rangle \tag{55}$$

Explicitly

$$D_0(\omega_{pu}, \mathbf{R}_g, \mathbf{P}_g) = \sum_e \int_{-\infty}^{\infty} dt_2' \int_0^{\infty} dt_1 \mathcal{E}_{pu}(t_2')\mathcal{E}_{pu}(t_2' - t_1) e^{i(\omega_{pu} - U_{eg}(\mathbf{R}_g))t_1} |\mu_{ge}(\mathbf{R}_g)|^2 \rho_g^{Wig}(\mathbf{R}_g, \mathbf{P}_g) + \text{H. c.} \tag{56}$$

$$D_I(\omega_{pu}, \mathbf{R}_g, \mathbf{P}_g) = \int_{-\infty}^{\infty} dt_2' \int_0^{\infty} dt_1 \mathcal{E}_{pu}(t_2')\mathcal{E}_{pu}(t_2' - t_1) e^{i(\omega_{pu} - U_{eg}(R_g))t_1} |\mu_{ge}(\mathbf{R}_g)|^2 \rho_g^{Wig}(\mathbf{R}_g, \mathbf{P}_g) + \text{H. c.} \tag{57}$$

are the doorway functions, while

$$W_0(\omega_{pr}, \tau_t, \mathbf{R}_g(T), \mathbf{P}_g(T)) = \sum_e \int_{-\infty}^{\infty} dt' \int_0^{\infty} dt_3 \mathcal{E}_{pr}(t')\mathcal{E}_{pr}(t' - \tau_t + t_3) e^{-i\omega_{pr}\tau_t} e^{i(\omega_{pr} - U_{eg}(\mathbf{R}_g(T)))t_3} |\mu_{ge}(\mathbf{R}_g(T))|^2 \tag{58}$$

$$W_I(\omega_{pr}, \tau_t, \mathbf{R}_e(T), \mathbf{P}_e(T)) = \int_{-\infty}^{\infty} dt' \int_0^{\infty} dt_3 \mathcal{E}_{pr}(t')\mathcal{E}_{pr}(t' - \tau_t + t_3) e^{-i\omega_{pr}\tau_t} e^{i(\omega_{pr} - U_{e(T)g}(\mathbf{R}_e(T)))t_3} |\mu_{ge(T)}(\mathbf{R}_e(T))|^2 \tag{59}$$

$$W_{II}(\omega_{pr}, \tau_t, \mathbf{R}_e(T), \mathbf{P}_e(T)) = \sum_f \int_{-\infty}^{\infty} dt' \int_0^{\infty} dt_3 \mathcal{E}_{pr}(t')\mathcal{E}_{pr}(t' - \tau_t + t_3) e^{-i\omega_{pr}\tau_t} e^{i(\omega_{pr} - U_{fe(T)}(\mathbf{R}_e(T)))t_3} |\mu_{e(T)f}(\mathbf{R}_e(T))|^2 \tag{60}$$

https://doi.org/10.1021/acs.jctc.1c00109
J. Chem. Theory Comput. 2021, 17, 2394−2408

are the window functions. The Condon transition frequencies $U_{eg}(\boldsymbol{R}_g)$ are defined in eqs 36 and 37, and the matrix elements of the transition dipole moment operators $\mu_{ge}(\boldsymbol{R}_g)$ are defined in eqs 34 and 35. All T-dependent quantities in eqs 58−60 are evaluated along nuclear trajectories either in the electronic ground state $(\boldsymbol{R}_g(T), \boldsymbol{P}_g(T))$ or in an excited electronic state $(\boldsymbol{R}_e(T), \boldsymbol{P}_e(T))$.

We are now in the position to derive explicit working expressions for the evaluation of TA PP signals. According to eq 4, the integral signal is given by eqs 55−60 with $\tau_t = 0$. Expressing the pulse envelopes $\mathcal{E}_a(t)$ through $\mathcal{E}_a(\omega)$ (a = pu, pr) via back Fourier transforms and evaluating simple integrals, we arrive at eqs 38−43. The terms proportional to W_0, W_I, and W_{II} in eq 38 give, correspondingly, the GSB, SE, and ESA contributions to the TA PP signal.

APPENDIX C

Explicit Formulas for Dispersed TA PP Signals

Following eq 5, the dispersed TA PP signal is obtained by performing the Fourier transform of eq 55 with respect to τ_t. In contrast to the integral PP signal, the dispersed PP signal is sensitive to electronic dephasing, which controls the free induction decay of the electronic polarization generated by the probe pulse. Introducing the electronic dephasing operator, $\exp(-\nu t_3)$, where ν is the electronic dephasing rate, and expressing $\mathcal{E}_a(t)$ through $\mathcal{E}_a(\omega)$, we obtain the final expressions

$$\begin{aligned} S_{dis}(T, \omega) \sim & \\ & \langle D_0(\omega_{pu}, \boldsymbol{R}_g, \boldsymbol{P}_g) W_0^{dis}(\omega_{pr}, \omega, \boldsymbol{R}_g(T), \boldsymbol{P}_g(T))\rangle \\ & + \langle D_I(\omega_{pu}, \boldsymbol{R}_g, \boldsymbol{P}_g) W_I^{dis}(\omega_{pr}, \omega, \boldsymbol{R}_e(T), \boldsymbol{P}_e(T))\rangle \\ & - \langle D_I(\omega_{pu}, \boldsymbol{R}_g, \boldsymbol{P}_g) W_{II}^{dis}(\omega_{pr}, \omega, \boldsymbol{R}_e(T), \boldsymbol{P}_e(T))\rangle \end{aligned} \tag{61}$$

where the doorway functions are defined by eqs 39 and 40 and

$$\begin{aligned} & W_0^{dis}(\omega_{pr}, \omega, \boldsymbol{R}_g(T), \boldsymbol{P}_e(T)) \\ & = \mathcal{E}_{pr}^2(\omega - \omega_{pr}) \sum_e \frac{\nu}{\nu^2 + (\omega - \omega_{eg}(R_g(T)))^2} \\ & \quad |\mu_{ge}(\boldsymbol{R}_g(T))|^2 \end{aligned} \tag{62}$$

$$\begin{aligned} & W_I^{dis}(\omega_{pr}, \omega, \boldsymbol{R}_e(T), \boldsymbol{P}_e(T)) \\ & = \mathcal{E}_{pr}^2(\omega - \omega_{pr}) \frac{\nu}{\nu^2 + (\omega - \omega_{e(T)g}(\boldsymbol{R}_e(T)))^2} \\ & \quad |\mu_{ge(T)}(\boldsymbol{R}_e(T))|^2 \end{aligned} \tag{63}$$

$$\begin{aligned} & W_{II}^{dis}(\omega_{pr}, \omega, \boldsymbol{R}_e(T), \boldsymbol{P}_e(T)) \\ & = \mathcal{E}_{pr}^2(\omega - \omega_{pr}) \sum_f \frac{\nu}{\nu^2 + (\omega - \omega_{fe(T)}(\boldsymbol{R}_e(T)))^2} \\ & \quad |\mu_{e(T)f}(\boldsymbol{R}_e(T))|^2 \end{aligned} \tag{64}$$

are the dispersed window functions.

It is assumed that the electronic dephasing time constant ν^{-1} entering the dispersed window functions is longer than the pulse duration τ_a. The dephasing rate ν determines the resolution of $S_{dis}(T,\omega)$ in the frequency domain. The averaging of the transition frequencies $\omega_{e(T)g}(\boldsymbol{R}_e(T))$ and $\omega_{fe(T)}(\boldsymbol{R}_e(T))$ over classical trajectories also gives rise to electronic dephasing. If the averaging over trajectories is the main source of dephasing, the simulated $S_{dis}(T,\omega)$ becomes independent of the parameter ν. If $\nu \to 0$, then $\nu/(\nu^2 + x^2) \sim \delta(x)$ and

$$S_{int}(T, \omega_{pr}) = \int_{-\infty}^{\infty} d\omega S_{dis}(T, \omega)$$

as it should be.[24] If the dispersed signal is detected by a spectrometer (i.e., without heterodyning with the probe pulse), then $S_{dis}(T, \omega) \sim \mathcal{P}(T, \omega)$. In this case, one has to replace $\mathcal{E}_{pr}^2(\omega - \omega_{pr}) \to \mathcal{E}_{pr}(\omega - \omega_{pr})$ in eqs 62−64. Hence, the ideal dispersed signal, which would be detected with perfect time and frequency resolution, is obtained by putting $\mathcal{E}_{pr}^2(\omega - \omega_{pr}) \to 1$ in eqs 62−64.

AUTHOR INFORMATION

Corresponding Author

Wolfgang Domcke − *Department of Chemistry, Technical University of Munich, D-85747 Garching, Germany;* orcid.org/0000-0001-6523-1246; Email: domcke@ch.tum.de

Authors

Maxim F. Gelin − *School of Sciences, Hangzhou Dianzi University, Hangzhou 310018, China;* orcid.org/0000-0003-3092-3343

Xiang Huang − *Department of Chemistry, Technical University of Munich, D-85747 Garching, Germany*

Weiwei Xie − *Institute of Physical Chemistry, Karlsruhe Institute of Technology, 76131 Karlsruhe, Germany;* orcid.org/0000-0001-8224-5340

Lipeng Chen − *Max Planck Institute for the Physics of Complex Systems, D-01187 Dresden, Germany*

Nađa Došlić − *Department of Physical Chemistry, Ruder Boscovic Institute, HR-10000 Zagreb, Croatia;* orcid.org/0000-0001-6535-9020

Complete contact information is available at: https://pubs.acs.org/10.1021/acs.jctc.1c00109

Notes

The authors declare no competing financial interest.

ACKNOWLEDGMENTS

M.F.G. acknowledges support from the Hangzhou Dianzi University through the startup funding. W.D. acknowledges the support by a grant of the Deutsche Forschungsgemeinschaft (DO 256/42-2). W.X. acknowledges support by a research project of the Virtual Material Design (VirtMat) program. L.P.C. acknowledges support from the Max-Planck Gesellschaft via the MPI-PKS visitors program. N.D. acknowledges support by the Humboldt Foundation Linkage Programme and by the Croatian Science Foundation (grant HRZZ IP-2016-06-1142). M.F.G. is grateful to Zhenggang Lan for stimulating discussions.

REFERENCES

(1) Car, R.; Parrinello, M. Unified Approach for Molecular Dynamics and Density-Functional Theory. *Phys. Rev. Lett.* **1985**, *55*, 2471−2474.

(2) Gordon, M. S.; Chaban, G.; Taketsugu, T. Interfacing Electronic Structure Theory with Dynamics. *J. Phys. Chem.* **1996**, *100*, 11512−11525.

(3) Schlegel, H. B.; Millam, J. M.; Iyengar, S. S.; Voth, G. A.; Daniels, A. D.; Scuseria, G. E.; Frisch, M. J. Ab Initio Molecular

Dynamics: Propagating the Density Matrix with Gaussian Orbitals. *J. Chem. Phys.* **2001**, *114*, 9758−9763.
(4) Doltsinis, N. L.; Marx, D. First Principles Molecular Dynamics Involving Excited States and Nonadiabatic Transitions. *J. Theor. Comput. Chem.* **2001**, *1*, 319−349.
(5) Ben-Nun, M.; Martínez, T. J. Ab Initio Quantum Molecular Dynamics. *Adv. Chem. Phys.* **2002**, *121*, 439−512.
(6) Worth, G. A.; Robb, M. A. Applying Direct Molecular Dynamics to Non-Adiabatic Systems. *The Role of Degenerate States in Chemistry*; Advances in Chemical Physics; Wiley, 2002; Vol. *124*, pp 355−422.
(7) Curchod, B. F. E.; Martínez, T. J. Ab Initio Nonadiabatic Quantum Molecular Dynamics. *Chem. Rev.* **2018**, *118*, 3305−3336.
(8) Crespo-Otero, R.; Barbatti, M. Recent Advances and Perspectives on Nonadiabatic Mixed Quantum-Classical Dynamics. *Chem. Rev.* **2018**, *118*, 7026−7068.
(9) Tully, J. C.; Preston, R. K. Trajectory Surface Hopping Approach to Nonadiabatic Molecular Collisions: The Reaction of H+ with D2. *J. Chem. Phys.* **1971**, *55*, 562−572.
(10) Tully, J. C. Molecular Dynamics with Electronic Transitions. *J. Chem. Phys.* **1990**, *93*, 1061−1071.
(11) Heller, E. J. Time-dependent Approach to Semiclassical Dynamics. *J. Chem. Phys.* **1975**, *62*, 1544−1555.
(12) Heller, E. J. Frozen Gaussians: A Very Simple Semiclassical Approximation. *J. Chem. Phys.* **1981**, *75*, 2923−2931.
(13) Sawada, S. I.; Metiu, H. A Gaussian Wave Packet Method for Studying Time Dependent Quantum Mechanics in a Curve Crossing System: Low Energy Motion, Tunneling, and Thermal Dissipation. *J. Chem. Phys.* **1986**, *84*, 6293−6311.
(14) Coalson, R. D.; Karplus, M. Multidimensional Variational Gaussian Wave Packet Dynamics with Application to Photodissociation Spectroscopy. *J. Chem. Phys.* **1990**, *93*, 3919−3930.
(15) Buch, V. Exploration of Multidimensional Variational Gaussian Wave Packets as a Simulation Tool. *J. Chem. Phys.* **2002**, *117*, 4738−4750.
(16) Begušić, T.; Roulet, J.; Vanicek, J. On-the-fly ab initio Semiclassical Evaluation of Time-Resolved Electronic Spectra. *J. Chem. Phys.* **2018**, *149*, 244115.
(17) Begušić, T.; Vaníček, J. On-the-fly ab initio Semiclassical Evaluation of Third-Order Response Functions for Two-Dimensional Electronic Spectroscopy. *J. Chem. Phys.* **2020**, *153*, 184110.
(18) Barbatti, M.; Ruckenbauer, M.; Plasser, F.; Pittner, J.; Granucci, G.; Persico, M.; Lischka, H. Newton-X: a Surface-Hopping Program for Nonadiabatic Molecular Dynamics. *Wiley Interdiscip. Rev.: Comput. Mol. Sci.* **2014**, *4*, 26−33.
(19) Curchod, B. F. E.; Rothlisberger, U.; Tavernelli, I. Trajectory-Based Nonadiabatic Dynamics with Time-Dependent Density Functional Theory. *ChemPhysChem* **2013**, *14*, 1314−1340.
(20) Wang, L.; Akimov, A.; Prezhdo, O. V. Recent Progress in Surface Hopping: 2011-2015. *J. Phys. Chem. Lett.* **2016**, *7*, 2100−2112.
(21) Du, L.; Lan, Z. An On-the-Fly Surface-Hopping Program JADE for Nonadiabatic Molecular Dynamics of Polyatomic Systems: Implementation and Applications. *J. Chem. Theory Comput.* **2015**, *11*, 1360−1374.
(22) Mai, S.; Marquetand, P.; González, L. Nonadiabatic Dynamics: The SHARC Approach. *Wiley Interdiscip. Rev.: Comput. Mol. Sci.* **2018**, *8*, No. e1370.
(23) Nelson, T. R.; White, A. J.; Bjorgaard, J. A.; Sifain, A. E.; Zhang, Y.; Nebgen, B.; Fernandez-Alberti, S.; Mozyrsky, D.; Roitberg, A. E.; Tretiak, S. Non-adiabatic Excited-State Molecular Dynamics: Theory and Applications for Modeling Photophysics in Extended Molecular Materials. *Chem. Rev.* **2020**, *120*, 2215−2287.
(24) Mukamel, S. *Principles of Nonlinear Optical Spectroscopy*; Oxford University Press: New York, 1995.
(25) Seidner, L.; Stock, G.; Domcke, W. Nonperturbative Approach to Femtosecond Spectroscopy: General Theory and Application to Multidimensional Nonadiabatic Photoisomerization Processes. *J. Chem. Phys.* **1995**, *103*, 3998−4011.
(26) Gelin, M. F.; Egorova, D.; Domcke, W. Efficient Calculation of Time- and Frequency-Resolved Four-Wave-Mixing Signals. *Acc. Chem. Res.* **2009**, *42*, 1290−1298.
(27) Hudock, H. R.; Martínez, T. J. Excited-State Dynamics of Cytosine Reveal Multiple Intrinsic Subpicosecond Pathways. *ChemPhysChem* **2008**, *9*, 2486−2490.
(28) Werner, U.; Mitrić, R.; Bonačić-Koutecký, V. Simulation of Time Resolved Photoelectron Spectra with Stieltjes Imaging Illustrated on Ultrafast Internal Conversion in Pyrazine. *J. Chem. Phys.* **2010**, *132*, 174301.
(29) Humeniuk, A.; Wohlgemuth, M.; Suzuki, T.; Mitrić, R. Time-Resolved Photoelectron Imaging Spectra from Non-Adiabatic Molecular Dynamics Simulations. *J. Chem. Phys.* **2013**, *139*, 134104.
(30) Thompson, A. L.; Martínez, T. J. Time-Resolved Photoelectron Spectroscopy from First Principles: Excited State Dynamics of Benzene. *Faraday Discuss.* **2011**, *150*, 293.
(31) Arbelo-González, W.; Crespo-Otero, R.; Barbatti, M. Steady and Time-Resolved Photoelectron Spectra Based on Nuclear Ensembles. *J. Chem. Theory Comput.* **2016**, *12*, 5037−5049.
(32) Cusati, T.; Granucci, G.; Persico, M. Photodynamics and Time-Resolved Fluorescence of Azobenzene in Solution: A Mixed Quantum-Classical Simulation. *J. Am. Chem. Soc.* **2011**, *133*, 5109−5123.
(33) Klaumünzer, B.; Kröner, D.; Lischka, H.; Saalfrank, P. Non-Adiabatic Excited State Dynamics of Riboflavin After Photoexcitation. *Phys. Chem. Chem. Phys.* **2012**, *14*, 8693−8702.
(34) Lan, Z.; Lu, Y.; Weingart, O.; Thiel, W. Nonadiabatic Decay Dynamics of a Benzylidene Malononitrile. *J. Phys. Chem. A* **2012**, *116*, 1510−1518.
(35) Roy, S.; Ardo, S.; Furche, F. 5-Methoxyquinoline Photobasicity Is Mediated by Water Oxidation. *J. Phys. Chem. A* **2019**, *123*, 6645−6651.
(36) Polli, D.; Altoè, P.; Weingart, O.; Spillane, K. M.; Manzoni, C.; Brida, D.; Tomasello, G.; Orlandi, G.; Kukura, P.; Mathies, R. A.; Garavelli, M.; Cerullo, G. Conical Intersection Dynamics of the Primary Photoisomerization Event in Vision. *Nature* **2010**, *467*, 440−443.
(37) Nenov, A.; Borrego-Varillas, R.; Oriana, A.; Ganzer, L.; Segatta, F.; et al. UV-Light-Induced Vibrational Coherences: The Key to Understand Kasha Rule Violation in trans-Azobenzene. *J. Phys. Chem. Lett.* **2018**, *9*, 1534−1541.
(38) Borrego-Varillas, R.; Teles-Ferreira, D. C.; Nenov, A.; Conti, I.; Ganzer, L.; Manzoni, C.; Garavelli, M.; de Paula, A. M.; Cerullo, G. Observation of the Sub-100 Femtosecond Population of a Dark State in a Thiobase Mediating Intersystem Crossing. *J. Am. Chem. Soc.* **2018**, *140*, 16087−16093.
(39) Picchiotti, A.; Nenov, A.; Giussani, A.; Prokhorenko, V. I.; Miller, R. J. D.; Mukamel, S.; Garavelli, M. Pyrene, a Test Case for Deep-Ultraviolet Molecular Photophysics. *J. Phys. Chem. Lett.* **2019**, *10*, 3481−3487.
(40) Conti, I.; Cerullo, G.; Nenov, A.; Garavelli, M. Ultrafast Spectroscopy of Photoactive Molecular Systems from First Principles: Where We Stand Today and Where We Are Going. *J. Am. Chem. Soc.* **2020**, *142*, 16117−16139.
(41) Khundkar, L. R.; Zewail, A. H. Ultrafast Molecular Reaction Dynamics in Real-Time: Progress Over a Decade. *Annu. Rev. Phys. Chem.* **1990**, *41*, 15−60.
(42) Martin, J. L.; Vos, M. H. Femtosecond Biology. *Annu. Rev. Biophys. Biomol. Struct.* **1992**, *21*, 199−222.
(43) Beddard, G. Molecular Photophysics. *Rep. Prog. Phys.* **1993**, *56*, 63−171.
(44) de Boeij, W. P.; Pshenichnikov, M. S.; Wiersma, D. A. Ultrafast Solvation Dynamics Explored by Femtosecond Photon Echo Spectroscopies. *Annnu. Rev. Phys. Chem.* **1998**, *49*, 99−123.
(45) Fushitani, M. Applications of Pump-Probe Spectroscopy. *Annu. Rep. Prog. Chem., Sect. C: Phys. Chem.* **2008**, *104*, 272−297.
(46) Buckup, T.; Motzkus, M. Multidimensional Time-Resolved Spectroscopy of Vibrational Coherence in Biopolyenes. *Annu. Rev. Phys. Chem.* **2014**, *65*, 39−57.

https://doi.org/10.1021/acs.jctc.1c00109
J. Chem. Theory Comput. 2021, 17, 2394−2408

(47) Chergui, M. Ultrafast Molecular Photophysics in the Deep-Ultraviolet. *J. Chem. Phys.* **2019**, *150*, 070901.
(48) Yan, Y. J.; Fried, L. E.; Mukamel, S. Ultrafast Pump-Probe Spectroscopy: Femtosecond Dynamics in Liouville Space. *J. Phys. Chem.* **1989**, *93*, 8149−8162.
(49) Bosma, W. B.; Yan, Y. J.; Mukamel, S. Intramolecular and Solvent Dynamics in Femtosecond Pump-Probe Spectroscopy. *J. Chem. Phys.* **1990**, *93*, 3863−3873.
(50) Yan, Y. J.; Mukamel, S. Femtosecond Pump-Probe Spectroscopy of Polyatomic Molecules in Condensed Phases. *Phys. Rev. A: At., Mol., Opt. Phys.* **1990**, *41*, 6485−6504.
(51) Yan, Y. J.; Mukamel, S. Photon Echoes of Polyatomic Molecules in Condensed Phases. *J. Chem. Phys.* **1991**, *94*, 179−190.
(52) Pollard, W. T.; Lee, S. Y.; Mathies, R. A. Wave Packet Theory of Dynamic Absorption Spectra in Femtosecond Pump-Probe Experiments. *J. Chem. Phys.* **1990**, *92*, 4012−4029.
(53) Pollard, W. T.; Mathies, R. A. Analysis of Femtosecond Dynamic Absorption Spectra of Nonstationary States. *Annu. Rev. Phys. Chem.* **1992**, *43*, 497−523.
(54) Fried, L. E.; Mukamel, S. A Classical Theory of Pump-Probe Photodissociation for Arbitrary Pulse Durations. *J. Chem. Phys.* **1990**, *93*, 3063−3071.
(55) Li, Z.; Fang, J. Y.; Martens, C. C. Simulation of Ultrafast Dynamics and Pump-Probe Spectroscopy Using Classical Trajectories. *J. Chem. Phys.* **1996**, *104*, 6919−6929.
(56) Che, J.; Zhang, W.; Yan, Y. A Classical Time-Frequency Theory of Transient Absorption Spectroscopy. *J. Chem. Phys.* **1997**, *106*, 6947−6956.
(57) Ungar, L. W.; Cina, J. A. Short-Time Fluorescence Stokes Shift Dynamics. *Advances in Chemical Physics*; Wiley, 1997; Vol. *100*, pp 171−228.
(58) Lax, M. The Franck-Condon Principle and Its Application to Crystals. *J. Chem. Phys.* **1952**, *20*, 1752−1760.
(59) Stock, G.; Schneider, R.; Domcke, W. Theoretical Studies on the Femtosecond Real-Time Measurement of Ultrafast Electronic Decay in Polyatomic Molecules. *J. Chem. Phys.* **1989**, *90*, 7184−7194.
(60) Schneider, R.; Domcke, W.; Köppel, H. Aspects of Dissipative Electronic and Vibrational Dynamics of Strongly Vibronically Coupled Systems. *J. Chem. Phys.* **1990**, *92*, 1045−1061.
(61) Woywod, C.; Domcke, W.; Sobolewski, A. L.; Werner, H. J. Characterization of the $S_1 - S_2$ Conical Intersection in Pyrazine by ab initio Multiconfiguration Self-Consistent-Field and Multireference Configuration-Interaction Methods. *J. Chem. Phys.* **1994**, *100*, 1400−1413.
(62) Raab, A.; Worth, G. A.; Meyer, H.-D.; Cederbaum, L. S. Molecular Dynamics of Pyrazine After Excitation to the S_2 Electronic State Using a Realistic 24-Mode Model Hamiltonian. *J. Chem. Phys.* **1999**, *110*, 936−946.
(63) Sala, M.; Lasorne, B.; Gatti, F.; Guérin, S. The Role of the Low-Lying Dark $n\pi^*$ States in the Photophysics of Pyrazine: a Quantum Dynamics Study. *Phys. Chem. Chem. Phys.* **2014**, *16*, 15957−15967.
(64) Hillery, M.; O'Connell, R. F.; Scully, M. O.; Wigner, E. P. Distribution Functions in Physics: Fundamentals. *Phys. Rep.* **1984**, *106*, 121−167.
(65) Belyaev, A. K.; Lebedev, O. V. Nonadiabatic Nuclear Dynamics of Atomic Collisions Based on Branching Classical Trajectories. *Phys. Rev. A: At., Mol., Opt. Phys.* **2011**, *84*, 014701.
(66) Belyaev, A. K.; Lasser, C.; Trigila, G. Landau-Zener type surface hopping algorithms. *J. Chem. Phys.* **2014**, *140*, 224108.
(67) Belyaev, A. K.; Domcke, W.; Lasser, C.; Trigila, G. Nonadiabatic Nuclear Dynamics of the Ammonia Cation Studied by Surface Hopping Classical Trajectory Calculations. *J. Chem. Phys.* **2015**, *142*, 104307.
(68) Xie, W.; Domcke, W. Accuracy of Trajectory Surface-Hopping Methods: Test for a Two-Dimensional Model of the Photodissociation of Phenol. *J. Chem. Phys.* **2017**, *147*, 184114.
(69) Xie, W.; Sapunar, M.; Došlić, N.; Sala, M.; Domcke, W. Assessing the Performance of Trajectory Surface Hopping Methods: Ultrafast Internal Conversion in Pyrazine. *J. Chem. Phys.* **2019**, *150*, 154119.
(70) Landau, L. D. On the Theory of Transfer of Energy at Collisions II. *Phys. Z. Sowjetunion* **1932**, *2*, 46−51.
(71) Zener, C. Non-Adiabatic Crossing of Energy Levels. *Proc. R. Soc. London, Ser. A* **1932**, *137*, 696−702.
(72) Suchan, J.; Janoš, J.; Slavíček, P. Pragmatic Approach to Photodynamics: Mixed Landau-Zener Surface Hopping with Intersystem Crossing. *J. Chem. Theory Comput.* **2020**, *16*, 5809−5820.
(73) Schwartz, B. J.; Bittner, E. R.; Prezhdo, O. V.; Rossky, P. J. Quantum Decoherence and the Isotope Effect in Condensed Phase Nonadiabatic Molecular Dynamics Simulations. *J. Chem. Phys.* **1996**, *104*, 5942−5955.
(74) Fang, J.-Y.; Hammes-Schiffer, S. Improvement of the Internal Consistency in Trajectory Surface Hopping. *J. Phys. Chem. A* **1999**, *103*, 9399−9407.
(75) Zhu, C.; Nangia, S.; Jasper, A. W.; Truhlar, D. G. Coherent Switching with Decay of Mixing: An Improved Treatment of Electronic Coherence for Non-Born-Oppenheimer Trajectories. *J. Chem. Phys.* **2004**, *121*, 7658−7670.
(76) Domcke, W.; Stock, G. Theory of Ultrafast Nonadiabatic Excited-State Processes and their Spectroscopic Detection in Real Time. *Advances in Chemical Physics*; Wiley, 1997; Vol. *100*, pp 1−169.
(77) Worth, G. A.; Meyer, H.-D.; Cederbaum, L. S. Relaxation of a System with a Conical Intersection Coupled to a Bath: A Benchmark 24-Dimensional Wave Packet Study Treating the Environment Explicitly. *J. Chem. Phys.* **1998**, *109*, 3518−3529.
(78) Burghardt, I.; Giri, K.; Worth, G. A. Multimode Quantum Dynamics Using Gaussian Wavepackets: The Gaussian-Based Multiconfiguration Time-Dependent Hartree (G-MCTDH) Method Applied to the Absorption Spectrum of Pyrazine. *J. Chem. Phys.* **2008**, *129*, 174104.
(79) Stock, G.; Thoss, M. Classical Description of Nonadiabatic Quantum Dynamics. In *Advances in Chemical Physics*, Vol. *131*; Rice, S. A., Ed.; Wiley, 2005; pp. 243−375.
(80) Shalashilin, D. V. Nonadiabatic Dynamics with the Help of Multiconfigurational Ehrenfest Method: Improved Theory and Fully Quantum 24D Simulation of Pyrazine. *J. Chem. Phys.* **2010**, *132*, 244111.
(81) Zimmermann, T.; Vaníček, J. Efficient on-the-fly ab initio Semiclassical Method for Computing Time-Resolved Nonadiabatic Electronic Spectra with Surface Hopping or Ehrenfest Dynamics. *J. Chem. Phys.* **2014**, *141*, 134102.
(82) Chen, L.; Gelin, M. F.; Domcke, W. Multimode Quantum Dynamics with Multiple Davydov D_2 Trial States: Application to a 24-Dimensional Conical Intersection Model. *J. Chem. Phys.* **2019**, *150*, 024101.
(83) Chen, L.; Gelin, M. F.; Zhao, Y.; Domcke, W. Mapping of Wave Packet Dynamics at Conical Intersections by Time- and Frequency-Resolved Fluorescence Spectroscopy: A Computational Study. *J. Phys. Chem. Lett.* **2019**, *10*, 5873−5880.
(84) Nishitani, J.; West, C. W.; Higashimura, C.; Suzuki, T. Time-Resolved Photoelectron Spectroscopy of Polyatomic Molecules Using 42-nm Vacuum Ultraviolet Laser Based on High Harmonics Generation. *Chem. Phys. Lett.* **2017**, *684*, 397−401.
(85) Werner, U.; Mitrić, R.; Suzuki, T.; Bonačić-Koutecký, V. Nonadiabatic Dynamics within the Time Dependent Density Functional Theory: Ultrafast Photodynamics in Pyrazine. *Chem. Phys.* **2008**, *349*, 319−324.
(86) Tomasello, G.; Humeniuk, A.; Mitrić, R. Exploring Ultrafast Dynamics of Pyrazine by Time-Resolved Photoelectron Imaging. *J. Phys. Chem. A* **2014**, *118*, 8437−8445.
(87) Mignolet, B.; Kanno, M.; Shimakura, N.; Koseki, S.; Remacle, F.; Kono, H.; Fujimura, Y. Ultrafast Nonradiative Transition Pathways in Photo-Excited Pyrazine: Ab initio Analysis of Time-Resolved Vacuum Ultraviolet Photoelectron Spectrum. *Chem. Phys.* **2018**, *515*, 704−709.
(88) Sun, K.; Xie, W.; Chen, L.; Domcke, W.; Gelin, M. F. Multi-Faceted Spectroscopic Mapping of Ultrafast Nonadiabatic Dynamics

Near Conical Intersections: A Computational Study. *J. Chem. Phys.* **2020**, *153*, 174111.
(89) Møller, C.; Plesset, M. S. Note on an Approximation Treatment for Many-Electron Systems. *Phys. Rev.* **1934**, *46*, 618−622.
(90) Dunning, T. H., Jr. Gaussian Basis Sets for Use in Correlated Molecular Calculations. I. The Atoms Boron Through Neon and Hydrogen. *J. Chem. Phys.* **1989**, *90*, 1007−1023.
(91) Trofimov, A. B.; Stelter, G.; Schirmer, J. A Consistent Third-Order Propagator Method for Electronic Excitation. *J. Chem. Phys.* **1999**, *111*, 9982−9999.
(92) *TURBOMOLE (V7.2), a Development of University of Karlsruhe and Forschungszentrum Karlsruhe GmbH, 1989−2007*; TURBOMOLE GmbH, since 2007.
(93) Hättig, C.; Weigend, F. CC2 Excitation Energy Calculations on Large Molecules Using the Resolution of the Identity Approximation. *J. Chem. Phys.* **2000**, *113*, 5154−5161.
(94) Köhn, A.; Hättig, C. Analytic Gradients for Excited States in the Coupled-Cluster Model CC2 Employing the Resolution-of-the-Identity Approximation. *J. Chem. Phys.* **2003**, *119*, 5021−5036.
(95) Piancastelli, M. N.; Keller, P. R.; Taylor, J. W. Angular Distribution Parameter as a Function of Photon Energy for Some Mono- and Diazabenzenes and its Use for Orbital Assignment. *J. Am. Chem. Soc.* **1983**, *105*, 4235−4239.
(96) Palacino-González, E.; Gelin, M. F.; Domcke, W. Analysis of Transient-Absorption Pump-probe Signals of Nonadiabatic Dissipative Systems: "Ideal" and "Real" spectra. *J. Chem. Phys.* **2019**, *150*, 204102.
(97) Hu, D.; Xie, Y.; Li, X.; Li, L.; Lan, Z. Inclusion of Machine Learning Kernel Ridge Regression Potential Energy Surfaces in On-the-Fly Nonadiabatic Molecular Dynamics Simulation. *J. Phys. Chem. Lett.* **2018**, *9*, 2725−2732.
(98) Dral, P. O.; Barbatti, M.; Thiel, W. Nonadiabatic Excited-State Dynamics with Machine Learning. *J. Phys. Chem. Lett.* **2018**, *9*, 5660−5663.
(99) Westermayr, J.; Gastegger, M.; Menger, M. F. S. J.; Mai, S.; González, L.; Marquetand, P. Machine Learning Enables Long Time Scale Molecular Photodynamics Simulations. *Chem. Sci.* **2019**, *10*, 8100−8107.
(100) Zhang, Y.; Zhou, X.; Jiang, B. Bridging the Gap between Direct Dynamics and Globally Accurate Reactive Potential Energy Surfaces Using Neural Networks. *J. Phys. Chem. Lett.* **2019**, *10*, 1185−1191.
(101) Smith, B.; Akimov, A. V. Modeling Nonadiabatic Dynamics in Condensed Matter Materials: Some Recent Advances and Applications. *J. Phys.: Condens. Matter* **2019**, *32*, 073001.
(102) Xie, W.; Holub, D.; Kubař, T.; Elstner, M. Performance of Mixed Quantum-Classical Approaches on Modeling the Crossover from Hopping to Bandlike Charge Transport in Organic Semiconductors. *J. Chem. Theory Comput.* **2020**, *16*, 2071−2084.
(103) Mališ, M.; Luber, S. Trajectory Surface Hopping Nonadiabatic Molecular Dynamics with Kohn-Sham ΔSCF for Condensed-Phase Systems. *J. Chem. Theory Comput.* **2020**, *16*, 4071−4086.
(104) Lu, D.; Gygi, F.; Galli, G. Dielectric Properties of Ice and Liquid Water from First-Principles Calculations. *Phys. Rev. Lett.* **2008**, *100*, 147601.
(105) Garbuio, V.; Cascella, M.; Pulci, O. Excited State Properties of Liquid Water. *J. Phys.: Condens. Matter* **2009**, *21*, 033101.
(106) Mattiat, J.; Luber, S. Time Domain Simulation of (Resonance) Raman Spectra of Liquids in the Short Time Approximation. *J. Chem. Theory Comput.* **2021**, *17*, 344−356.
(107) Senn, H. M.; Thiel, W. QM/MM Methods for Biomolecular Systems. *Angew. Chem., Int. Ed.* **2009**, *48*, 1198−1229.
(108) Mata, R. A. Application of High Level Wavefunction Methods in Quantum Mechanics/Molecular Mechanics Hybrid Schemes. *Phys. Chem. Chem. Phys.* **2010**, *12*, 5041−5052.
(109) Yost, S. R.; Wang, L.-P.; Van Voorhis, T. Molecular Insight Into the Energy Levels at the Organic Donor/Acceptor Interface: A Quantum Mechanics/Molecular Mechanics Study. *J. Phys. Chem. C* **2011**, *115*, 14431−14436.
(110) Mennucci, B. Modeling Environment Effects on Spectroscopies Through QM/Classical Models. *Phys. Chem. Chem. Phys.* **2013**, *15*, 6583−6594.
(111) Egorova, D.; Gelin, M. F.; Domcke, W. Time- and Frequency-Resolved Fluorescence Spectra of Nonadiabatic Dissipative Systems: What Photons Can Tell Us. *J. Chem. Phys.* **2005**, *122*, 134504.
(112) Cho, M. *Two-Dimensional Optical Spectroscopy*; CRC Press: Boca Raton, 2009.
(113) Valkunas, L.; Abramavicius, D.; Mancal, T. *Molecular Excitation Dynamics and Relaxation*; Wiley-VCH: Weinheim, 2013.
(114) Gelin, M. F.; Egorova, D.; Pisliakov, A. V.; Domcke, W. Unified Description of Sequential and Coherent Contributions to Time-Resolved Spontaneous Emission Signals: Generalized Doorway-Window Approach. *Chem. Phys. Lett.* **2004**, *391*, 234−242.
(115) Gelin, M. F.; Egorova, D.; Pisliakov, A. V.; Domcke, W. Transient Phenomena in Time- and Frequency-Gated Spontaneous Emission. *J. Phys. Chem. A* **2005**, *109*, 3587−3597.

https://doi.org/10.1021/acs.jctc.1c00109
J. Chem. Theory Comput. 2021, 17, 2394−2408

THE JOURNAL OF PHYSICAL CHEMISTRY LETTERS
A JOURNAL OF THE AMERICAN CHEMICAL SOCIETY

pubs.acs.org/JPCL Letter

Ab Initio Quasiclassical Simulation of Femtosecond Time-Resolved Two-Dimensional Electronic Spectra of Pyrazine

Xiang Huang, Weiwei Xie, Nađa Došlić, Maxim F. Gelin,* and Wolfgang Domcke

Cite This: *J. Phys. Chem. Lett.* 2021, 12, 11736−11744 Read Online

ACCESS | Metrics & More | Article Recommendations | Supporting Information

ABSTRACT: Two-dimensional (2D) electronic spectroscopy is a powerful nonlinear technique which provides spectroscopic information on two frequency axes as well as dynamical information as a function of the so-called waiting time. Herein, an ab initio theoretical framework for the simulation of electronic 2D spectra has been developed. The method is based on the classical approximation to the doorway−window representation of three-pulse photon-echo signals and the description of nuclear motion by classical trajectories. Nonadiabatic effects are taken into account by a trajectory surface-hopping algorithm. 2D electronic spectra were simulated with ab initio on-the-fly trajectory calculations using the ADC(2) electronic-structure method for the pyrazine molecule, which is a benchmark system for ultrafast radiationless decay through conical intersections. It is demonstrated that 2D spectroscopy with subfemtosecond UV pulses can provide unprecedented detailed information on the ultrafast photodynamics of polyatomic molecules.

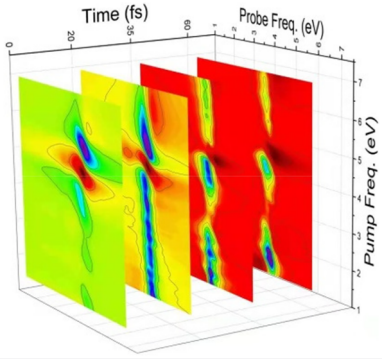

Femtosecond time-resolved two-dimensional (2D) spectroscopy in the infrared and optical regimes was stimulated by prior developments in NMR spectroscopy.[1,2] The key concept of 2D spectroscopy is the spreading of the third-order photon-echo signal on two frequency axes ω_τ and ω_t, while the photoinduced electronic population dynamics is recorded as a function of the so-called waiting time T. Electronic 2D spectroscopy was primarily applied to the investigation of energy transfer processes in multichromophoric systems, in particular biological antenna complexes.[3,4] More recently, it has been shown by several groups that 2D spectroscopy with ultrashort (∼10 fs) UV pulses is also well suited to probe the ultrafast nonadiabatic dynamics of excited states in polyatomic molecules.[5−13] The application of 2D spectroscopy to chromophores of biological interest, such as retinal, DNA bases or aromatic amino acids, has become possible through the development of ultrashort laser pulses in the deep UV as well as white-light continua.[5,7,9,11,13]

The theory of electronic 2D spectroscopy was primarily developed in application to Frenkel exciton Hamiltonians including exciton−phonon coupling.[14−17] 2D spectra of molecular chromophores were simulated with nuclear quantum dynamics calculations for few-state few-mode vibronic coupling models, with applications, for example, to retinal[18] or pyrazine.[19−21] Begušić and Vaníček applied Heller's semiclassical frozen Gaussian method to compute 2D spectra of phenol[22] and azulene.[23] Garavelli, Mukamel, Nenov, Rivalta, and co-workers developed an alternative approach for the simulation of electronic 2D spectra of polyatomic molecules which focuses on the ab initio calculation of fixed-nuclei electronic excitations energies and transition dipole moments with multiconfiguration multireference electronic structure methods. These authors developed comprehensive computational protocols which allow the inclusion of the effects of vibrational modes by harmonic-oscillator or Brownian-oscillator line-shape functions as well as the inclusion of solvent effects in the QM/MM approximation.[24−27] Ab initio based simulations of 2D spectra were performed for a variety of molecular chromophores, such as phenol,[28] indole,[29] azobenzene,[30] retinal,[31] and nucleobases,[32−34] as well as for several dimers or oligomers (see the reviews).[26,27] Most of these applications excluded the study of excited-state dynamics by considering either zero waiting time or waiting times in the picosecond range, when excited states can be assumed to be relaxed to their local energy minima. In a few cases, the excited-state dynamics was described by kinetic master equations with empirical parameters. Richter and Fingerhut performed simulations of 2D spectra of diphenylmethane, treating the nonadiabatic excited-state dynamics with quasiclassical trajectory surface hopping (TSH) calculations at the complete-active-space self-consistent-field (CASSCF) electronic-structure level and assuming delta-function laser pulses.[35] This work represents the so-far most ambitious attempt toward the first-principles simulation of 2D spectra of molecular systems exhibiting ultrafast nonadiabatic

Received: November 2, 2021
Accepted: November 24, 2021
Published: December 1, 2021

excited-state dynamics, although only the stimulated emission signal was evaluated.

In the present work, we developed an ab initio protocol for the simulation of electronic 2D spectra of polyatomic molecular systems with ultrafast nonadiabatic excited-state dynamics which is driven by conical intersections. The theory combines quasi-classical TSH simulations of the nonadiabatic nuclear dynamics with the doorway-window (DW) approximation for the evaluation of spectroscopic signals. The DW picture was introduced by Yan, Fried, and Mukamel at the dawn of the theory of femtosecond time-resolved nonlinear spectroscopy for two-pulse transient absorption (TA) pump−probe (PP) spectra.[36−38] The conditions for the validity of the DW approximation are laser pulses which are short on the time scale of the intrinsic system dynamics and are nonoverlapping in time. The DW approximation was generalized to three-pulse photo-echo spectroscopy and 2D spectroscopy in refs 39 and 40. In the DW approximation, the signal is expressed as the trace of the product of the doorway operator, the propagator of the field-free material system, and the window operator. It has early on been recognized that the DW formula for TA PP spectroscopy is well suited for evaluation by sampling over classical trajectories.[38,41,42] In the classical approximation for the nuclear motion, the doorway and window operators become classical phase-space functions which account for the duration and spectral shape of the laser pulses. The field-free nuclear dynamics is described by swarms of classical trajectories in the electronic ground state and in excited electronic states. Nonadiabatic couplings can be taken into account with a TSH algorithm. Simulations of 2D spectra with the quasiclassical DW formula can be implemented with ab initio on-the-fly trajectory calculations, as recently demonstrated for TA PP spectra.[43,44] The only empirical parameter entering the computational protocol is the rate of optical dephasing which cannot be retrieved from classical trajectory calculations.

Electronic 2D spectra have been computed herein for the pyrazine molecule with the ADC(2) (algebraic−diagrammatic construction of second order) electronic-structure method. To our knowledge, these are the first ab initio simulations of 2D spectra which take into account both the duration and shape of the laser pulses as well as ultrafast nonadiabatic excited-state dynamics.

In 2D spectroscopy, three ultrashort laser pulses with pulse envelopes $\mathcal{E}_a(t)$, carrier frequencies ω_a, and wave vectors $\boldsymbol{k}_a$, $a = 1, 2, 3$, interact with the sample, generating a third-order nonlinear polarization which is detected by heterodyning with a so-called local oscillator field $\mathcal{E}_4(t)$ with wave vector $\boldsymbol{k}_4$. The signal is generated in two phase-matching directions, the so-called rephasing (R) direction ($\boldsymbol{k}_4 = -\boldsymbol{k}_1 + \boldsymbol{k}_2 + \boldsymbol{k}_3$) and the nonrephasing (NR) direction ($\boldsymbol{k}_4 = \boldsymbol{k}_1 - \boldsymbol{k}_2 + \boldsymbol{k}_3$), which can be measured separately.[45] For a given waiting time T of the third pulse, the signal is recorded as a function of the excitation and detection frequencies ω_τ, ω_t by Fourier transformation of the signal in the corresponding time intervals. The signal consists of the ground-state bleach (GSB), stimulated emission (SE), and excited-state absorption (ESA) contributions.[46]

In a typical closed-shell molecule, such as pyrazine, the energy of the electronic ground state is well separated from the manifold of low-lying excited states, which can be bright or dark in absorption from the ground state. The excitation energy of the lowest bright state typically defines the carrier frequency ω_1 of the pump pulse. The probe pulses with carrier frequency ω_2 may stimulate emission to the ground state, but can also excite higher electronic states, giving rise to the ESA signal. The excited electronic states relevant for the ESA signal are located at an energy of $\approx \hbar\omega_1 + \hbar\omega_2$. It is therefore convenient to introduce the manifold {I} of excited states which are approximately in resonance with the pump pulse and the manifold {II} of higher excited states which are approximately in resonance with $\hbar\omega_1 + \hbar\omega_2$. We denote the potential-energy (PE) function of the electronic ground state as $V_g(\boldsymbol{R})$, the PE functions of the states of manifold {I} as $V_e(\boldsymbol{R})$ and the PE functions of manifold {II} as $V_f(\boldsymbol{R})$, where $\boldsymbol{R}$ denotes the Cartesian coordinates of the nuclei. The relevant electronic transition dipole moments (TDMs) are denoted as $\mu_{ge}(\boldsymbol{R})$ and $\mu_{ef}(\boldsymbol{R})$. The PE differences are denoted as $U_{eg}(\boldsymbol{R}) = V_e(\boldsymbol{R}) - V_g(\boldsymbol{R})$ and $U_{fe}(\boldsymbol{R}) = V_f(\boldsymbol{R}) - V_e(\boldsymbol{R})$. The spectral functions of the laser pulses, given by the Fourier transform of the pulse envelopes $E_a(t)$, are denoted as $E_a(\omega)$. The initial phase-space distribution of the nuclear motion is approximated by the harmonic Wigner distribution,[47] $\rho_g^{\mathrm{Wig}}(\boldsymbol{R}, \boldsymbol{P})$, where $\boldsymbol{P}$ denotes the momenta conjugated to $\boldsymbol{R}$.

With these definitions, the 2D signal $S^\alpha(\omega_\tau, T, \omega_t)$, $\alpha = R, NR$, can be written as (see section S1 of the Supporting Information for the derivation)

$$S^{(\alpha)}(\omega_\tau, T, \omega_t) = S^{(\alpha)}_{\mathrm{GSB}}(\omega_\tau, T, \omega_t) + S^{(\alpha)}_{\mathrm{SE}}(\omega_\tau, T, \omega_t) + S^{(\alpha)}_{\mathrm{ESA}}(\omega_\tau, T, \omega_t) \tag{1}$$

$$S^{(\alpha)}_{\mathrm{GSB}}(\omega_\tau, T, \omega_t) \sim \mathrm{Re}\langle D_0^{(\alpha)}(\omega_\tau, \boldsymbol{R}_g, \boldsymbol{P}_g) W_0(\omega_t, \boldsymbol{R}_g(T), \boldsymbol{P}_g(T))\rangle \tag{2}$$

$$S^{(\alpha)}_{\mathrm{SE}}(\omega_\tau, T, \omega_t) \sim \mathrm{Re}\langle D_{\mathrm{I}}^{(\alpha)}(\omega_\tau, \boldsymbol{R}_g, \boldsymbol{P}_g) W_{\mathrm{I}}(\omega_t, \boldsymbol{R}_{e(T)}(T), \boldsymbol{P}_{e(T)}(T))\rangle \tag{3}$$

$$S^{(\alpha)}_{\mathrm{ESA}}(\omega_\tau, T, \omega_t) \sim -\mathrm{Re}\langle D_{\mathrm{I}}^{(\alpha)}(\omega_\tau, \boldsymbol{R}_g, \boldsymbol{P}_g) W_{\mathrm{II}}(\omega_t, \boldsymbol{R}_{e(T)}(T), \boldsymbol{P}_{e(T)}(T))\rangle \tag{4}$$

Here $D_0^{(\alpha)}(\omega_\tau, \boldsymbol{R}_g, \boldsymbol{P}_g)$ and $D_{\mathrm{I}}^{(\alpha)}(\omega_\tau, \boldsymbol{R}_g, \boldsymbol{P}_g)$ are doorway functions associated with the pump pulses and $W_0(\omega_t, \boldsymbol{R}_{e(T)}(T), \boldsymbol{P}_{e(T)}(T))$, $W_{\mathrm{I}}(\omega_t, \boldsymbol{R}_{e(T)}(T), \boldsymbol{P}_{e(T)}(T))$, $W_{\mathrm{II}}(\omega_t, \boldsymbol{R}_{e(T)}(T), \boldsymbol{P}_{e(T)}(T))$ are window functions associated with the probe process. The subscripts g, I, and II refer to the electronic ground state and the electronic manifolds {I}, {II}. The angular brackets in eqs 2−4 denote Monte Carlo sampling of the classical initial conditions $\boldsymbol{R}_g$, $\boldsymbol{P}_g$ from $\rho_g^{\mathrm{Wig}}(\boldsymbol{R}_g, \boldsymbol{P}_g)$ as well as stochastic sampling of nonadiabatic surface-hopping probabilities of trajectories in manifold {I} for the SE and ESA contributions. For the GSB contribution, the trajectories are propagated in the electronic ground state and are not subject to nonadiabatic transitions.

The doorway functions are defined as

$$D_0^{(\mathrm{R})}(\omega_\tau, \boldsymbol{R}_g, \boldsymbol{P}_g) = \rho_g^{\mathrm{Wig}}(\boldsymbol{R}_g, \boldsymbol{P}_g) \sum_e \frac{\mathcal{E}_1^2(\omega_\tau - \omega_p)|\mu_{ge}(\boldsymbol{R}_g)|^2}{\nu - i(U_{eg}(\boldsymbol{R}_g) - \omega_\tau)} \tag{5}$$

$$D_{\mathrm{I}}^{(\mathrm{R})}(\omega_\tau, \boldsymbol{R}_g, \boldsymbol{P}_g) = \rho_g^{\mathrm{Wig}}(\boldsymbol{R}_g, \boldsymbol{P}_g) \frac{\mathcal{E}_1^2(\omega_\tau - \omega_p)|\mu_{ge}(\boldsymbol{R}_g)|^2}{\nu - i(U_{eg}(\boldsymbol{R}_g) - \omega_\tau)} \tag{6}$$

for the R signal and as

$$D_0^{(\mathrm{NR})}(\omega_\tau, \boldsymbol{R}_g, \boldsymbol{P}_g) = \rho_g^{\mathrm{Wig}}(\boldsymbol{R}_g, \boldsymbol{P}_g) \sum_e \frac{\mathcal{E}_1^2(\omega_\tau - \omega_p)|\mu_{ge}(\boldsymbol{R}_g)|^2}{\nu + i(U_{eg}(\boldsymbol{R}_g) - \omega_\tau)} \tag{7}$$

https://doi.org/10.1021/acs.jpclett.1c03589
J. Phys. Chem. Lett. 2021, 12, 11736−11744

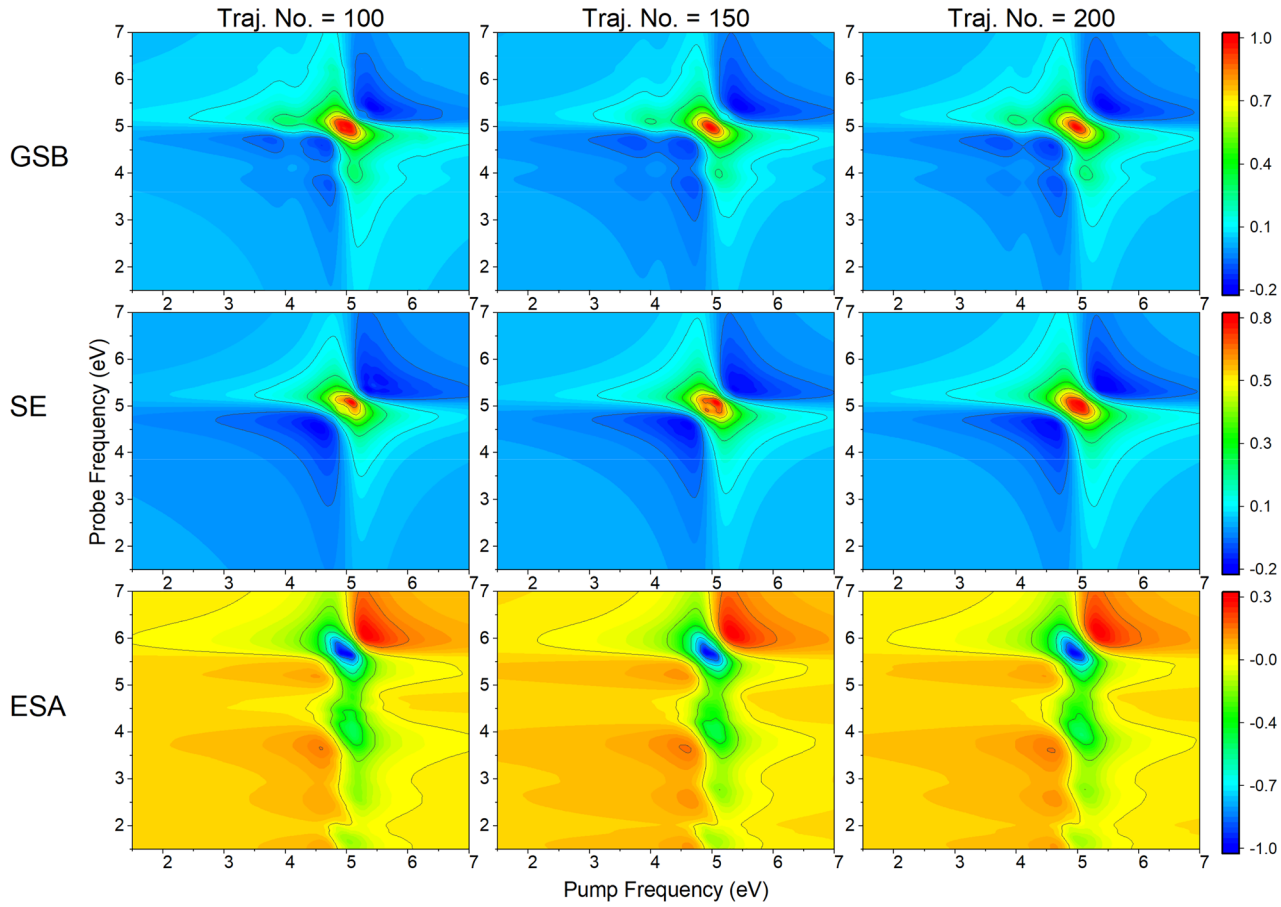

Figure 1. GSB, SE, and ESA contributions (from top to bottom) to the 2D spectra computed for the NR phase-matching condition and zero waiting time T by sampling over 100, 150, and 200 trajectories (from left to right).

$$D_{\mathrm{I}}^{(\mathrm{NR})}(\omega_\tau, \boldsymbol{R}_g, \boldsymbol{P}_g) = \rho_g^{\mathrm{Wig}}(\boldsymbol{R}_g, \boldsymbol{P}_g)\frac{\mathcal{E}_1^2(\omega_\tau - \omega_p)|\mu_{ge}(\boldsymbol{R}_g)|^2}{\nu + i(U_{eg}(\boldsymbol{R}_g) - \omega_\tau)} \tag{8}$$

for the NR signal. The window functions at waiting time T are given by

$$W_0(\omega_t, \boldsymbol{R}_g(T), \boldsymbol{P}_g(T)) = \sum_e \frac{\mathcal{E}_4^2(\omega_t - \omega_p)|\mu_{ge}(\boldsymbol{R}_g(T))|^2}{\nu + i(U_{eg}(\boldsymbol{R}_g(T)) - \omega_t)} \tag{9}$$

$$W_{\mathrm{I}}(\omega_t, \boldsymbol{R}_{e(T)}(T), \boldsymbol{P}_{e(T)}(T)) = \frac{\mathcal{E}_4^2(\omega_t - \omega_p)|\mu_{ge(T)}(\boldsymbol{R}_{e(T)}(T))|^2}{\nu + i(U_{e(T)g}(\boldsymbol{R}_{e(T)}(T)) - \omega_t)} \tag{10}$$

$$W_{\mathrm{II}}(\omega_t, \boldsymbol{R}_{e(T)}(T), \boldsymbol{P}_{e(T)}(T)) = \sum_f \frac{\mathcal{E}_4^2(\omega_t - \omega_p)|\mu_{e(T)f}(\boldsymbol{R}_{e(T)}(T))|^2}{\nu + i(U_{fe(T)}(\boldsymbol{R}_{e(T)}(T)) - \omega_t)} \tag{11}$$

where ν denotes the optical dephasing rate which is taken to be the same for all excited electronic states. $\boldsymbol{R}_g$, $\boldsymbol{P}_g$ denote position and momenta of trajectories in the electronic ground state and $\boldsymbol{R}_e$, $\boldsymbol{P}_e$ denote positions and momenta of trajectories in the electronic states of manifold {I}. The notation $\boldsymbol{R}_{e(T)}(T)$ is a reminder that a trajectory launched in state e of manifold {I} may end up in another electronic state $e(T) \neq e$ at time T. For simplicity, it has been assumed that $\mathcal{E}_1(\omega) = \mathcal{E}_2(\omega)$ and $\mathcal{E}_3(\omega) = \mathcal{E}_4(\omega)$. It should be noted that the doorway and window functions of 2D spectroscopy are, other than the doorway and window functions of TA PP spectroscopy,[43] complex-valued. If 2D signals are detected with a spectrometer (that is, without the heterodyning pulse $\mathcal{E}_4(t)$), $\mathcal{E}_4^2(\omega_t - \omega_4)$ should be replaced by $\mathcal{E}_4(\omega_t - \omega_4)$ in eqs 9−11. 2D spectra in the impulsive limit ($\mathcal{E}_a(t) \to \delta(t)$) are recovered by setting $\mathcal{E}_a(\omega) = 1$. As follows from eqs 1−11 and section S1, the DW representation permits us to perform the integration of the nonlinear response functions over the coherence times t_1 and t_3 analytically, as well as to associate the population time T with the propagation time along nuclear trajectories. It is essential for the computational efficiency of the DW simulation protocol.

The 2D signals of eqs 1−4 were evaluated for the pyrazine molecule using the ADC(2) electronic-structure method[48,49] with the cc-pVDZ basis set. ADC(2) is a single-reference propagator method yielding excitation energies. It is consistent with the second-order Møller−Plesset (MP2)[50] approximation for the electronic ground state. Because ADC(2) excitation energies are obtained by diagonalizing a Hermitian secular matrix, the method describes correctly the topography of conical intersections among excited electronic states.[51] As a result, ADC(2) has become the method of choice in studies of excited-state dynamics.[52−54] When the electronic ground state is not well described by a single determinant, for instance in the region of a conical intersection between the ground state and the first

https://doi.org/10.1021/acs.jpclett.1c03589
J. Phys. Chem. Lett. 2021, 12, 11736−11744

exited state, the ADC(2) method may fail.[55] This situation is not encountered in pyrazine on time scales shorter than 10 ps. All electronic-structure calculations were performed with the Turbomole program package[56] using the resolution-of-the-identity approximation.

The lowest four excited singlet states of pyrazine, $B_{3u}(n\pi^*)$, $A_u(n\pi^*)$, $B_{2u}(\pi\pi^*)$, $B_{2g}(n\pi^*)$, are included in manifold {I}. The next 30 excited singlet states with vertical excitation energies up to ∼10 eV are included in manifold {II}. Trajectories in manifold {I} were sampled from $\rho_g^{\mathrm{Wig}}(\boldsymbol{R}_g, \boldsymbol{P}_g)$ and the oscillator strengths of the $B_{3u}(n\pi^*)$, $A_u(n\pi^*)$, $B_{2u}(\pi\pi^*)$, $B_{2g}(n\pi^*)$ states at the reference geometry and were propagated with the Landau−Zener-based surface-hopping (LZSH) algorithm[53,57−59] up to 200 fs. It has been shown for several systems that the LZSH algorithm gives essentially identical results as the widely used Tully's fewest switching algorithm[60] for ultrafast electronic population dynamics driven by conical intersections.[53,61] Because no derivatives of electronic wave functions have to be computed, the LZSH algorithm is computationally somewhat less expensive than the fewest-switching surface-hopping (FSSH) algorithm and the empirical decoherence correction of the FSSH method is superfluous, since electronic wave functions are not propagated in time. More importantly, the LZSH algorithm combined with the ADC(2) electronic-structure method is a highly robust ab initio computational scheme for nonadiabatic photodynamics in confined regions of nuclear coordinate space, that is, in the absence of photo-isomerization or photodissociation reactions on the time scale of interest. The generation of large nonadiabatic trajectory samples and the evaluation of spectroscopic signals can therefore be fully automated.

Herein, we made use of previously generated 1000 ab initio on-the-fly trajectories for pyrazine[53] in manifold {I} to evaluate the SE signal up to 200 fs. To compute the GSB signal, 300 trajectories were sampled from $\rho_g^{\mathrm{Wig}}(\boldsymbol{R}_g, \boldsymbol{P}_g)$ and propagated in the electronic ground state up to 200 fs (see ref 43 for technical details). To compute the ESA signal, excitation energies from manifold {I} to manifold {II} and the corresponding TDMs were calculated for 200 randomly selected trajectories in manifold {I} up to 200 fs. The laser pulses were tuned into resonance with the S_0−$B_{2u}(\pi\pi^*)$ transition ($\hbar\omega_a$ = 5.2 eV). Gaussian pulse envelopes were chosen ($\mathcal{E}_a(t) = \exp\{-(t/\tau_a)^2\}$, $\mathcal{E}_a(\omega) \sim \exp\{-(\omega\tau_a)^2/4\}$) with τ_a = 100 as. Our choice of such short pulses is motivated by the desire to cover the entire spectral width of the 2D spectra of pyrazine along ω_t which spreads over several eV. In 2D experiments, the spectral width of the detected signals is determined by the spectral widths of the laser pulses involved, although probing with a white-light-continuum would also permit a broad coverage of spectra along ω_t. Here, we consider transform-limited pulses, which require a subfemtosecond pulse duration for the coverage of the full 2D spectra. The dephasing parameter is chosen as ν = 0.1 eV, corresponding to a dephasing time constant of 6.6 fs. Very fast optical dephasing, faster than the population decay of excited electronic states, is characteristic for the optical spectra of higher excited states in polyatomic molecules.[62]

Because the doorway and window functions for 2D signals, eqs 5−11, are complex-valued, the convergence of the Monte Carlo sampling over trajectories is not a priori guaranteed. We therefore checked the convergence of the computed GSB, SE, and ESA spectra. Figure 1 displays spectra computed for the NR phase-matching condition for zero waiting time T, obtained by sampling over 100, 150, and 200 trajectories. It is found that the convergence is fast. The spectra are fully converged with 200 trajectories. For the SE signal, calculations with up to 1000 trajectories were performed, and no change of the signal with increasing number of trajectories was observed.

For the selection of suitable snapshots in the waiting time and for the analysis and interpretation of the 2D spectra, it is useful to know the time-dependent population probabilities of the relevant states of manifold {I} as a function of the physical time after the pump pulse. While the ab initio TSH calculations are performed in the adiabatic representation, it is possible to transform the adiabatic populations to a diabatic representation if a suitable global adiabatic-to-diabatic transformation matrix can be found. For pyrazine, such a transformation could be constructed by requiring the smoothness of the electronic TDMs in the relevant range of the nuclear coordinate space, see ref 53 for details.

The population probabilities of the adiabatic (S_1, S_2, S_3) and diabatic ($B_{3u}(n\pi^*)$, $A_u(n\pi^*)$, $B_{2u}(\pi\pi^*)$) electronic states of pyrazine after instantaneous initial excitation of the $B_{2u}(\pi\pi^*)$ state at $t = 0$ are displayed in Figure 2 panels a and b, respectively.

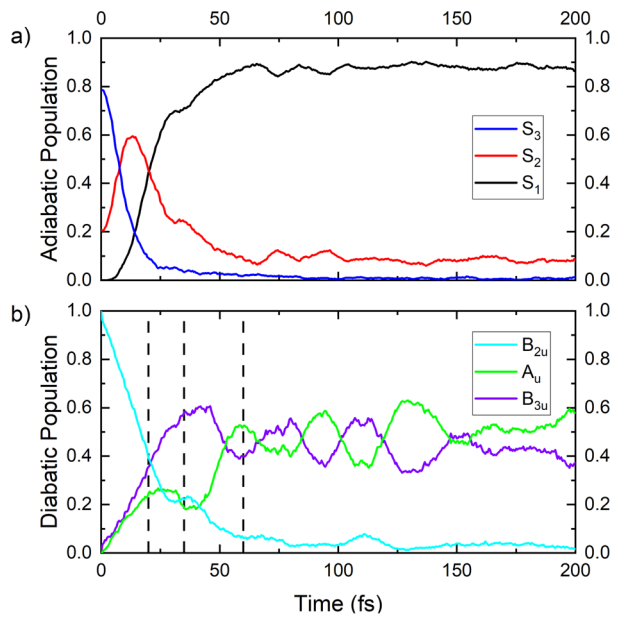

Figure 2. Population probabilities of the adiabatic (S_1, S_2, S_3) (a) and diabatic ($B_{3u}(n\pi^*)$, $A_u(n\pi^*)$, $B_{2u}(\pi\pi^*)$) (b) electronic states of pyrazine after instantaneous initial excitation of the $B_{2u}(\pi\pi^*)$ state at $t = 0$, computed by sampling over 1000 trajectories.

The initial conditions for the evaluation of populations are selected from the ground state Wigner distribution $\rho_g^{\mathrm{Wig}}(\boldsymbol{R}_g, \boldsymbol{P}_g)$ which accounts for the zero-point motion of the vibrational normal modes. As the B_{2u}/B_{3u} conical-intersection seam is close to the geometry of the minimum of the electronic ground state, for some displaced geometries the diabatic B_{2u} state is not the third excited state, S_3, but the second adiabatic state, S_2. This happens in ≈20% of cases of the Wigner sample, hence, the initial values of the adiabatic S_2 and S_3 populations. As pointed out previously, the adiabatic populations of pyrazine are largely structureless as functions of time, while the diabatic populations exhibit pronounced oscillatory features which reflect driving of the diabatic populations by coherent motion in some of the tuning modes of the conical intersections.[53] Figure 2b shows the well-established[63−65] rapid (≈20 fs) decay of the B_{2u} population

https://doi.org/10.1021/acs.jpclett.1c03589
J. Phys. Chem. Lett. 2021, 12, 11736−11744

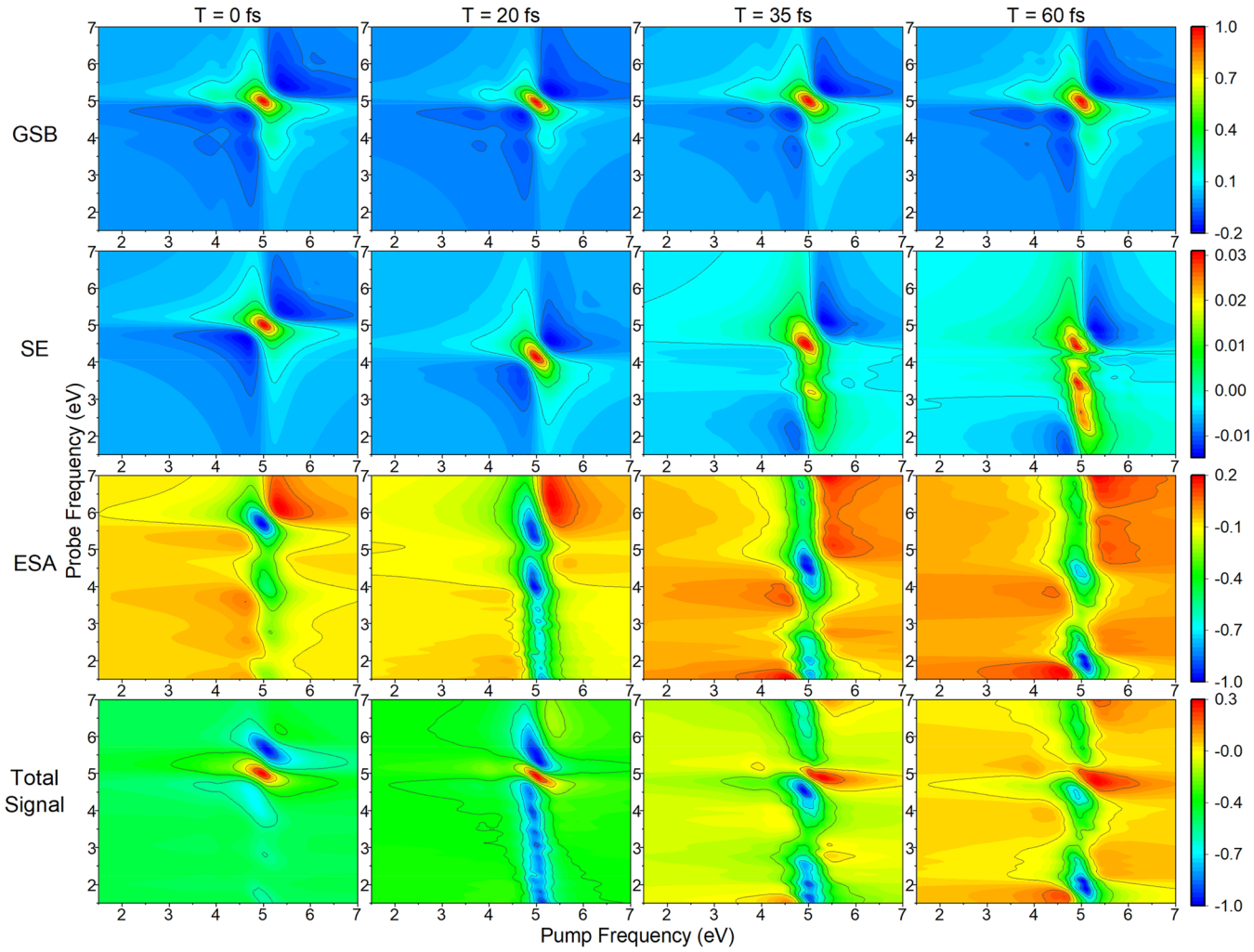

Figure 3. NR 2D spectra of pyrazine at waiting times $T = 0$, 20, 35, and 60 fs. For better visibility, each of the GSB, SE, ESA, and total signals (from top to bottom) is rescaled to cover the same intensity range for different T.

due to strong B_{2u}−B_{3u} vibronic coupling at the B_{2u}/B_{3u} conical intersection. The B_{3u} state, in turn, is strongly vibronically coupled to the A_u state via another conical intersection, which results in a transient oscillatory dynamics and eventual equilibration of the B_{3u} and A_u populations, as shown in Figure 2b. The adiabatic populations in Figure 2a do not show this transient oscillatory nonadiabatic dynamics. Since the laser fields couple to the diabatic electronic states with smooth electronic TDMs, it is to be expected that the 2D spectra will reflect the diabatic electronic population dynamics rather than the adiabatic population dynamics.

Calculated NR 2D spectra of pyrazine are displayed in Figure 3 for four selected waiting times, $T = 0$, 20, 35, and 60 fs. These waiting times are indicated as dashed vertical lines in Figure 2b. The GSB, SE, and ESA signals are shown from top to bottom. The lowest row shows the total NR 2D signal. For better visibility, the signals in Figure 3 are scaled to equal intensity range within each row. The signals plotted without rescaling can be found in the Supporting Information, Figure S12. To illustrate the vivid dynamics of the 2D signal, a movie showing the ESA signal up to 200 fs in time steps of 1.0 fs is available in the Supporting Information. It illustrates the rich temporal and spectral dynamical information contained in the high-resolution ESA signal of pyrazine. The calculated rephasing signals are presented in Figure S13. Their consideration adds nothing profound to the discussion, except of the trivial change of peak shapes—from rephasing to nonrephasing.

We begin with a general characterization of the peak patterns. For pyrazine, ω_τ-positions of all peaks reveal, predominantly, excitation of the bright $B_{2u}(\pi\pi^*)$ state in the Franck−Condon region. Hence all peaks with $\omega_t \neq \omega_\tau$ will be cross-peaks. The cross-peak in the SE contribution at $T = 35$ fs is a direct signature of the stimulated emission from the $B_{3u}(n\pi^*)$ state. It is caused both by the intensity borrowing from the bright $B_{2u}(\pi\pi^*)$ state and by the nonzero (though rather small) oscillator strength of the $B_{2u}(n\pi^*)$−S_0 transition. All ESA peaks are caused by transitions from the $B_{3u}(n\pi^*)$, $A_u(n\pi^*)$, and $B_{2u}(\pi\pi^*)$ states to the higher-lying excited electronic states of manifold {II}. The peak shapes, on the other hand, are caused by the combination of three factors which—in the order of decreasing significance—can be specified as follows: homogeneous broadening owing to the electronic dephasing ν, broadening due to the sampling of nuclear coordinates and momenta from the Wigner distribution $\rho_g^{\mathrm{Wig}}(\boldsymbol{R}_g, \boldsymbol{P}_g)$, and dynamical broadening caused by the wave packet evolutions and passings through conical intersections.

For the ultrafast laser pulses applied (100 as), the GSB signal is essentially independent of T and therefore is of limited interest. It is represented by a single peak, the intensity of which is determined by the Franck−Condon factors of the B_{2u} state and the optical dephasing rate. Yet the peak shape and position

https://doi.org/10.1021/acs.jpclett.1c03589
J. Phys. Chem. Lett. 2021, 12, 11736−11744

change slightly with T. This is predominantly caused by non-Condon effects resulting in low-amplitude vibrational modulations of the transition dipole moment (cf. ref 44).

The second row shows the SE signal. At $T = 0$, intensities of the overlapping SE and GSB peaks are approximately the same (see Figure S12, in which the spectra are presented without rescaling), while the subsequent decrease of the SE intensity with T is caused by the population transfer from the bright B_{2u} state to the dark A_u/B_{3u} states. At $T = 20$ fs, the SE peak exhibits a significant redshift, which reflects the movement of the wave packet toward the minimum of the B_{2u} surface, where the conical intersection with the B_{3u} surface is located. The snapshot at $T = 35$ fs reflects the bifurcation of the wave packet at the B_{2u}/B_{3u} conical intersection. The cross peak located at $\hbar\omega_\tau = 5.0$ eV, $\hbar\omega_t = 3.5$ eV represents emission from the nominally dark $B_{3u}(n\pi^*)$ state which borrows intensity from the bright $B_{2u}(\pi\pi^*)$ state. The waiting time $T = 60$ fs was selected because the population of the A_u state exhibits a local maximum at this moment, while the B_{2u} and B_{3u} populations exhibit local minima (Figure 2b). The extension of the SE peak toward lower values of $\hbar\omega_t$ at $T = 60$ fs reflects the emission from the flat PE minimum of the vibronically coupled A_u and B_{3u} states which borrow the emission intensity from the B_{2u} state. The intensity of the SE signal fades away along the time coordinate, which is not visible in Figure 3 due to the scaling of the intensity. The intensity of the SE signal at $T = 20$ fs is about half of the intensity at $T = 0$ and the SE intensity at $T = 35$ fs is one-fourth of the intensity at $T = 20$ fs. The ab initio quasiclassical SE signal is in good qualitative agreement with the SE signal simulated with quantum wave packet dynamics for an ab initio based three-state nine-mode model of the excited states of pyrazine.[20]

The third row of Figure 3 displays the ESA signal. It is overall considerably more intense than the SE signal. The ESA signal shows a rich structure of dynamically varying absorption peaks which are aligned along $\hbar\omega_\tau = 5.0$ eV and cover a range from about 5.8 eV down to below 1.8 eV in $\hbar\omega_t$. Because of the high density of electronic states in manifold {II}, the detailed assignment of the ESA signal is challenging. However, the number of strong ESA transitions from the B_{2u}, B_{3u}, and A_u states is limited and the transitions can be classified in terms of diabatic molecular orbitals and electronic configurations. Interestingly, the strong geometry dependence of the adiabatic molecular orbitals, which is the characteristic signature of vibronic coupling, takes place in the frontier orbitals associated with the lower excited electronic states of the manifold {I}, while the higher-lying states of the manifold {II} involved in the ESA signal do not show this phenomenon. In other words, the strong vibronic mixing effects seem to occur in the B_{2u}, B_{3u}, and A_u states of manifold {I}, while the upper excited states of manifold {II} appear to be mostly spectators.

A detailed analysis of the most intense ESA transitions is given in section S2. The analysis is relatively simple at the reference geometry of high symmetry (D_{2h}), where molecular orbitals and electronic configurations can be classified by their symmetry (Figures S1−S3). When diabatic orbitals are employed, this analysis can be extended one-to-one to the Wigner sample of initial conditions which covers the zero-point amplitudes of all normal modes. In the diabatic picture, these classifications of ESA transitions can also qualitatively be extended to the waiting times $T = 20$ fs and $T = 35$ fs. Interestingly, we find only "particle-type" transitions, in which the electron in the ground-state LUMO is excited to higher π^* orbitals, or "hole-type" transitions, in which the hole in the $6a_g(n)$ orbital is filled by transitions out of lower occupied orbitals (Figures S1−S3).

The ESA signal for $T = 0$ exhibits a series of peaks along the line $\hbar\omega_\tau = 5.0$ eV (Figure 3). The most intense ESA peak at $\hbar\omega_t = 5.7$ eV is the characteristic ESA signal of the B_{2u} state. It represents a particle-type transition from the $2b_{3u}$ orbital (LUMO of the ground state) to the fully antibonding $2b_{2g}(\pi^*)$ orbital (Figure S5a). The weaker peak at $\hbar\omega_t = 4.0$ eV represents a hole-type transition from the $1b_{3u}$ orbital to the half occupied $1b_{1g}$ orbital (Figure S5b). The very weak peak at $\hbar\omega_t = 2.8$ eV originates from a hole-type transition from the $3b_{3g}$ orbital to the half occupied $1b_{1g}$ orbital (Figure S5c). This transition is forbidden in the D_{2h} symmetry of the reference geometry and gains its weak intensity by symmetry-lowering vibrational distortions in the Wigner sample.

At $T = 20$ fs, the ESA spectrum shows two intense peaks at $\hbar\omega_\tau = 5.0$ eV which are strongly broadened along $\hbar\omega_t$ (Figure 3). The intensity profile of these peaks along $\hbar\omega_t$ is displayed in Figure S6b. It reveals that these intensity maxima are overlapping composite peaks. All three valence excited states of pyrazine contribute to these peaks. The assignments of these ESA transitions are given in Figure S7. The peak at $\hbar\omega_t = 5.3$ eV arising from the B_{2u} state is the same transition as at $T = 0$, red-shifted by 0.3 eV. The B_{3u} state gives rise to a peak at $\hbar\omega_t = 4.3$ eV which is assigned as a $2b_{3u} \rightarrow 2b_{2g}$ particle-type orbital transition (Figure S7c). Despite the relatively low population (25%) of the A_u state at $T = 20$ fs, this state shows up in the ESA spectrum via intense peaks at $\hbar\omega_t = 4.0$ eV and $\hbar\omega_t = 5.5$ eV (Figure S6b). One of them is a particle-type transition, the other a hole-type transition (Figure S7a,d). The ESA signal thus clearly reflects the ultrafast radiationless transition from the B_{2u} state to the B_{3u} and A_u states around $T = 20$ fs.

At $T = 35$ fs, an intense ESA peak at $\hbar\omega_\tau = 5.0$ eV is observed which is strongly elongated along $\hbar\omega_t$ (Figure 3). The intensity profile along $\hbar\omega_t$ is shown in Figure S8b. ESA transitions from the B_{3u} state and the A_u state contribute to this broad peak (Figure S8b). Another intensity maximum occurs near $\hbar\omega_t = 1.5-1.8$ eV which also reflects ESA transitions from the B_{3u} and A_u states. The orbital transitions are assigned in Figure S9a−d. The characteristic ESA transition of the B_{2u} state is no longer observed at $T = 35$ fs, although the B_{2u} population has not yet completely decayed.

The ESA spectrum at $T = 60$ fs is characterized by an intense peak near $\hbar\omega_t = 2.0$ eV and a less intense peak at $\hbar\omega_t = 4.4$ eV (Figure 3). Two transitions from the A_u state and one transition from the B_{3u} state can be identified (Figure S10b). The orbital configurations of these transitions are assigned in Figure S11a−c. At $T = 60$ fs, the population of the A_u state exhibits a local maximum (Figure 2b) and transitions from the A_u state correspondingly dominate the ESA spectrum. The following maxima of the A_u population (at $T \approx 95$ and 130 fs, Figure 2b) also are reflected by intense ESA peaks near $\hbar\omega_t = 4.0$ eV (SI movie). The ESA peak at $\hbar\omega_\tau \approx 5.0$ eV and $\hbar\omega_t \approx 4.0$ eV is thus a fingerprint of the population of the A_u state.

The total 2D signal is displayed in the lowest row of Figure 3. At $T = 0$, the GSB peak at $\hbar\omega_t = 5.0$ eV is accompanied by a strong ESA signal of the B_{2u} state at $\hbar\omega_t = 5.7$ eV and a weaker one at $\hbar\omega_t = 4.0$ eV. In the $T = 20$ fs spectrum, the ESA peaks arising from the B_{3u} and A_u states near $\hbar\omega_t = 4.0$ eV are clearly visible. In the $T = 35$ fs signal, the ESA peak from the B_{3u} state has moved below the GSB peak as a function of $\hbar\omega_t$. At $T = 60$ fs, the high transient population of the A_u state is reflected by the intense ESA peaks at $\hbar\omega_t = 2.0$ and 4.0 eV.

https://doi.org/10.1021/acs.jpclett.1c03589
J. Phys. Chem. Lett. 2021, 12, 11736−11744

While the ESA contribution to the transient-absorption pump−probe signals of pyrazine simulated in ref 43 clearly reveals the wave packet motion in manifold {I}, the detailed interpretation of the features is hardly possible due to significant spectral overlap of the contributions from different electronic states of manifold {II}. It is the spectral resolution along of ω_τ in the 2D signal which allows the decomposition of the ESA signal into a series of peaks, the origin of which can be traced back to transitions between specific electronic states. This finding illustrates the higher information content of 2D spectroscopy in comparison with transient-absorption pump−probe spectroscopy.

The ultrafast nonadiabatic photodynamics of pyrazine presumably has been more extensively investigated by theory and is more thoroughly understood than the photodynamics of any other polyatomic chromophore. Pyrazine therefore represents a natural benchmark system for the ab initio simulation of femtosecond time-resolved nonlinear spectra. Experimentally, the photodynamics of pyrazine was studied by Suzuki and co-workers with femtosecond time-resolved photoelectron spectroscopy (TRPES) in the UV[66−68] and very recently by Leone and co-workers with femtosecond X-ray absorption spectroscopy.[69] The transient population of the dark A_u state in the photophysics of pyrazine has become a controversially discussed topic in the recent literature.[66,69−71] While Suzuki and co-workers could not find evidence for the intermediate population of the A_u state,[66−68] Leone and co-workers reported detection of population in the A_u state with a time delay of 200 fs.[69] A recent computational simulation of the TRPES of pyrazine confirmed that the A_u population indeed cannot be clearly distinguished from the B_{3u} population in TRPES.[71] According to quantum dynamics calculations for an ab initio based three-state nine-mode model of pyrazine[65] as well as full-dimensional ab initio quasiclassical SH simulations for pyrazine,[53] the (diabatic) B_{3u} and A_u states are comparably populated already after 50 fs (Figure 2b). In view of the 200 fs overall time resolution of the X-ray absorption experiment,[69] this experimental result is not in contradiction with the ab initio theoretical predictions. The issue could be further clarified by 2D spectroscopy in the UV with a time resolution which is better than 10 fs. According to the present predictions, the B_{3u} population gives rise to peaks with oscillatory intensity at $\hbar\omega_t \approx 4.8$ eV in the 2D spectrum, while the A_u population gives rise to peaks with oscillatory intensity at $\hbar\omega_t \approx 4.4$ and 2.0 eV (Figure 3 and the SI movie). The example of pyrazine suggests that the ultrafast photodynamics of biologically relevant chromophores, such as DNA bases or aromatic amino acids, can potentially be dissected in exquisite detail with high-resolution 2D spectroscopy in the UV.

■ ASSOCIATED CONTENT

Supporting Information

The Supporting Information is available free of charge at https://pubs.acs.org/doi/10.1021/acs.jpclett.1c03589.

Derivation of classical DW approximation for 2D spectra, analysis of the most intense ESA transitions of pyrazine (PDF)

Movie showing ESA signal up to 200 fs (AVI)

■ AUTHOR INFORMATION

Corresponding Author

Maxim F. Gelin − *School of Sciences, Hangzhou Dianzi University, Hangzhou 310018, China;* orcid.org/0000-0003-3092-3343; Email: maxim@hdu.edu.cn

Authors

Xiang Huang − *Department of Chemistry, Technical University of Munich, Garching D-85747, Germany*

Weiwei Xie − *Institute of Physical Chemistry, Karlsruhe Institute of Technology, Karlsruhe 76131, Germany;* orcid.org/0000-0001-8224-5340

Nađa Došlić − *Department of Physical Chemistry, Ruder Boscovic Institute, Zagreb HR-10000, Croatia;* orcid.org/0000-0001-6535-9020

Wolfgang Domcke − *Department of Chemistry, Technical University of Munich, Garching D-85747, Germany;* orcid.org/0000-0001-6523-1246

Complete contact information is available at: https://pubs.acs.org/10.1021/acs.jpclett.1c03589

Notes

The authors declare no competing financial interest.

■ ACKNOWLEDGMENTS

W.X. acknowledges support by a research project of the Virtual Material Design (VirtMat) program. W.D. acknowledges support by a grant of the Deutsche Forschungsgemeinschaft (DO 256/42-2). N.D. acknowledges support by the Institute Linkage Program of the Alexander von Humboldt Foundation and by the Croatian Science Foundation (Grant HRZZ IP-2016-06-1142). M.F.G. acknowledges support from the Hangzhou Dianzi University through startup funding. We are grateful to Lipeng Chen for useful discussions and suggestions. M.F.G. thanks Zhenggang Lan for stimulating discussions.

■ REFERENCES

(1) Jonas, D. M. Optical Analogs of 2D NMR. *Science* **2003**, *300*, 1515−1517.

(2) Tian, P.; Keusters, D.; Suzaki, Y.; Warren, W. S. Femtosecond Phase-Coherent Two-Dimensional Spectroscopy. *Science* **2003**, *300*, 1553−1555.

(3) Brixner, T.; Stenger, J.; Vaswani, H. M.; Cho, M.; Blankenship, R. E.; Fleming, G. R. Two-Dimensional Spectroscopy of Electronic Couplings in Photosynthesis. *Nature* **2005**, *434*, 625−628.

(4) Engel, G. S.; Calhoun, T. R.; Read, E. L.; Ahn, T.-K.; Mančal, T.; Cheng, Y.-C.; Blankenship, R. E.; Fleming, G. R. Evidence for Wavelike Energy Transfer Through Quantum Coherence in Photosynthetic Systems. *Nature* **2007**, *446*, 782−786.

(5) West, B. A.; Womick, J. M.; Moran, A. M. Probing Ultrafast Dynamics in Adenine With Mid-UV Four-Wave-Mixing Spectroscopies. *J. Phys. Chem. A* **2011**, *115*, 8630−8637.

(6) West, B. A.; Moran, A. M. Two-Dimensional Electronic Spectroscopy in the Ultraviolet Wavelength Range. *J. Phys. Chem. Lett.* **2012**, *3*, 2575−2581.

(7) Tseng, C.-h.; Sandor, P.; Kotur, M.; Weinacht, T. C.; Matsika, S. Two-Dimensional Fourier Transform Spectroscopy of Adenine and Uracil Using Shaped Ultrafast Laser Pulses in the Deep UV. *J. Phys. Chem. A* **2012**, *116*, 2654−2661.

(8) West, B. A.; Molesky, B. P.; Montoni, N. P.; Moran, A. M. Nonlinear Optical Signatures of Ultraviolet Light-Induced Ring Opening in α-Terpinene. *New J. Phys.* **2013**, *15*, 025007.

(9) Krebs, N.; Pugliesi, I.; Hauer, J.; Riedle, E. Two-Dimensional Fourier Transform Spectroscopy in the Ultraviolet With Sub-20 fs

Pump Pulses and 250−720 Supercontinuum Probe. *New J. Phys.* **2013**, *15*, 085016.
(10) Kitney-Hayes, K. A.; Ferro, A. A.; Tiwari, V.; Jonas, D. M. Two-Dimensional Fourier Transform Electronic Spectroscopy at a Conical Intersection. *J. Chem. Phys.* **2014**, *140*, 124312.
(11) Prokhorenko, V. I.; Picchiotti, A.; Pola, M.; Dijkstra, A. G.; Miller, R. J. D. New Insights into the Photophysics of DNA Nucleobases. *J. Phys. Chem. Lett.* **2016**, *7*, 4445−4450.
(12) Johnson, P. J. M.; Farag, M. H.; Halpin, A.; Morizumi, T.; Prokhorenko, V. I.; Knoester, J.; Jansen, T. L. C.; Ernst, O. P.; Miller, R. J. D. The Primary Photochemistry of Vision Occurs at the Molecular Speed Limit. *J. Phys. Chem. B* **2017**, *121*, 4040−4047.
(13) Borrego-Varillas, R.; Ganzer, L.; Cerullo, G.; Manzoni, C. Ultraviolet Transient Absorption Spectrometer With Sub-20-fs Time Resolution. *Appl. Sci.* **2018**, *8*, 989.
(14) Mukamel, S.; Abramavicius, D. Many-Body Approaches for Simulating Coherent Nonlinear Spectroscopies of Electronic and Vibrational Excitons. *Chem. Rev.* **2004**, *104*, 2073−2098.
(15) Abramavicius, D.; Palmieri, B.; Voronine, D. V.; Sanda, F.; Mukamel, S. Coherent Multidimensional Optical Spectroscopy of Excitons in Molecular Aggregates; Quasiparticle vs Supermolecule Perspective. *Chem. Rev.* **2009**, *109*, 2350−2408.
(16) Tempelaar, R.; van der Vegte, C. P.; Knoester, J.; Jansen, T. L. C. Surface Hopping Modeling of Two-Dimensional Spectra. *J. Chem. Phys.* **2013**, *138*, 164106.
(17) Jain, A.; Petit, A. S.; Anna, J. M.; Subotnik, J. E. Simple and Efficient Theoretical Approach To Compute 2D Optical Spectra. *J. Phys. Chem. B* **2019**, *123*, 1602−1617.
(18) Farag, M. H.; Jansen, T. L. C.; Knoester, J. The Origin of Absorptive Features in the Two-Dimensional Electronic Spectra of Rhodopsin. *Phys. Chem. Chem. Phys.* **2018**, *20*, 12746−12754.
(19) Krčmář, J.; Gelin, M. F.; Domcke, W. Simulation of Femtosecond Two-Dimensional Electronic Spectra of Conical Intersections. *J. Chem. Phys.* **2015**, *143*, 074308.
(20) Sun, K.; Xie, W.; Chen, L.; Domcke, W.; Gelin, M. F. Multi-Faceted Spectroscopic Mapping of Ultrafast Nonadiabatic Dynamics Near Conical Intersections: A Computational Study. *J. Chem. Phys.* **2020**, *153*, 174111.
(21) Chen, L.; Sun, K.; Shalashilin, D. V.; Gelin, M. F.; Zhao, Y. Efficient Simulation of Time- and Frequency-Resolved Four-Wave-Mixing Signals with a Multiconfigurational Ehrenfest Approach. *J. Chem. Phys.* **2021**, *154*, 054105.
(22) Begušić, T.; Vaníček, J. On-the-fly Ab Initio Semiclassical Evaluation of Third-Order Response Functions for Two-Dimensional Electronic Spectroscopy. *J. Chem. Phys.* **2020**, *153*, 184110.
(23) Begušić, T.; Vaníček, J. Finite-Temperature, Anharmonicity, and Duschinsky Effects on the Two-Dimensional Electronic Spectra from Ab Initio Thermo-Field Gaussian Wavepacket Dynamics. *J. Phys. Chem. Lett.* **2021**, *12*, 2997−3005.
(24) Rivalta, I.; Nenov, A.; Cerullo, G.; Mukamel, S.; Garavelli, M. Ab Initio Simulations of Two-Dimensional Electronic Spectra: The SOS//QM/MM Approach. *Int. J. Quantum Chem.* **2014**, *114*, 85−93.
(25) Segarra-Marti, J.; Mukamel, S.; Garavelli, M.; Nenov, A.; Rivalta, I. Towards Accurate Simulation of Two-Dimensional Electronic Spectroscopy. *Top. Curr. Chem. (Z)* **2019**, *376:24*, 63.
(26) Borrego-Varillas, R.; Nenov, A.; Ganzer, L.; Oriana, A.; Manzoni, C.; Tolomelli, A.; Rivalta, I.; Mukamel, S.; Garavelli, M.; Cerullo, G. Two-Dimensional UV Spectroscopy: A New Insight into the Structure and Dynamics of Biomolecules. *Chem. Sci.* **2019**, *10*, 9907−9921.
(27) Conti, I.; Cerullo, G.; Nenov, A.; Garavelli, M. Ultrafast Spectroscopy of Photoactive Molecular Systems from First Principles: Where We Stand Today and Where We Are Going. *J. Am. Chem. Soc.* **2020**, *142*, 16117−16139.
(28) Nenov, A.; Mukamel, S.; Garavelli, M.; Rivalta, I. Two-Dimensional Electronic Spectroscopy of Benzene, Phenol, and Their Dimer: An Efficient First-Principles Simulation Protocol. *J. Chem. Theory Comput.* **2015**, *11*, 3755−3771.
(29) Nenov, A.; Rivalta, I.; Mukamel, S.; Garavelli, M. Bidimensional Electronic Spectroscopy on Indole in Gas Phase and in Water from First Principles. *Comput. Theor. Chem.* **2014**, *1040−1041*, 295−303.
(30) Nenov, A.; Borrego-Varillas, R.; Oriana, A.; Ganzer, L.; Segatta, F.; Conti, I.; Segarra-Marti, J.; Omachi, J.; Taioli, S.; Dapor, M.; et al. UV-Light-Induced Vibrational Coherences: The Key to Understand Kasha Rule Violation in trans-Azobenzene. *J. Phys. Chem. Lett.* **2018**, *9*, 1534−1541.
(31) Rivalta, I.; Nenov, A.; Weingart, O.; Cerullo, G.; Garavelli, M.; Mukamel, S. Modeling Time-Resolved Two-Dimensional Electronic Spectroscopy of the Primary Photoisomerization Event in Rhodopsin. *J. Phys. Chem. B* **2014**, *118*, 8396−8405.
(32) Nenov, A.; Segarra-Marti, J.; Giussani, A.; Conti, I.; Rivalta, I.; Dumont, E.; Jaiswal, V. K.; Altavilla, S. F.; Mukamel, S.; Garavelli, M. Probing Deactivation Pathways of DNA Nucleobases by Two-Dimensional Electronic Spectroscopy: First-Principles Simulations. *Faraday Discuss.* **2015**, *177*, 345−362.
(33) Borrego-Varillas, R.; Teles-Ferreira, D. C.; Nenov, A.; Conti, I.; Ganzer, L.; Manzoni, C.; Garavelli, M.; de Paula, A. M.; Cerullo, G. Observation of the Sub-200 fs Population of a Dark State in a Thiobase Mediating Intersystem Crossing. *J. Am. Chem. Soc.* **2018**, *140*, 16087−16093.
(34) Segarra-Marti, J.; Segatta, F.; Mackenzie, T. A.; Nenov, A.; Rivalta, I.; Bearpark, M. J.; Garavelli, M. Modeling Multidimensional Spectral Lineshapes from First Principles: Application to Water-Solvated Adenine. *Faraday Discuss.* **2020**, *221*, 219−244.
(35) Richter, M.; Fingerhut, B. P. Simulation of Multi-Dimensional Signals in the Optical Domain: Quantum-Classical Feedback in Nonlinear Exciton Propagation. *J. Chem. Theory Comput.* **2016**, *12*, 3284−3294.
(36) Yan, Y. J.; Fried, L. E.; Mukamel, S. Ultrafast Pump-Probe Spectroscopy: Femtosecond Dynamics in Liouville Space. *J. Phys. Chem.* **1989**, *93*, 8149−8162.
(37) Yan, Y. J.; Mukamel, S. Femtosecond Pump-Probe Spectroscopy of Polyatomic Molecules in Condensed Phases. *Phys. Rev. A: At., Mol., Opt. Phys.* **1990**, *41*, 6485.
(38) Fried, L. E.; Mukamel, S. Classical Theory of Pump-Probe Photodissociation for Arbitrary Pulse Durations. *J. Chem. Phys.* **1990**, *93*, 3063−3071.
(39) Gelin, M. F.; Kosov, D. S. Doorway-Window Description of Sequential Three-Pulse Photon Echo Signals. *Chem. Phys.* **2008**, *347*, 177−184.
(40) Gelin, M. F.; Domcke, W. Alternative View of Two-Dimensional Spectroscopy. *J. Chem. Phys.* **2016**, *144*, 194104.
(41) Li, Z.; Fang, J. Y.; Martens, C. C. Simulationof Ultrafast Dynamics and Pump-Probe Spectroscopy Using Classical Trajectories. *J. Chem. Phys.* **1996**, *104*, 6919−6929.
(42) Che, J.; Zhang, W.; Yan, Y. A Classical Time-Frequency Theory of Transient Absorption Spectroscopy. *J. Chem. Phys.* **1997**, *106*, 6947−6956.
(43) Gelin, M. F.; Huang, X.; Xie, W.; Chen, L.; Došlić, N.; Domcke, W. Ab Initio Surface-Hopping Simulation of Femtosecond Transient-Absorption Pump-Probe Signals of Nonadiabatic Excited-State Dynamics Using the Doorway-Window Representation. *J. Chem. Theory Comput.* **2021**, *17*, 2394−2408.
(44) Hu, D.; Peng, J.; Chen, L.; Gelin, M. F.; Lan, Z. Spectral Fingerprint of Excited-State Energy Transfer in Dendrimers through Polarization-Sensitive Transient-Absorption Pump-Probe Signals: On-the-Fly Nonadiabatic Dynamics Simulations. *J. Phys. Chem. Lett.* **2021**, *12*, 9710−9719.
(45) Cowan, M. L.; Ogilvie, J. P.; Miller, R. J. D. Two-Dimensional Spectroscopy Using Diffractive Optics Based Phase-Locked Photon Echos. *Chem. Phys. Lett.* **2004**, *386*, 184−189.
(46) Mukamel, S. Multidimensional Femtosecond Correlation Spectroscopies of Electronic and Vibrational Excitations. *Annu. Rev. Phys. Chem.* **2000**, *51*, 691−729.
(47) Hillery, M.; O'Connell, R.F.; Scully, M.O.; Wigner, E.P. Distribution Functions in Physics: Fundamentals. *Phys. Rep.* **1984**, *106*, 121−167.

https://doi.org/10.1021/acs.jpclett.1c03589
J. Phys. Chem. Lett. 2021, 12, 11736−11744

(48) Schirmer, J. Beyond the Random Phase Approximation: A New Approximation Scheme for the Polarization Propagator. *Phys. Rev. A: At., Mol., Opt. Phys.* **1982**, *26*, 2395−2416.
(49) Trofimov, A. B.; Schirmer, J. An Efficient Polarization Propagator Approach to Valence Electron Excitation Spectra. *J. Phys. B: At., Mol. Opt. Phys.* **1995**, *28*, 2299−2324.
(50) Møller, C.; Plesset, M. S. Note on an Approximation Treatment for Many-Electron Systems. *Phys. Rev.* **1934**, *46*, 618−622.
(51) Dreuw, A.; Wormit, M. The Algebraic Diagrammatic Construction Scheme for the Polarization Propagator for the Calculation of Excited States. *WIREs Comput. Mol. Sci.ence* **2015**, *5*, 82−95.
(52) Plasser, F.; Crespo-Otero, R.; Pederzoli, M.; Pittner, J.; Lischka, H.; Barbatti, M. Surface Hopping Dynamics with Correlated Single-Reference Methods: 9H-Adenine as a Case Study. *J. Chem. Theory Comput.* **2014**, *10*, 1395−1405.
(53) Xie, W.; Sapunar, M.; Došlić, N.; Sala, M.; Domcke, W. Assessing the Performance of Trajectory Surface Hopping Methods: Ultrafast Internal Conversion in Pyrazine. *J. Chem. Phys.* **2019**, *150*, 154119.
(54) Milovanović, B.; Novak, J.; Etinski, M.; Domcke, W.; Došlić, N. Simulation of UV Absorption Spectra and Relaxation Dynamics of Uracil and Uracil−Water Clusters. *Phys. Chem. Chem. Phys.* **2021**, *23*, 2594−2604.
(55) Tuna, D.; Lefrancois, D.; Wolański, Ł; Gozem, S.; Schapiro, I.; Andruniow, T.; Dreuw, A.; Olivucci, M. Assessment of Approximate Coupled-Cluster and Algebraic-Diagrammatic-Construction Methods for Ground- and Excited-State Reaction Paths and the Conical-Intersection Seam of a Retinal-Chromophore Model. *J. Chem. Theory Comput.* **2015**, *11*, 5758−5781.
(56) *TURBOMOLE*, ver. 6.3.1; A development of the University of Karlsruhe and Forschungszentrum Karlsruhe GmbH, 1989−1977; TURBOMOLE GmbH, 1989.
(57) Belyaev, A. K.; Lebedev, O. V. Nonadiabatic Nuclear Dynamics of Atomic Collisions Based on Branching Classical Trajectories. *Phys. Rev. A: At., Mol., Opt. Phys.* **2011**, *84*, 014701.
(58) Belyaev, A. K.; Lasser, C.; Trigila, G. Landau-Zener Type Surface Hopping Algorithm. *J. Chem. Phys.* **2014**, *140*, 224108.
(59) Belyaev, A. K.; Domcke, W.; Lasser, C.; Trigila, G. Nonadiabatic Nuclear Dynamics of the Ammonia Cation Studied by Surface Hopping Classical Trajectory Calculations. *J. Chem. Phys.* **2015**, *142*, 104307.
(60) Tully, J. C. Molecular Dynamics with Electronic Transitions. *J. Chem. Phys.* **1990**, *93*, 1061−1071.
(61) Suchan, J.; Janos, J.; Slaviček, P. Pragmatic Approach to Photodynamics: Mixed Landau-Zener Surface Hopping with Inter-system Crossing. *J. Chem. Theory Comput.* **2020**, *16*, 5809−5820.
(62) Mukamel, S. *Principles of Nonlinear Optical Spectroscopy*; Oxford University Press: New York, 1995.
(63) Woywod, C.; Domcke, W.; Sobolewski, A. L.; Werner, H.-J. Characterization of the $S_1 - S_2$ Conical Intersection in Pyrazine by Ab Initio Multiconfiguration Self-Consistent-Fieldand Multireference Configuration-Interaction Methods. *J. Chem. Phys.* **1994**, *100*, 1400−1413.
(64) Raab, A.; Worth, G. A.; Meyer, H.-D.; Cederbaum, L. S. Molecular Dynamics of Pyrazine after Excitation to the S_2 Electronic State Using a Realistic 24-mode Model Hamiltonian. *J. Chem. Phys.* **1999**, *110*, 936−946.
(65) Sala, M.; Lasorne, B.; Gatti, F.; Guerin, S. The Role of the Low-Lying Dark $n\pi^*$ States in the Photophysics of Pyrazine: a Quantum Dynamics Study. *Phys. Chem. Chem. Phys.* **2014**, *16*, 15957−15967.
(66) Suzuki, Y.-I.; Fuji, T.; Horio, T.; Suzuki, T. Time-Resolved Photoelectron Imaging of Ultrafast $S_2 \rightarrow S_1$ Internal Conversion Through Conical Intersections in Pyrazine. *J. Chem. Phys.* **2010**, *132*, 174302.
(67) Horio, T.; Suzuki, Y.-I.; Suzuki, T. Ultrafast Photodynamics of Pyrazine in the Vaccum Ultraviolet Region Studied by Time-Resolved Photoelectron Imaging Using 7.8-eV Pulses. *J. Chem. Phys.* **2016**, *145*, 044307.
(68) Horio, T.; Spesyvtsev, R.; Nagashima, K.; Ingle, R. A.; Suzuki, Y.; Suzuki, T. Full Observation of Ultrafast Cascaded Radiationless Transitions from S_2 ($\pi\pi^*$) State of Pyrazine Using Vacuum Ultraviolet Photoelectron Imaging. *J. Chem. Phys.* **2016**, *145*, 044306.
(69) Scutelnic, V.; Tsuru, S.; Pápai, M. I.; Yang, Z.; Epshtein, M.; Xue, T.; Haugen, E.; Kobayashi, Y.; Krylov, A.; Møller, K. B.; Coriani, S.; Leone, S. X-Ray Transient Absorption Reveals the $^1A_u(n\pi^*)$ State of Pyrazine in Electronic Relaxation. *Nat. Commun.* **2021**, *12*, 5003.
(70) Kanno, M.; Mignolet, B.; Remacle, F.; Kono, H. Identification of an Ultrafast Internal Conversion Pathway of Pyrazine by Time-Resolved Vacuum Ultraviolet Photoelectron Spectrum Simulations. *J. Chem. Phys.* **2021**, *154*, 224304.
(71) Pitesa, T.; Sapunar, M.; Ponzi, A.; Gelin, M. F.; Došlić, N.; Domcke, W.; Decleva, P. Combined Surface-Hopping, Dyson Orbital, and B-Spline Approach for the Computation of Time-Resolved Photoelectron Spectroscopy Signals: The Internal Conversion of Pyrazine. *J. Chem. Theory Comput.* **2021**, *17*, 5098−5109.

https://doi.org/10.1021/acs.jpclett.1c03589
J. Phys. Chem. Lett. 2021, 12, 11736−11744